Hydrogen Adsorbents with High Volumetric Density: New Materials and System Projections

Donald J. Siegel (Primary Contact, UM), Alauddin Ahmed (UM), Yiyang Liu (UM), Adam Matzger (UM), Justin Purewal (Ford), Saona Seth (UM), Mike Veenstra (Ford), and Antek Wong-Foy (UM)

University of Michigan (UM)
Ann Arbor, MI 48109
Phone: (734) 764-4808
Email: djsiege@umich.edu

DOE Manager: Jesse Adams
Phone: (720) 356-1421
Email: Jesse.Adams@ee.doe.gov

Contract Number: DE-EE0007046
Subcontractor: Ford Motor Company, Dearborn, MI
Project Start Date: August 1, 2015
Project End Date: July 31, 2018

Acknowledgment: This material is based upon work supported by the U.S. Department of Energy's Office of Energy Efficiency and Renewable Energy (EERE) under the Fuel Cell Technologies Office (FCTO) under Award Number DE-EE0007046.

Overall Objectives

- Demonstrate metal-organic frameworks (MOFs) that exhibit high volumetric and gravimetric hydrogen densities simultaneously, and that exceed the performance of the benchmark adsorbent, MOF-5, at cryogenic conditions
- Project the performance of most promising compounds to the system level by parameterizing models developed by the Hydrogen Storage Engineering Center of Excellence (HSECoE)

Technical Targets

The outcomes of this project contribute to the optimization and assessment of hydrogen storage materials, and also provide input to models that project the performance of these materials at the system level. Insights gained from this study can be applied towards the development of materials that attempt to meet the DOE 2020 hydrogen storage targets, which are summarized in Table 0 below.

The ultimate success of this project rests upon developing MOFs that out-perform the baseline MOF-5 adsorbent. The table lists system-level technical targets compared to materials-level performance of the baseline MOF-5 adsorbent and to the values measured for several MOFs identified and demonstrated by this project: IRMOF-20, SNU-70, UMCM-9, and PCN-610/NU-100. Capacities are reported for two usable conditions: the first number refers to a temperature+pressure swing from 77 K, 100 bar to 160 K, 5 bar; the second value refers to an isothermal pressure swing at 77 K between 100 bar and 5 bar. All reported MOF capacities are reported at the materials-level and are based on single-crystal densities.

Table 0. Comparison of DOE 2020 system level hydrogen storage targets to the materials-levels capacities measured for several MOFs examined in this project.

Storage Parameter	Units	DOE 2020 Target (system level)	MOF-5 Baseline	Project Status: IRMOF-20	Project Status: SNU-70	Project Status: UMCM-9	Project Status: PCN-610 / NU-100
Gravimetric Capacity	wt.%	4.5	7.8 / 4.5	9.1 / 5.7	10.6 / 7.3	11.3 / 7.8	13.9 / 10.1
Volumetric Capacity	g·H_2/L	30	51.9 / 31.1	51 / 33.4	47.9 / 34.3	47.4 / 34.1	47.6 / 35.5

Overview

A high-capacity, low-cost method for storing hydrogen remains one of the primary barriers to the widespread commercialization of fuel cell vehicles. Although many storage technologies have been proposed, storage via adsorption remains one of the more promising approaches due to its fast kinetics, facile reversibility, and high gravimetric densities. Adsorbents struggle, however, in two key measures: volumetric density and operating temperature. For example, it is well known that high surface area adsorbents such as MOFs can achieve high gravimetric densities. Nevertheless, high volumetric densities are uncommon in these materials, and it has recently been suggested that total volumetric density and gravimetric density are inversely related beyond a threshold surface area. In the case of operating temperatures, the relatively weak enthalpy of H_2 adsorption implies that high hydrogen densities are possible only at cryogenic temperatures.

Although an ideal adsorbent would overcome both of these shortcomings, it is important to recognize that volumetric density and operating temperature are controlled by different factors: the former depends upon the adsorbent's structure, whereas the latter depends on the chemistry of the H_2-adsorbent interaction. Therefore, distinct approaches are needed to address these independent issues. While some effort has previously been devoted to increasing ΔH (e.g., MOFs with open metal sites), attempts to increase volumetric densities have received much less attention. This is unfortunate, as analysis by the HSECoE has indicated that vehicle range is highly sensitive to volumetric density. Consequently, the development of adsorbents that simultaneously achieve high volumetric and gravimetric hydrogen densities—while maintaining reversibility and fast kinetics—would constitute a significant advance. Moreover, these materials would serve as logical starting points for follow-on efforts aimed at increasing the operating temperature.

This project aims to circumvent the tradeoff between total volumetric and gravimetric hydrogen densities typical of most hydrogen adsorbents. This is accomplished by combining computational screening for promising compounds with experimental synthesis and measurement of hydrogen storage densities within those compounds. The ultimate goal is to demonstrate materials having balanced gravimetric and volumetric performance that can surpass the storage density of the benchmark compound, MOF-5. The performance of the most promising compounds are projected to the system level by parameterizing system models developed by the HSECoE.

Organization of this Final Report

This final project report is presented in two parts. **Part 1** describes efforts focused on materials development. This includes the identification, synthesis, and characterization of MOFs that exhibit high volumetric and gravimetric capacities simultaneously. **Part 2** describes the outcome of system-level modeling. These latter efforts include the measurement of temperature-dependent isotherms for the MOFs discussed in Part 1, parameterization of the HSECoE system models, and, finally, exercising those models to make predictions of system capacities for the materials described in Part 1. Additional data related to system-level issues is described in Appendix B.

PART 1: Materials Development

Introduction

Hydrogen is a promising vehicular fuel due to its high specific energy, renewability, and its ability to be produced and oxidized without CO_2 emissions.[1–3] However, due to the low volumetric density of H_2 gas, efficient and cost-effective storage of hydrogen remains a challenge.[1–3] To overcome this challenge, storage in solid adsorbents has received significant attention as an alternative to compression in high-pressure tanks.[1–4] Adsorbents have the potential to match or surpass the capacities typical of physical storage systems, while doing so at lower pressures and with the potential to reduce cost.[1]

Metal-organic frameworks (MOFs) are perhaps the most intensively-researched hydrogen adsorbents.[1,5–22] Microporous crystalline MOFs are formed by the self-assembly of inorganic metal clusters and organic linkers.[23–26] The many possible variations of these building blocks allow MOFs to exhibit a wide range of properties, some of which (e.g., surface area) are unmatched by other materials.[27–39] Although this design flexibility allows for the tuning of MOF properties, it also complicates the identification of optimal compositions, because the parameter space that must be searched is very large.[1]

Computational methods[40,41] have been of great value in accelerating this search.[7,8,10,16,17,42–51] In the case of hydrogen storage, high-throughput calculations have assisted in the identification of MOFs with the potential to achieve high capacities. These techniques also allow for the identification of property-performance trends, resulting in design guidelines.[52–54] Table 1 summarizes recent high-throughput studies of hydrogen storage in MOFs. These studies have examined real MOFs (i.e., based on crystal structures of synthesized compounds), and larger collections of hypothetical compounds, which are generated computationally.[8,9,50,51,55,56] For example, a recent study by the present authors identified MOFs that simultaneously exhibit high volumetric and gravimetric hydrogen densities from a database of 5,309 real compounds.[1] Promising MOFs were identified using Grand Canonical Monte Carlo calculations employing the pseudo-Feynman-Hibbs interatomic potential. [1,57–59] Consistent with the computational predictions, IRMOF-20 was demonstrated experimentally to exhibit an uncommon combination of

Table 1. Summary of recent high-throughput calculations of hydrogen storage in MOFs.

Database	Number of MOFs screened	H_2 storage condition	Literature
CoRE +UM (real) [12,40]	5309	Usable: (77 K, 100 bar) → (77 K, 5 bar) Usable: (77 & 298 K, 100 bar) → (77 & 298 K, 1 bar)	Ahmed et al. (2017) Thornton et al. (2017)
Northwestern (hypothetical)[55]	137 953	Usable: (77 & 298 K, 100 bar) → (77 & 298 K, 1 bar) Usable: (77 K, 100 bar) → (77 K, 2 bar) Total: 1, 50, and 100 atm at 77 K	Thornton et al. (2017) Bobbitt et al. (2016) Gomez et al. (2014)
ToBaCCo (hypothetical)[8]	13 512	Total: 100 bar at 130, 200, and 243 K Usable: (77 K, 100 bar) → (77 K, 5 bar)	Colón et al. (2017) Gómez-Gualdrón et al. (2016)
Mg-MOFs (hypothetical)[65]	18 383	Usable: (243 K, 100bar) → (243 K, 2 bar) Total: 243 K & 100 bar	Colón et al. (2014)
UM (real)[12]	~4000	Total: 77 K & 35 bar	Goldsmith et al. (2013)

high usable volumetric and gravimetric capacities.[1] Importantly, the measured capacities exceeded those of the benchmark compound MOF-5,[57,60] the record-holder for combined volumetric/gravimetric performance.[1]

The demonstration of IRMOF-20 raises the question 'is there anything better?' Indeed, many other databases of MOFs exist beyond those examined in Ref. 1. Nevertheless, to our knowledge a systematic assessment of hydrogen capacities across all publicly-available databases of real and hypothetical MOFs has not been reported. The present study expands upon prior work by casting a significantly wider net: by assembling a 'database of databases' nearly 500,000 real and hypothetical MOFs have been examined computationally. The most promising materials identified computationally were subsequently synthesized and characterized experimentally. Importantly, three MOFs with usable capacities surpassing that of IRMOF-20 have been demonstrated: SNU-70, UMCM-9, and PCN-610/NU-100. These materials establish a new high-water mark for usable hydrogen capacities in MOFs under physisorptive, pressure-swing conditions. Analysis of trends across the database reveals the existence of a 'volumetric ceiling' at ~40 g H_2/L. This ceiling highlights the need to develop new adsorbents that are specifically constructed to exhibit larger volumetric capacities. Counter to earlier studies of *total* hydrogen uptake in MOFs,[12] *usable* capacities in the highest performing materials identified here were found to be negatively correlated with density and volumetric surface area. Instead, usable capacities are maximized by increasing gravimetric surface area and porosity. These observations suggest that property-performance trends identified for total capacities may not apply to usable capacities.

Table 2. Details of the MOF meta-database, including the number of MOFs in a given database, the number with negligible internal surface area, and the number of compounds identified by GCMC that exceed the usable, pressure swing capacities of MOF-5 and IRMOF-20. Additional details can be found in Section S1.1 and Figure S1.

Database	No. of MOFs	No. with zero surface area	Capacity exceeds MOF-5	Exceeds IRMOF-20
Real MOFs:[12,40,41] UM+CoRE+CSD	15,235	2,950	405	102
Mail-order[51]	112	4	30	19
In-silico deliverable[50]	2,816	154	27	6
In-silico surface[62]	8, 885	283	236	77
MOF-74 analogs[11]	61	0	0	0
ToBaCCo[8]	13,512	214	135	72
Zr-MOFs[44]	204	0	126	35
Northwestern[55]	137,000	30,160	4,397	2,154
Univ. of Ottawa[56]	324,500	32,993	7,612	3,581
In-house	18	0	18	13
Total	493,458	66,758	12,986	6,059

Methodology

A database of 493,458 MOF crystal structures, summarized in Table 2, was compiled by combining 11 published databases.[8,12,40,41,44,50,51,56,61–63] This meta-database consists of both real and hypothetical MOFs: 15,235 real MOFs were included from the UM,[12] CoRE,[40] and CSD[41] databases; 478,205 hypothetical MOFs were aggregated from the

Northwestern,[55] University of Ottawa,[56] mail-order,[51] *in silico* deliverable,[50] *in silico* surface,[62] MOF-74 analogs,[11] ToBaCCo,[8] and Zr-MOFs[44] databases. Eighteen additional MOFs were included based on 'in-house' designs. These latter compounds include hypothetical functionalized MOFs, as well as modeled crystal structures of real MOFs (such as UMCM-9) whose structures exhibit extensive disorder and are absent from the CSD. Additional details regarding the database is available in Table S1.

Crystallographic properties of all MOFs – single crystal density, gravimetric and volumetric surface areas, pore volume, void fraction, largest pore diameter, and pore limiting diameter – were calculated using the Zeo++ code.[64] As an initial screen, total gravimetric (TG) and volumetric (TV) H_2 capacities were estimated at 77 K and 35 bar using the semi-empirical Chahine rule.[1,65] MOFs that surpassed the predicted capacity of MOF-5 under these conditions (TG > 8.4 wt.% and TV > 54.4 g H_2 per L),[65] amounting to 43,777 compounds, underwent further evaluation using Grand Canonical Monte Carlo (GCMC) calculations (see Section S1.4 for details), as described in an earlier study.[66] Usable capacities were calculated by GCMC assuming an isothermal pressure swing between 5 and 100 bar at 77 K. MOFs predicted to have usable capacities exceeding MOF-5 (4.5 wt.% and 31.1 g H_2/L) and IRMOF-20 (5 .7 wt.% and 33.4 g H_2/L) were identified and assessed for possible experimental characterization. Finally, the capacities for a subset of MOFs were predicted using GCMC under temperature + pressure swing conditions between 77 K/100 bar and 160 K/5 bar. Additional details regarding these calculations can be found in the SI.

Promising MOFs identified by computation were synthesized following procedures described in the literature. These included: SNU-70 (CSD refcode GEBPEK), PCN-610/NU-100 (CSD refcodes: HABQUY/GAGZEV), and UMCM-9 (CIF available in the Supporting Information).[18,67–69] With the exception of the PCN-610/NU-100 linker, all the metal salts and organic linkers were obtained from commercial sources. The linker for PCN-610/NU-100 was synthesized following the reaction scheme shown in Figure S2.[67,69] Notably, this synthetic scheme involves only three steps (figures S3-S5 show ligand characterization via NMR spectroscopy) leading to much higher yield of the final linker as compared to both reported procedures.[67,69] SNU-70 and PCN-610/NU-100 were activated by flowing supercritical CO_2.[70] UMCM-9 was activated by successive exchanges of the guest solvent in the MOF pores with DMF, DCM, and *n*-hexane, and subsequently applying vacuum.[71] MOFs were characterized by powder X-ray diffraction (PXRD) and surface areas were calculated from measured N_2 isotherms following the recommendations by Roquerol.[72] Figures S6 – S8 show the N_2 isotherms used in Brunauer-Emmett-Teller (BET) surface area measurements. Comparisons of measured and simulated powder X-ray diffraction patterns (Figures S9 – S11) confirm the crystallinity and phase purity of all three compounds. Hydrogen adsorption and desorption measurements were performed using a manometric Sievert's-type instrument (HPVA-200, Micromeritics Instrument Corporation). Additional details on MOF synthesis, activation, and characterization are provided in the SI.

Results and Discussion

Figure 1a shows the calculated usable volumetric (UV) capacities of the 43,777 MOFs examined with GCMC as a function of their usable gravimetric (UG) capacities. These capacities are compared to that of IRMOF-20, which was identified in prior work as having the best combination of gravimetric & volumetric capacities under these pressure-temperature conditions,[1] and to MOF-5, a benchmark MOF adopted by the Hydrogen Storage Engineering Center of Excellence (HSECoE).[3,60] Irrespective of the database used, Fig. 1a shows that volumetric capacities increase monotonically with increasing gravimetric capacity up to ~10 wt.%, at which point volumetric performance plateaus below ~40 g H_2/L. A similar trend was reported in our earlier study, which examined a smaller database containing 5,109 real MOFs.[1] Considering first the performance of the real MOFs,[12,40,41] only 102 compounds are predicted to exhibit usable capacities greater than that of IRMOF-20 on both a volumetric and gravimetric basis. Table S3 lists the 50 highest-capacity MOFs ranked according to volumetric H_2 density. Out of the identified compounds, ECOLEP exhibits the best UV performance, as well as an appealing UG capacity: 39 g H_2/L & 8.2 wt.%. On the other hand, the highest UG capacity (irrespective of UV) is predicted for BAZGAM (MOF-399): 34.3 g H_2/L & 19.3 wt. %.

Regarding the relative performance of the different databases, the capacities of the real MOFs mostly fall within a lower capacity region between 0-5 wt. % and 0-25 g/L. This behavior is again consistent with our prior study.[1] In contrast, compounds drawn from the hypothetical MOF databases can exhibit much higher capacities. For example, the Univ. of Ottawa database contains the largest number of MOFs that exceed IRMOF-20 in terms of UV and UG capacities; 3,581 MOFs surpass this threshold. Similarly, 2,154 and 222 MOFs from the Northwestern and remaining (combined) hypothetical MOF databases, respectively, show promise for achieving capacities in excess of IRMOF-20.[55,56] Tables S4-S10 list the 20 highest capacity MOFs from each database in Table 2 that exceed the volumetric capacity of IRMOF-20. The synthesizability of these hypothetical MOFs remains unclear.

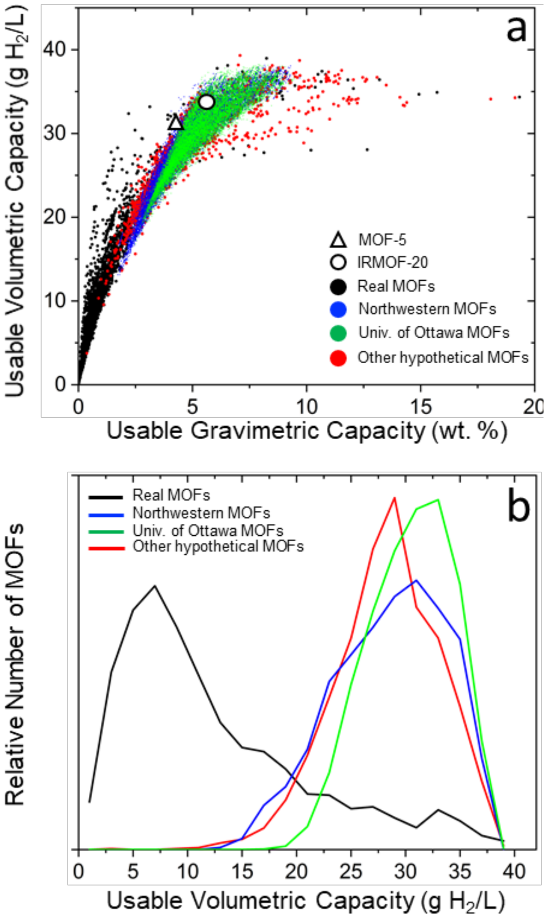

Figure 1. (a) Calculated usable hydrogen capacities of 43,777 MOFs compared to the measured capacity of IRMOF-20 (5.7 wt.%, 33.4 g/L) and MOF-5 (4.5 wt.% and 31.1 g/L). (b) Relative number of MOFs as a function of usable volumetric capacity and their originating database.

Figure 1b shows the relative number of MOFs having a given UV capacity as a function of the MOF database in which they are found. For the real MOFs the probability distribution is asymmetric and peaked at low capacities: the number of MOFs increases rapidly with UV up to a maximum around 7 g H_2/L, but then exhibits a long tail extending out to nearly 40 g H_2/L. In contrast, the distributions for the hypothetical MOF databases show opposite behavior: these distributions are skewed to higher UV, with maxima between 28 to 32 g H_2/L. As expected from Fig 1a, the distributions in Fig. 1b all approach zero for UV capacities approaching 40 g H_2/L. It is unclear if this 'volumetric ceiling' represents an intrinsic limitation of MOFs, or simply reflects the design decisions made in the assembly of the MOFs present in these databases. A maximum materials-level UV capacity of 40 g H_2/L could in principle surpass the DOE 2020 system level target of 30 g H_2/L, assuming modest volumetric penalties associated with the system. Nevertheless, a MOF below this ceiling could achieve neither the 2025 (40 g H_2/L) nor the Ultimate targets (50 g H_2/L).[4,73] Thus it is suggested that MOF designs that specifically target higher UV be pursued.

Several of the highest-capacity MOFs predicted by GCMC calculations were targeted for synthesis. These MOFs were selected based on their perceived stability and synthetic accessibility, in addition to their potential to exhibit high capacities exceeding that of IRMOF-20 and MOF-5. These considerations initially resulted in the selection of PCN-610/NU-100, SNU-70 (MOF-5_cooh_2_567_1_basic_opt), and ZELROZ. (Although ECOLEP was also predicted to have the highest UV capacity overall, it could not be synthesized in a phase-pure form.) Figure 2 illustrates the structures of these MOFs. PCN-610/NU-100 is a well-known MOF which was identified from the database of real MOFs.[12,40,41] To our knowledge its usable capacity for the pressure range 5-100 bar has not been

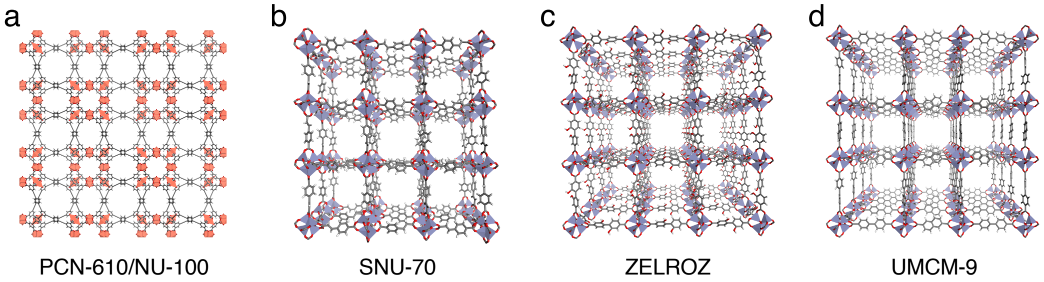

Figure 2. Crystal structures of MOFs whose hydrogen uptake was assessed experimentally following their identification by computational screening. (a) PCN-610/NU-100, (b) SNU-70, (c) ZELROZ and (d) UMCM-9 (C: gray, H: white, O: red, Cu: orange and Zn: blue).

reported. MOF-5_cooh_2_567_1_basic_opt is a hypothetical MOF identified from the mail-order MOF database.[51] Analysis of its structure revealed that is an ordered variant of the known MOF, SNU-70 (GEBPEK).[18] ZELROZ contains 2,2'-dihydroxy-[1,1'-biphenyl]-4,4'-dicarboxylate linkers and is isoreticular with MOF-5 and IRMOF-20.[74] Although it has a higher projected usable capacity than IRMOF-20, it could not be realized in a fully activated form; only ~70% of the calculated gravimetric surface area was achieved.

Further, the calculations also identified non-interpenetrated IRMOF-10 as having higher usable capacities than IRMOF-20 (Table S1). This MOF is an unfunctionalized variant of ZELROZ, and also contains the 1,1'-biphenyl-4,4'-dicarboxylate linker. [32] Unfortunately, the structure of IRMOF-10 is missing from the CSD, likely due to the presence of disorder. In addition, IRMOF-10 has never been obtained with high surface area, likely due to interpenetration or pore collapse during activation. As an alternative, a mixed linker-based approach was explored as a means to realize non-interpenetrated MOFs from 1,1'-biphenyl-4,4'-dicarboxylate linkers.[68] UMCM-9, containing 1,1'-biphenyl-4,4'-dicarboxylate and 2,6-naphthalenedicarboxylate linkers (Figure 2) is known to have a non-interpenetrated framework with high experimental gravimetric surface area. Its structure is, however, highly disordered and therefore is not present in the CSD. An ordered structure of the MOF was constructed for GCMC calculations, and favorable capacity predictions from these calculations prompted experimental investigation of its hydrogen storage capacity here. The present calculations on UMCM-9 employed a structure developed from powder diffraction data.[68]

Table 3 summarizes the measured and calculated crystallographic properties of these MOFs. (N_2 isotherms used in Brunauer-Emmett-Teller (BET) surface area measurements are shown in Figs. S10 – S12.) Correlations between these crystallographic properties and usable capacities are discussed below.

Figure 3 shows the measured H_2 adsorption isotherms of PCN-610/NU-100, SNU-70, and UMCM-9 at 77 K. Isotherms for IRMOF-20 and MOF-5 are also shown for comparison.[1] A comparison between the measured and

Table 3. Measured and calculated crystallographic properties of high-capacity MOFs examined in this study.

MOF	Gravimetric Surface Area (m^2/g) Expt. / Calc.	Volumetric Surface Area (m^2/cm^3) Calc.	Pore Volume (cm^3/g) Calc.	Void Fraction Calc.
MOF-5	3512 / 3563	2172	1.36	0.81
IRMOF-20	4073 / 4127	2000	1.65	0.84
SNU-70	4944 / 4756	1905	2.14	0.86
UMCM-9	5039 / 4847	1805	2.31	0.86
PCN-610/NU-100	6050 / 5777	1603	3.17	0.88

calculated isotherms are shown in Figures S12-S14. In general, good agreement is achieved between the measurements and calculations.

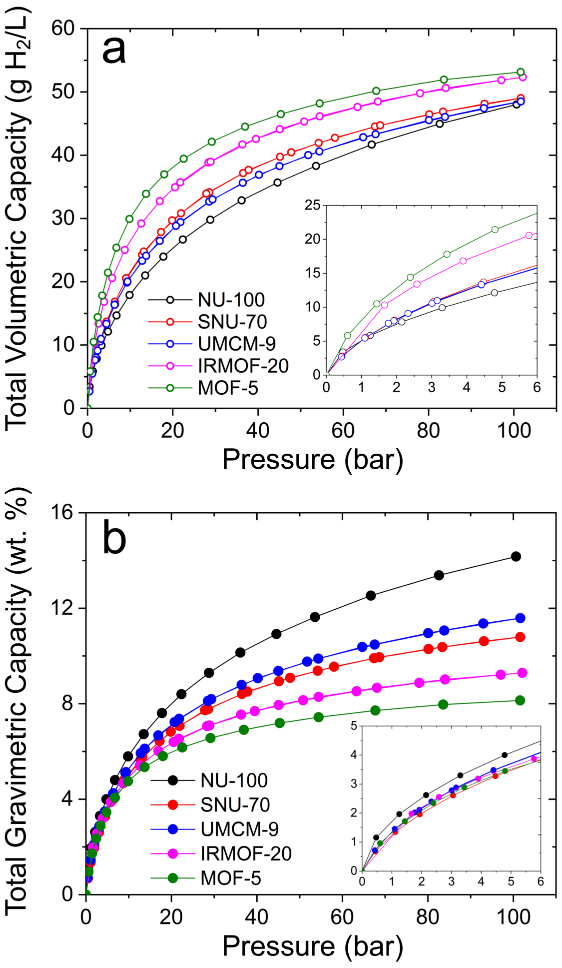

Figure 3. Measured total (a) volumetric and (b) gravimetric H_2 adsorption isotherms of NU-100, SNU-70, and UMCM-9 at 77 K. For comparison, isotherms (Ref 1) for the two benchmark MOFs, MOF-5 and IRMOF-20, are also shown.

Regarding the total volumetric capacities of these MOFs, Fig. 3a shows that MOF-5 and IRMOF-20 are, respectively, the two highest capacity MOFs for all pressures greater than ~1 bar. SNU-70, UMCM-9, and PCN-610/NU-100 all exhibit lower total capacities. Nevertheless, these latter three MOFs are superior on a *usable basis*, as shown in Figure 4a. UV capacities range from 34.1 to 35.5 g H_2/L, which exceed those of MOF-5 and IRMOF-20 (31.1 and 33.4 g H_2/L, respectively). To our knowledge these usable capacities are the highest demonstrated for an adsorbent under these conditions. The superior usable performance of these MOFs can be understood by recalling that usable capacity is defined as the difference in total uptake at 100 bar (filled tank condition) and at 5 bar (empty tank). A significantly lower total uptake at 5 bar (compared to MOF-5 & IRMOF-20), combined with a modest difference in uptake at 100 bar, results in a larger usable capacity.

Regarding total gravimetric capacities, Fig. 3b shows that the trio of MOFs examined here outperform the benchmark MOF-5 and IRMOF-20 compounds for pressures exceeding 10 bar. Below this pressure (Fig. 3b inset) all 5 MOFs behave similarly, while at high pressures PCN-610/NU-100 is clearly superior. The similar low-pressure total capacities imply that that usable capacities will track with the capacities observed at high pressure. Fig. 4b confirms that this is the case: usable gravimetric capacities range from 7.3 (SNU-70) to 10.1 (PCN-610/NU-100), surpassing those of MOF-5 (4.5 wt.%) and IRMOF-20 (5.7 wt.%).

These data show that PCN-610/NU-100 has the highest usable pressure-swing capacity overall, on both a gravimetric and volumetric basis. We previously reported that MOFs with high total gravimetric capacities typically exhibit total volumetric capacities that are unexceptional.[1] Consistent with that trend, Fig 3a shows that the total gravimetric capacity of PCN-610/NU-100 at 100 bar is the largest of the 5 MOFs examined, yet its total volumetric capacity is the lowest. Nevertheless, on a usable basis PCN-610/NU-100 emerges as a promising MOF due to its low uptake at 5 bar. Thus, we conclude that total capacities can be a poor indicator of useable capacity under pressure swing conditions.

How do these materials-level capacities compare to the DOE system-level targets? Due of penalties associated with the mass and volume of the storage system, to meet these targets a storage material will need to exceed the desired system capacity considerably. The usable gravimetric capacity of PCN-610/NU-100 exceeds the 2020 target^{4,73} (4.5 wt.%) by 124% and exceeds the Ultimate target^{4,73}(6.5 wt.%) by 55%. These values provide hope that a PCN-610/NU-100-based storage system could meet the targets, even when accounting for the mass of the system. In contrast, meeting the volumetric targets will be more challenging. PCN-610/NU-100 exceeds the DOE's 2020 system level target^{4,73} by only 18%, and falls 29% below the Ultimate targets.^{4,73} Factoring in the volume of components other than the storage medium, we conclude that a PCN-610/NU-100-based system is either unlikely (in the case of the 2020 target^{4,73}) or unable (Ultimate target^{4,73}) to satisfy the DOE goals. This shortcoming points to the importance of emphasizing volumetric hydrogen density in the design of new storage materials.

Do the properties of the MOFs characterized here correlate with their capacities? Figure 5 plots UV and UG capacities as a function of 5 crystallographic features: density (D), pore volume (PV), gravimetric & volumetric surface areas (GSA & VSA), and void fraction (VF). Roughly linear relationships are observed in all cases. Moreover, the same MOFs that bound the capacity range examined in Fig. 4, MOF-5 and PCN-610/NU-100, also bound the range of each crystallographic property. Usable capacities are positively correlated with pore volume (Fig. 5c-d), gravimetric surface area (Fig.

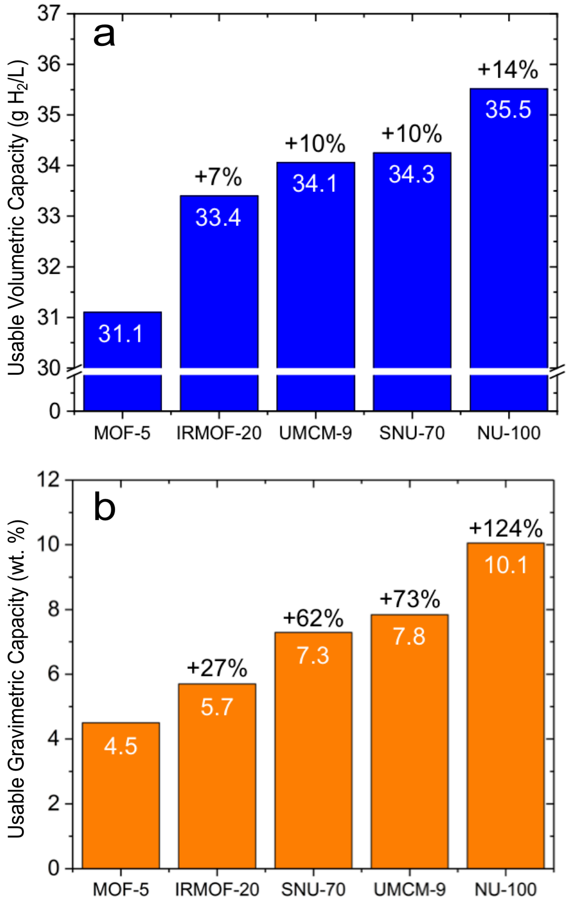

Figure 4. Measured usable H_2 storage capacities of MOFs synthesized in the present study on a (a) volumetric and (b) gravimetric basis. Capacities are reported for an isothermal pressure swing at 77 K between 5 and 100 bar. Data for MOF-5 and IRMOF-20 are taken from Ref. 1. Percentages listed at the top of each bar correspond to improvements over MOF-5.

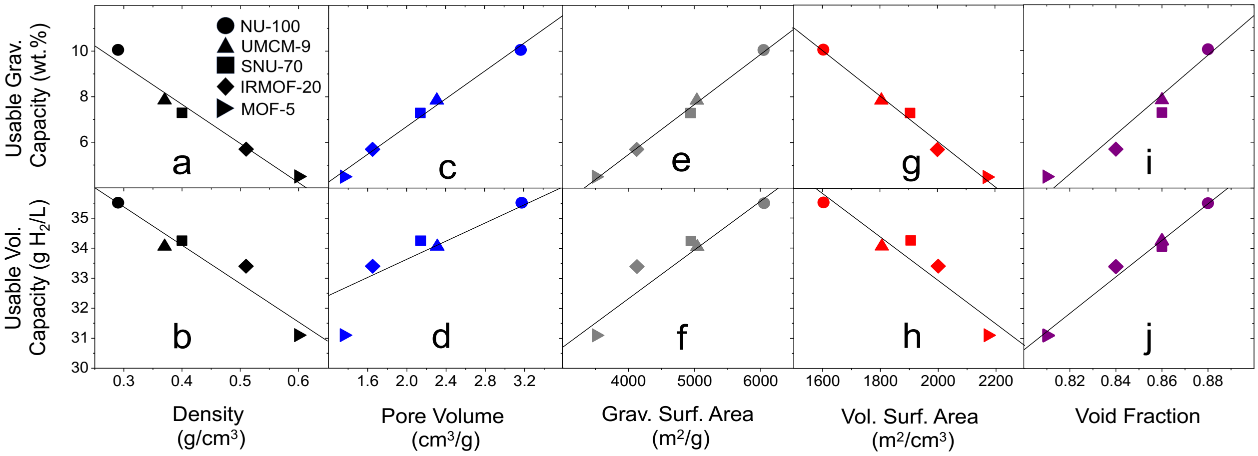

Figure 5. Relationship between five crystallographic properties and the usable capacities of the highest-capacity MOFs examined in the present study. Capacities are evaluated assuming an isothermal pressure swing between 5 and 100 bar at 77 K.

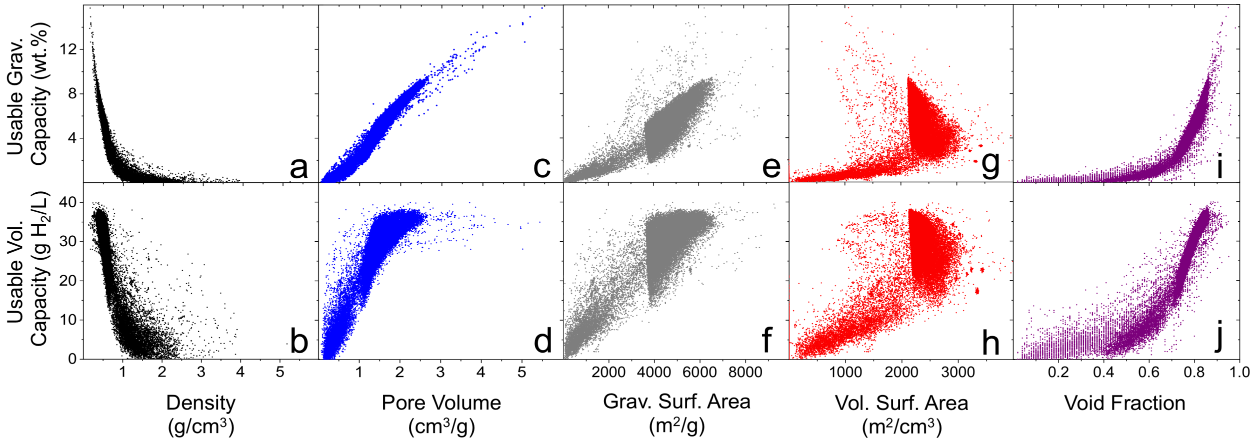

Figure 6. Usable gravimetric (top) and volumetric (bottom) capacities of ~43,000 MOFs as a function of five crystallographic properties, assuming pressure swing operation between 100 and 5 bar at 77 K.

5e-f), and void fraction(5i-j). In contrast, capacities are inversely related to single crystal density (Fig. 5a-b) and volumetric surface area (Fig. 5g-h). Thus, under these conditions, high usable capacities are achieved by maximizing pore volume, gravimetric surface area, and void fraction, while simultaneously minimizing density and volumetric surface area.

Figure 6 examines these capacity-property trends more broadly across the set of ~43,000 MOFs examined with GCMC calculations. Turning first to the properties which were revealed in Fig. 5 to correlate positively with capacity (PV, GSA, and VF), Fig. 6 demonstrates that these same trends generally hold across the entire MOF dataset: maximizing PV, GSA, and VF maximizes UV and UG capacities. In contrast, Fig. 6 reveals that the inverse correlations that hold for D and VSA for the highest-capacity MOFs (Fig. 5) do not apply generally. For example, Fig. 5a-b suggests that capacity can be maximized by minimizing D. While this is indeed true for the narrow range of D examined in Fig. 5a-b (0.3 to 0.6 g/cm³), Fig. 6a-b shows that capacity decreases for densities outside of this range. Thus, a 'sweet-spot' exists for D near 0.6 g/cm³. Similar behavior is observed for VSA: comparing Fig. 5g-h with Fig. 6g-h shows that VSA and usable capacity are in general related in a non-linear fashion. The linear relation observed in Fig. 5g-h is unique to the high-capacity MOFs examined here, and applies across a subset of VSA range from 1600 to 2200 m²/cm³.

Our analysis has thus far considered pressure swing operation of the storage system. An important advantage of this scheme is its simplicity. Nevertheless, higher capacities can be achieved by adopting a more complex operating scheme. For example, the HSECoE has proposed an alternative operating scenario involving a combined temperature and pressure swing (TPS) from T_{min} =77 K, P_{max} = 100 bar (filled) to T_{max} =160 K, P_{min} = 5 bar (empty).[3,60] By heating during desorption, the TPS approach increases capacity by minimizing the amount of H_2 retained in the MOF in the low-pressure 'empty' state.[4]

Figure 7 compares the measured usable TPS capacities of the present MOFs with the two highest-capacity MOFs identified in a recent study by García-Holley et al.,[75] NU-1103 and NU-125, and with the benchmark compounds MOF-5 and IRMOF-20.[1] Regarding volumetric capacities, Fig. 7a reveals that MOF-5 remains the top MOF (as previously noted),[1] followed closely by IRMOF-20. The three MOFs identified in the present study as having high-capacities under pressure swing (PS) conditions surpass the TPS capacity of NU-1103, but fall slightly below that of NU-125.[75] Assuming PS operation, the usable volumetric capacity of NU-125 is 24 g/L, which is ~30% less than that of SNU-70 and UMCM-9, and ~32% less than that of PCN-610/NU-100. Additionally, the three MOFs

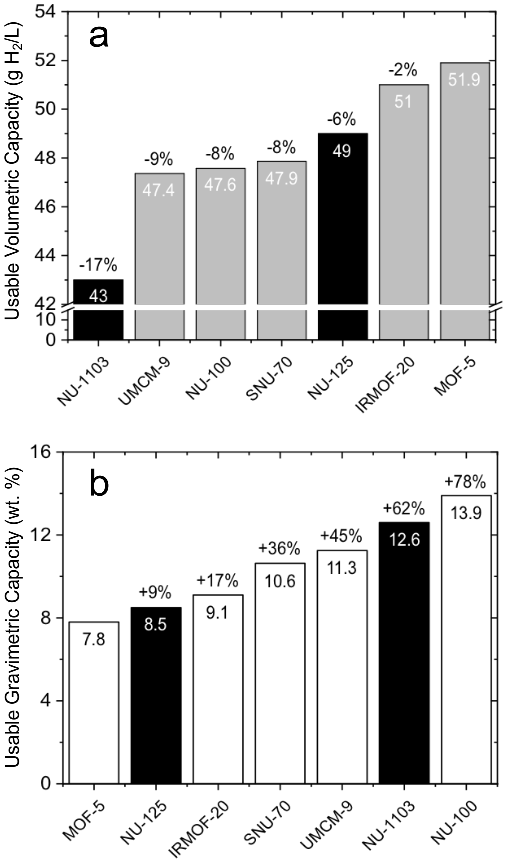

Figure 7. Comparison of measured usable (a) volumetric and (b) gravimetric H_2 storage capacities of MOFs assuming temperature+pressure swing operation between 100 bar-77 K and 5 bar-160 K. Grey bars depict the performance of compounds reported in the present study or in the authors' earlier report.[1] Black bars depict the performance of two high-capacity MOFs reported in Ref. 75. Percentages on top of each bar depict performance relative to MOF-5.

synthesized here exhibit TPS volumetric capacities that surpass that of MFU-4*l* (47 g/L), the top performing compound recently identified via machine learning screening of 50,000 MOFs.[76]

Regarding gravimetric TPS capacities, Fig. 7b shows that PCN-610/NU-100 is the top-performer, with a capacity of 13.9 wt.%. This exceptional gravimetric capacity contrasts with its volumetric performance, Fig. 7a, which is comparable to that of UMCM-9 and SNU-70. An even larger tradeoff in gravimetric/volumetric performance is evident for MOF-5, whose gravimetric capacity is the smallest of the 7 MOFs considered here.

More generally, Fig. 7 reveals that no single MOF studied here excels both gravimetrically and volumetrically under TPS operation. This situation differs from PS operation, where Fig. 4 shows that PCN-610/NU-100 is unambiguously the highest-capacity MOF. An ideal MOF would balance gravimetric and volumetric performance. In this regard, IRMOF-20 and SNU-70 both exhibit an appealing combination of volumetric and gravimetric TPS capacities. Furthermore, SNU-70, like UMCM-9, is derived from a commercially-available linker and may therefore provide cost advantages relative to MOFs requiring multistep synthesis of linkers.

Summary – Materials Discovery

A systematic assessment of hydrogen storage capacities in MOFs drawn from all publicly-available MOF databases has been presented. The goal was to identify MOFs that exhibit a balance of high volumetric and gravimetric hydrogen capacities under usable, physisorptive operating conditions. In total, nearly 500,000 compounds were screened computationally, and the most promising materials identified were synthesized and assessed experimentally. Three MOFs with usable, pressure-swing capacities surpassing that of IRMOF-20, the record-holder for balanced hydrogen capacity (wherein gravimetric and volumetric capacities are both maximized), were demonstrated: SNU-70 (identified from a hypothetical, ordered variant), UMCM-9, and PCN-610/NU-100. A similar analysis of the capacities of these MOFs under temperature + pressure-swing conditions also revealed them to be high-capacity materials.

Analysis of trends across the database points toward the existence of a 'volumetric ceiling' at a capacity of ~40 g H_2/L. Surpassing this ceiling under usable, pressure-swing conditions is proposed as a new capacity target for hydrogen adsorbents. Counter to earlier studies of *total* hydrogen uptake in MOFs, *usable* capacities in the highest-capacity materials are negatively correlated with density and volumetric surface area. Instead, capacity is maximized by increasing gravimetric surface area and porosity. These observations suggest that property-performance trends identified for total capacities may not translate to usable capacities.

PART 2: SYSTEM MODELING

Introduction

Fuel cell vehicles store hydrogen on-board as a 700 bar compressed gas in expensive and bulky pressure vessels. An alternative hydrogen storage method is to pack high-surface area adsorbents into low pressure tanks (roughly 7 times lower) which are held at cryogenic temperatures. There are numerous benefits to this approach, including a lower working pressure which enables the use of lower-cost type-1 tanks. It can also benefit the refueling infrastructure by relaxing the extreme requirements on hydrogen compressors. Further, cryo-adsorption systems would take full advantage of a liquid hydrogen infrastructure pathway, in which hydrogen fuel is delivered as a cryogenic liquid (which would potentially be more efficient at high delivery and usage rates).

Many adsorbent materials have been studied to evaluate their potential storage capability, ranging from activated carbons to highly tunable metal-organic framework (MOF) materials. Interestingly, the much-studied metal-organic framework, $Zn_4O(BDC)_3$ (called MOF-5 and/or IRMOF-1), may still be considered as a benchmark material for hydrogen adsorbents due to its ability to adsorb hydrogen at both high gravimetric and volumetric capacities.[35] However, further improvements to the hydrogen storage capacities of adsorbents are required in order to match and surpass 700 bar compressed storage. In particular, the design and testing of sub-scale cryo- adsorbent systems based on MOF-5 has revealed that volumetric capacity (i.e., the mass of hydrogen stored within a specific volume) is a key material property of adsorbents which currently limits system performance.[3] While the gravimetric excess hydrogen adsorption amounts of MOFs at 77 K now exceed 9 wt.% (with BET surface areas exceeding 6000 m^2/g), the low crystal densities of such MOFs often limit or negate any corresponding increase in volumetric capacity.[12] Inefficient packing of low-density MOF powders within sorbent beds further erodes volumetric capacity.

Between 2009 and 2015 the Hydrogen Storage Engineering Center of Excellence (HSECoE) designed and built two sub-scale prototypes of a cryo-adsorption hydrogen storage system that utilized MOF-5 as the adsorbent.[3] Design details and performance data that emerged from these prototypes were used to develop a model that calculates the gravimetric and system storage capacities for a full scale cryo-adsorbent system with 5.6 kg of usable hydrogen.[77] Initial estimates (based on conservative assumptions for material-level MOF-5 properties) indicated that a cryo-adsorbent system was actually close to matching a 700 bar compressed system in terms of volumetric capacity.[78] Based on these findings, MOFs with moderately improved hydrogen storage capacities have to potential to surpass 700 bar compressed H_2 storage at the system level.

In this report we have evaluated the hydrogen adsorption properties for a number of high- surface-area MOFs which have the potential of surpassing MOF-5 in both volumetric and gravimetric storage capacity. Further, the effect of compaction density on hydrogen storage capacity is characterized for a number of the top performing MOFs. Material-level hydrogen storage proper- ties are then incorporated into a system model in order to estimate the hydrogen storage capacity at the system-level. Based on these findings, strategies are discussed for improving the system-level volumetric storage capacity.

Experimental Methods

BET Surface Area

Nitrogen BET surface areas were measured for each MOF immediately following H_2 adsorption isotherms (Micromeritics ASAP2420). Sample loading was performed inside a high-purity argon glovebox. Before transferring it out of the glovebox, a glass filler rod was inserted in the sample cell, and a seal frit with rubber O-ring was used to seal the sample cell and prevent exposure to moisture. Free space was calculated from the previously measured values for an empty sample cell and the measured sample skeletal density (typically measured during H_2 adsorption measurements).

Recent results have confirmed that the BET surface area, when calculated in a consistent manner, can be useful as a metric for comparing and benchmarking microporous MOFs.[79] In other words, when calculated according to the criteria in Ref. [72], the BET surface areas compare favorably with the physical surface area computed from molecular models of the defect-free MOF crystal structure. Therefore, the BET consistency criteria[72] have been followed when selecting N_2 adsorption data points to fit to the BET model.

Excess Hydrogen Adsorption

Hydrogen excess adsorption and desorption measurements were performed using a manometric Sievert's-type instrument (HPVA-2, Micromeritics). Excess adsorption is equal to the amount of gas present in the free space minus the amount of gas which would be present in that same volume if it were at the gas density (ρ_{gas}). Therefore, the excess adsorption is the extra amount of the gas present in the sample cell due to the enhanced hydrogen gas density within the sorbent pores. Defining the "free space" requires knowing the skeletal density (ρ_{sk}) of the sorbent, which can be thought of as the "hard" volume which is impenetrable to helium (and hydrogen) gas. For a porous material this can include closed pores which even helium molecules cannot reach, but does not include inter-particle, inter-granular or inter-crystallite spaces. The free space is defined as

$$V_{fs} = V_{ext} - \frac{m}{\rho_{sk}} \tag{1}$$

where V_{ext} is the external geometrical volume of interest (which could be the volume of the empty sample cell, or the volume of a hypothetical single crystal sample of MOF, or the geometrical volume of a pellet), and m is the mass of sorbent loaded in the sample cell.

Free space measurements were performed using helium at room temperature to estimate both the internal volume of an empty sample cell, and the skeletal density (ρ_{sk}) of the microporous sample. The free space was then calculated by subtracting the skeletal volume (i.e., $V_{sk} = m/\rho_{sk}$) from the empty sample cell volume as described in Eq. 1.

With the exception of room temperature measurements, hydrogen adsorption measurements were performed with the sample cell immersed in a cryogenic bath. The ambient volume (sub-volume at room temperature) and cold volume (sub-volume at sample temperature) of an empty sample cell were calibrated with the cryogenic bath filled to a marked level on the sample cell. A porous polymer isothermal jacket was strapped onto the sample stem to mitigate temperature fluctuations arising from evaporation of the cryogenic liquid and gradual lowering of the liquid level. Temperature was measured using a calibrated platinum resistance thermometer.

Hydrogen adsorption isotherms were measured at four temperatures using cryogenic liquid baths (77 K, 87 K), solvent slush baths (195 K) or at room temperature (297 K). To maintain a sample temperature of 195 K, the sample cell was immersed in a slurry prepared from solid CO_2 dry ice granules and isopropanol. Because the method in which the slurry is prepared was found to affect the temperature stability, a short description is provided. Large pellets of dry ice were ground up into a small granules and then mixed thoroughly with isopropanol in a small beaker. Successive batches were then transferred to a Dewar until the slurry level reached the required height on the sample cell stem. The temperature of the slurry remained steady within ±0.1 K during the span of the measurement.

Hydrogen adsorption measurements at variable MOF packing densities were performed by compacting the MOF sample directly within the sample cell to successively higher densities. The internal diameter of the sample cell was 4.6 mm and the internal depth was 39.4 mm. Powder MOF samples were loaded in the sample cell inside the glovebox and compacted to a specified density using a 4.5 mm outer diameter pellet press punch and die set. The same MOF sample was used for successive measurements without loading fresh MOF. It was assumed that the density remained constant during the adsorption measurements. The packing densities of the MOF was measured before and after each measurement and no change in density was detected. Skeletal density was measured only for the MOF at powder density and was assumed to not change as a result of compaction (while the skeletal density may decrease due to the formation of closed pores, the adsorption instrument as configured did not have the accuracy to detect such a small change in volume).

Total Hydrogen Storage

Total hydrogen volumetric and gravimetric capacities were calculated following recommended conventions.[80] The total adsorption is equal to the excess adsorption plus the H_2 present at normal gas density within the free space. Referring to Eq. 1, the external volume can be equal to the MOF crystal volume ($V_{ext} = m/\rho_{crystal}$), or it could be equal to the geometrical volume enclosing a packed powder ($V_{ext} = m/\rho_{pwd}$) or compacted pellet ($V_{ext} = m/\rho_{pellet}$). For generality, it is assumed that the external volume is defined by some type of sorbent packing density (ρ_x).

The amount of H_2 (in grams) stored per 1 L of sorbent (total volumetric storage) is

$$n_v = \rho_x n_{ex} + \rho_{gas}\left(1 - \frac{\rho_x}{\rho_{sk}}\right) \tag{2}$$

The units for density used in Eq. 2 can be confusing, as the skeletal (ρ_{sk}) and sorbent density (ρ_x) are both expressed in kg/L, while the units for the bulk H_2 gas density, ρ_{gas}, are expressed in g/L. Meanwhile, the excess adsorption n_{ex} is expressed in units of g/kg (grams H_2 per kg sorbent).

Material-level volumetric capacities are calculated from Eq. 2 using the MOF crystal density $\rho_x = \rho_{crys}$. The argument in favor of using the MOF crystal density, rather than the practical powder packing density, is that the crystal density reflects an intrinsic material property, making it more appropriate for comparisons between different MOFs.[81] However, it is the powder packing properties of MOFs that actually have a more significant impact on the practical system-level storage capacities. The total gravimetric storage capacity in wt. % may be calculated from the volumetric storage capacity,

$$n_g = \frac{n_v}{n_v + 1000 \times \rho_x} \times 100 \tag{3}$$

which follows the convention of including the combined mass of the adsorbent material and the stored hydrogen in the denominator

Usable Capacity

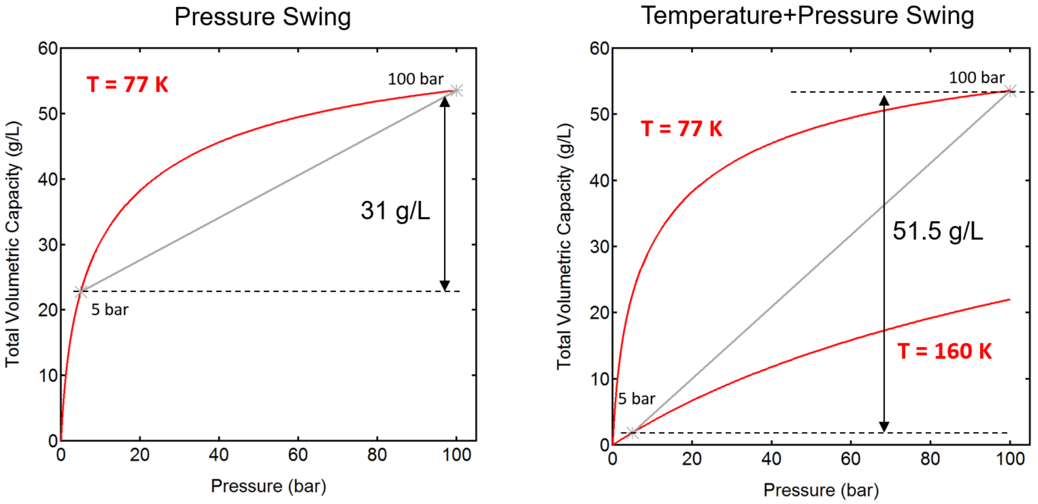

Figure 8: Two definitions of material-level H_2 storage capacity for MOF adsorbents. (left) Pressure swing (PS) between 100 bar and 5 bar at 77 K. (right) Temperature plus pressure swing (TPS) between 100 bar, 77 K and 5 bar, 160 K. MOF-5 data is used as the example, using a crystal density of $\rho_{crys} = 0.605$ g/cm^3 and data from Ref. 82.

The pressure swing (PS) hydrogen storage capacity is equal to the difference between the 77 K volumetric H_2 storage at 100 bar and 5 bar. In other words, hydrogen below 5 bar is defined as not usable for delivery to the fuel cell system without heating the MOF. The hydrogen storage system therefore is assumed to be isothermal, although during operation heating should be available from either heat transfer through the tank insulation, or from internal heating (resistive heating or heat exchanger connected to the fuel cell coolant system). The PS capacity at T = 77 K for MOF-5 is illustrated in the left panel of Fig. 8.

The second material-level capacity definition is based on the temperature and pressure swing (TPS)

process. In this case, the capacity is the difference between hydrogen volumetric capacity at a full state of 100 bar, 77 K state and an empty state of 5 bar and 160 K. An upper temperature of 160 K is chosen because it provides a compromise between maximizing the usable H_2 capacity while at the same time maintaining an acceptable cool-down time to 77 K during refilling. Figure 8 illustrates the distinction between PS and TPS capacity using published MOF-5 data (from Ref. [82]) as an example. The TPS capacity is clearly larger than the PS capacity owing to the lower concentration of hydrogen that is retained at 160 K versus 77 K.

Results

Usable Hydrogen Capacity at 77 K

Computational screening has identified MOFs which surpass the usable T = 77 K PS capacity of MOF-5.[1,12,83] Within this list of candidates, many were successfully synthesized, including IRMOF-20, SNU-70, NH2-MOF-177, DUT-23 (Co), UMCM-9 and NU-100. While IRMOF-20 and SNU-70 possess the same zinc cluster secondary building unit as MOF-5, and exhibit an equivalent cubic topology, they possess slightly longer organic linkers compared to the 1,4-benzene-dicarboxylic acid linker for MOF-5. This results in larger pore sizes and slightly lower 77 K hydrogen adsorption at low pressures. Despite the crystal density of IRMOF-20 (0.51 g/cm^3) and SNU-70 (0.405 g/cm^3) being slightly lower than that of MOF-5 (0.605 g/cm^3), their isothermal PS volumetric capacity at 77 K actually surpasses that of MOF-5.

The mixed-linker metal-organic framework material UMCM-9 contains two linkers joined through the same zinc cluster, with a similar orthogonal geometry as MOF-5, IRMOF-20 and SNU-70. Despite its low crystal density of 0.37

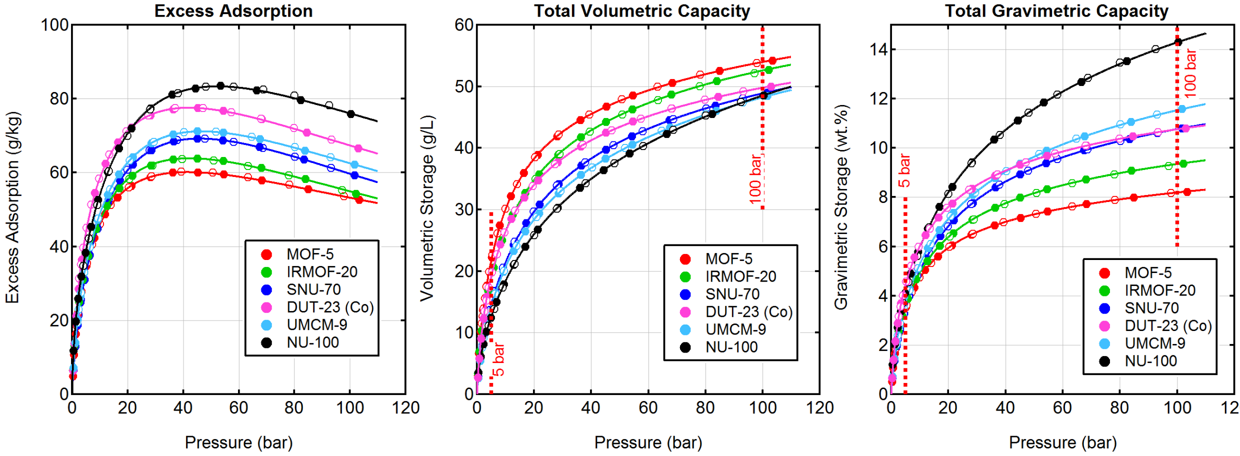

Figure 9: (left) Excess H_2 gravimetric adsorption isotherms measured at 77 K for the top performing synthesized MOFs. Adsorption points are plotted as filled markers and desorption points as unfilled markers. (center) Total volumetric storage at 77 K based on each MOF's crystal density. (right) Total gravimetric H_2 storage at 77 K based on crystal density.

g/cm^3, UMCM-9 has a PS usable volumetric capacity which exceeds that of IRMOF-20 and SNU-70. DUT-23 (Co) was a MOF which had a high excess H_2 adsorption quantity at 77 K, but which did not surpass MOF-5 in PS-usable volumetric capacity. With a low crystal density of 0.291 g/cm^3, NU-100 had both the highest excess gravimetric adsorption at 77 K, along with the highest PS usable volumetric capacity at 77 K. Figure 9 summarizes the excess 77 K H_2 adsorption isotherms, and the volumetric and gravimetric total H_2 storage based on each MOF's ideal crystal density.

BET surface area versus H_2 Excess Adsorption

Hydrogen adsorption isotherms at 77 K were measured for MOFs that were stable after activation and possessed a sufficiently large BET surface area (generally > 2500 m^2/g). In addition to these MOFs, a number of reference samples were also characterized to supplement these MOFs. These include two readily-synthesized MOFs (UiO-66, UiO-67), MOFs available commercially (Ni-MOF-74, MIL-101-NH2, MOF-177, ZIF-8, HKUST-1), and activated carbons (Norit ROW, MSC-20, MSC-30).

A graphical summary of the adsorbents characterized during this work is provided in Fig. 10. The y-axis corresponds to the excess H_2 adsorption at 35 bar and 77 K measured for each of the sample, interpolated at 35 bar from nearest neighbor data points. The x-axis provides the BET specific surface area that was determined from N_2 adsorption isotherms at 77 K. The measured data is consistent with published empirical correlation for MOFs.[84] This supports both the accuracy of the excess H_2 measurements, as well as quality of the synthesized MOF materials. Notably, for MOFs with a BET surface area above 4000 m^2/g, the correlation between surface area and excess H_2 uptake is significantly smaller, and deviates notably from the frequently used 1 wt.% per 500 m^2/g correlation.

Hydrogen Storage Between 80 K and 160 K

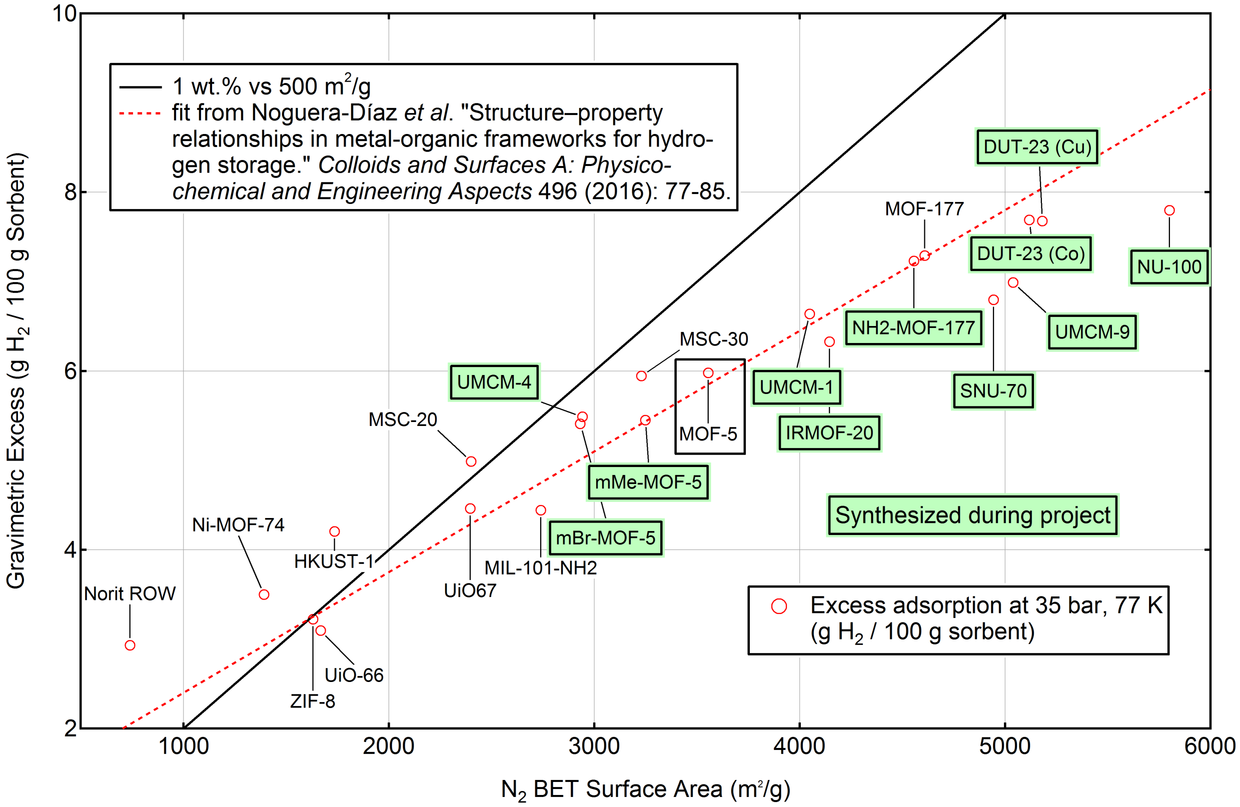

Figure 10: Measured excess H_2 adsorption at 35 bar and 77 K plotted versus the measured N_2 BET specific surface area. MOFs synthesized by the authors are highlighted in green. The standard 1 wt.% per 500 m^2/g correlation is plotted as a solid black line. A more recent empirical correlation from Ref. 84 is plotted as dashed red line.

Volumetric temperature-pressure swing (TPS) capacities were measured for the highest performing MOFs, following the definition illustrated in the right panel of Fig. 8. These TPS capacities are input for the system-level model used to estimating the gravimetric and volumetric capacity. The default lower and upper temperatures for the system model are 80 K (not 77 K) and 160 K, but there was no temperature control capability to maintain these temperatures. Instead, isotherms were measured at four different temperatures, using cryogenic liquid baths (77 K, 87 K) solvent slush baths (195 K) or room temperature (297 K), and the 80 K and 160 K isotherm were determined from the modified Dubinin-Astakhov (D-A) model.[85]

$$n_{ex} = n_{max} \exp\left[-\left(\frac{RT}{a+bT}\right)^2 \ln\left(\frac{p_0}{p}\right)\right] - \rho_g v_a \qquad (4)$$

The modified D-A model is implemented within the system-level analysis to describe the temperature-pressure-composition properties of H_2 uptake in MOFs, as described in greater detail Ref. [77]. While there are difficulties in fitting the modified D-A model to MOF-5 and similar MOFs,[82] the quality of fits are sufficient for describing hydrogen storage capacity within the temperature range explored here. The model parameters were not constrained in the non-linear optimization procedure. Parameters which produced the best fits to the data were chosen, regardless of whether those values were feasible from a literal interpretation of the physical property that the parameter describes. Hydrogen adsorption isotherms measured at variable temperatures, together with fits to the modified D-A model, are available for MOF-5, IRMOF-20, SNU-70, UMCM-9 and NU-100 in the Supporting Information.

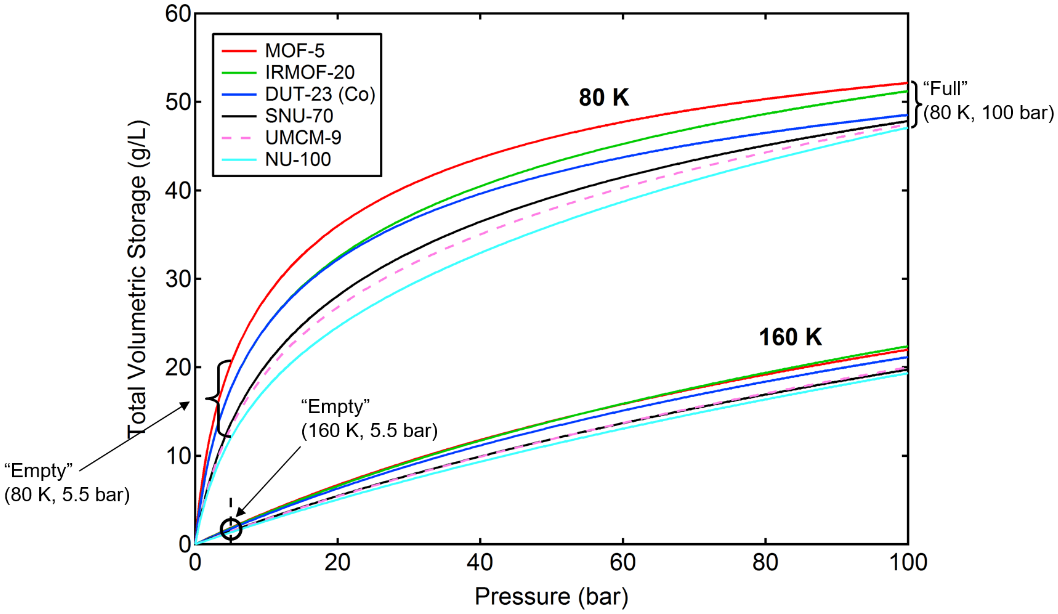

Figure 11: Total volumetric hydrogen storage calculated at 80 K and 160 K using fits to the modified D-A model. Hydrogen storage densities are calculated based the crystal density of each individual MOF. The full state (100 bar, 80 K) for both PS and TPS capacities is indicated. Similarly, the empty state for the PS capacity (5 bar, 80 K) and for the TPS capacity (5 bar, 160 K) are indicated.

Calculated volumetric storage amounts at 80 K and 160 K for the highest-performing MOFs are summarized in Fig. 4, with the volumetric capacity based on the crystal density of each MOF. There is a comparatively large variation in the empty state for the 80 K PS capacity (80 K, 5 bar) for the MOFs in Fig. 11. In contrast, the empty state for the TPS capacity (5 bar, 160 K) exhibits little variation for the MOFs included in the plot. Therefore, the TPS capacity is determined primarily by the full state at 80 K and 100 bar. It is notable that MOFs which beat MOF-5 in terms of 77 K PS capacity actually have a lower 80 K/160 K TPS capacity compared to MOF-5. Indeed, the baseline material MOF-5 actually has the highest TPS capacity on a crystal density basis.[83]

System Model

The HSECoE designed and built two sub-scale prototypes of cryo-adsorption hydrogen storage systems using MOF-5 as the adsorbent.[3] These prototypes were used to develop a model that calculates the gravimetric and volumetric system storage capacities for a full scale 5.6 kg cryo-adsorbent system. Complete details of the system model have been published in Ref. [77].

A schematic of the full-sized cryo-adsorbent system used for the system capacity estimates is provided in Fig. 12. To minimize costs, and also to reduce system mass and volume, only a single tank design is considered in the model. The system utilizes a low-cost type 1 tank made of 6061-T6 aluminum alloy. By keeping the gas pressure below 100 bar, the type-1 tanks can be used instead of type-3 tanks without adding significant additional volume.[77] The tank exterior is wrapped with multi-layer vacuum insulation (MLVI), while the interior of the tank houses a lightweight honeycomb-shaped aluminum heat exchanger which contains holes for cross-sectional hydrogen flow. A benefit of a type-1 tank is that there is no hydrogen permeation through the metal shell, and no out-gassing of volatile organic compounds (which occurs for carbon fiber composite), both of which are known to degrade the vacuum of the MLVI layer.[86]

The outer shell contains a layer of embedded liquid N_2 channels to help cool the type-1 tank rapidly during refueling, and an additional 2 mm aluminum outer shell for dormancy and protection purposes. The balance of plant includes

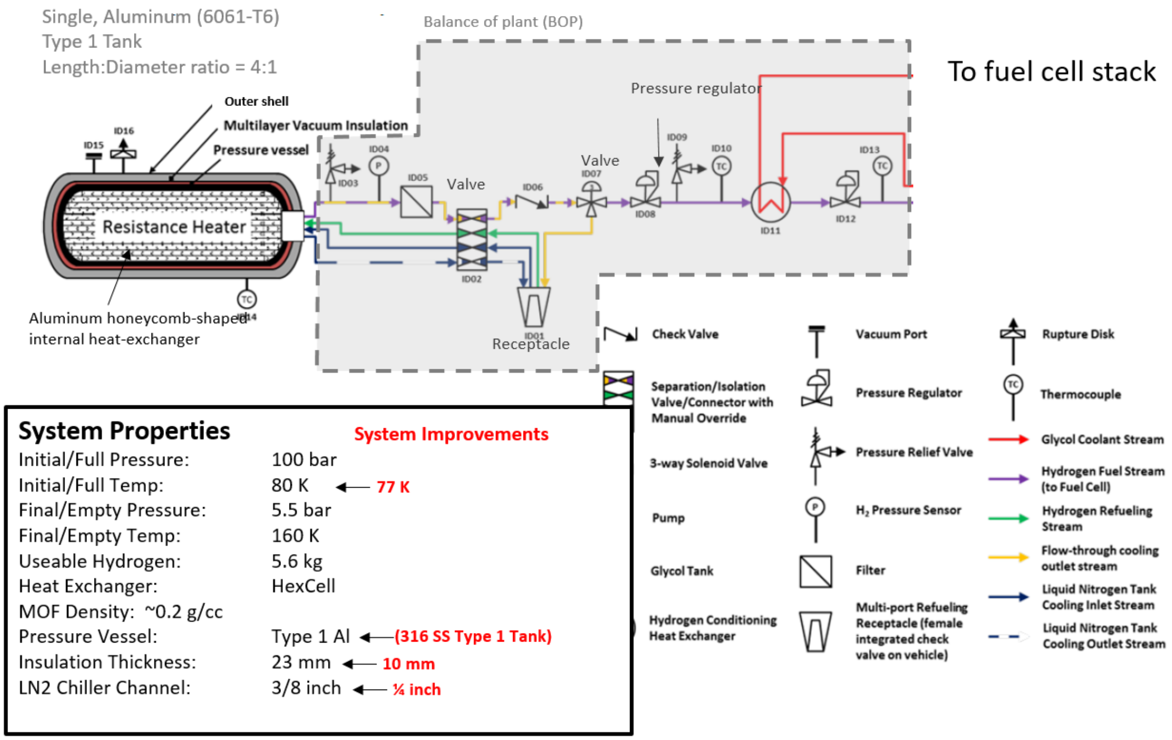

System Properties		System Improvements
Initial/Full Pressure:	100 bar	
Initial/Full Temp:	80 K	← 77 K
Final/Empty Pressure:	5.5 bar	
Final/Empty Temp:	160 K	
Useable Hydrogen:	5.6 kg	
Heat Exchanger:	HexCell	
MOF Density: ~0.2 g/cc		
Pressure Vessel:	Type 1 Al	←(316 SS Type 1 Tank)
Insulation Thickness:	23 mm	← 10 mm
LN2 Chiller Channel:	3/8 inch	← ¼ inch

Figure 12: Schematic of a full-scale cryo-adsorbent hydrogen storage system designed for a 5.6 kg usable capacity. Adjustable system attributes are indicated in the System Properties box at the lower left. Values printed in black indicate the conservative figures, while those printed in red indicate values that could be realistically achieved through engineering improvements. Adapted from Ref. 77.

an on-tank valve, a refueling receptacle, a pressure regulator, and a heat exchanger element that warms the dispensed hydrogen using the fuel cell coolant loop before it enters the FC stack. Additional balance-of-plant (BOP) components are described in Ref. [77]. Due to the scarcity of commercially available balance-of-plant components that are suitable for the operating conditions (e.g., -195 °C to +50 °C, 1 bar to 100 bar) required for a cryo-adsorbent system, assumptions about their attributes (particularly mass, volume) may be overly-conservative. The system is cooled to its base temperature through the combination of a liquid nitrogen cooling loop layer around the outside of the tank, and by re-circulating cold hydrogen gas (at 77 K) through the tank interior. Hydrogen gas is cooled to 77 K at the forecourt through heat exchangers submersed in liquid N_2. These cool-down procedures also help to dissipate the moderate heat of H_2 adsorption, which is around 3–5 kJ/mol·H_2 for the MOFs studied in this project (see Supporting Information for comparisons of the isosteric heats). Additional studies on heat transfer issues in MOF-5-based sub-scale systems have been reported previously.[87,88]

When MOFs are packed to a high density, hydrogen gas flow-through-cooling may no longer be effective. Therefore, there has also been work on a different type of sub-scale prototype tank that houses high-density compacted MOF monoliths separated by heat spreader plates containing internal liquid N_2 micro-channels.[89] This alternative tank architecture in not considered in the system model estimates presented here.

Some system attributes are fixed based on operating conditions and material properties. For example, the tank wall thickness is determined by material tensile strength, pressure range, temperature range, and tank design (type-1, or type-3). Similarly, the heat exchanger size is limited by the heat capacity and heat transfer properties of the highly-insulating MOF powders (which potentially could be mixed with conductive additives like graphite).

A number of the system attributes can be adjusted, and potentially optimized. Using MOF-5 as the adsorbent, Ref. [77] previously reported the results of a sensitivity analysis of temperature and MOF-5 density on the overall system capacity. Conservative values for the full state and empty state are 100 bar/80 K and 5.5 bar/160 K, respectively. Lowering the full state temperature from 80 K to 77 K without increasing cool-down time is a challenge, as the LN_2 coolant itself has a temperature of 77 K. Raising the upper empty temperature above 160 K would also increase the refueling time needed to bring the temperature back down to the base value.[77]

While 23 mm is a conservative default value for the MLVI thickness, thicknesses as thin as 10 mm have been demonstrated for cryo-compressed H_2 storage systems.[86] Additionally, changing the type-1 tank material from Al alloy to 316 stainless steel can improve volumetric capacity due to thinner tank walls, although increasing cost and weight. Lastly, the material-level H_2 storage properties of each MOF were determined by adsorption measurements, and were considered as non-adjustable parameters for a given adsorbent material.

System-level storage capacities are highly sensitive to the MOF packing density within the tank. Not only does this adjustable parameter dictate the fraction of internal volume that is void space versus MOF-occupied space, it can alter the integrity of the MOF pore structure. While lightly tamping down a loosely packed MOF powder will not necessarily generate this effect, mechanically compacting the MOF powder to densities approaching the crystal density will induce degradation to the pore structure, reducing both pore volume and hydrogen adsorption capacity.[90] The characterization of the compaction properties of the top performing MOFs are presented in the next section.

MOF Powder Packing

To accurately model the effect of MOF packing density on the system level capacity, it was necessary to develop a transfer function that accounts for how mechanically compacting MOFs beyond certain densities can damage the pore structure and lower the surface area. We performed measurements for several of the top-performing MOFs to quantify the effect of mechanical compaction on the hydrogen adsorption capacity at 77 K. Selected measurements are provided in Fig. 13, which shows the excess H_2 adsorption isotherms for SNU-70, MOF-177, and MOF-5 after compacting a powder sample to successively higher densities.

As expected in Fig. 13, excess H_2 adsorption amounts decrease as the MOFs are compacted to higher densities. It may be possible to improve the compaction efficiency through the addition of lubricants or particle size control, although there is little data in the literature to assess the effectiveness of these strategies. An additional approach is to compact the MOF before the activation step, while pores are filled with solvent, which may provide additional support against

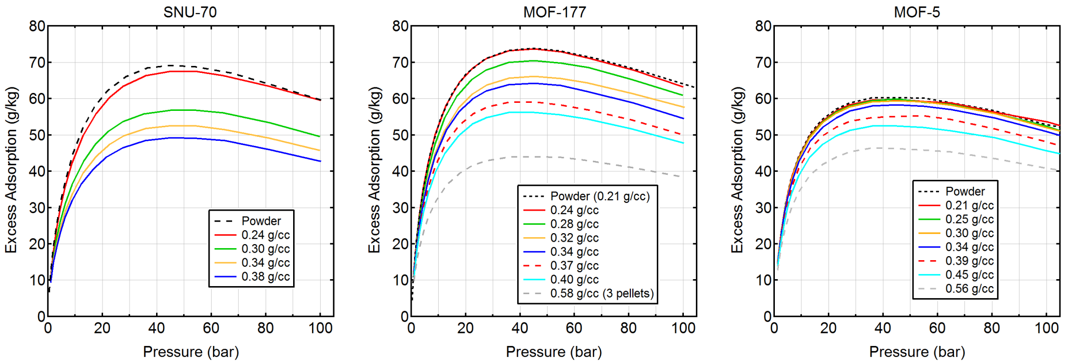

Figure 13: Excess H_2 adsorption isotherms measured at 77 K for SNU-70 (left), MOF-177 (center) and MOF-5 (right), after compacting MOFs to specified densities. The powders were densified by uniaxial compaction directly inside the sample cell using a manual pellet press.

framework compression or shear.

The modified D-A model parameters used to describe material-level hydrogen storage capacities must be scaled down to capture the mechanical degradation effect. It is impractical to perform the many variable density and variable temperature hydrogen adsorption measurements for all of the high-performing MOFs studied during this project. Therefore, an approximate method was used to correlate a unit-less degradation factor for each MOF with a unit-less compaction parameter. First, the mechanical degradation parameter is defined as the ratio of the maximum 77 K excess H_2 adsorption at a particular MOF density against its maximum excess adsorption as a powder. Similarly, the compaction parameter is defined as the packing density divided by the MOF crystal density. The correlation between these two parameters is displayed in Fig. 14.

The compaction-induced capacity loss for MOF-5, MOF-177, SNU-70 and NU-100 appear to follow a similar trend in Fig. 14. Hydrogen excess adsorption retains its full capacity up to a density of approximately 50% of the crystal density. At that point the maximum excess adsorption value starts to decrease with continued mechanical compaction. The empirical trend for the combined data set of all three MOFs shown in Fig. 14 can be approximated as,

$$Y = \frac{n_{ex}^{max}\{compacted\}}{n_{ex}^{max}\{powder\}} = \begin{cases} 1 & \text{if } \left(\rho_{pack}/\rho_{crys}\right) < 0.519 \\ 1.32 - 0.616 \times \left(\dfrac{\rho_{pack}}{\rho_{crys}}\right) & \text{if } \left(\rho_{pack}/\rho_{crys}\right) > 0.519 \end{cases} \tag{5}$$

where the left-hand-side equals the ratio of the maximum excess adsorption of the compacted MOF at density ρ_{pack} to the maximum excess adsorption for the powder MOF at density ρ_{pwd}. The ratio of H2 adsorption for compacted versus powder MOFs can then be used to apply D-A parameters (measured for the powder sample) to a system in which the MOF has been compacted beyond its powder density. In this case, two of the D-A model parameters are transformed by multiplying by a pre-factor Y,

$$\begin{aligned} n_{max}^* &= Y \times n_{max} \\ v_a^* &= Y \times v_a \end{aligned} \tag{6}$$

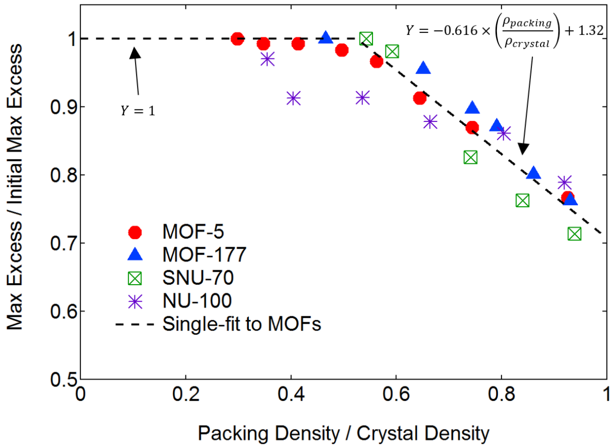

Figure 14: Mechanical degradation of MOF versus compaction density. The y-axis corresponds to the ratio between the maximum excess adsorption at 77 K for a MOF compacted to a specific density divided by the value for the initial value measured for the powder. The x-axis corresponds to the density of the compacted MOF divided by its crystal density.

System-Level Capacity versus MOF Density

As described in Sec. 3.3, modified D-A parameters were measured for powder samples of MOF-5, MOF-177, IRMOF-20, DUT-23(Co), SNU-70 and NU-100. Using Eqs. 5 and 6, system level hydrogen storage capacities were calculated for these MOFs at densities above their powder packing density. Baseline parameter values (such as pressure and temperature ranges, insulation thickness, and tank type) are described earlier. The results of these system-level estimates are shown in Fig. 15.

Based on real MOF powder packing behavior, MOF-5 ultimately attains the highest volumetric capacity at the system level when it is compacted to a density between 0.4 g/cm^3 and 0.5 g/cm^3. At these high densities, however, rapid flow-through cooling of the sorbent media may not be realistically achievable. At a lower packing such as 0.2 g/cm^3, closer to what would be obtained for a bulk powder, MOFs with lower crystal density yield a higher volumetric capacity than MOF-5.

The optimum MOF for the cryo-adsorbent system therefore depends on the target MOF density, which itself may be restricted on both the system architecture, on requirements for H_2 permeability through the MOF monoliths, and on methods for loading and compacting the MOF powder within the tank. From panel (b) in Fig. 15, it is clear that increasing the MOF density generally causes the system-level gravimetric capacity to decrease due to the addition of additional mass from the MOF. Therefore, the increase in volumetric capacity must be balanced against the corresponding decrease in gravimetric capacity.

How Material-Level Capacity Translates to System-Level Capacity

One goal of this study was to better understand how material-level hydrogen storage properties translate to system-level performance. Referring to Fig. 9, the baseline material (MOF-5) has a maximum excess hydrogen adsorption of 60.0 g/kg at 77 K. Meanwhile, the maximum excess adsorption for NU-100 was measured at 80.5 g/kg, a nearly 35% increase. Similarly, the total gravimetric hydrogen storage of NU-100 (at crystal density and T = 77 K) at 100 bar is 14.1 wt.% versus 8.2 wt.% for MOF-5. However, such large increases in material level gravimetric storage do not translate into significant increases in gravimetric or volumetric capacity at the system level.

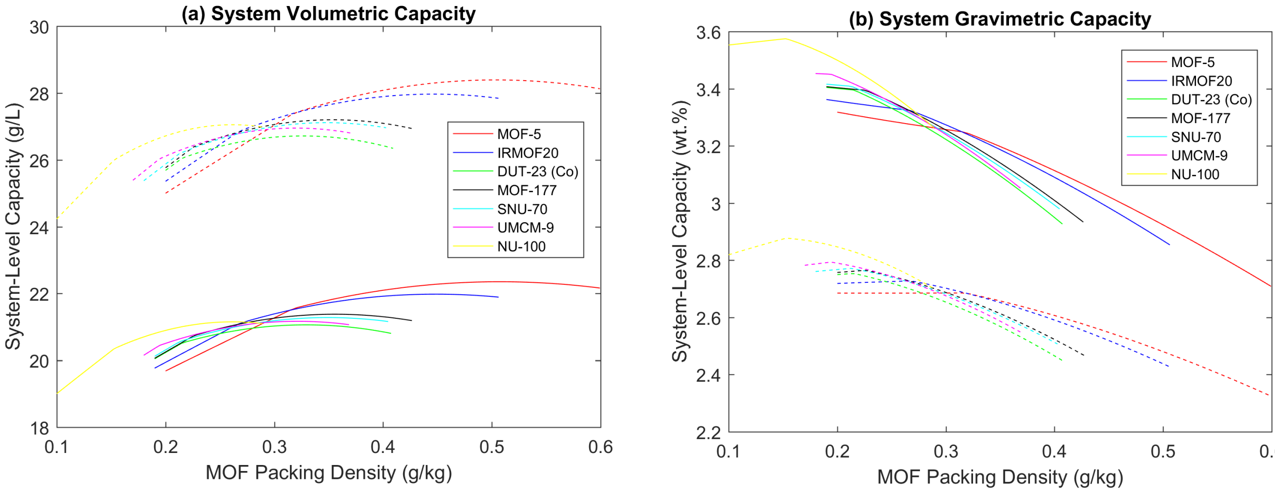

Figure 15: Projected usable volumetric hydrogen storage capacity for MOFs at the system-level when compacted above their powder packing density. (a) Volumetric capacity in g/L versus compaction density of MOFs. (b) Gravimetric capacity in wt.% versus compaction density of MOFs. Dashed lines indicate the system capacities based on optimized system attributes (e.g., baseline temperature, wall thickness, tank material, LN_2 cooling channel thickness). Solid lines indicate system capacities based on initial estimates for system attributes.

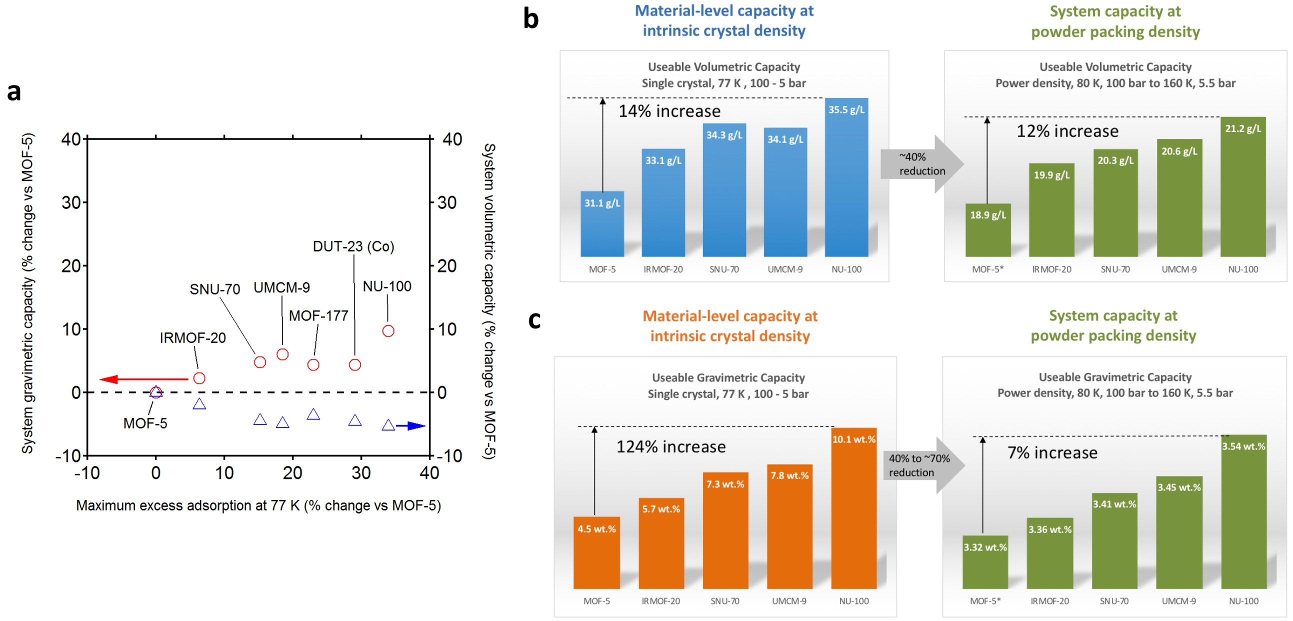

*HSECoE MOF-5 HexCell Projection with powder density of 0.13 g/cm^3. Powder packing density of 0.2 g/cm^3 assumed for other MOFs.

Figure 16: Correlation between material level storage and projected system-level H_2 storage capacities. a) Bottom axis is the maximum excess gravimetric H_2 adsorption at 77 K for the indicated MOFs, expressed as a percent change versus MOF-5. The left axis (red circles) is the system-level gravimetric hydrogen storage capacity at the powder packing density for each MOF, defined here at the half the MOF crystal density. It is expressed as the percent change versus MOF-5. The right axis (blue triangles) is the system-level volumetric storage capacity at the MOF powder packing density, expressed as the percent change versus MOF-5. (b-c) Relationship between usable volumetric (b) and gravimetric (c) capacities at the materials level to projected hydrogen capacities at the system level. Projections were made using the HSECoE system model and assumed a HexCell system geometry.

Figure 16a illustrates the weak correlation between material-level excess hydrogen adsorption and system-level hydrogen storage capacity. On the x-axis, the maximum excess hydrogen adsorption measured for each MOF is expressed as a percent change versus that of MOF-5. The left and right y-axes indicate the system-level capacities for each MOF at their maximum powder packing density. For this example, the MOF powder packing density is assumed to be equal to one half of the crystal density. Referring back to Fig. 14, this is the density that many MOFs can be compacted to without impacting the pore volume and excess adsorption. Empirically, we also found that this was close to the density that we could attain by tamping down the powder by hand, although this depends on the crystallite size and shape. The system-level gravimetric capacity (red circles) increases with increasing excess adsorption, but the gains are relatively modest (< 10%). On the other hand, system-level volumetric capacity (blue triangles) actually decreases going from MOF-5 to NU-100, due primarily to the lower packing density.

Figures 16b-c illustrate the degree to which increases in usable capacities (achieved by subsititing different MOF storage media) influence capacities at the system level. These materials-to-system projections were made using the HSECoE system model, and assume that the MOF is packed as a powder in the HexCell system architecture. Fig. 16b shows that a 14% increase in usable volumetric capacity at the materials level (achieved by substituting NU-100 for MOF-5) translates into a similar volumetric improvement of 12% at the system level. This data suggests that improvments to volumetric capacity at the materials level can translate to the system. Due to the volume of the balance of plant components and tank insulation, volumetric capacities at the system level are roughly 40% smaller than for the materials alone. Finally, Fig. 16c shows that improvements in usable gravimetric capacity at the materials level do not redilly translate to the system (at least for the HexCell system examined here). Substition of NU-100 for MOF-5 increases gravimetric capacity by 124% at the materials level, yet yields only a 7% increase in system performance. On average, system gravimetric capacities are 40% to 70% smaller than for the materials alone. The limited gains in system gravimetric performance can be traced to the large mass assumed for the system components.

Strategies to Improve System Capacity

The system-level storage capacities presented in Fig. 15 remain below the 2020 DOE target of 30 g/L, and do not even match the typical volumetric capacities for a 700 bar compressed system (25 g/L).

However, there are a number of opportunities for improving the capacity of the cryo-adsorbent hydrogen storage system. These improvements include:

- Switching the type-1 tank material from aluminum alloy to 316 stainless steel. This reduces wall thickness and saves volume at the expense of increased cost
- Reducing the MLVI thickness from 23 mm to 10 mm. Prototype cryo-compressed H_2 storage tanks have demonstrated the feasibility MLVI thicknesses as thin as 10 mm. Because the insulation is pivotal to the dormancy performance of the cryo-adsorbent system, this would require extensive optimization and validation. If implemented, this could significantly reduce the outer volume of the tank.
- Reducing the liquid nitrogen cooling channel thickness from 3/8 inch to 1/4 inch. This would help to reduce the outer volume of the tank assembly.
- Lower the baseline fill temperature from 80 K to 77 K. This may be technically feasible with an optimized cool-down procedure which utilizes both an external LN_2 loop and internal recirculation of pre-cooled 77 K hydrogen gas. Even a small decrease in temperature can increase amount of hydrogen gas that can be loaded into the tank.
- Lastly, methods of synthesizing MOFs as high density monoliths without the corresponding mechanical degradation and decrease in H_2 adsorption are an area of active research. We allowed for the possibility of compacting a MOF to its crystal density without any deterioration in its hydrogen adsorption

The effects of these improvements on the projected system-level volumetric capacity are depicted as a waterfall chart in Fig. 17. The starting quantity is simply the outer volume for an "empty" single-tank cryo-adsorbent system (no MOF loaded) sized to store 5.6 kg of hydrogen gas at 77 K. Next, the outer volume of the system is calculated after filling the tank with powder MOF-5 at a conservative packing density of 0.13 g/cm^3.[78] Storing the same 5.6 kg of usable hydrogen gas, the external volume of the system decreases by 41 L due to the enhanced storage density of MOF-5. Next, the MOF material is switched from MOF-5 to UMCM-9 packed at a moderate density of 0.2 g/cm^3. The external volume now decreases by an additional 28 L due to the increased storage capacity of UMCM-9 at 0.2 g/cm^3. Next, the effect of the system engineering improvements itemized above is considered in Fig. 17. These improvements include reducing the MLVI thickness, reducing the LN_2 cooling channel thickness, and lowering the baseline fill temperature. These simple optimizations lead to a surprisingly large decrease in the system volume of about 68 L, sufficient to surpass the 25 g/L baseline volumetric H_2 density of a typical 700 bar compressed storage system.

The last hypothetical improvement comes from compacting the UMCM-9 powder to its crystal density (ρ_{crys}= 0.37 g/cm^3) with no resulting decrease in excess adsorption (i.e., not including the degradation shown in Fig. 12). This trims off an additional 20 L of external system volume, such that the final volumetric system capacity is over 30 g/L and meets the 2020 targets. This highlights the importance of developing a compaction method which does not induce mechanical degradation to the MOF pore structure. Strategies for optimizing MOF powder compaction include engineering the crystallite size and shapes, along with minimizing friction sources during mechanical compaction.

Summary – System Modeling

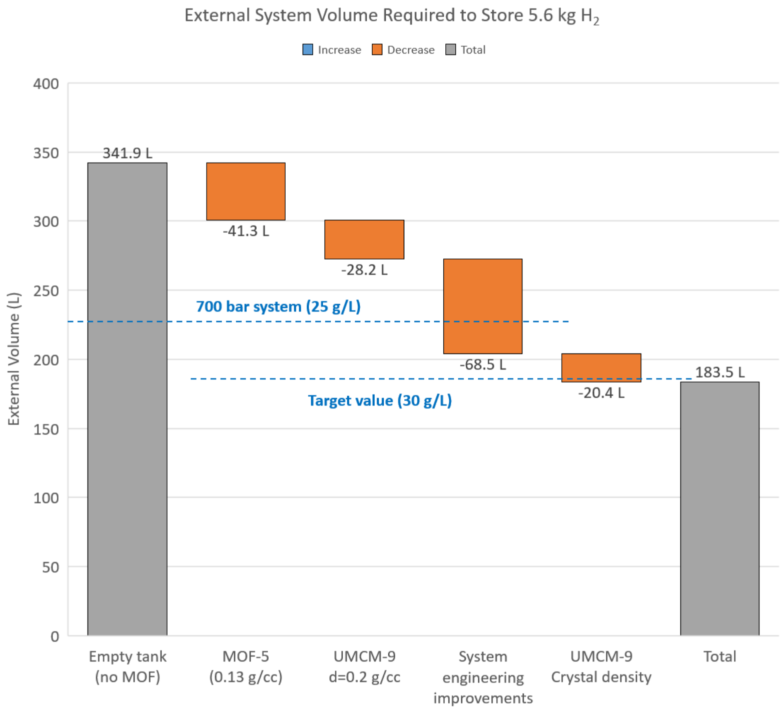

Figure 17: Waterfall chart depicting the total external system volume required to store 5.6 kg of usable hydrogen gas. Starting from an empty tank at 77 K, the reduction in external volume is shown for each modification to the system. Engineering improvements (described in Sec. 3.8) include reducing the MLVI thickness, reducing the LN_2 cooling channel thickness, and lowering the baseline fill temperature.

In this study, we have estimated the hydrogen storage capacities at the system-level for a number of MOFs with high demonstrated volumetric and gravimetric H_2 storage density. System estimates are based on a single tank cryo-adsorbent system that utilizes a type-1 aluminum tank, with multi-layer vacuum insulation, liquid N_2 cooling channels, in-tank heat exchanger, and a packed MOF powder inside the tank. It was found that developing MOFs with ultra-high gravimetric surface areas and hydrogen adsorption amounts does not necessarily translate into high volumetric (or even gravimetric) storage capacities at the system-level. Meanwhile, attributes such as powder packing efficiency and system cool-down temperatures were shown to have a larger impact on the amount of hydrogen that is stored within a fixed system volume.

ACKNOWLEDGMENT. A. A. acknowledges Profs. Randall Snurr and Tom Woo for providing access to their MOF databases. A. A. also acknowledges Dr. Maciej Haranczyk for use of the Zeo++ code and the mail-order MOF database. Financial support for this study was provided by the US Department of Energy, Office of Energy Efficiency and Renewable Energy, Grant no. DE-EE0007046. Computing resources were provided by NSF grant MRI-1531752: Acquisition of Conflux, A Novel Platform for Data-Driven Computational Physics (Tech. Monitor: Ed Walker). The model structure for UMCM-9 was constructed by Dr. Kyoungmoo Koh.

REFERENCES

(1) Ahmed, A.; Liu, Y.; Purewal, J.; Tran, L. D.; Veenstra, M.; Wong-Foy, A.; Matzger, A.; Siegel, D. Balancing Gravimetric and Volumetric Hydrogen Density in MOFs. *Energy Environ. Sci.* **2017**, *10*, 2459–2471.
(2) Yang, J.; Sudik, A.; Wolverton, C.; Siegel, D. J. High Capacity Hydrogen Storage Materials: Attributes for Automotive Applications and Techniques for Materials Discovery. *Chem. Soc. Rev.* **2010**, *39*, 656–675.
(3) Siegel, D. J.; Hardy, B. Engineering an Adsorbent-Based Hydrogen Storage System: What Have We Learned? https://energy.gov/sites/prod/files/2015/02/f19/fcto_h2_storage_summit_siegel.pdf (accessed May 9, 2017).
(4) Allendorf, M. D.; Hulvey, Z.; Gennett, T.; Ahmed, A.; Autrey, T.; Furukawa, H.; Haranczyk, M.; Head-gordon, M.; Karkamkar, A.; Nazarov, R.; et al. An Assessment of Strategies for the Development of Solid-State Adsorbents for

Vehicular Hydrogen Storage. *Energy Environ. Sci.* **2018**, 1–29.

(5) Wong-Foy, A. G.; Matzger, A. J.; Yaghi, O. M. Exceptional H2 Saturation Uptake in Microporous Metal-Organic Frameworks. *J. Am. Chem. Soc.* **2006**, *128*, 3494–3495.

(6) Wahiduzzaman, M.; Walther, C. F. J.; Heine, T. Hydrogen Adsorption in Metal-Organic Frameworks: The Role of Nuclear Quantum Effects. *J. Chem. Phys.* **2014**, *141* (6), 064708.

(7) Bobbitt, N. S.; Chen, J.; Snurr, R. Q. High-Throughput Screening of Metal–Organic Frameworks for Hydrogen Storage at Cryogenic Temperature. *J. Phys. Chem. C* **2016**, *120* (48), 27328–27341.

(8) Colón, Y. J.; Gómez-Gualdrón, D. A.; Snurr, R. Q. Topologically Guided, Automated Construction of Metal–Organic Frameworks and Their Evaluation for Energy-Related Applications. *Cryst. Growth Des.* **2017**, *17* (11), 5801–5810.

(9) Gómez-Gualdrón, D. A.; Colón, Y. J.; Zhang, X.; Wang, T. C.; Chen, Y.-S.; Hupp, J. T.; Yildirim, T.; Farha, O. K.; Zhang, J.; Snurr, R. Q. Evaluating Topologically Diverse Metal–Organic Frameworks for Cryo-Adsorbed Hydrogen Storage. *Energy Environ. Sci.* **2016**, *9* (10), 3279–3289.

(10) Witman, M.; Ling, S.; Gladysiak, A.; Stylianou, K. C.; Smit, B.; Slater, B.; Haranczyk, M. Rational Design of a Low-Cost, High-Performance Metal-Organic Framework for Hydrogen Storage and Carbon Capture. *J. Phys. Chem. C* **2017**, *121* (2), 1171–1181.

(11) Hyeon, S.; Kim, Y.-C.; Kim, J. Computational Prediction of High Methane Storage Capacity in V-MOF-74. *Phys. Chem. Chem. Phys. Phys. Chem. Chem. Phys* **2113**, *19* (19), 21132–21139.

(12) Goldsmith, J.; Wong-Foy, A. G.; Cafarella, M. J.; Siegel, D. J. Theoretical Limits of Hydrogen Storage in Metal–Organic Frameworks: Opportunities and Trade-Offs. *Chem. Mater.* **2013**, *25* (16), 3373–3382.

(13) Rowsell, J. L. C.; Yaghi, O. M. Strategies for Hydrogen Storage in Metal-Organic Frameworks. *Angew. Chemie Int. Ed.* **2005**, *44* (30), 4670–4679.

(14) Lollar, C. T.; Qin, J.-S.; Pang, J.; Yuan, S.; Becker, B.; Zhou, H.-C. Interior Decoration of Stable Metal-Organic Frameworks. **2018**.

(15) Kaye, S. S.; Dailly, A.; Yaghi, O. M.; Long, J. R. Impact of Preparation and Handling on the Hydrogen Storage Properties of Zn4O(1,4-Benzenedicarboxylate)3 (MOF-5). *J. Am. Chem. Soc.* **2007**, *129*, 14176–14177.

(16) Thornton, A. W.; Simon, C. M.; Kim, J.; Kwon, O.; Deeg, K. S.; Konstas, K.; Pas, S. J.; Hill, M. R.; Winkler, D. A.; Haranczyk, M.; et al. Materials Genome in Action: Identifying the Performance Limits of Physical Hydrogen Storage. *Chem. Mater.* **2017**, *29* (7), 2844–2854.

(17) Huong, T. T. T.; Thanh, P. N.; Huynh, N. T. X.; Son, D. N. Metal – Organic Frameworks: State-of-the-Art Material for Gas Capture and Storage. *VNU J. Sci. Math. – Phys.* **2016**, *32* (1), 67–85.

(18) Prasad, T. K.; Suh, M. P. Control of Interpenetration and Gas-Sorption Properties of Metal-Organic Frameworks by a Simple Change in Ligand Design. *Chem. - A Eur. J.* **2012**, *18* (28), 8673–8680.

(19) Broom, D. P.; Webb, C. J.; Hurst, K. E.; Parilla, P. A.; Gennett, T.; Brown, C. M.; Zacharia, R.; Tylianakis, E.; Klontzas, E.; Froudakis, G. E.; et al. Outlook and Challenges for Hydrogen Storage in Nanoporous Materials. *Appl. Phys. A* **2016**, *122* (3), 151.

(20) Gomez-Gualdron, D. A.; Wang, T. C.; García-Holley, P.; Sawelewa, R. M.; Argueta, E.; Snurr, R. Q.; Hupp, J. T.; Yildirim, T.; Farha, O. K. Understanding Volumetric and Gravimetric Hydrogen Adsorption Trade-off in Metal–Organic Frameworks. *ACS Appl. Mater. Interfaces* **2017**, *9* (39), 33419–33428.

(21) Collins, D. J.; Zhou, H.-C. Hydrogen Storage in Metal–Organic Frameworks. *J. Mater. Chem.* **2007**, *17*, 3154–3160.

(22) Rosi, N. L.; Eckert, J.; Eddaoudi, M.; Vodak, D. T.; Kim, J.; O'Keeffe, M.; Yaghi, O. M. Hydrogen Storage in Microporous Metal-Organic Frameworks. *Science (80-.).* **2003**, *300* (5622), 1127–1129.

(23) Batten, S. R.; Champness, N. R.; Chen, X.-M.; Garcia-Martinez, J.; Kitagawa, S.; Öhrström, L.; O'Keeffe, M.; Paik Suh, M.; Reedijk, J. Terminology of Metal–Organic Frameworks and Coordination Polymers (IUPAC Recommendations 2013). *Pure Appl. Chem.* **2013**, *85* (8), 1715–1724.

(24) Fischer, R. A.; Schwedler, I. Terminologie von Metall-Organischen Gerüstverbindungen Und Koordinationspolymeren (IUPAC-Empfehlungen 2013). *Angew. Chemie* **2014**, *126* (27), 7209–7214.

(25) Öhrström, L. Let's Talk about MOFs—Topology and Terminology of Metal-Organic Frameworks and Why We Need Them. *Crystals* **2015**, *5* (1), 154–162.

(26) Zhou, H.-C.; Long, J. R.; Yaghi, O. M. Introduction to Metal–Organic Frameworks. *Chem. Rev.* **2012**, *112* (2), 673–674.

(27) Deng, H.; Doonan, C. J.; Furukawa, H.; Ferreira, R. B.; Towne, J.; Knobler, C. B.; Wang, B.; Yaghi, O. M. Multiple

Functional Groups of Varying Ratios in Metal-Organic Frameworks. *Science* **2010**, *327* (5967), 846–850.

(28) Chae, H. K.; Siberio-Pérez, D. Y.; Kim, J.; Go, Y.; Eddaoudi, M.; Matzger, A. J.; O'Keeffe, M.; Yaghi, O. M. A Route to High Surface Area, Porosity and Inclusion of Large Molecules in Crystals. *Nature* **2004**, *427* (6974), 523–527.

(29) Zhang, M.; Bosch, M.; Gentle Iii, T.; Zhou, H.-C. Rational Design of Metal–Organic Frameworks with Anticipated Porosities and Functionalities.

(30) Yuan, S.; Zou, L.; Qin, J.-S.; Li, J.; Huang, L.; Feng, L.; Wang, X.; Bosch, M.; Alsalme, A.; Cagin, T.; et al. Construction of Hierarchically Porous Metal–Organic Frameworks through Linker Labilization. *Nat. Commun.* **2017**, *8*, 15356.

(31) Lu, W.; Wei, Z.; Gu, Z.-Y.; Liu, T.-F.; Park, J.; Park, J.; Tian, J.; Zhang, M.; Zhang, Q.; Gentle III, T.; et al. Tuning the Structure and Function of Metal–Organic Frameworks via Linker Design. *Chem. Soc. Rev.* **2014**, *43* (16), 5561–5593.

(32) Eddaoudi, M.; Kim, J.; Rosi, N.; Vodak, D.; Wachter, J.; O'Keeffe, M.; Yaghi, O. M. Systematic Design of Pore Size and Functionality in Isoreticular MOFs and Their Application in Methane Storage. *Science (80-.).* **2002**, *295* (5554).

(33) Deng, H.; Grunder, S.; Cordova, K. E.; Valente, C.; Furukawa, H.; Hmadeh, M.; Gándara, F.; Whalley, A. C.; Liu, Z.; Asahina, S.; et al. Large-Pore Apertures in a Series of Metal-Organic Frameworks. *Science (80-.).* **2012**, *336* (6084).

(34) Cheetham, A. K.; Bennett, T. D.; Coudert, F.-X.; Goodwin, A. L.; Fang, Z. L.; Bueken, B.; Vos, D. E. De; Fischer, R. A.; Wagner, C.; Schottky, W.; et al. Defects and Disorder in Metal Organic Frameworks. *Dalt. Trans.* **2016**, *45* (10), 4113–4126.

(35) Yaghi, O. M.; Li, H.; Eddaoudi, M.; O'Keeffe, M. Design and Synthesis of an Exceptionally Stable and Highly Porous Metal-Organic Framework. *Nature* **1999**, *402* (6759), 276–279.

(36) Tranchemontagne, D. J.; Mendoza-Cortés, J. L.; O'Keeffe, M.; Yaghi, O. M. Secondary Building Units, Nets and Bonding in the Chemistry of Metal–Organic Frameworks. *Chem. Soc. Rev.* **2009**, *38* (5), 1257.

(37) Jeong, W.; Lim, D.-W.; Kim, S.; Harale, A.; Yoon, M.; Suh, M. P.; Kim, J.; Yaghi, O. M. Modeling Adsorption Properties of Structurally Deformed Metal–Organic Frameworks Using Structure–Property Map.

(38) Rowsell, J. L. C.; Yaghi, O. M. Effects of Functionalization, Catenation, and Variation of the Metal Oxide and Organic Linking Units on the Low-Pressure Hydrogen Adsorption Properties of Metal–Organic Frameworks. *J. Am. Chem. Soc.* **2006**, *128*, 1304.

(39) Li, J.-R.; Kuppler, R. J.; Zhou, H.-C. Selective Gas Adsorption and Separation in Metal–Organic Frameworks. *Chem. Soc. Rev.* **2009**, *38* (5), 1477.

(40) Chung, Y. G.; Camp, J.; Haranczyk, M.; Sikora, B. J.; Bury, W.; Krungleviciute, V.; Yildirim, T.; Farha, O. K.; Sholl, D. S.; Snurr, R. Q. Computation-Ready, Experimental Metal–Organic Frameworks: A Tool To Enable High-Throughput Screening of Nanoporous Crystals. *Chem. Mater.* **2014**, *26*, 6185–6192.

(41) Moghadam, P. Z.; Li, A.; Wiggin, S. B.; Tao, A.; Maloney, A. G. P.; Wood, P. A.; Ward, S. C.; Fairen-Jimenez, D. Development of a Cambridge Structural Database Subset: A Collection of Metal–Organic Frameworks for Past, Present, and Future. *Chem. Mater.* **2017**, *29* (7), 2618–2625.

(42) Martin, R. L.; Simon, C. M.; Smit, B.; Haranczyk, M. *In Silico* Design of Porous Polymer Networks: High-Throughput Screening for Methane Storage Materials. *J. Am. Chem. Soc.* **2014**, *136* (13), 5006–5022.

(43) Chung, Y. G.; Gómez-Gualdrón, D. A.; Li, P.; Leperi, K. T.; Deria, P.; Zhang, H.; Vermeulen, N. A.; Stoddart, J. F.; You, F.; Hupp, J. T.; et al. In Silico Discovery of Metal-Organic Frameworks for Precombustion CO2 Capture Using a Genetic Algorithm. *Sci. Adv.* **2016**, *2* (10), e1600909.

(44) Gomez-Gualdron, D. A.; Gutov, O. V.; Krungleviciute, V.; Borah, B.; Mondloch, J. E.; Hupp, J. T.; Yildirim, T.; Farha, O. K.; Snurr, R. Q. Computational Design of Metal–Organic Frameworks Based on Stable Zirconium Building Units for Storage and Delivery of Methane. *Chem. Mater.* **2014**, *26* (19), 5632–5639.

(45) Getman, R. B.; Bae, Y.-S.; Wilmer, C. E.; Snurr, R. Q. Review and Analysis of Molecular Simulations of Methane, Hydrogen, and Acetylene Storage in Metal–Organic Frameworks. *Chem. Rev.* **2012**, *112* (2), 703–723.

(46) Müller, K.; Felderhoff, M. Special Issue: Application of Hydrogen Storage Materials, Carriers, and Processes. *Energy Technol.* **2018**.

(47) Groom, C. R.; Bruno, I. J.; Lightfoot, M. P.; Ward, S. C. The Cambridge Structural Database. *Acta Cryst.* **2016**, *72* (2), 171–179.

(48) Wilmer, C. E.; Leaf, M.; Lee, C. Y.; Farha, O. K.; Hauser, B. G.; Hupp, J. T.; Snurr, R. Q. Large-Scale Screening of Hypothetical Metal–Organic Frameworks. *Nat. Chem.* **2011**, *4* (2), 83–89.

(49) Fernandez, M.; Boyd, P. G.; Daff, T. D.; Aghaji, M. Z.; Woo, T. K. Rapid and Accurate Machine Learning Recognition of High Performing Metal Organic Frameworks for CO $_2$ Capture. *J. Phys. Chem. Lett.* **2014**, *5* (17), 3056–3060.

(50) Bao, Y.; Martin, R. L.; Simon, C. M.; Haranczyk, M.; Smit, B.; Deem, M. W. In Silico Discovery of High Deliverable Capacity Metal–Organic Frameworks. *J. Phys. Chem. C* **2015**, *119* (1), 186–195.

(51) Martin, R. L.; Lin, L.-C.; Jariwala, K.; Smit, B.; Haranczyk, M. Mail-Order Metal–Organic Frameworks (MOFs): Designing Isoreticular MOF-5 Analogues Comprising Commercially Available Organic Molecules. *J. Phys. Chem. C* **2013**, *117* (23), 12159–12167.

(52) Slater, A. G.; Cooper, A. I. Function-Led Design of New Porous Materials. *Science (80-.).* **2015**, *348* (6238).

(53) Smit, B. Screening Materials Relevant for Energy Technologies. *Chim. Int. J. Chem.* **2015**, *69* (5), 248–252.

(54) Simon, C. M.; Kim, J.; Gomez-Gualdron, D. A.; Camp, J. S.; Chung, Y. G.; Martin, R. L.; Mercado, R.; Deem, M. W.; Gunter, D.; Haranczyk, M.; et al. The Materials Genome in Action: Identifying the Performance Limits for Methane Storage. *Energy Environ. Sci.* **2015**, *8* (4), 1190–1199.

(55) Wilmer, C. E.; Leaf, M.; Lee, C. Y.; Farha, O. K.; Hauser, B. G.; Hupp, J. T.; Snurr, R. Q. Large-Scale Screening of Hypothetical Metal–Organic Frameworks. *Nat. Chem.* **2011**, *4* (2), 83–89.

(56) Aghaji, M. Z.; Fernandez, M.; Boyd, P. G.; Daff, T. D.; Woo, T. K. Quantitative Structure-Property Relationship Models for Recognizing Metal Organic Frameworks (MOFs) with High CO2 Working Capacity and CO2/CH4 Selectivity for Methane Purification. *Eur. J. Inorg. Chem.* **2016**.

(57) Hydrogen Storage Engineering Center of Excellence," Donald L. Anton and Theodore Motyka; U.S. Department of Energy, Hydrogen and Fuel Cells Program 2015 Annual Merit Review Proceedings, Pr0jec ST004: https://www.hydrogen.energy.gov/pdfs/review15/st004_anton_2015_o.pdf.

(58) Fischer, M.; Hoffmann, F.; Fröba, M. Preferred Hydrogen Adsorption Sites in Various MOFs-A Comparative Computational Study. *ChemPhysChem* **2009**, *10* (15), 2647–2657.

(59) Feynman, R. P.; Hibbs, A. R. *Quantum Mechanics and Path Integrals*; McGraw-Hill: New York, 1965.

(60) "Ford/BASF-SE/UM Activities in Support of the Hydrogen Storage Engineering Center of Excellence," Mike Veenstra, Jun Yang, Chunchuan Xu, Manuela Gaab, Lena Arnold, Ulrich Muller, Donald J. Siegel, and Yang Ming.; U.S. Department of Energy, Hydrogen and Fuel Cells Program 2014 Annual Merit Review Proceedings: Project ST010.https://www.hydrogen.energy.gov/pdfs/review14/st010_veenstra_2014_o.pdf.

(61) Colón, Y. J.; Fairen-Jimenez, D.; Wilmer, C. E.; Snurr, R. Q. High-Throughput Screening of Porous Crystalline Materials for Hydrogen Storage Capacity near Room Temperature. *J. Phys. Chem. C* **2014**, *118* (10), 5383–5389.

(62) Bao, Y.; Martin, R. L.; Haranczyk, M.; Deem, M. W. In Silico Prediction of MOFs with High Deliverable Capacity or Internal Surface Area. *Phys. Chem. Chem. Phys.* **2015**, *17* (18), 11962–11973.

(63) Gómez-Gualdrón, D. A.; Wilmer, C. E.; Farha, O. K.; Hupp, J. T.; Snurr, R. Q. Exploring the Limits of Methane Storage and Delivery in Nanoporous Materials. *J. Phys. Chem. C* **2014**, *118* (13), 6941–6951.

(64) Willems, T. F.; Rycroft, C. H.; Kazi, M.; Meza, J. C.; Haranczyk, M. Algorithms and Tools for High-Throughput Geometry-Based Analysis of Crystalline Porous Materials. *Microporous Mesoporous Mater.* **2012**, *149* (1), 134–141.

(65) Goldsmith, J.; Wong-Foy, A. G.; Cafarella, M. J.; Siegel, D. J. Theoretical Limits of Hydrogen Storage in Metal–Organic Frameworks: Opportunities and Trade-Offs.

(66) Dubbeldam, D.; Calero, S.; Ellis, D. E.; Snurr, R. Q. RASPA: Molecular Simulation Software for Adsorption and Diffusion in Flexible Nanoporous Materials. *Mol. Simul.* **2016**, *42* (2), 81–101.

(67) Farha, O. K.; Özgür Yazaydın, A.; Eryazici, I.; Malliakas, C. D.; Hauser, B. G.; Kanatzidis, M. G.; Nguyen, S. T.; Snurr, R. Q.; Hupp, J. T. De Novo Synthesis of a Metal–Organic Framework Material Featuring Ultrahigh Surface Area and Gas Storage Capacities. *Nat. Chem.* **2010**, *2* (11), 944–948.

(68) Koh, K.; Van Oosterhout, J. D.; Roy, S.; Wong-Foy, A. G.; Matzger, A. J. Exceptional Surface Area from Coordination Copolymers Derived from Two Linear Linkers of Differing Lengths. *Chem. Sci.* **2012**, *3* (8), 2429.

(69) Yuan, D.; Zhao, D.; Sun, D.; Zhou, H.-C. An Isoreticular Series of Metal-Organic Frameworks with Dendritic Hexacarboxylate Ligands and Exceptionally High Gas-Uptake Capacity. *Angew. Chem. Int. Ed* **2010**, *49*, 5357–5361.

(70) Mondloch, J. E.; Karagiaridi, O.; Farha, O. K.; Hupp, J. T. Activation of Metal–Organic Framework Materials. *CrystEngComm* **2013**, *15*, 9258–9264.

(71) Ma, J.; Kalenak, A. P.; Wong-Foy, A. G.; Matzger, A. J. Rapid Guest Exchange and Ultra-Low Surface Tension Solvents Optimize Metal-Organic Framework Activation. *Angew. Chemie Int. Ed.* **2017**, *56* (46), 14618–14621.

(72) Thommes, M.; Kaneko, K.; Neimark, A. V.; Olivier, J. P.; Rodriguez-Reinoso, F.; Rouquerol, J.; Sing, K. S. W. Physisorption of Gases, with Special Reference to the Evaluation of Surface Area and Pore Size Distribution (IUPAC Technical Report). *Pure Appl. Chem.* **2015**, *87* (9–10), 1051–1069.

(73) Target Explanation Document: Onboard Hydrogen Storage for Light-Duty Fuel Cell Vehicles, U.S. Department of 1 5 10 15 20 25 30 35 40 45 50 55 1 5 10 15 20 25 30 35 40 45 50 55 24 | Energy Environ. Sci., 2018, 00, 1"29 This Journal Is !C The Royal Society .

(74) Rankine, D.; Avellaneda, A.; Hill, M. R.; Doonan, C. J.; Sumby, C. J. Control of Framework Interpenetration for in Situ Modified Hydroxyl Functionalised IRMOFswz ChemComm. *Chem. Commun* **2012**, *48*, 10328–10330.

(75) García-Holley, P.; Schweitzer, B.; Islamoglu, T.; Liu, Y.; Lin, L.; Rodriguez, S.; Weston, M. H.; Hupp, J. T.; Gómez-Gualdrón, D. A.; Yildirim, T.; et al. Benchmark Study of Hydrogen Storage in Metal–Organic Frameworks under Temperature and Pressure Swing Conditions. *ACS Energy Lett.* **2018**, 748–754.

(76) Bucior, B. J.; Bobbitt, N. S.; Islamoglu, T.; Goswami, S.; Gopalan, A.; Yildirim, T.; Farha, O. K.; Bagheri, N.; Snurr, R. Q. Energy-Based Descriptors to Rapidly Predict Hydrogen Storage in Metal-Organic Frameworks. *Mol. Syst. Des. Eng. 2018. DOI 10.1039/c8me00050f.*

(77) Tamburello, D.; Hardy, B.; Corgnale, C.; Sulic, M.; Anton, D. 2017 Proceedings of the ASME 2017 Fluids Engineering Division Summer Meeting, American Society of Mechanical Engineers. In *2017 Proceedings of the ASME 2017 Fluids Engineering Division Summer Meeting, American Society of Mechanical Engineers* ; 2017; p V01BT08A005–V01BT08A005.

(78) Veenstra, M.; Yang, J.; Xu, C.; Gaab, M.; Arnold, L.; Muller, U.; Siegel, D. J.; Ming, Y. Ford/BASF-SE/UM Activities in Support of the Hydrogen Storage Engineering Center of Excellence. In *U.S. Department of Energy, Hydrogen and Fuel Cells Program 2014 Annual Merit Review Proceedings: Project ST010*; https://www.hydrogen.energy.gov/pdfs/review14/st010_veenstra_2014_o.pdf.

(79) Walton, K. S.; Snurr, R. Q. Applicability of the BET Method for Determining Surface Areas of Microporous Metal–Organic Frameworks. *J. Am. Chem. Soc.* **2007**, *129* (27), 8552–8556.

(80) Parilla, P. A.; Gross, K.; Hurst, K.; Gennett, T. Recommended Volumetric Capacity Definitions and Protocols for Accurate, Standardized and Unambiguous Metrics for Hydrogen Storage Materials. *Appl. Phys. A* **2016**, *122* (3), 201.

(81) Mason, J. A.; Veenstra, M.; Long, J. R. Evaluating Metal–Organic Frameworks for Natural Gas Storage. *Chem. Sci.* **2014**, *5* (1), 32–51.

(82) Purewal, J.; Liu, D.; Sudik, A.; Veenstra, M.; Yang, J.; Maurer, S.; Müller, U.; Siegel, D. J. Improved Hydrogen Storage and Thermal Conductivity in High-Density MOF-5 Composites. *J. Phys. Chem. C* **2012**, *116* (38), 20199–20212.

(83) Ahmed, A.; Seth, S.; Purewal, J.; Wong-Foy, A. G.; Veenstra, M.; Matzger, A. J.; Siegel, D. J. Exceptional H2 Storage Achieved by Screening Half-a-Million MOFs. *(Submitted)*.

(84) Noguera-Díaz, A.; Bimbo, N.; Holyfield, L. T.; Ahmet, I. Y.; Ting, V. P.; Mays, T. J. Structure–Property Relationships in Metal-Organic Frameworks for Hydrogen Storage. *Colloids Surfaces A Physicochem. Eng. Asp.* **2016**, *496*, 77–85.

(85) Richard, M.-A.; Bénard, P.; Chahine, R. Gas Adsorption Process in Activated Carbon over a Wide Temperature Range above the Critical Point. Part 1: Modified Dubinin-Astakhov Model. *Adsorption* **2009**, *15* (1), 43–51.

(86) Aceves, S. M.; Petitpas, G.; Espinosa-Loza, F.; Matthews, M. J.; Ledesma-Orozco, E. Safe, Long Range, Inexpensive and Rapidly Refuelable Hydrogen Vehicles with Cryogenic Pressure Vessels. *Int. J. Hydrogen Energy* **2013**, *38* (5), 2480–2489.

(87) Ubaid, S.; Zacharia, R.; Xiao, J.; Chahine, R.; Bénard, P.; Tessier, P. Effect of Flowthrough Cooling Heat Removal on the Performances of MOF-5 Cryo-Adsorptive Hydrogen Reservoir for Bulk Storage Applications. *Int. J. Hydrogen Energy* **2015**, *40* (30), 9314–9325.

(88) Hou, X. X.; Sulic, M.; Ortmann, J. P.; Cai, M.; Chakraborty, A. Experimental and Numerical Investigation of the Cryogenic Hydrogen Storage Processes over MOF-5. *Int. J. Hydrogen Energy* **2016**, *41* (6), 4026–4038.

(89) Drost, K.; Jovanovic, G.; Paul, B. *Microscale Enhancement of Heat and Mass Transfer for Hydrogen Energy Storage*; Golden, CO (United States), 2015.

(90) Purewal, J. J.; Liu, D.; Yang, J.; Sudik, A.; Siegel, D. J.; Maurer, S.; Müller, U. Increased Volumetric Hydrogen Uptake of MOF-5 by Powder Densification. *Int. J. Hydrogen Energy* **2012**, *37* (3), 2723–2727.

Appendix A
Additional information: Materials Development

Alauddin Ahmed,[†] Saona Seth,[‡] Justin Purewal,[#] Antek G. Wong-Foy,[‡] Mike Veenstra,[#] Adam J. Matzger,[‡] and Donald J. Siegel[†,§,Δ,ß,*]

[†]Mechanical Engineering Department, [‡]Department of Chemistry, [§]Materials Science & Engineering, [Δ]Applied Physics Program, and [ß]University of Michigan Energy Institute, University of Michigan, Ann Arbor, MI 48109, United States
[#]Ford Motor Company, Research and Advanced Engineering, 1201 Village Rd., Dearborn, MI 48121, United States

S1. Computational Details
S1.1. Details of the MOF Database

A database (DB) of 493,458 real and hypothetical MOFs was compiled, Table 1. The database includes 15,235 experimentally-derived MOF crystal structures from the UM[1], CoRE[2], and Cambridge Structural Database (CSD) 2017[3] databases. The UM and CoRE DBs are based on structures from the CSD versions 2011 and 2014 and were refined using an algorithm developed by Goldsmith *et al* for solvent removal.[1,4] In addition to these 'real-MOF' databases, eight hypothetical MOF DBs from the literature were also examined.[5–10] Wilmer *et al.*[5] developed the first hypothetical database containing 137,953 MOFs constructed from 102 building blocks. Martin *et al.*[6] developed a DB of 116 MOF-5 analogs using commercially available ("Mail-Oder") organic linkers. Bao *et al.*[7] used an evolutionary algorithm for the *de novo* design of 2,816 MOFs using an *in silico* technique for identifying appropriate linkers. Gomez-Gualdron *et al.*[8] designed a zirconium-based database consisting of 204 members using reverse topological engineering of 4 nets (fcu, ftw, scu, and csq). Finally, Aghaji *et al.*[9] generated a database of 324, 500 hypothetical MOF structures combining 70 SBUs and 19 functional groups.

Table S1. List of custom hypothetical or reconstructed MOFs examined in this work.

MOF Description	Density (g/cm^3)	Gravimetric Surface Area (m^2/g)	Volumetric Surface Area (m^2/cm^3)	Void Fraction	Pore Volume (cm^3/g)	Usable Gravimetric Capacity (wt.%)	Usable Volumetric Capacity (g/L)
Thiophenecarboxylateacrylate	0.46	4236	1961	0.85	1.84	7.0	36.8
Me-SNU-70	0.42	4569	1917	0.85	2.02	7.5	36.0
IRMOF-10_NIP	0.33	4999	1641	0.87	2.65	9.6	37.6
IRMOF-8_NIP	0.45	4379	1964	0.83	1.86	6.8	35.3
UMCM-8	0.51	4098	2096	0.82	1.61	5.7	33.4
UMCM-9	0.37	4847	1805	0.86	2.31	8.3	36.2
NU-110-anthracene	0.27	6000	1628	0.88	3.26	10.3	34.5
DichloroUMCM-1	0.42	4107	1709	0.85	2.04	6.9	33.7
DimethylUMCM-1	0.40	1713	4276	0.85	2.12	7.2	33.6
AnthraceneUMCM-1	0.43	3830	1640	0.84	1.95	6.3	31.7
dihydroisobenzofuranUMCM-1	0.41	4129	1677	0.85	2.09	7.1	33.9
NaphthaleneUMCM-1	0.41	4203	1719	0.85	2.07	6.9	33.2
Hydroxy-BPDC_IRMOF	0.36	4999	1809	0.87	2.39	8.6	36.4
Acetate-BPDC_IRMOF	0.45	5122	2281	0.83	1.85	6.3	32.3
NU-110-anthracene	0.27	6000	1628	0.88	3.26	10.3	34.5
BrMOF-5	1.3	1445	1911	0.76	0.57	1.5	21.0
MOF-5_25%_Ethynyl	0.61	3534	2154	0.80	1.31	3.6	25.4
MOF-177-NH_2	0.45	4514	2045	0.82	1.82	6.4	33.7

Table S2. Examples of CSD 2017 MOFs not considered in the screening.[11]

MOF Identifier	Rationale for exclusion	CSD17 MOF	Rationale for exclusion	CSD17 MOF	Rationale for exclusion
VIJNOT	1D polymer	NATBAL	1D polymer	HACQOS	1D polymer
SUVMAY	1D polymer	ZODWAS	1D polymer	HACQUY	1D polymer
TEWMIS	1D polymer	HURHEI	2D polymer	HICLAH	1D polymer
NUSTIF	1D polymer	QIYKIU	1D polymer	LADQEM	1D polymer
PORZAZ	1D polymer	PEZVEW	1D polymer	LADQEM01	1D polymer
SIBDIS	1D polymer	HINQAY	1D polymer	NOZQEY	1D polymer
UZIDOX	1D polymer	KALZUU	1D polymer	TUBTOB	1D polymer
WUNPIE	1D polymer	BUQKOP	2D polymer	ULUBAE	1D polymer
HUBWUY	1D polymer	AXILOI	1D polymer	ULUBEI	1D polymer
LADQIQ	1D polymer	AHAZAM	2D polymer	WAJPED	2D polymer
SOFGIF	1D polymer	AFEJEB	2D polymer	XAWBOO	1D polymer
HICKOU	1D polymer	MEVBUK	1D polymer	XOTBUF	1D polymer
LADQOW	1D polymer	CERGIQ	1D polymer	COPBOZ	1D polymer
POBWIM	discrete complex	DAKYUL	1D polymer	WUYBIB	1D polymer
HUVBIK	1D polymer	DAKZEW	1D polymer	MAMKEQ	1D polymer
HUDHET	2D polymer	DIHKIP	1D polymer	YOQPEA	1D polymer
XOKYOM	1D polymer	EGUGIY	1D polymer	DAKXOE	1D polymer
KIQCIW	1D polymer	ENUKUU	1D polymer	ENAPAL	1D polymer
HIGMOA	1D polymer	GUTQIX	1D polymer	BIVVEI	1D polymer
BEWRUR	Doubly interpenetrated 3D MOF	BEMFOQ	1D polymer	FASZUW	1D polymer
BEWSAY	Doubly interpenetrated 3D MOF	AHAYUF	2D polymer	AHAYOZ	2D polymer
JOVKOW	2D polymer	GOVMEJ	2D polymer	FOXMIQ	1D polymer
ENIDOV	1D polymer	WOKLOZ	discrete metal complex	EGUGUK	1D polymer
GOBKEN	1D polymer	AHAYIT	1D polymer	EQADAC	1D polymer
BEJZIA	1D polymer	ICETER	1D polymer	BUKSAD	MOF, low experimental SA

S1.2. Calculations of MOF's Crystallographic Properties

Single crystal density, pore volume, void fraction, pore diameter, gravimetric surface area, and volumetric surface areas of all MOFs were calculated using Zeo++ code[12] using a Voronoi decomposition method. Except for single crystal density, all other properties were computed using a N_2 probe molecule of radius 1.86 Å.

S1.3. Details of Grand Canonical Monte Carlo Simulations

A. Interatomic Potentials

Hydrogen molecules were modeled using the pseudo-Feynman-Hibbs model of Fischer et al.[13–15] This model has been extensively verified against measured hydrogen adsorption isotherms for MOF-5, IRMOF-20, UMCM-4, MOF-177, NH2-MOF-177, and Cu-DUT-23, as reported in our earlier work.[15] MOF atoms were described using interatomic potential parameters from Refs. 16,17

B. GCMC Simulation Conditions

All GCMC simulations were carried out using the RASPA[18] package. H_2-H_2 and H_2-MOF interactions were computed within a 12 Å cutoff radius. The MOF unit cell was replicated if smaller than 24 Å in length in any direction. Long range corrections were used to compensate for the exclusion of interactions beyond the cutoff radius.[19,20]All MOF structures were deemed to be rigid. Lorentz-Berthelot[21,22] combination rules were used in computing MOF-H_2 interaction parameters. Initially, H_2 capacity was determined at each pressure and temperature by averaging the number of H_2 molecules in the simulation cell over 1,000 GCMC production cycles, preceded by 1,000 initial cycles.[23] GCMC simulations were carried out using 20,000 cycles for a subset of high preforming MOFs; in these cases the last 10,000 cycles were used for computing H_2 adsorption. Each GCMC cycle was comprised of moves equal to the number of molecules in the system at the beginning of the cycle.[24] Translation, insertion, and deletion moves were performed with equal probabilities.[24] The average percentage deviations between short and long runs storage capacities are less than a few percent. That suggests short simulations are sufficient for high-throughput GCMC simulations of hydrogen uptakes, which is consistent with the conclusion recently drawn by Bobbit et al.[23]

S1.4. MOF Screening

Figure S1 illustrates the workflow for computational screening. First, accessible surface areas and pore volumes were computed using the Zeo++ code. It was determined that 426,700 MOFs exhibit non-zero porosity or surface area. MOFs with zero accessible surface area were excluded from further screening. Second, the Chahine rule was used for computing total hydrogen storage capacities at 35 bar and 77 K as discussed in our earlier publications.[1,25] Third, MOFs that perform better than or equal to Chahine-rule-predicted MOF-5 capacities (i.e., 8.4 wt.% and 54.4 g/L) were retained for GCMC simulations. GCMC simulations were carried out on a total of 43,227 MOFs at 100 and 5 bar at 77 K. All MOFs contained in the real MOFs (UM+CoRE+CSD), mail-order, Zr-MOFs, and MOF-74 analogs databases and our custom-designed in-house MOFs as shown in Table 1 were screened using GCMC simulations without pre-screening. However, due to their large size, a multi-stage screening protocol as shown in Figure S1 was used for screening rest of the hypothetical databases. Finally, MOFs were screened based on the usable capacity of MOF-5 (4.5 wt% & 31.1 g/L) and IRMOF-20 (5.7 wt.% & 33.4 g/L) for a pressure swing between 5 and 100 bar at 77 K.

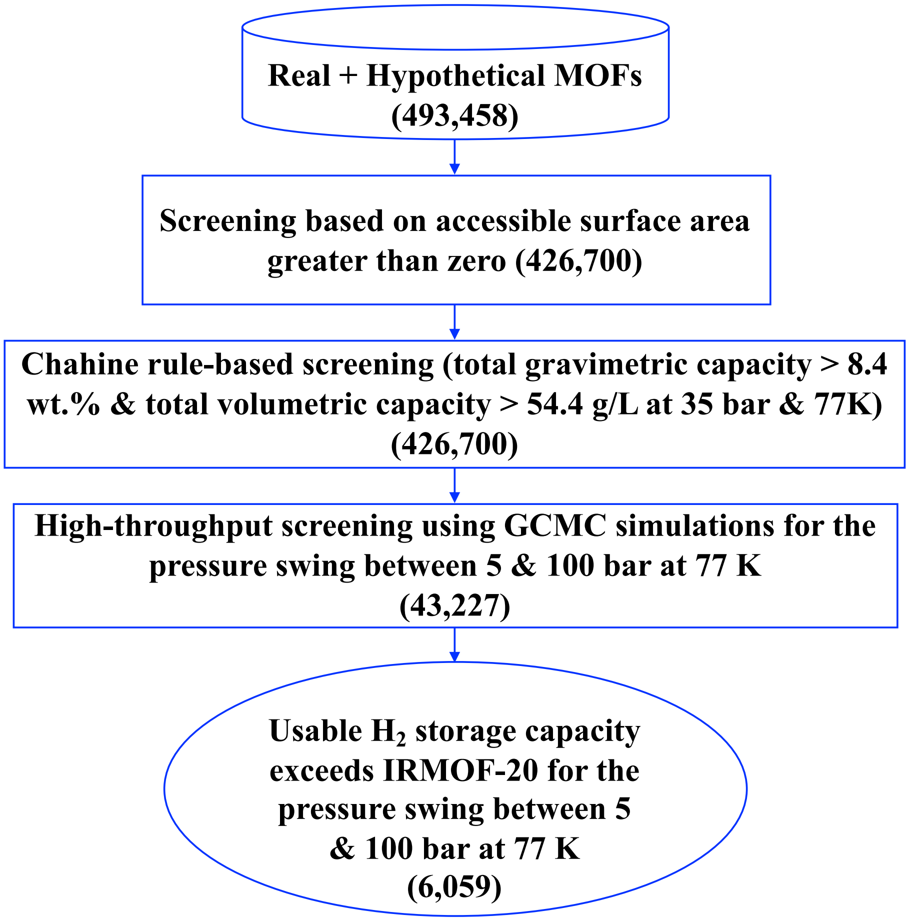

Figure S1. Workflow for computational screening.

Table S3. 50 Real MOFs that exceed the usable capacity of IRMOF-20.[1,2,11]

CSD Refcode	Single Crystal Density (g/cm³)	Gravimetric Surface Area (m²/g)	Volumetric Surface Area (m²/cm³)	Void Fraction	Pore Volume (cm³/g)	Largest Pore Diameter (Å)	Pore Limiting Diameter (Å)	Usable Gravimetric Capacity, Pressure Swing (wt.%)	Usable Volumetric Capacity, Pressure Swing (g/L)
ECOLEP	0.41	4510	1836	0.89	2.09	11.6	10.9	8.2	39.0
VUSJUP	0.52	4142	2151	0.83	1.63	14.9	8.7	6.5	38.1
GAQYIH	0.56	3713	2079	0.84	1.52	20.3	9.0	6.1	37.8
XUKYEI	0.29	6327	1817	0.88	3.02	13.2	10.8	10.7	37.4
VEBHUG	0.45	4302	1936	0.87	1.89	17.3	10.0	7.2	37.4
BAZFUF	0.34	5470	1860	0.91	2.54	20.2	8.6	9.1	37.1
HABQUY	0.29	5750	1664	0.91	3.04	25.7	12.1	10.5	37.1
GAGZEV	0.28	5777	1613	0.92	3.17	28.7	11.5	10.8	37.0
ZELROZ	0.36	4947	1790	0.88	2.4	16.9	11.1	8.7	36.8
XAFFIV	0.36	5329	1910	0.89	2.36	14.2	13.2	8.5	36.6
VAGMAT	0.36	5203	1898	0.89	2.33	14.9	13.3	8.5	36.5
XAFFAN	0.37	5181	1892	0.89	2.33	14.9	13.2	8.3	36.5
NIBJAK	0.22	5417	1210	0.94	4.09	32.0	17.6	13.2	36.4
XAFFOB	0.37	5195	1907	0.89	2.32	14.8	13.2	8.3	36.4
HEXVEM	0.25	5455	1373	0.93	3.58	28.4	15.9	11.8	36.4
XAFFER	0.36	5171	1861	0.89	2.37	14.2	13.3	8.5	36.3
VAGMEX	0.35	5152	1815	0.9	2.43	15.3	14.5	8.7	36.3
NIBHOW	0.28	5103	1427	0.92	3.19	27.5	14.9	10.6	36.2
ADATIK	0.38	4566	1724	0.89	2.3	24.6	12.2	8.1	36.0
ADATAC	0.34	5145	1735	0.9	2.57	26.3	10.3	8.9	35.9
VETMIS	0.31	5713	1782	0.9	2.77	17.2	12.0	9.5	35.7
XAHPON	0.28	5268	1498	0.92	3.1	17.3	15.3	10.4	35.5
FEBXIV	0.29	5166	1517	0.91	3	17.3	15.8	10.1	35.5
LEJCIO	0.33	5275	1722	0.91	2.66	18.5	14.1	8.9	35.4
RUTNOK	0.24	6200	1493	0.9	3.73	24.6	14.7	12.1	35.4
MEHMET	0.41	4594	1878	0.89	2.06	21.8	9.1	7.3	35.2
LEJCEK	0.33	5776	1929	0.88	2.58	17.2	11.7	8.9	35.0
EHIJAH	0.39	4503	1734	0.88	2.21	18.5	11.7	7.6	35.0
EDUVOO	0.37	4857	1814	0.91	2.31	20.9	10.6	8.0	35.0
XAHPIH	0.36	4683	1668	0.89	2.42	14.3	13.4	8.2	35.0
HABRAF	0.38	4850	1854	0.89	2.21	24.3	9.0	7.8	35.0
LURRIA	0.41	4586	1864	0.92	2.08	22.4	9.7	7.2	34.9
XAHQAA	0.17	6250	1065	0.95	5.44	23.0	21.6	15.7	34.9
WIYMOG	0.41	6833	2788	0.81	2.05	12.1	7.6	7.3	34.8
XAFFUH	0.33	5152	1696	0.9	2.63	23.7	19.6	8.8	34.8
XAHPUT	0.18	6301	1126	0.94	5.15	21.8	20.6	14.9	34.7
ADASEF	0.44	4168	1816	0.89	1.96	21.6	10.9	6.8	34.5
HOMXIR	0.39	4388	1731	0.88	2.16	23.7	22.9	7.6	34.5
ECOKAJ	0.33	3575	1163	0.89	2.69	19.0	17.6	8.9	34.5
BAZGAM	0.13	6581	833	0.97	7.46	42.8	24.2	19.3	34.3
BIBXOB	0.41	4924	2017	0.87	2.04	19.7	8.0	7.2	34.2
HOHMEX	0.32	4986	1575	0.88	2.74	18.8	14.9	9.0	34.1
PIBPIA	0.46	2982	1368	0.85	1.83	15.5	14.3	6.6	34.1
XAHPED	0.37	5131	1921	0.87	2.26	12.4	10.9	7.8	34.0
PIBNUK	0.42	3289	1391	0.85	1.98	15.4	14.2	7.1	34.0
ALULEZ	0.43	3447	1468	0.84	1.96	18.8	13.4	6.9	34.0
DITJIB	0.52	3398	1772	0.87	1.6	20.4	9.0	5.8	33.9
RICBEM	0.4	5745	2293	0.88	2.07	11.4	8.6	7.1	33.9
LEHXUT	0.41	4560	1857	0.88	2.06	25.0	9.1	7.1	33.9
PIBNUK01	0.42	3297	1394	0.85	1.97	15.4	14.2	7.0	33.8

Table S4. Mail-order MOFs that exceed the usable capacity of IRMOF-20.[26]

MOF Name	Single Crystal Density (g/cm^3)	Gravimetric Surface Area (m^2/g)	Vol. Surface Area (m^2/cm^3)	Void Frac.	Pore Vol. (cm^3/g)	Largest Pore Diameter (Å)	Pore Limiting Diameter (Å)	Usable Grav. Capacity, Pressure Swing (wt.%)	Usable Volumetric Capacity, Pressure Swing (g/L)
MOF-5_cooh_2_2738_1_basic_opt	0.47	4548	2149	0.78	1.34	7.8	15.8	7.1	39.3
MOF-5_cooh_2_2796_1_basic_opt	0.37	4965	1838	0.87	2.36	10.0	16.4	8.8	37.8
MOF-5_cooh_2_394_1_basic_opt	0.29	5743	1640	0.89	3.13	11.8	20.3	10.9	36.9
MOF-5_cooh_2_68_1_basic_opt	0.32	5233	1679	0.88	2.74	11.1	20.1	9.7	36.9
MOF-5_cooh_2_567_1_basic_opt	0.40	4756	1905	0.86	2.14	10.0	16.5	8.0	36.8
MOF-5_cooh_2_2368_1_basic_opt	0.23	5938	1351	0.91	4.01	14.7	23.4	13.1	36.7
MOF-5_cooh_2_646_1_basic_opt	0.24	5781	1392	0.91	3.76	14.0	22.3	12.5	36.7
MOF-5_cooh_2_790_1_basic_opt	0.30	5149	1529	0.89	2.99	13.0	21.6	10.3	36.6
MOF-5_cooh_2_1929_1_basic_opt	0.45	4045	1823	0.84	1.87	9.5	17.8	7.0	36.5
MOF-5_cooh_2_1505_1_basic_opt	0.25	5714	1421	0.91	3.64	13.6	22.3	12.1	36.4
MOF-5_cooh_2_239_2_basic_opt	0.49	4225	2071	0.84	1.72	8.7	13.7	6.6	36.4
MOF-5_cooh_2_1861_1_basic_opt	0.30	5236	1594	0.88	2.90	12.1	20.3	10.1	36.3
MOF-5_cooh_2_11_1_basic_opt	0.33	5282	1746	0.87	2.65	12.3	18.1	9.3	36.0
MOF-5_cooh_2_2349_1_basic_opt	0.26	5948	1548	0.90	3.45	12.6	21.2	11.4	35.9
MOF-5_cooh_2_2558_1_basic_opt	0.21	5955	1262	0.91	4.31	15.1	24.3	13.5	35.8
MOF-5_cooh_2_1239_1_basic_opt	0.29	5834	1699	0.88	3.03	11.3	19.8	10.2	35.7
MOF-5_cooh_2_861_1_basic_opt	0.42	4556	1929	0.84	1.98	9.3	16.2	7.3	35.3
MOF-5_cooh_2_779_1_basic_opt	0.13	6997	934	0.94	7.07	20.4	30.9	19.1	34.3
MOF-5_cooh_2_1589_1_basic_opt	0.14	6581	940	0.94	6.59	20.7	31.3	18.1	34.1

Table S5. *In silico* deliverable MOFs that exceed the usable capacity of IRMOF-20.[7]

MOF Name	Single Crystal Density (g/cm^3)	Grav. Surface Area (m^2/g)	Vol. Surface Area (m^2/cm^3)	Void Frac.	Pore Vol. (cm^3/g)	Largest Pore Diameter (Å)	Pore Limiting Diameter (Å)	Usable Grav. Capacity, Pressure Swing (wt.%)	Usable Volumetric Capacity, Pressure Swing (g/L)
Syn014648	0.48	4686	2248	0.84	1.75	11.1	7.8	7.0	38.2
Syn028362	0.40	5733	2272	0.83	2.10	11.7	9.2	7.6	35.3
Syn031169	0.47	4833	2294	0.83	1.75	11.4	8.5	6.5	34.9
Syn029009	0.40	5449	2204	0.82	2.04	12.0	9.2	7.4	34.6
Syn015166	0.42	5329	2240	0.83	1.97	11.4	8.8	7.0	34.2
Syn014460	0.50	4310	2172	0.83	1.64	16.3	8.8	5.9	33.6

Table S6. *In silico* surface MOFs that exceed the usable capacity of IRMOF-20.[10]

MOF Name	Single Crystal Density (g/cm^3)	Grav. Surface Area (m^2/g)	Vol. Surface Area (m^2/cm^3)	Void Frac.	Pore Vol. (cm^3/g)	Largest Pore Diameter (Å)	Pore Limiting Diameter (Å)	Usable Grav. Capacity, Pressure Swing (wt.%)	Usable Vol. Capacity, Pressure Swing (g/L)
cds_Syn029752	0.45	4898	2192	0.83	1.86	2.6	11.9	7.2	36.9
cds_Syn027014	0.40	5484	2191	0.84	2.11	3.0	12.2	7.9	36.7
cds_Syn015279	0.43	5075	2179	0.84	1.97	3.2	14.0	7.4	36.7
cds_Syn034835	0.42	5346	2262	0.84	1.97	2.8	12.4	7.5	36.6
cds_Syn025813	0.42	5218	2210	0.85	2.00	3.2	13.9	7.4	36.4
cds_Syn032331	0.43	5170	2204	0.84	1.97	2.8	12.4	7.4	36.3
cds_Syn035762	0.42	5287	2213	0.84	2.01	3.3	14.3	7.5	36.3
sod_B_Syn000038	0.38	5836	2232	0.84	2.20	3.3	12.9	8.1	36.0
cds_Syn038557	0.48	4740	2294	0.83	1.72	3.0	14.8	6.5	35.9
cds_Syn025253	0.43	5108	2206	0.84	1.94	3.2	14.5	7.2	35.9
cds_Syn024908	0.46	4900	2241	0.83	1.82	2.8	13.4	6.9	35.9
cds_A_Syn008586	0.38	5938	2254	0.84	2.22	3.6	14.3	8.0	35.8
cds_Syn037641	0.46	4990	2271	0.83	1.83	3.3	15.4	6.8	35.5
cds_Syn035184	0.44	5085	2251	0.83	1.88	3.2	14.4	7.0	35.4
cds_Syn024117	0.45	4982	2221	0.84	1.87	3.3	15.2	6.9	35.3
cds_Syn030154	0.44	5307	2322	0.83	1.90	3.3	14.8	7.0	35.3
cds_Syn039995	0.43	5203	2237	0.84	1.95	3.5	15.5	7.1	35.2
sod_B_Syn000903	0.37	5956	2216	0.83	2.24	3.7	14.4	8.0	35.2
cds_Syn024859	0.45	4995	2261	0.83	1.84	3.3	15.4	6.8	35.1
cds_Syn030819	0.49	4767	2340	0.83	1.68	3.0	15.3	6.3	35.1

Table S7. ToBaCCo MOFs that exceed the usable capacity of IRMOF-20.[27]

MOF Name	Single Crystal Density (g/cm^3)	Grav. Surface Area (m^2/g)	Vol. Surface Area (m^2/cm^3)	Void Frac.	Pore Vol. (cm^3/g)	Largest Pore Diameter (Å)	Pore Limiting Diameter (Å)	Usable Grav. Capacity, Pressure Swing (wt.%)	Usable Vol. Capacity, Pressure Swing (g/L)
mof_4690	0.33	7327	2437	0.86	2.59	12.4	12.2	9.7	38.7
mof_7599	0.38	5589	2127	0.85	2.24	12.7	9.0	8.5	38.1
mof_4699	0.35	6949	2461	0.86	2.42	13.4	13.1	9.0	37.8
mof_4639	0.38	5876	2246	0.85	2.22	13.3	11.3	8.4	37.8
mof_6830	0.40	5404	2139	0.84	2.13	16.5	7.7	8.2	37.6
mof_4707	0.36	6546	2359	0.86	2.38	14.8	14.3	8.8	37.6
mof_6831	0.38	5664	2177	0.85	2.20	15.8	8.4	8.4	37.5
mof_4738	0.36	6848	2447	0.85	2.38	12.4	12.2	8.8	37.5
mof_4978	0.36	6815	2439	0.85	2.38	12.4	12.2	8.8	37.4
mof_4930	0.34	7160	2469	0.85	2.48	12.9	11.6	9.1	37.4
mof_4947	0.36	6572	2378	0.86	2.37	14.8	14.0	8.7	37.4
mof_4952	0.27	8067	2216	0.87	3.17	15.8	15.1	11.0	37.3
mof_4939	0.36	6968	2496	0.86	2.39	12.7	12.6	8.7	37.3
mof_6954	0.44	5044	2229	0.84	1.90	16.2	7.2	7.3	37.1
mof_4747	0.37	6461	2419	0.85	2.27	13.6	13.2	8.3	36.8
mof_6522	0.43	4922	2140	0.84	1.93	10.4	9.3	7.3	36.7
mof_4987	0.38	6401	2414	0.85	2.25	13.6	13.2	8.2	36.6
mof_6074	0.43	4946	2132	0.84	1.96	11.9	9.5	7.4	36.5
mof_3988	0.32	6732	2185	0.84	2.58	12.7	9.0	9.3	36.3
mof_4995	0.37	6154	2305	0.85	2.28	15.3	15.0	8.2	36.3

Table S8. Top ranked Zr-MOFs that exceed the usable capacity of IRMOF-20.[8]

MOF Name	Single Crystal Density (g/cm³)	Grav. Surface Area (m²/g)	Vol. Surface Area (m²/cm³)	Void Frac.	Pore Vol. (cm³/g)	Largest Pore Diameter (Å)	Pore Limiting Diameter (Å)	Usable Grav. Capacity, Pressure Swing (wt.%)	Usable Vol. Capacity, Pressure Swing (g/L)
NU-TPE-4PTT-ftw	0.27	6323	1684	0.88	3.30	10.8	21.6	11.5	37.5
NU-Pyr-4PTT-ftw	0.33	5741	1875	0.86	2.64	10.2	21.4	9.5	37.3
NU-Por-4PTT-ftw	0.33	5576	1836	0.86	2.61	8.9	22.0	9.4	37.2
NU-TPE-4TTP	0.27	5838	1569	0.88	3.27	11.2	22.4	11.4	37.0
NU-TPE-4TPT-ftw	0.27	6335	1704	0.88	3.26	11.1	22.5	11.2	36.9
NU-Pyr-4TTP-ftw	0.33	5144	1678	0.86	2.63	10.6	19.4	9.5	36.8
NU-Py-4PTT-scu-s	0.28	5438	1531	0.89	3.15	18.0	20.1	10.9	36.8
NU-2_P_4PTT_Por_PTT-ftw	0.37	5469	2002	0.84	2.31	9.3	16.8	8.5	36.7
NU-P-4TTP-scu-s	0.35	4774	1655	0.86	2.49	13.4	17.9	9.1	36.7
NU-Por-4TTP-ftw	0.32	5209	1672	0.86	2.68	9.7	22.3	9.6	36.7
NU-P-4PTT-scu-s	0.35	4988	1728	0.86	2.50	13.8	15.9	9.0	36.6
NU-TPE-4TPT-scu-s	0.28	5450	1517	0.88	3.17	15.2	19.0	11.0	36.6
NU-TPE-4PTT-scu-s	0.28	5703	1587	0.88	3.17	15.8	18.4	11.0	36.6
NU-Por-4PTT-scu	0.26	5461	1446	0.89	3.37	19.0	20.5	11.5	36.6
NU-Py-4TPT-scu-s	0.28	5407	1512	0.89	3.17	18.2	22.5	10.8	36.5
NU-P-4TPT-scu-s	0.35	4903	1700	0.86	2.49	13.2	18.2	9.0	36.5
NU-TTTT-fcu	0.48	4262	2041	0.83	1.74	8.6	17.3	6.7	36.5
NU-TPE-4PTT-scu-l	0.24	5863	1383	0.90	3.82	18.4	21.1	12.6	36.5
NU-TPE-4TPT-scu-l	0.24	5754	1356	0.90	3.82	18.1	21.4	12.6	36.4
NU-Py-4TTP-scu-s	0.27	5126	1404	0.89	3.25	17.7	21.1	10.9	36.4

Table S9. Top ranked Northwestern MOFs that exceed the usable capacity of IRMOF-20.[5]

MOF Name	Single Crystal Density (g/cm^3)	Grav. Surface Area (m^2/g)	Vol. Surface Area (m^2/cm^3)	Void Frac.	Pore Vol. (cm^3/g)	Largest Pore Diameter (Å)	Pore Limiting Diameter (Å)	Usable Grav. Capacity, Pressure Swing (wt.%)	Usable Vol. Capacity, Pressure Swing (g/L)
hypotheticalMOF_5048108_i_1_j_25_k_20_m_3	0.40	5285	2140	0.86	2.12	10.3	12.5	8.2	38.1
hypotheticalMOF_5048221_i_1_j_25_k_20_m_10	0.35	6165	2144	0.86	2.47	10.3	12.6	9.3	38.1
hypotheticalMOF_3000771_i_1_j_26_k_24_m_0_cat_1	0.40	5762	2333	0.85	2.11	8.1	10.9	8.2	37.9
hypotheticalMOF_5072982_i_2_j_25_k_20_m_2	0.37	5758	2144	0.86	2.30	9.7	12.7	8.7	37.9
hypotheticalMOF_5018670_i_0_j_25_k_19_m_11	0.42	5124	2143	0.85	2.04	10.6	12.8	7.9	37.9
hypotheticalMOF_5048082_i_1_j_25_k_20_m_1	0.37	5808	2143	0.86	2.33	10.3	13.2	8.8	37.9
hypotheticalMOF_5073022_i_2_j_25_k_20_m_4	0.35	6114	2137	0.86	2.45	9.7	12.4	9.2	37.9
hypotheticalMOF_3000644_i_1_j_26_k_23_m_0_cat_1	0.41	5831	2382	0.85	2.08	8.1	10.6	8.1	37.8
hypotheticalMOF_5038380_i_1_j_20_k_19_m_14	0.43	4962	2133	0.84	1.96	8.4	12.6	7.7	37.8
hypotheticalMOF_5072986_i_2_j_25_k_20_m_3	0.42	5200	2192	0.85	2.02	9.7	12.3	7.8	37.8
hypotheticalMOF_5048278_i_1_j_25_k_21_m_0	0.35	6163	2134	0.86	2.48	9.7	12.7	9.3	37.8
hypotheticalMOF_5001093_i_0_j_19_k_6_m_13	0.40	5342	2157	0.85	2.11	9.0	12.1	8.1	37.8
hypotheticalMOF_5072970_i_2_j_25_k_20_m_2	0.37	5725	2131	0.86	2.30	9.7	12.4	8.7	37.8
hypotheticalMOF_5018606_i_0_j_25_k_19_m_6	0.42	5222	2169	0.85	2.05	10.6	12.3	7.9	37.7
hypotheticalMOF_5018699_i_0_j_25_k_19_m_14	0.42	5142	2136	0.86	2.07	10.6	13.4	7.9	37.7
hypotheticalMOF_5072946_i_2_j_25_k_20_m_1	0.36	5843	2127	0.86	2.35	9.7	12.8	8.9	37.7
hypotheticalMOF_5072954_i_2_j_25_k_20_m_1	0.36	5871	2137	0.86	2.36	9.7	13.2	8.9	37.6
hypotheticalMOF_5039680_i_1_j_21_k_11_m_1	0.38	5676	2153	0.86	2.26	8.8	13.2	8.6	37.6
hypotheticalMOF_5053154_i_1_j_27_k_21_m_11	0.36	5877	2138	0.86	2.35	9.7	12.3	8.8	37.6
hypotheticalMOF_5041161_i_1_j_21_k_21_m_14	0.36	5972	2165	0.86	2.36	9.2	13.4	8.9	37.6

Table S10. Top ranked University of Ottawa MOFs that exceed the usable capacity of IRMOF-20.[28]

MOF Name	Single Crystal Density (g/cm³)	Grav. Surface Area (m²/g)	Vol. Surface Area (m²/cm³)	Void Frac.	Pore Vol. (cm³/g)	Largest Pore Diameter (Å)	Pore Limiting Diameter (Å)	Usable Grav. Capacity, Pressure Swing (wt.%)	Usable Vol. Capacity, Pressure Swing (g/L)
str_m3_o5_o25_f0_nbo.sym.193.out	0.42	5147	2166	0.86	2.04	13.3	7.9	7.9	38.2
str_m2_o5_o25_f0_nbo.sym.167.out	0.42	5119	2142	0.86	2.05	13.2	7.9	7.9	38.2
str_m3_o20_o21_f0_pcu.sym.19.out	0.40	5428	2151	0.85	2.16	12.8	10.3	8.3	38.2
str_m2_o20_o25_f0_pcu.sym.10.out	0.36	5957	2170	0.86	2.36	12.5	9.8	8.9	38.1
str_m3_o5_o25_f0_nbo.sym.19.out	0.43	5031	2179	0.86	1.98	13.3	8.3	7.7	38.1
str_m2_o5_o28_f0_nbo.sym.24.out	0.41	5164	2132	0.85	2.06	12.9	7.2	8.0	38.1
str_m2_o5_o25_f0_nbo.sym.110.out	0.41	5255	2156	0.86	2.09	13.3	7.9	8.1	38.0
str_m2_o5_o25_f0_nbo.sym.112.out	0.43	5081	2178	0.85	1.99	13.2	7.9	7.8	38.0
str_m2_o20_o25_f0_pcu.sym.33.out	0.37	5817	2139	0.86	2.34	13.2	9.8	8.8	38.0
str_m2_o5_o25_f0_nbo.sym.115.out	0.43	5030	2154	0.85	1.99	13.2	7.9	7.8	38.0
str_m2_o5_o25_f0_nbo.sym.35.out	0.42	5147	2174	0.86	2.03	13.4	7.9	7.8	38.0
str_m2_o5_o25_f0_nbo.sym.122.out	0.41	5319	2180	0.86	2.09	13.3	7.9	8.1	38.0
str_m3_o5_o25_f0_nbo.sym.139.out	0.43	5049	2183	0.86	1.98	13.3	7.8	7.6	38.0
str_m2_o20_o25_f0_pcu.sym.31.out	0.36	6037	2157	0.86	2.40	12.9	9.8	9.1	38.0
str_m2_o5_o25_f0_nbo.sym.132.out	0.42	5127	2166	0.86	2.03	13.2	8.3	7.8	37.9
str_m2_o20_o25_f0_pcu.sym.23.out	0.36	5918	2133	0.86	2.38	13.2	9.8	9.0	37.9
str_m3_o5_o25_f0_nbo.sym.173.out	0.46	4780	2199	0.85	1.86	12.8	8.0	7.2	37.9
str_m2_o20_o25_f0_pcu.sym.67.out	0.36	5951	2168	0.86	2.36	12.5	9.8	8.9	37.9
str_m3_o20_o25_f0_pcu.sym.28.out	0.42	5196	2178	0.86	2.05	13.0	10.1	7.8	37.9
str_m3_o5_o25_f0_nbo.sym.44.out	0.43	5103	2197	0.86	1.99	13.3	8.3	7.7	37.9

S2. Experimental Details

S2.1. General considerations

All reagents were obtained from commercial sources and used without further purification unless otherwise mentioned. Phase purity of the MOFs was determined prior to activation by powder X-ray diffraction (PXRD) on a Rigaku Smartlab diffractometer using Cu-Kα radiation (λ = 1.54187 Å) operating at 40 kV and 44 mA. The MOFs soaked in DMF were packed in a glass capillary, and PXRDs were recorded in transmission mode using a point focus source (0.5 mm collimator) and a 2D Pilatus detector. The powder diffraction patterns were in good agreement with their respective powder patterns simulated from the single crystal structures. BET surface areas and pore volumes of the MOFs were calculated from the nitrogen adsorption and desorption isotherm at 77 K from 0.005 to 1 bar using a NOVA e-series 4200 surface area analyzer from Quantachrome Instruments (Boynton Beach, Florida, USA).

S2.2. MOF Synthesis and Activation Procedure

S2.2.1 Synthesis and Activation of NU-100

A. Ligand Synthesis Scheme for NU-100

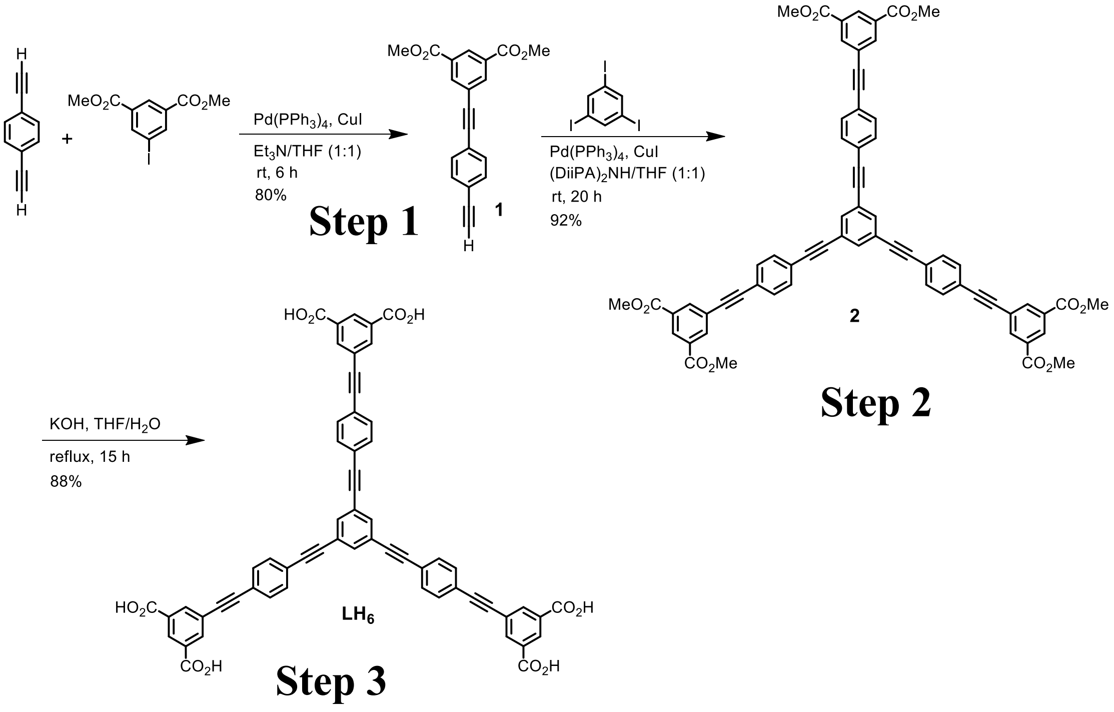

Figure S2. Synthesis of the Organic Linker 1,3,5-Tris[(1,3-carboxylic acid-5-(4-(ethynyl)phenyl))ethynyl] benzene (LH_6).

Step-1: *Dimethyl 5-((4-ethynylphenyl)ethynyl)isophthalate* (**1**)

In a 250 mL round bottom flask were added tetrahydrofuran (THF, 60 mL) and triethylamine (Et_3N, 60 mL), and nitrogen was bubbled through the solution for 15 min. To the solution were added 1,4-diethynylbenzene (1.575 g, 12.5 mmol), methyl 3-iodoisophthalate (1.000 g, 3.125 mmol), tetrakis(triphenylphosphine)palladium (0.060 g, 0.052 mmol) and cuprous iodide (0.010 g, 0.0525 mmol) under nitrogen atmosphere, and the resulting mixture was stirred under nitrogen at room temperature. The progress of the reaction was monitored by TLC analysis. After about 8 h the iodoester was consumed as observed in TLC. The reaction mixture was filtered through celite, and the residue was washed with 20 mL of 1:1 THF/Et_3N mixture, followed by 15 mL chloroform. The combined organic layer was evaporated to obtain the crude product. The crude material was purified by column chromatography on silica gel to obtain the pure product as off white solid (0.796 g, 80%).

Step-2: *1,3,5-Tris[(1,3-dimethylcarboxylate-5-(4-(ethynyl)phenyl))ethynyl]benzene* (**2**)

A mixture of THF (80 mL) and diisopropylamine (60 mL) was taken in a 250 mL round bottom flask, and nitrogen was bubbled through the solution for 15 min. To the solution were added 1,3,5-triiodobenzene (0.501 g, 1.099 mmol), compound **1** (1.4 g, 4.398 mmol), tetrakis(triphenylphosphine)palladium (0.063 g, 0.055 mmol) and cuprous iodide (0.010 g, 0.0525 mmol). The mixture was stirred at room temperature for 3h. The reaction mixture was filtered, and residual solid washed with 10 mL THF to obtain the crude product. The crude product was dispersed in THF, stirred for 15 min, and then filtered to obtain the pure product as pale yellow solid (1.039 g, 92%).

Step-3: *1,3,5-Tris[(1,3-carboxylic acid-5-(4-(ethynyl)phenyl))ethynyl]benzene* (**LH_6**)

To the compound **2** (1.008 g, 0.981 mmol) taken in a round bottom flask was added 40 mL THF. KOH (2.006 g, 35.821 mmol) was dissolved in 40 mL water, the solution was slowly added to the THF solution of the ester, and the resulting mixture was refluxed for 15 h. The reaction mixture was then cooled down to room temperature, THF was removed in vacuuo, and the remaining solution was acidified by addition of c. HCl. The product was collected by centrifugation, washed with deionized water, and dried under vacuuo to obtain the pure product (0.814 g, 88 %).

B. MOF Synthesis and Activation

NU-100 was synthesized following the literature procedure.[29] 1,3,5-Tris[(1,3-carboxylic acid-5-(4-(ethynyl)phenyl)) ethynyl]benzene (LH_6) (0.300 g, 0.32 mmol) and $Cu(NO_3)_2{\cdot}2.5H_2O$ (0.600 g, 2.579 mmol) were dissolved in 36 mL DMF in a glass vial. Subsequently, 0.2 mL HBF_4 was added to the solution, and the color of the solution turned teal. The solution was divided into thirty 4 mL vials (1.2 mL solution in each vial), and the vials were heated to 75 °C for 20 h. Teal colored octahedral crystals were formed at the bottom of the vial, which were collected together in a 60 mL jar, immersed in DMF for one day, and the supernatant liquid was replaced with fresh DMF (20 mL×4) in this time. Subsequently, the MOF was immersed in ethanol for another day, and the liquid was replaced with fresh ethanol four times (20 mL×4). The compound was then activated by flowing liquid CO_2 at 2 mL min^{-1} flowrate for 1 h at room temperature, subsequently by supercritical CO_2 at 2 mL min^{-1} flowrate for 2 h at 55 °C, and finally by supercritical CO_2 at 1 mL min^{-1} flowrate for 6 h at 55 °C to result a purple solid (0.123 g, 34.4 % based on LH_6).

S2.2.2 Synthesis and Activation of UMCM-9

UMCM-9 was synthesized following the reported procedure.[30] In five 60 mL glass jars with teflon-lined lids were added naphthalene-2,6-dicarboxylic acid (H_2NDC, 0.0285 mg, 0.131 mmol), 1,1′-biphenyl-4,4′-dicarboxylic acid (H_2BPDC, 0.0354 mg, 0.146 mmol), 6.7 mL of DEF and 13.3 mL of N-methylpyrrolidone, and the solids were dissolved in the solvent mixtures by sonication. Subsequently, $Zn(NO_3)_2{\cdot}6H_2O$ (0.235 g, 0.790 mmol) was added to the solution and the mixture was sonicated until a transparent solutions were obtained. The reaction mixtures were heated to 85 °C for 4 days. Cubic crystals of UMCM-9 were formed at the inner surface of the vials along with minor amount of flocculent precipitate. After cooling to room temperature the mother liquor was decanted, the precipitate was removed by multiple DMF washes, and the crystals were collected together in a different vial. The MOF crystals were immersed in DMF for 3 days (washed several times with fresh DMF), then in dichloromethane for 18 hours (washed with DCM, 20 mL×8), and finally, in dry *n*-hexane for 12 hours (washed with dry *n*-hexane 20 mL×4). Subsequently, the solvent was decanted, the vial was placed in a vacuum chamber, and exposed to vacuum very slowly at room temperature. Finally, the material was activated under high vacuum (below 10^{-4} torr) for 26 hours to yield clear pale yellow crystals (average yield 0.0523 g, 38%, based on H_2NDC).

S2.2.3 Synthesis and Activation of SNU-70

SNU-70 was synthesized following the reported procedure with slight modification.[31] (E)-4-(2-Carboxyvinyl)benzoic acid (0.075 g, 0.390 mmol) and $Zn(NO_3)_2{\cdot}6H_2O$ (0.150 g, 0.504 mmol) were dissolved in 25 mL DEF in a 60 mL glass jars with a teflon-lined lid. Six such reaction mixtures were heated to 105 °C for 12.5 h. At the end of this period, the glass jars were removed from the oven, and allowed to cool down to room temperature. Colorless cubic crystals (along with some fluffy precipitate) were formed at the bottom and the wall of the jars. The fluffy precipitate was removed from the MOF crystals by multiple wash with DMF. The remaining crystals were then collected together in a 60 mL glass vial, soaked in DMF and kept emerged for 2 d. The supernatant liquid was replaced with fresh DMF six times (20 mL each) in this time. The material was activated by SC CO_2 flow by the same procedure as NU-100 (0.567 g, 51%).

S2.3. NU-100 Ligand Characterization via NMR Spectroscopy

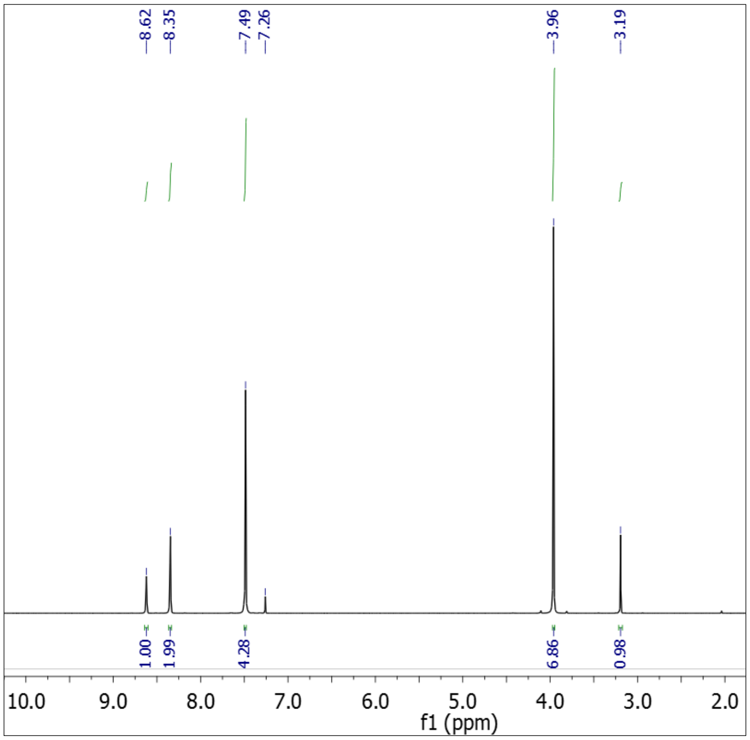

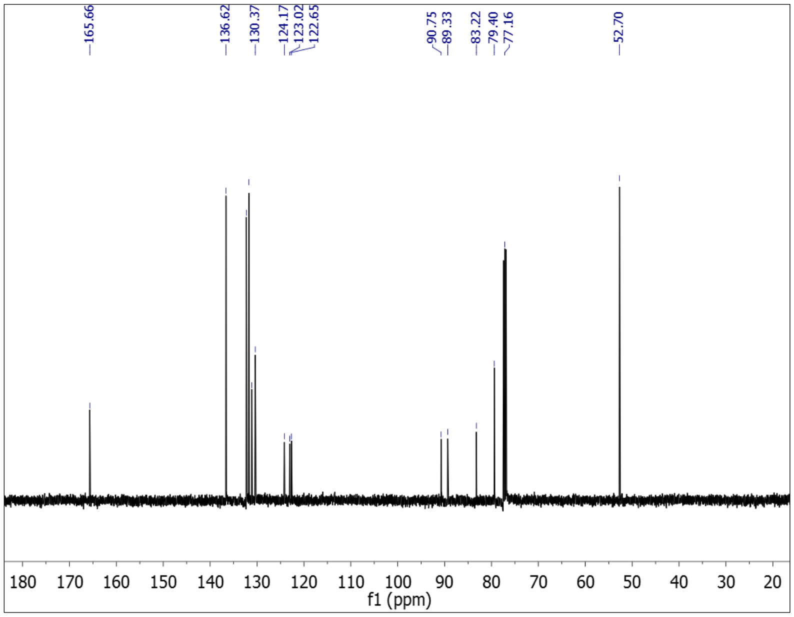

Figure S3. ^{1}H (500 MHz) and ^{13}C (125 MHz) NMR spectra of dimethyl 5-((4-ethynylphenyl)ethynyl) isophthalate (**1**) in $CDCl_3$.

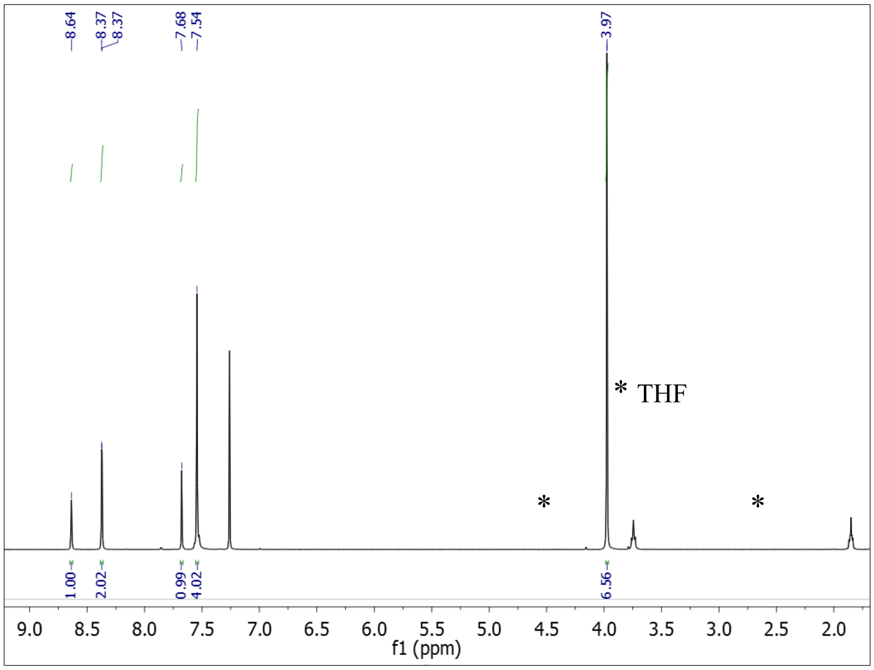

Figure S4. ^{1}H (500 MHz) NMR spectrum of 1,3,5-Tris[(1,3-dimethylcarboxylate-5-(4-(ethynyl)phenyl)) ethynyl]benzene (**2**) in $CDCl_3$.

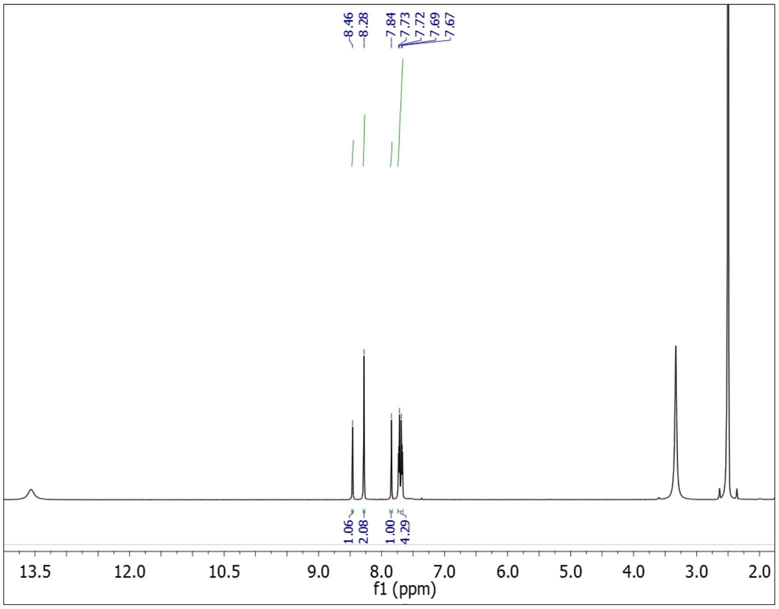

Figure S5. ^{1}H (500 MHz) NMR spectrum of 1,3,5-Tris[(1,3-carboxylic acid-5-(4-(ethynyl)phenyl)) ethynyl]benzene (**LH$_6$**) in DMSO-*d6*.

S 2.4. Measured Nitrogen Adsorption Isotherms Used in BET Surface Estimations

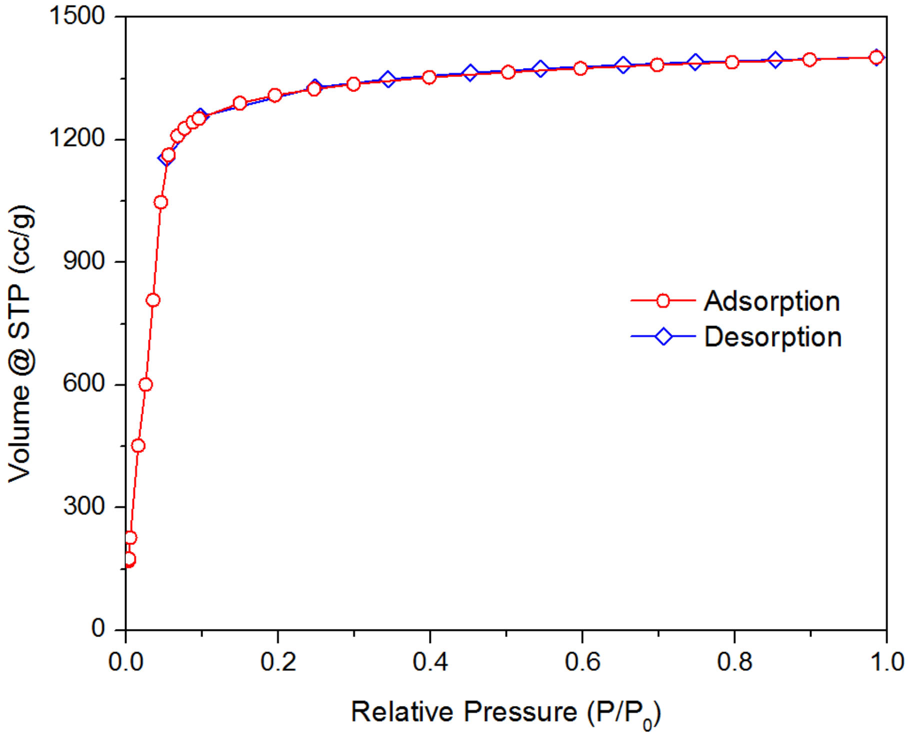

Figure S6. N_2 Isotherm of UMCM-9.

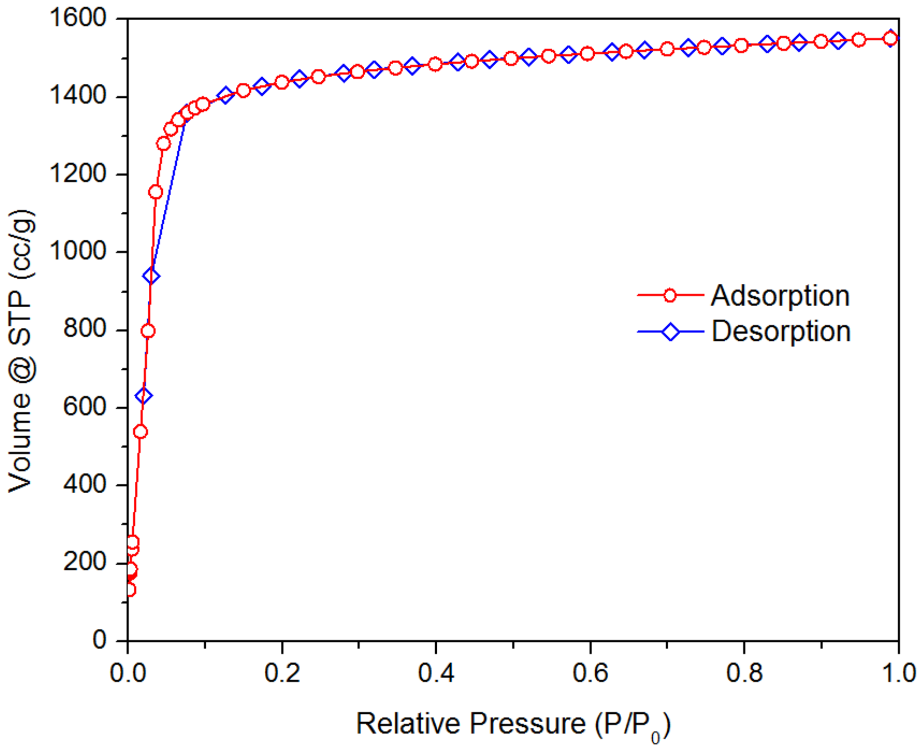

Figure S7. N_2 Isotherm of SNU-70.

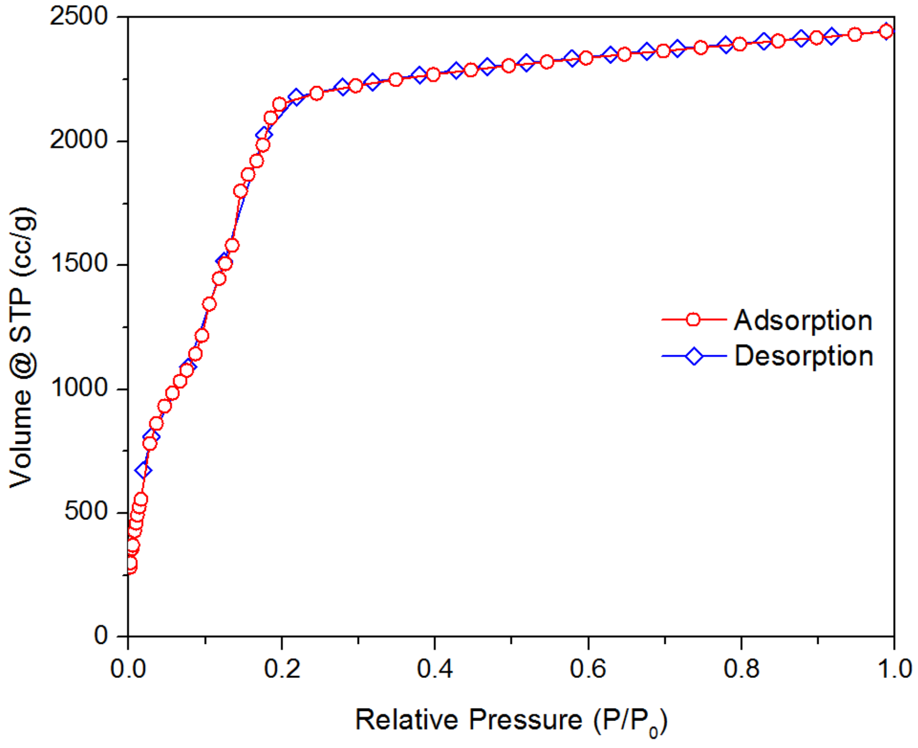

Figure S8. N_2 Isotherm of NU-100.

S.2.4. Powder X-Ray Diffraction (PXRD) Patterns

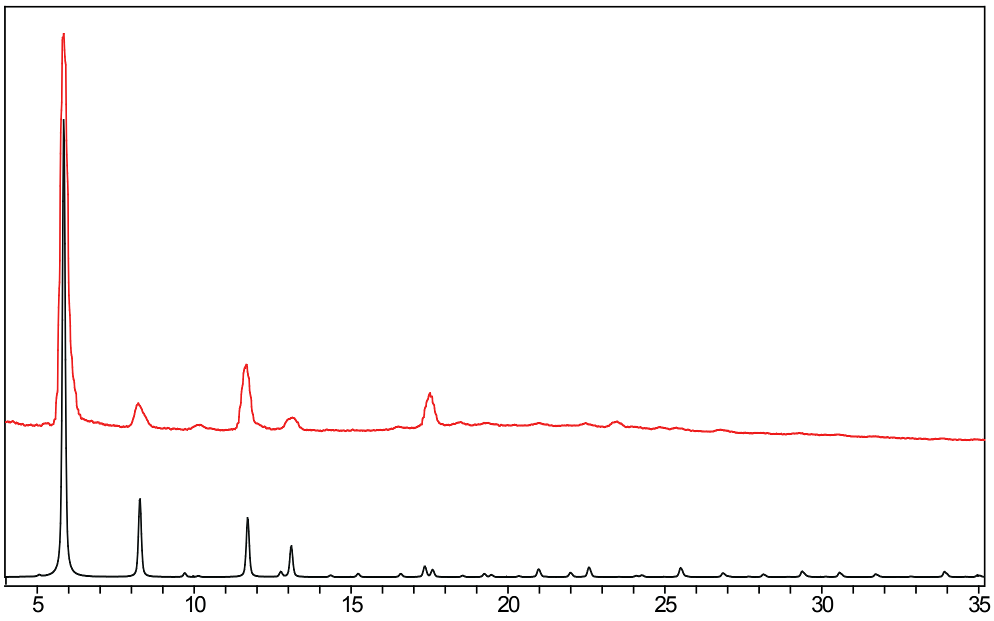

Figure S9. The PXRD pattern of SNU-70. Red is the experimental pattern and black is the simulated pattern derived from the single crystal X-ray structure.

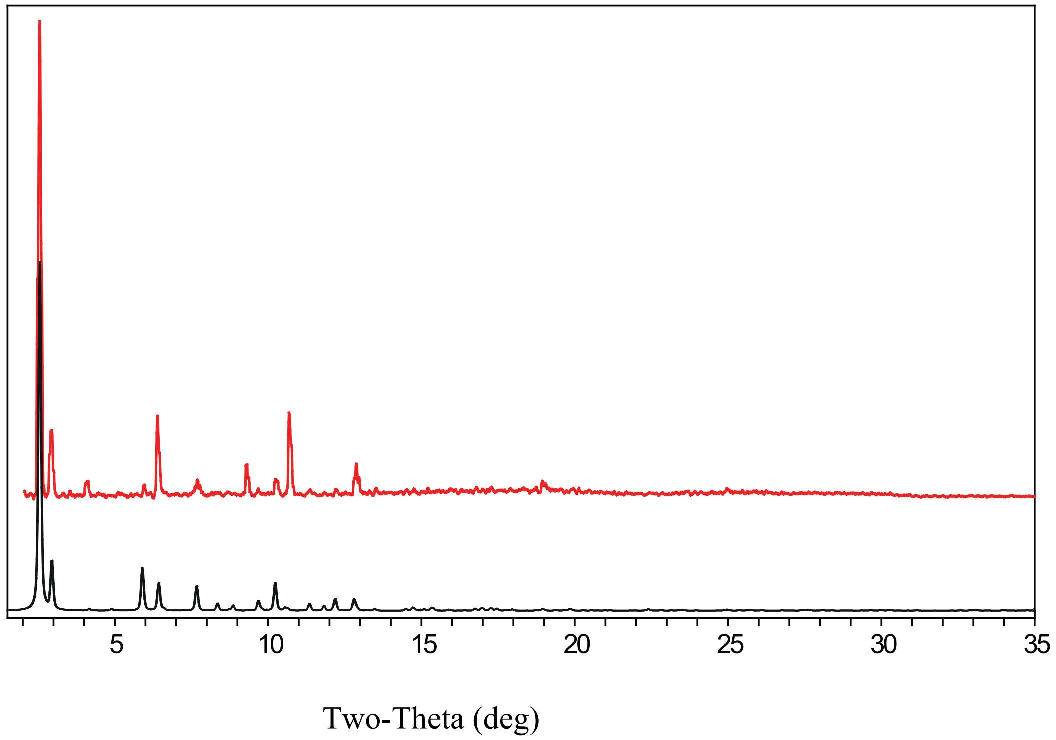

Figure S10. The PXRD pattern of NU-100. Red is the experimental pattern and black is the simulated pattern derived from the single crystal X-ray structure.

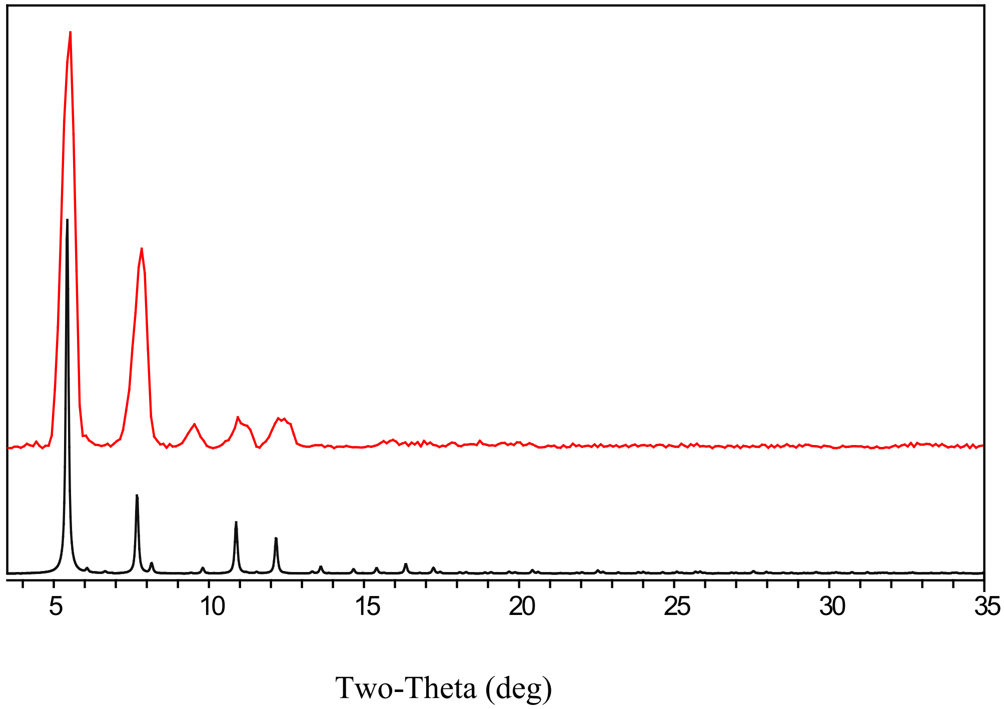

Figure S11. The PXRD pattern of UMCM-9. Red is the experimental pattern and black is the simulated pattern derived from the single crystal X-ray structure.

S3. Comparison Between Measured and GCMC Calculated H_2 Adsorption Isotherms

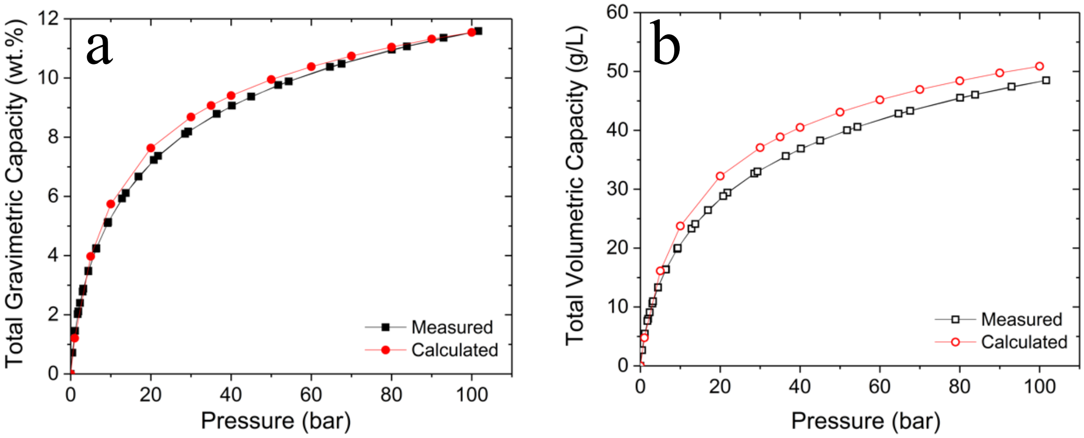

Figure S12. Comparison between measured and GCMC calculated total (a) gravimetric and (b) volumetric H_2 adsorption isotherms of UMCM-9 at 77 K.

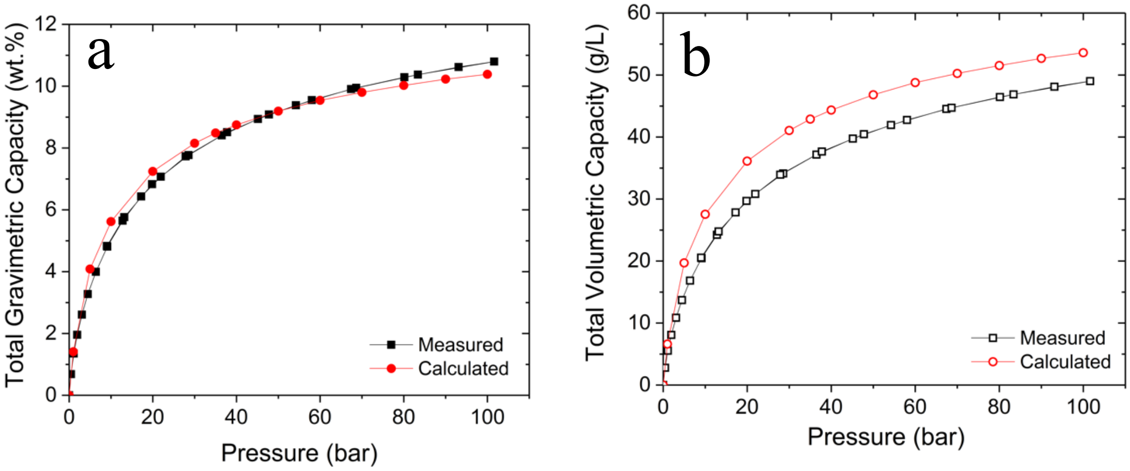

Figure S13. Comparison between measured and GCMC calculated total (a) gravimetric and (b) volumetric H_2 adsorption isotherms of SNU-70 at 77 K.

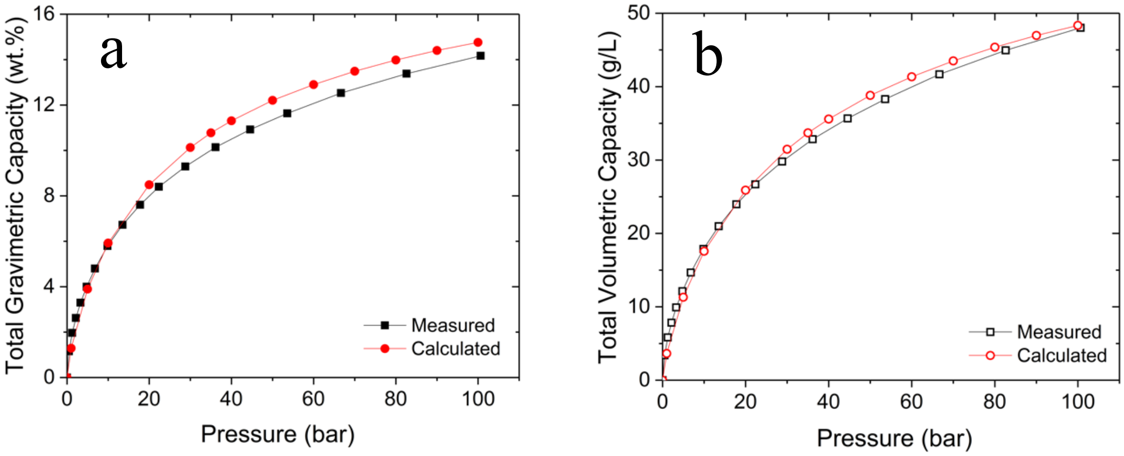

Figure S14. Comparison between measured and GCMC calculated total (a) gravimetric and (b) volumetric H_2 adsorption isotherms of NU-100 at 77 K.

References

1 J. Goldsmith, A. G. Wong-Foy, M. J. Cafarella and D. J. Siegel, *Chem. Mater.*, 2013, **25**, 3373–3382.

2 Y. G. Chung, J. Camp, M. Haranczyk, B. J. Sikora, W. Bury, V. Krungleviciute, T. Yildirim, O. K. Farha, D. S. Sholl and R. Q. Snurr, *Chem. Mater.*, 2014, **26**, 6185–6192.

3 P. Z. Moghadam, A. Li, S. B. Wiggin, A. Tao, A. G. P. Maloney, A. Wood, S. C. Ward and D. Fairen-jimenez, 1–16.

4 C. R. Groom, I. J. Bruno, M. P. Lightfoot and S. C. Ward, *Acta Cryst.*, 2016, **72**, 171–179.

5 C. E. Wilmer, M. Leaf, C. Y. Lee, O. K. Farha, B. G. Hauser, J. T. Hupp and R. Q. Snurr, *Nat. Chem.*, 2011, **4**, 83–89.

6 R. L. Martin, C. M. Simon, B. Smit and M. Haranczyk, *J. Am. Chem. Soc.*, 2014, **136**, 5006–5022.

7 Y. Bao, R. L. Martin, C. M. Simon, M. Haranczyk, B. Smit and M. W. Deem, *J. Phys. Chem. C*, 2015, **119**, 186–195.

8 D. A. Gomez-Gualdron, O. V. Gutov, V. Krungleviciute, B. Borah, J. E. Mondloch, J. T. Hupp, T. Yildirim, O. K. Farha and R. Q. Snurr, *Chem. Mater.*, 2014, **26**, 5632–5639.

9 M. Z. Aghaji, M. Fernandez, P. G. Boyd, T. D. Daff and T. K. Woo, *Eur. J. Inorg. Chem.*, , DOI:10.1002/ejic.201600365.

10 Y. Bao, R. L. Martin, M. Haranczyk and M. W. Deem, *Phys. Chem. Chem. Phys.*, 2015, **17**, 11962–11973.

11 P. Z. Moghadam, A. Li, S. B. Wiggin, A. Tao, A. G. P. Maloney, P. A. Wood, S. C. Ward and D. Fairen-Jimenez, *Chem. Mater.*, 2017, **29**, 2618–2625.

12 T. F. Willems, C. H. Rycroft, M. Kazi, J. C. Meza and M. Haranczyk, *Microporous Mesoporous Mater.*, 2012, **149**, 134–141.

13 M. Fischer, F. Hoffmann and M. Fröba, *ChemPhysChem*, 2009, **10**, 2647–2657.

14 R. P. Feynman and A. R. Hibbs, *Quantum mechanics and path integrals*, McGraw-Hill, New York, 1965.

15 A. Ahmed, Y. Liu, J. Purewal, L. D. Tran, M. Veenstra, A. Wong-Foy, A. Matzger and D. Siegel, *Energy Environ. Sci.*, 2017, **10**, 2459–2471.

16 A. K. Rappe, C. J. Casewit, K. S. Colwell, W. A. Goddard and W. M. Skiff, *J. Am. Chem. Soc.*, 1992, **114**, 10024–10035.

17 S. L. Mayo, B. D. Olafson and W. A. Goddard Iii, *J . Phys. Chem*, 1990, **94**, 8897–8909.

18 D. Dubbeldam, S. Calero, D. E. Ellis and R. Q. Snurr, *Mol. Simul.*, 2016, **42**, 81–101.

19 M. P. Allen and D. J. Tildesley, *Computer simulation of liquids*, Oxford University Press, New York, NY, 1989.

20 R. J. Sadus, *Molecular simulation of fluids: theory, algorithms, and object-orientation.*, Elsevier, Amsterdam, 1999.

21 H. A. Lorentz, *Ann. Phys.*, 1881, **248**, 127–136.

22 S. I. Sandler, *Chemical, biochemical, and engineering thermodynamics*, Wiley, 4th edn., 2006.

23 N. S. Bobbitt, J. Chen and R. Q. Snurr, *J. Phys. Chem. C*, 2016, **120**, 27328–27341.

24 D. Dubbeldam, S. Calero, D. E. Ellis and R. Q. Snurr, *Mol. Simul.*, 2016, **42**, 81–101.

25 A. Ahmed, Y. Liu, J. Purewal, L. D. Tran, M. Veenstra, A. Wong-Foy, A. Matzger and D. Siegel, *Energy Environ. Sci.*, 2017, **10**, 2459–2471.

26 R. L. Martin, L.-C. Lin, K. Jariwala, B. Smit and M. Haranczyk, *J. Phys. Chem. C*, 2013, **117**, 12159–12167.

27 Y. J. Colón, D. A. Gómez-Gualdrón and R. Q. Snurr, *Cryst. Growth Des.*, 2017, **17**, 5801–5810.

28 M. Z. Aghaji, M. Fernandez, P. G. Boyd, T. D. Daff and T. K. Woo, 2016, 4505–4511.

29 O. K. Farha, A. Özgür Yazaydın, I. Eryazici, C. D. Malliakas, B. G. Hauser, M. G. Kanatzidis, S. T. Nguyen, R. Q. Snurr and J. T. Hupp, *Nat. Chem.*, 2010, **2**, 944–948.

30 K. Koh, J. D. Van Oosterhout, S. Roy, A. G. Wong-Foy and A. J. Matzger, *Chem. Sci.*, 2012, **3**, 2429.

31 T. K. Prasad and M. P. Suh, *Chem. - A Eur. J.*, 2012, **18**, 8673–8680.

Appendix B
Additional information: System-Level Modeling

Justin Purewal[a], Mike Veenstra[a], David Tamburello[b], Alauddin Ahmed[c], Donald J. Siegel[c],
Adam Matzger[d], Antek G. Wong-Foy[d], Saona Seth[d]
[a]Ford Motor Company, Research & Advanced Engineering, 1201 Village Rd, Dearborn, MI 48121, USA
[b]Savannah River National Laboratory, Aiken, SC 29808, USA
[c]Mechanical Engineering Department, University of Michigan, Ann Arbor, MI 48109, USA
[d]Department of Chemistry, University of Michigan, Ann Arbor, MI 48109, USA

1. MOF Material-Level Hydrogen Adsorption and Surface Area Properties

		Excess H_2 Adsorption at 77 K		Total H_2 Storage Capacity at 77 K				Usable Capacity (100 bar – 5 bar) at 77 K		Surface Area
Material	Crystal Density	Max excess	Excess at 35 bar	Gravimetric (35 bar)	Gravimetric (100 bar)	Volumetric (35 bar)	Volumetric (100 bar)	Gravimetric	Volumetric	N2 BET SSA
	g/cm^3	g/kg	g/kg	wt.%	wt.%	g/L	g/L	wt.%	g/L	m^2/g
MOF-5 (BASF)	0.605	60.08	59.8	6.82	8.21	43.9	53.7	32.1	4.74	3555
MOF-177	0.43	73.9	72.9	8.45	10.4	39.68	50.3	32.94	6.52	4608
NH2-MOF-177	0.44	73.1	72.3	8.33	10.33	40.01	50.7	32.56	6.37	4556
IRMOF-20	0.51	63.87	63.29	7.49	9.33	41.3	52.46	33.4	5.73	4145
DUT-23 (Co)	0.413	77.54	76.9	8.8	10.74	39.8	49.7	30.53	6.31	5117
DUT-23 (Cu)	0.413	77.7	76.78	8.78	10.83	39.78	50.14	32.4	6.7	5181
SNU-70	0.405	69.16	67.98	8.32	10.76	36.6	48.82	34.25	7.29	4944
UMCM-4	0.57	55.05	54.87	6.55	8.15	39.68	50.25	29.69	4.65	2942
UMCM-1	0.39	66.55	66.39	8.25	10.63	35.08	46.39	30.96	6.82	4048
MIL-101-NH2	0.44	44.59	44.43	6.04	8.4	28.27	40.37	26.1	5.27	2740
HKUST-1	0.879	42.33	42.06	4.79	5.41	44.26	50.26	17.93	1.86	1736
Ni-MOF-74	1.195	35	34.98	3.72	3.93	46.2	48.92	13.83	1.08	1392
UiO-66	0.4[d]	30.96	30.96	4.98	7.78	21.63	34.84	23.82	5.18	1668
UiO-67	0.5[d]	44.64	44.63	5.71	7.41	30.29	40.04	23.46	4.21	2397
MSC-30	0.48[c]	59.57	59.45	7.22	9.14	37.37	48.3	25.78	4.66	3229
ZIF-8	0.95	32.33	32.24	3.49	3.73	34.37	36.85	11.82	1.17	1631
mBr-MOF-5[b]	0.61	54.29	54.08	6.31	7.78	41.1	51.4	30.59	4.47	2931
mMe-MOF-5[a]	0.61	54.51	54.51	6.29	7.19	41.59	47.93	25.69	3.72	3248
MSC-20	0.43[c]	50.01	49.88	6.63	8.95	30.55	42.26	23.33	4.73	2400
Norit ROW	0.40[c]	29.69	29.33	5.03	7.88	21.19	34.21	22.74	5.09	740
NU-100	0.291	80.468	77.966	10.01	14.14	32.38	47.91	35.51	10.05	5800
UMCM-9	0.37	71.18	69.9	8.67	11.54	35.11	48.26	34.06	7.84	5039

[a] Mixed linker MOF-5 with 33% mMe-BDC and 67% BDC

[b] Mixed linker MOF-5 with 50% Br-BDC and 50% BDC

[c] Since activated carbons (MSC-20, MSC-30, Norit ROW) are not crystalline, the apparent density, $\rho_a = \rho_{sk}/(\rho_{sk} v_{pore} + 1)$, was used in place of it. The apparent density was calculated from the measured pore volumes and skeletal densities of the materials. For a defect-free crystal, it should equal the crystal density.

[d] The crystal densities of UiO-66 and UiO-67 could not be determined unambiguously. Estimates were used instead.

2. MOF Synthesis Conditions

Name	Metal Source	Linker	Conditions	Reference
UMCM-4	$Zn(NO_3)_2 \bullet 6H_2O$ (6.6 equiv)	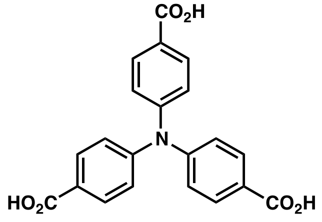 (1.0 equiv) 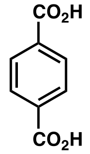 (1.5 equiv)	DEF 85 °C, 72 h	*J. Am. Chem. Soc.* **2010**, *132*, 15005–15010
mBr-MOF-5 (30% Br-BDC incorp.)	$Zn(NO_3)_2 \bullet 6H_2O$ (3.5 equiv)	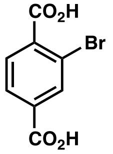 (0.5 equiv) 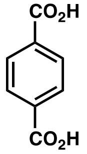 (0.5 equiv)	DEF 100 °C, 16 h	(New MOF)
mMe-MOF-5 (27% Me-BDC incorp.)	$Zn(NO_3)_2 \bullet 6H_2O$ (3.5 equiv)	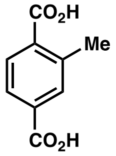 (0.33 equiv) 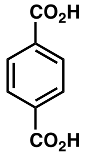 (0.67 equiv)	DEF 100 °C, 22 h	(New MOF)
MOF-177-NH2	$Zn(NO_3)_2 \bullet 6H_2O$ (2.6 equiv)	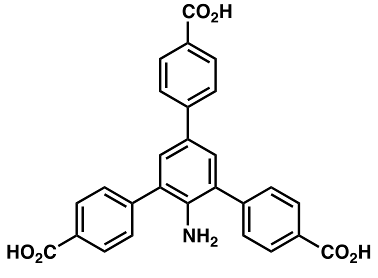 (1.0 equiv)	DMF 100 °C, 72 h	*Angew. Chem., Int. Ed.* **2015**, *54*, 3983–3987

Name	Metal Source	Linker	Conditions	Reference
DUT-23(Co)	$Co(NO_3)_2{\bullet}6H_2O$ (4.0 equiv)	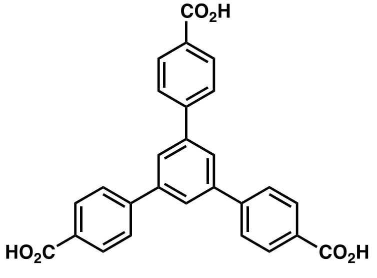 (1.0 equiv) 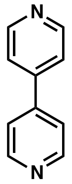 (1.08 equiv)	DEF 100 °C, 48 h	*Chem. Eur. J.* **2011**, *17*, 13007–13016
DUT-23(Cu)	$Cu(NO_3)_2{\bullet}2.5H_2O$ (4.0 equiv)	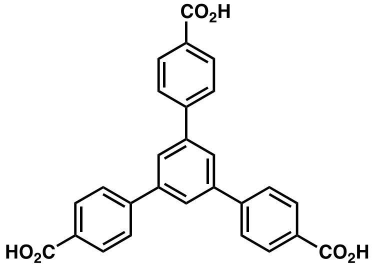 (1.0 equiv) 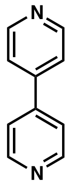 (1.08 equiv)	cat. trifluoroacetic acid DMF/EtOH 1:1 80 °C, 20 h	*Chem. Eur. J.* **2011**, *17*, 13007–13016
SNU-70	$Zn(NO_3)_2{\bullet}6H_2O$	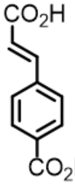	DEF, 105°C, 13.5 h	Suh et. al. *Chem. Eur. J.* **2012**, 18, 8673
UMCM-9	$Zn(NO_3)_2{\bullet}6H_2O$	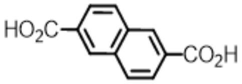 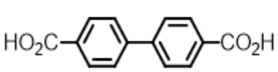	DEF/NMP, 85°C, 8 d	Matzger et. al., *Chem.Sci.* **2012**, *3,* 2429.
IRMOF-20	$Zn(NO_3)_2{\bullet}4H_2O$	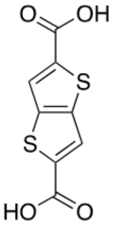	DEF, 100°C	Rowsell, J. L. C.; Yaghi, O.M. *J. Am. Chem. Soc.* **2006**, *128*, 1304.

3. Excess Hydrogen Adsorption at 77 K

MOF-5 (BASF)

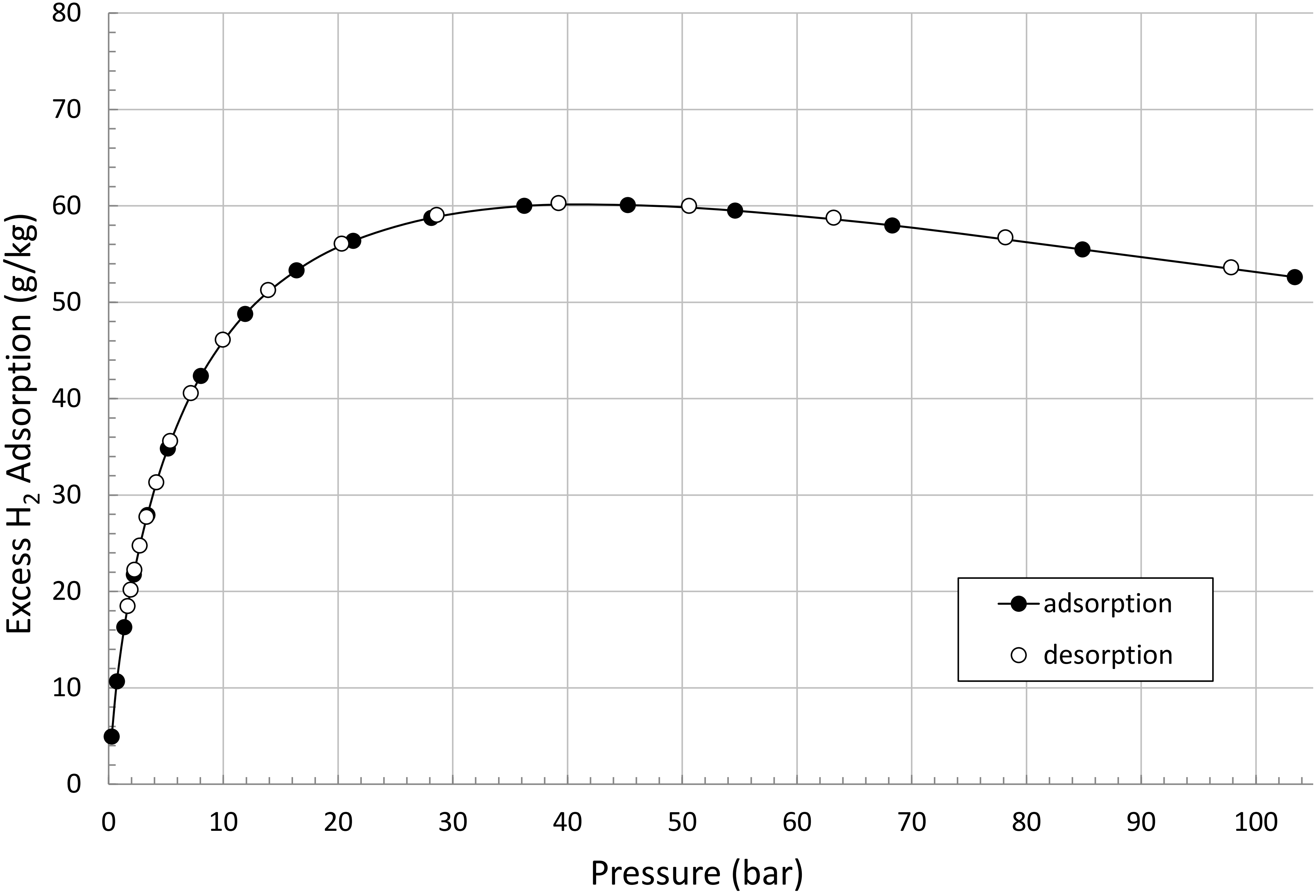
80
70
60
50
40
30
20
10
0
Excess H_2 Adsorption (g/kg)
0
10
20
30
40
50
60
70
80
90
100
Pressure (bar)
adsorption
desorption

MOF-5 (Air-Free Synthesis)

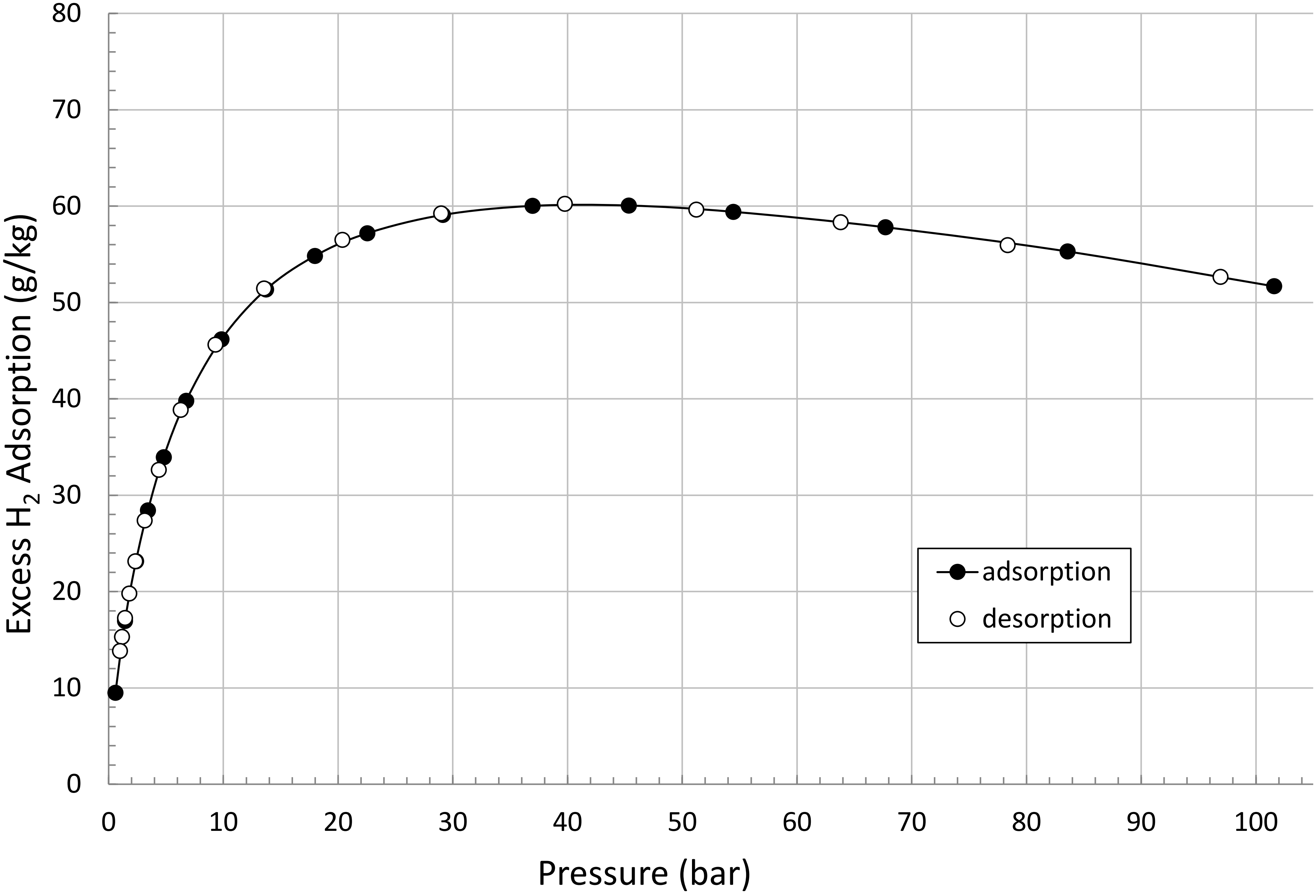

IRMOF-20

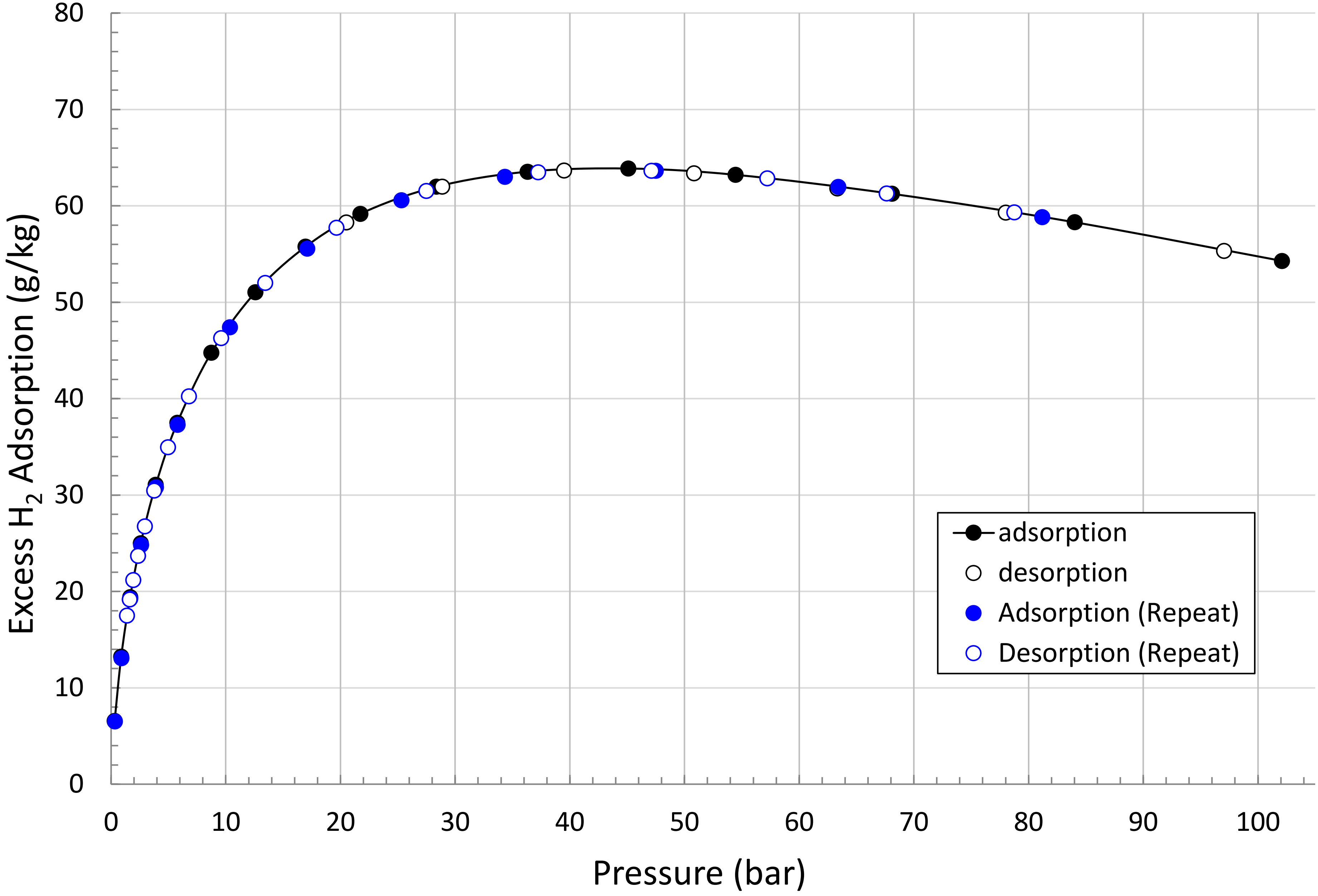
Excess H_2 Adsorption (g/kg)
0
10
20
30
40
50
60
70
80
Pressure (bar)
0
10
20
30
40
50
60
70
80
90
100
adsorption
desorption
Adsorption (Repeat)
Desorption (Repeat)

Me-MOF-5

(50% Me-BDC, 50% BDC linker)

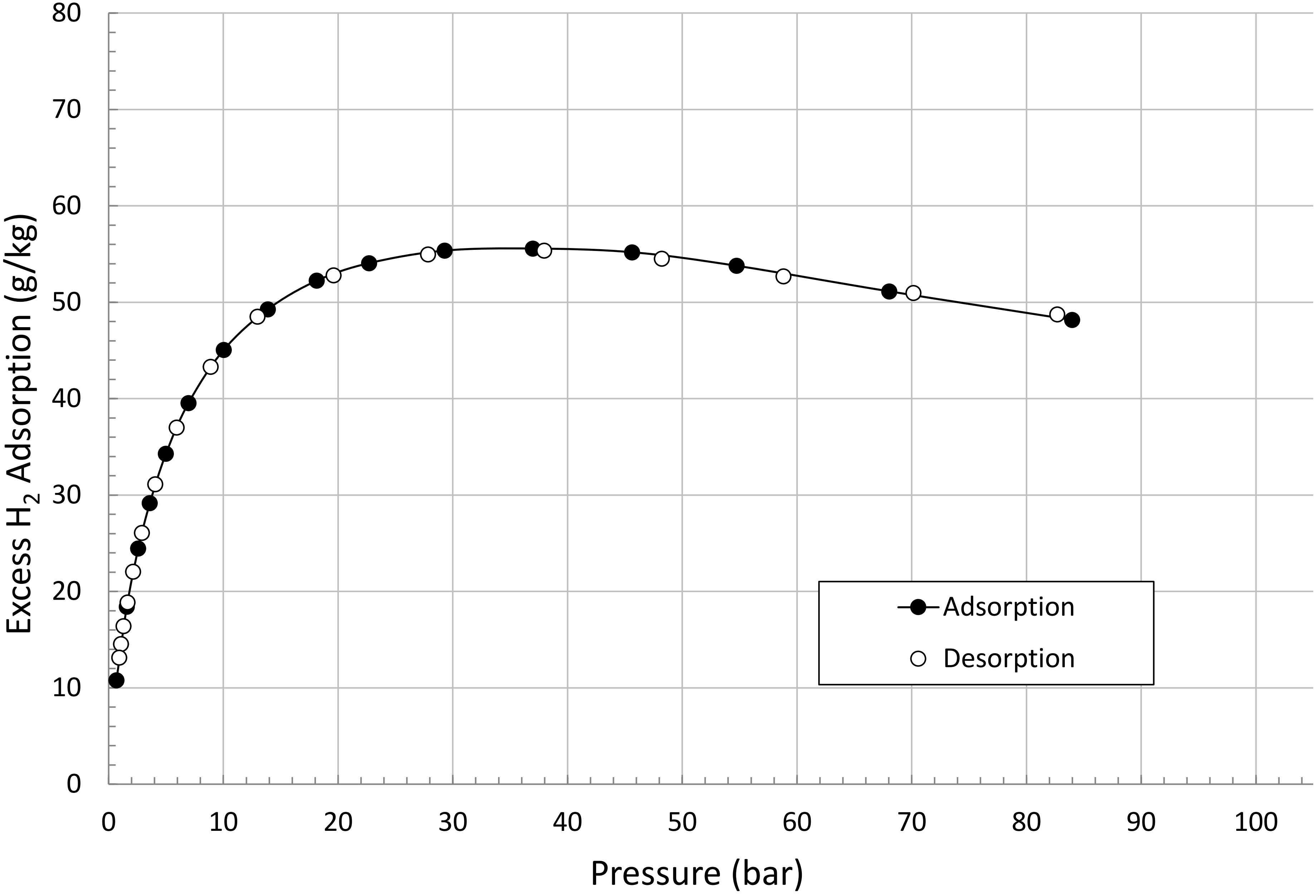

Br-MOF-5

(30% Br-BDC, 70% BDC linker)

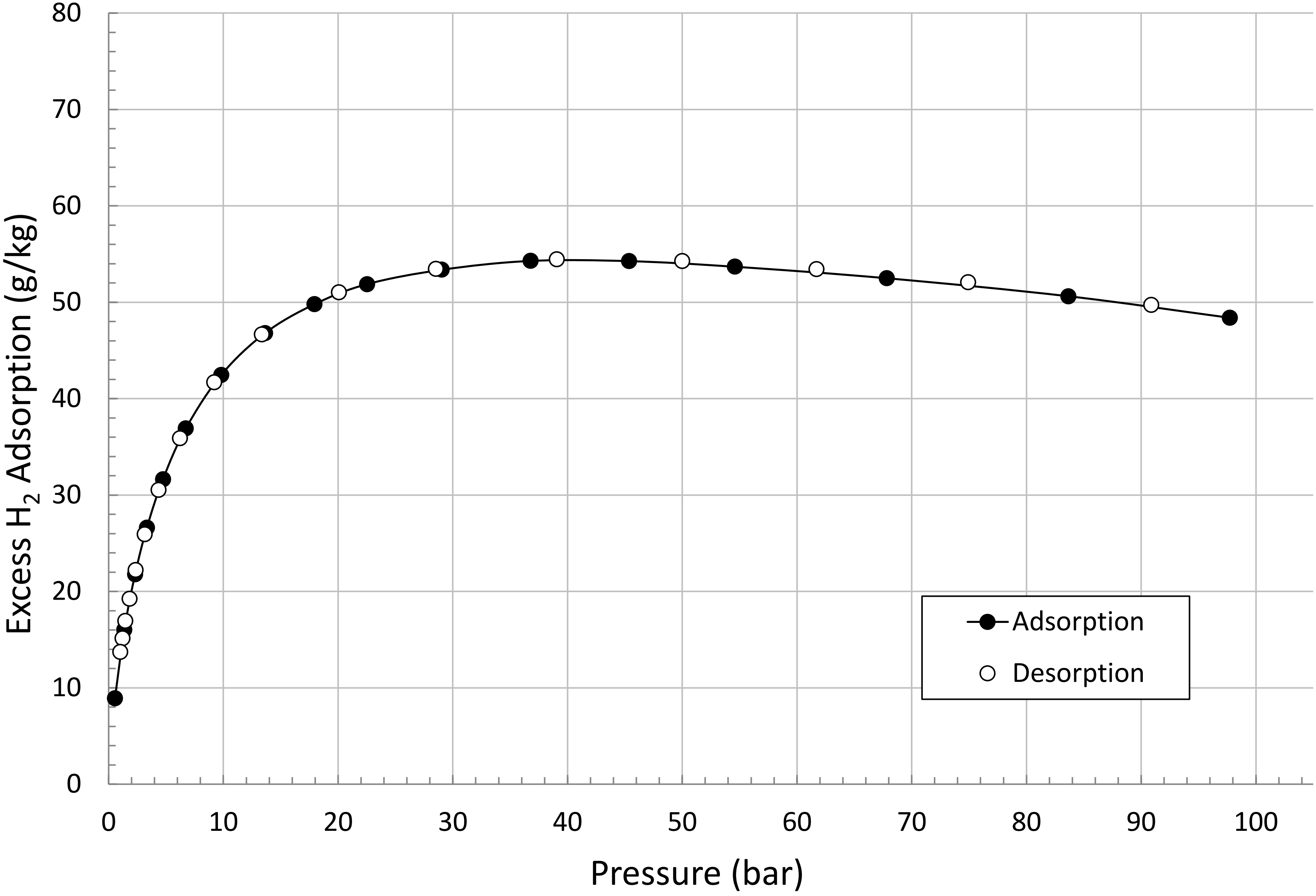

MOF-5 –PS-4Hr

(MOF-5 polystyrene Composite, 4 hr synthesis)

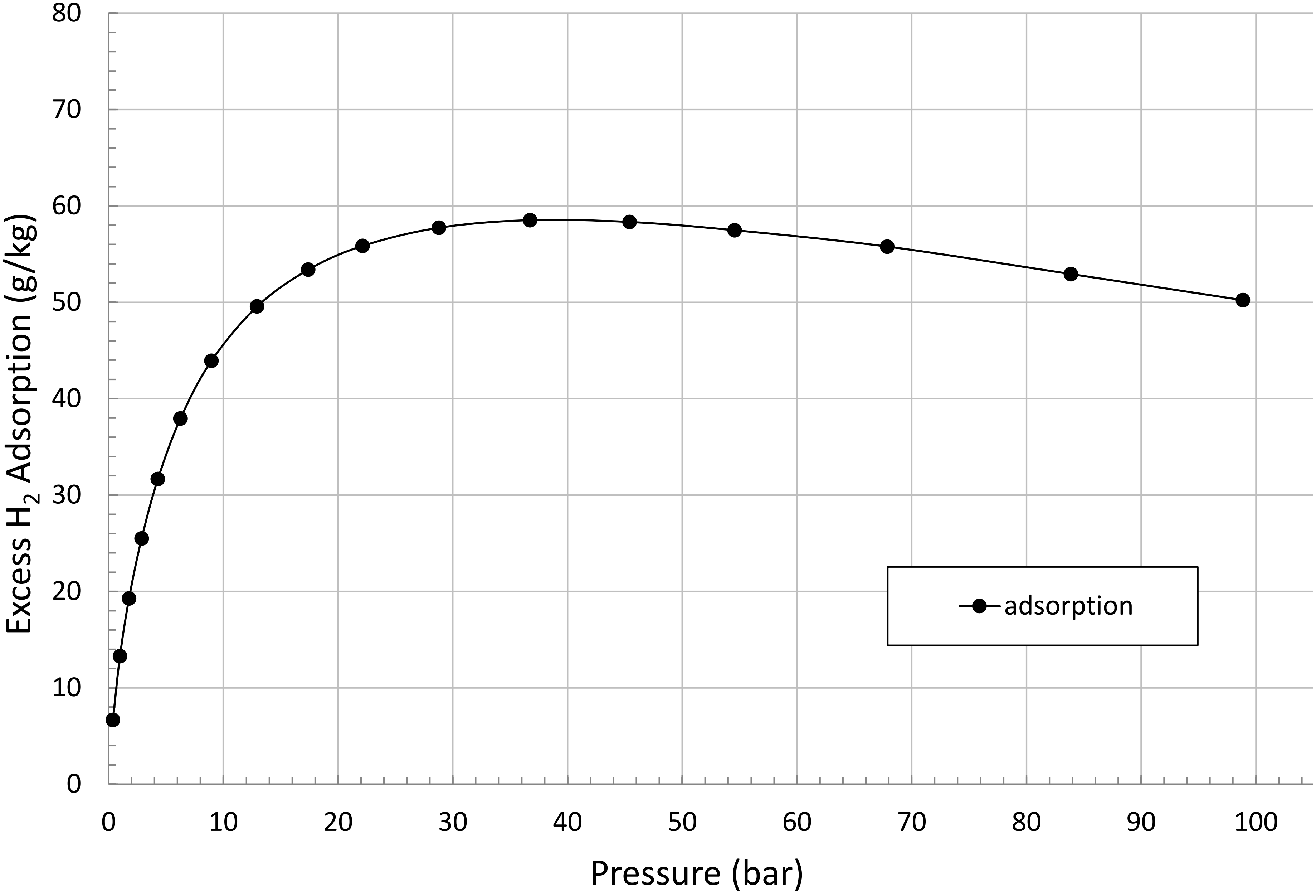

NH_2-MOF-177

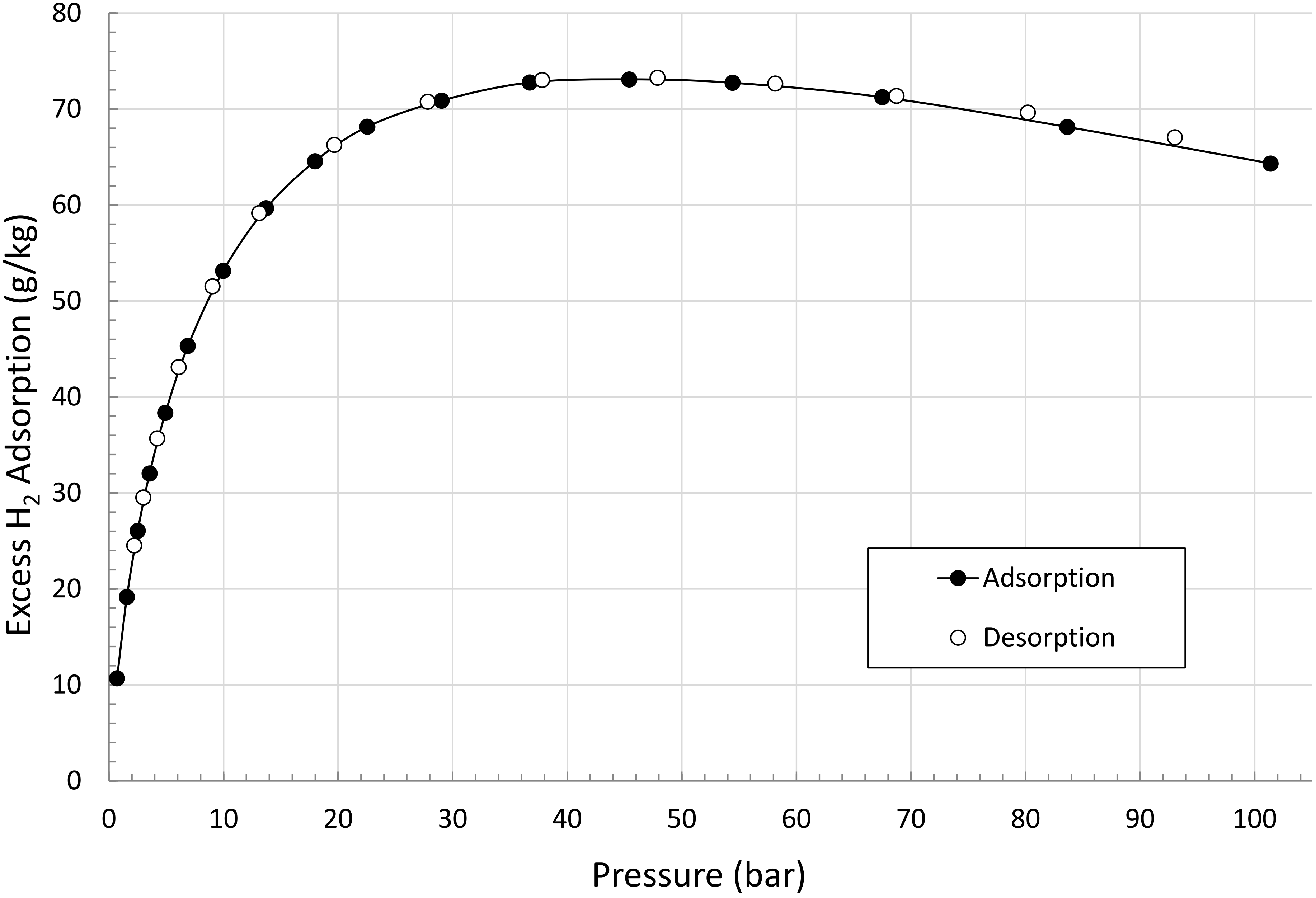

Excess H_2 Adsorption (g/kg)
0
10
20
30
40
50
60
70
80
0
10
20
30
40
50
60
70
80
90
100
Pressure (bar)
● Adsorption
○ Desorption

DUT-23 (Co)

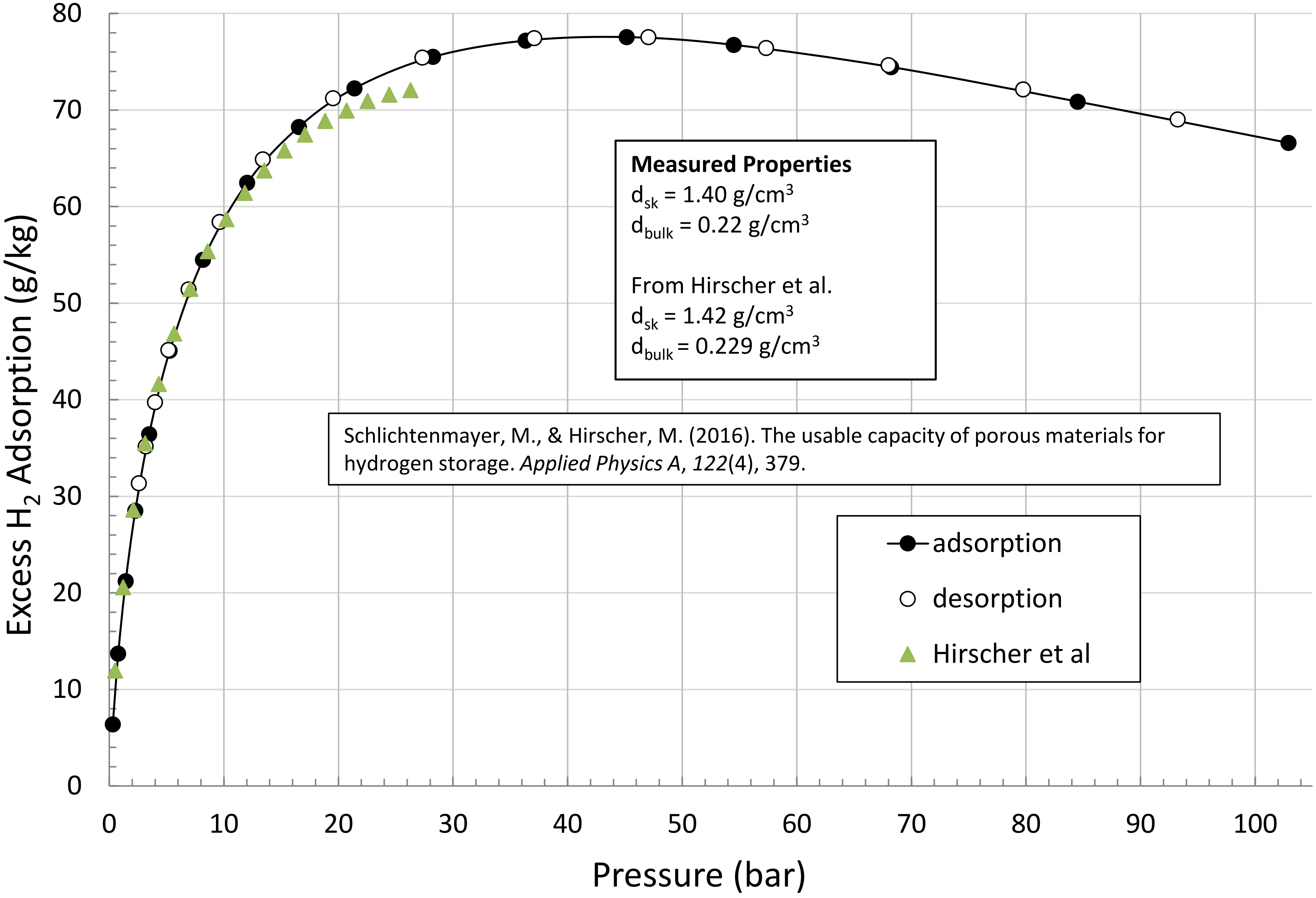

Measured Properties
d_{sk} = 1.40 g/cm^3
d_{bulk} = 0.22 g/cm^3

From Hirscher et al.
d_{sk} = 1.42 g/cm^3
d_{bulk} = 0.229 g/cm^3

Schlichtenmayer, M., & Hirscher, M. (2016). The usable capacity of porous materials for hydrogen storage. *Applied Physics A*, *122*(4), 379.

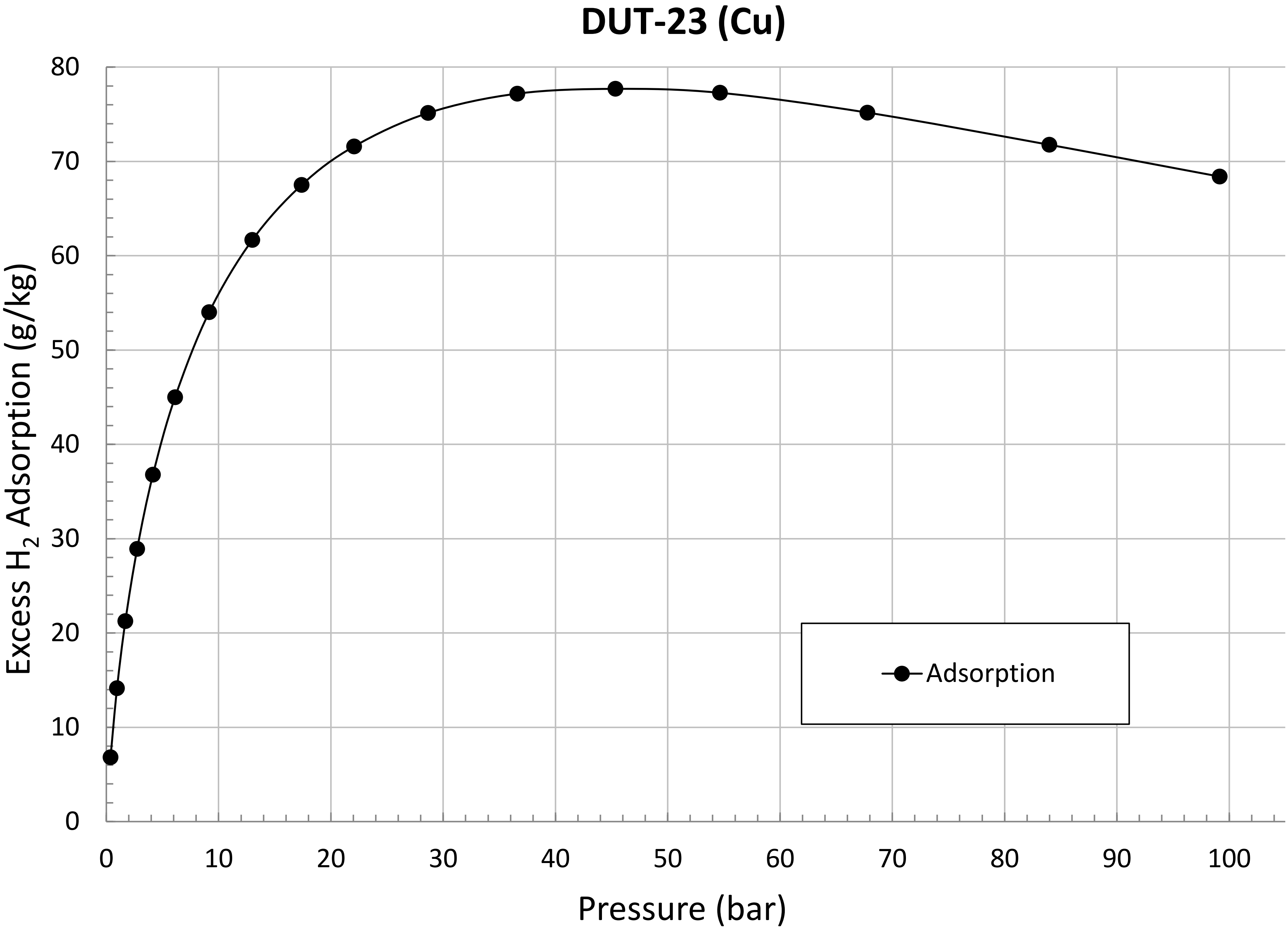
DUT-23 (Cu)
Excess H_2 Adsorption (g/kg)
0
10
20
30
40
50
60
70
80
Pressure (bar)
0
10
20
30
40
50
60
70
80
90
100
Adsorption

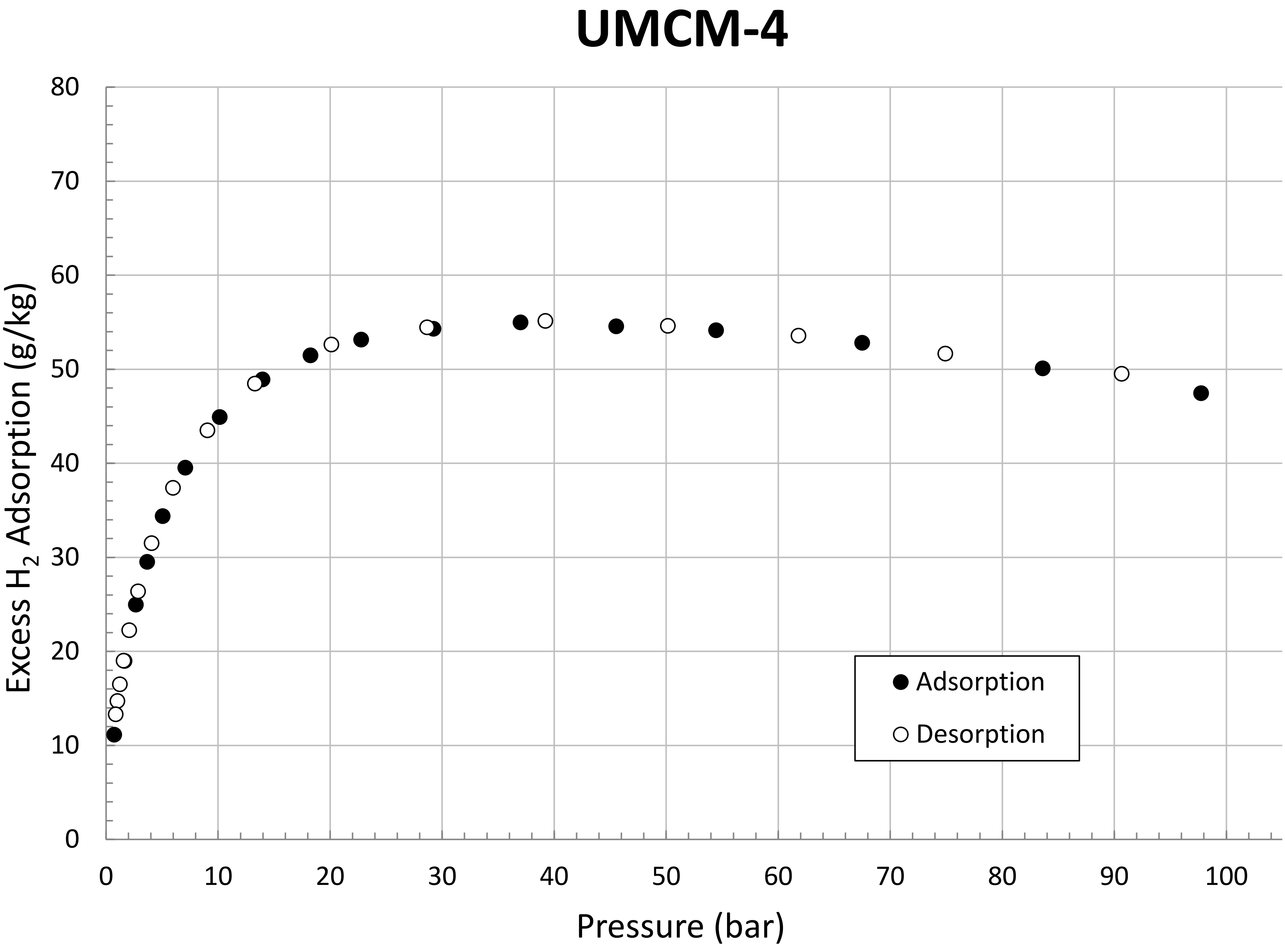
UMCM-4
Excess H_2 Adsorption (g/kg)
0
10
20
30
40
50
60
70
80
Pressure (bar)
0
10
20
30
40
50
60
70
80
90
100
● Adsorption
○ Desorption

UMCM-1

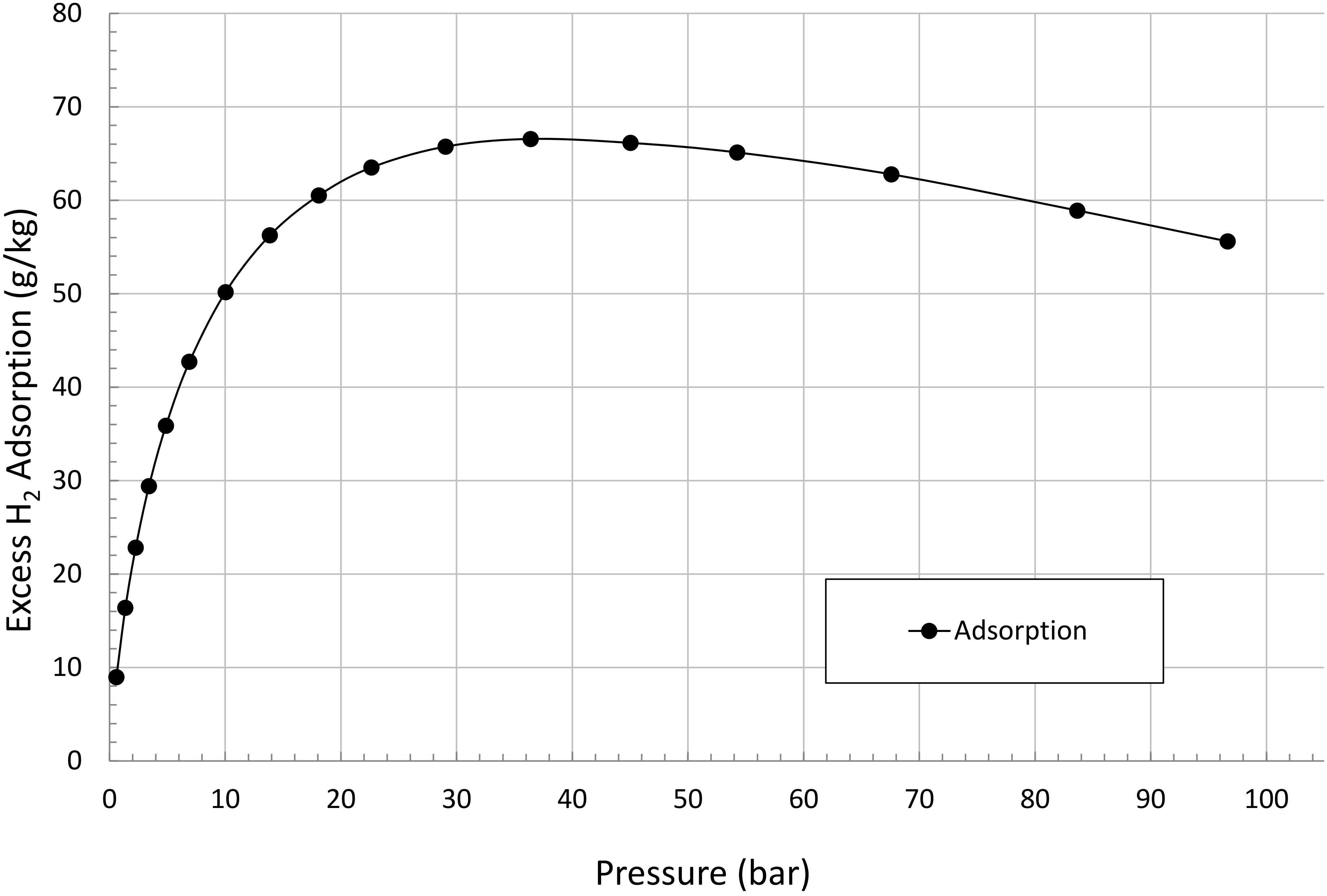
Excess H_2 Adsorption (g/kg)
0
10
20
30
40
50
60
70
80
Pressure (bar)
0
10
20
30
40
50
60
70
80
90
100
Adsorption

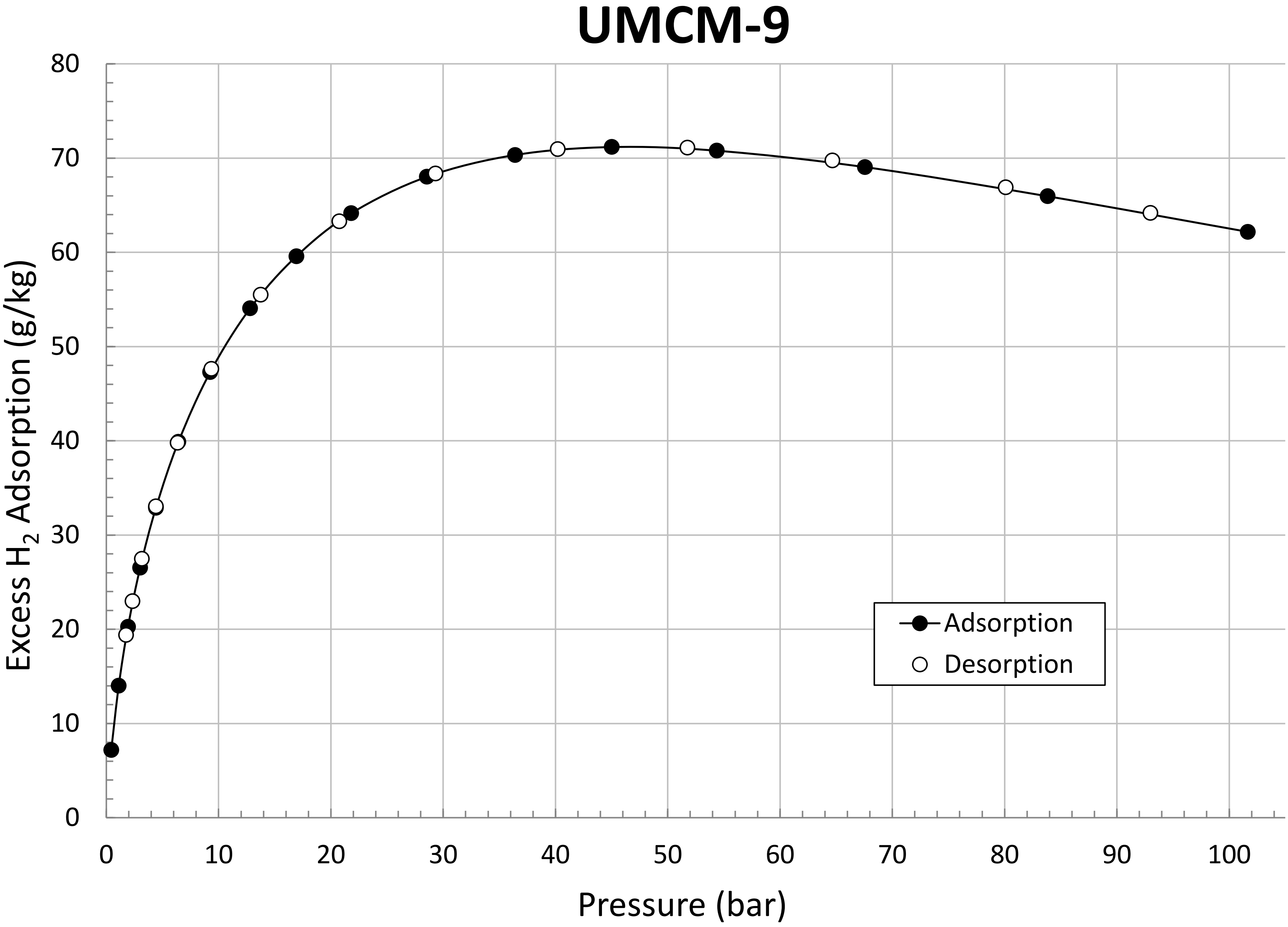
UMCM-9
Excess H_2 Adsorption (g/kg)
0
10
20
30
40
50
60
70
80
Pressure (bar)
0
10
20
30
40
50
60
70
80
90
100
Adsorption
Desorption

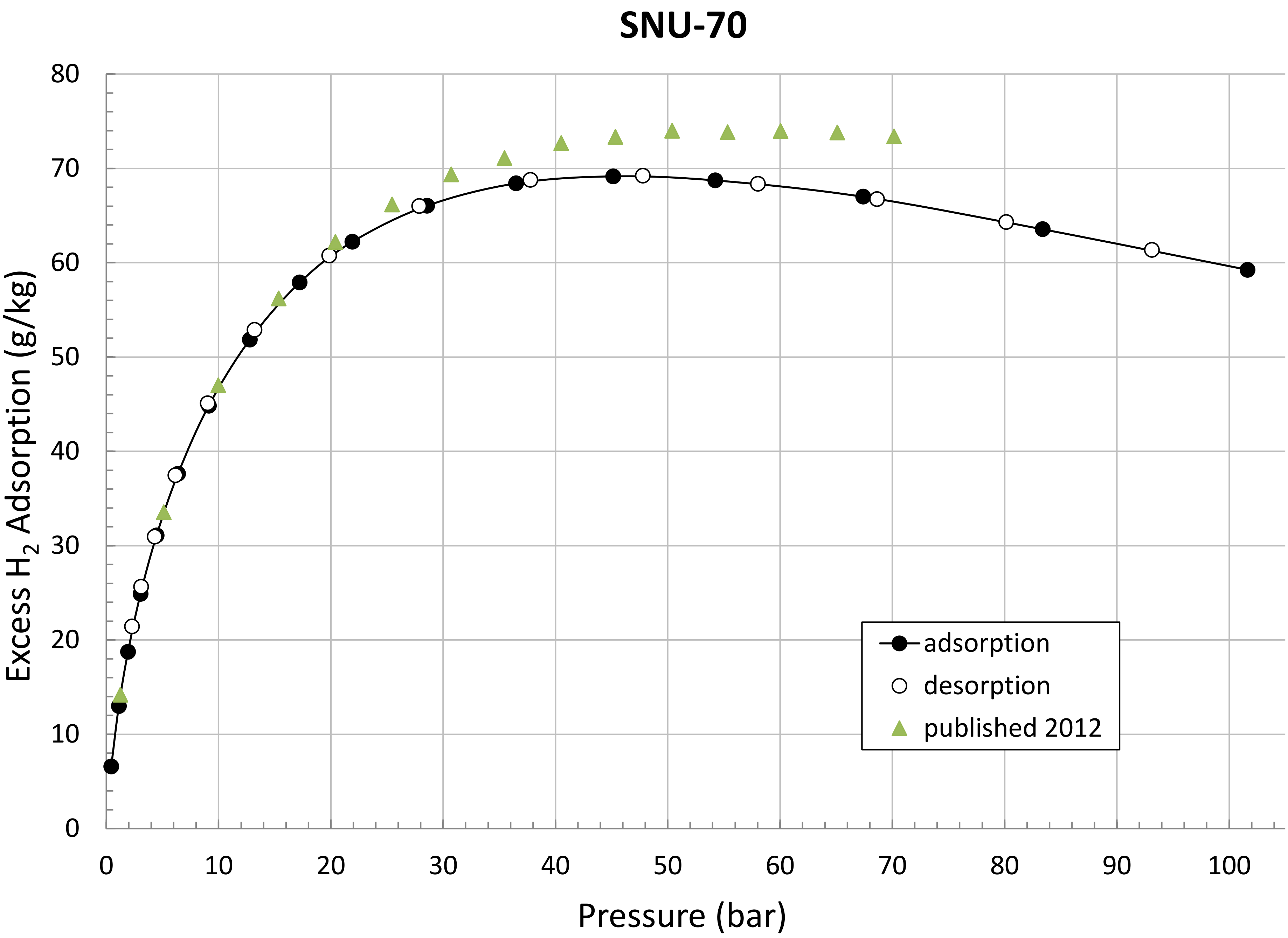
SNU-70
Excess H_2 Adsorption (g/kg)
0
10
20
30
40
50
60
70
80
0
10
20
30
40
50
60
70
80
90
100
Pressure (bar)
adsorption
desorption
published 2012

NU-100

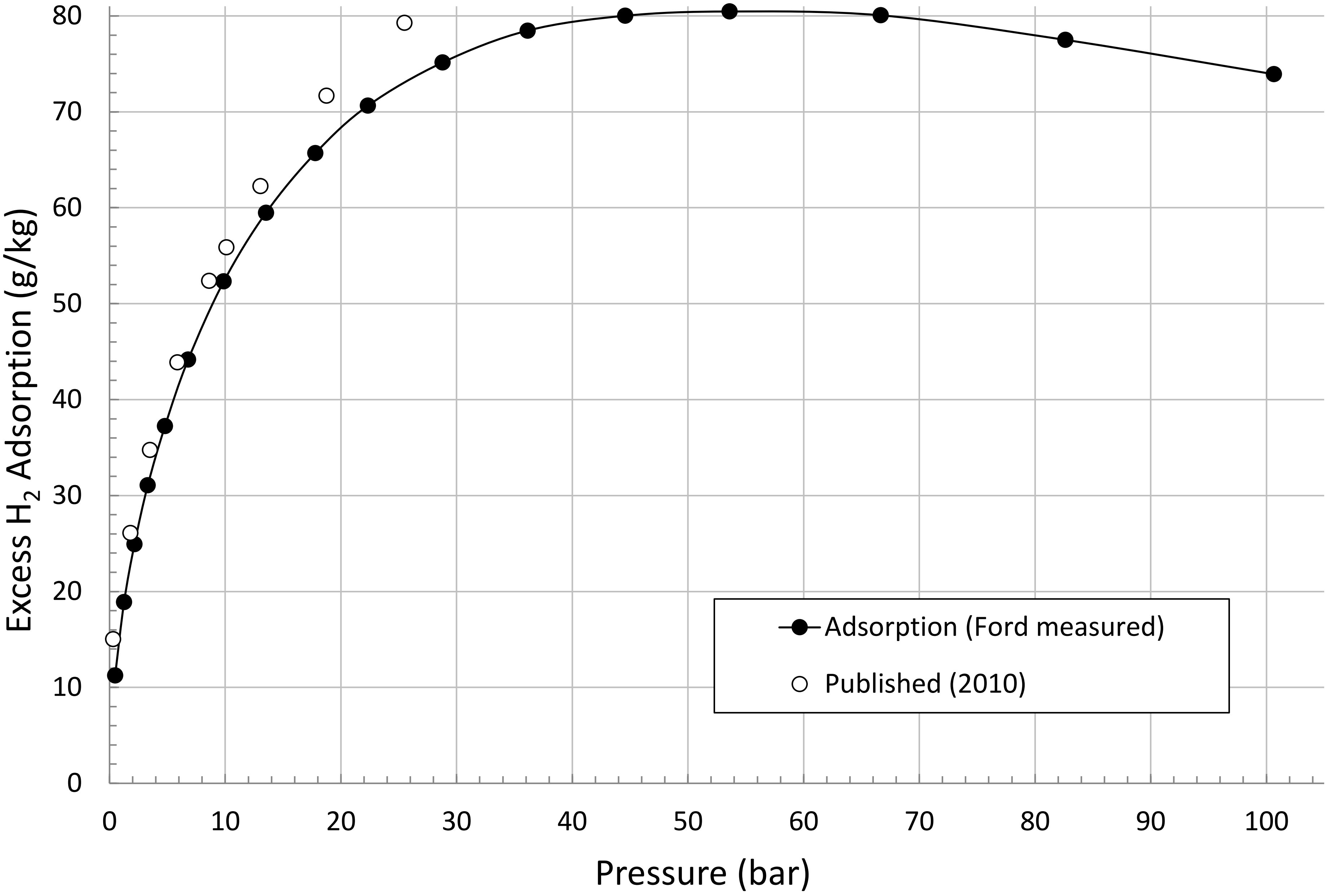
Excess H_2 Adsorption (g/kg)
0
10
20
30
40
50
60
70
80
Pressure (bar)
0
10
20
30
40
50
60
70
80
90
100
Adsorption (Ford measured)
Published (2010)

Cu-BTC

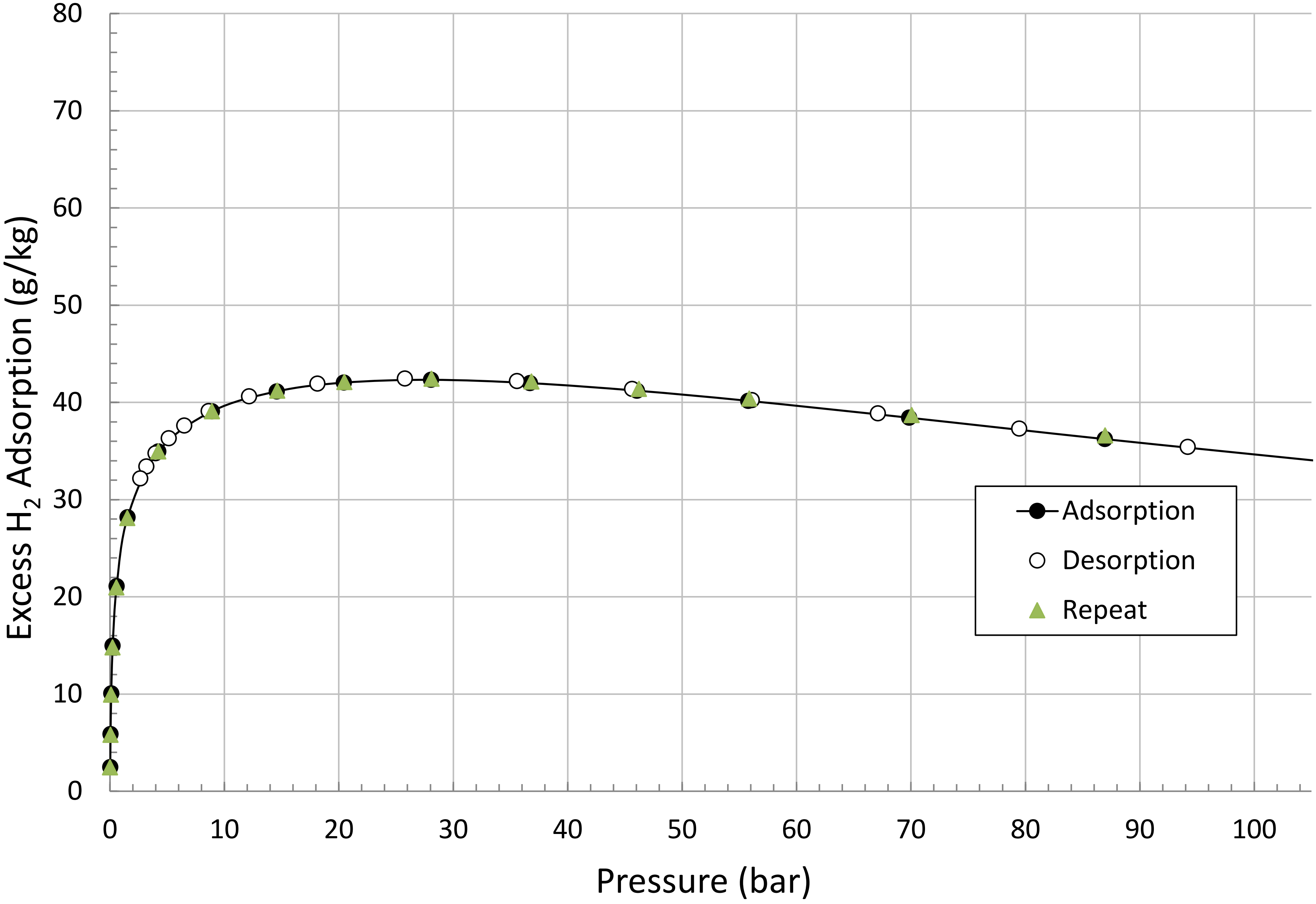
80
70
60
50
40
30
20
10
0
Excess H_2 Adsorption (g/kg)
0
10
20
30
40
50
60
70
80
90
100
Pressure (bar)
Adsorption
Desorption
Repeat

Co(bdp)

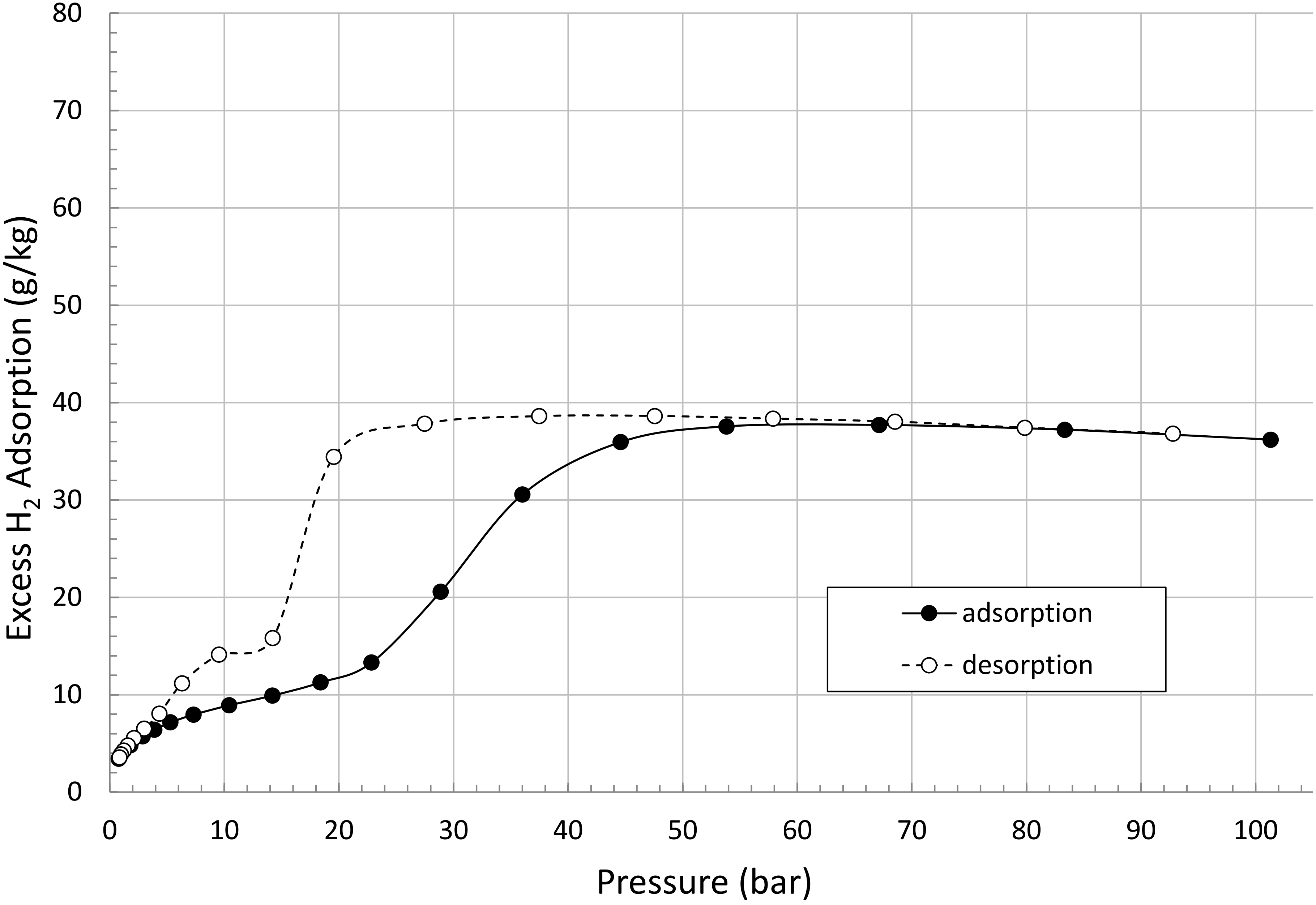
Excess H_2 Adsorption (g/kg)
0
10
20
30
40
50
60
70
80
Pressure (bar)
0
10
20
30
40
50
60
70
80
90
100
adsorption
desorption

Ni-MOF-74

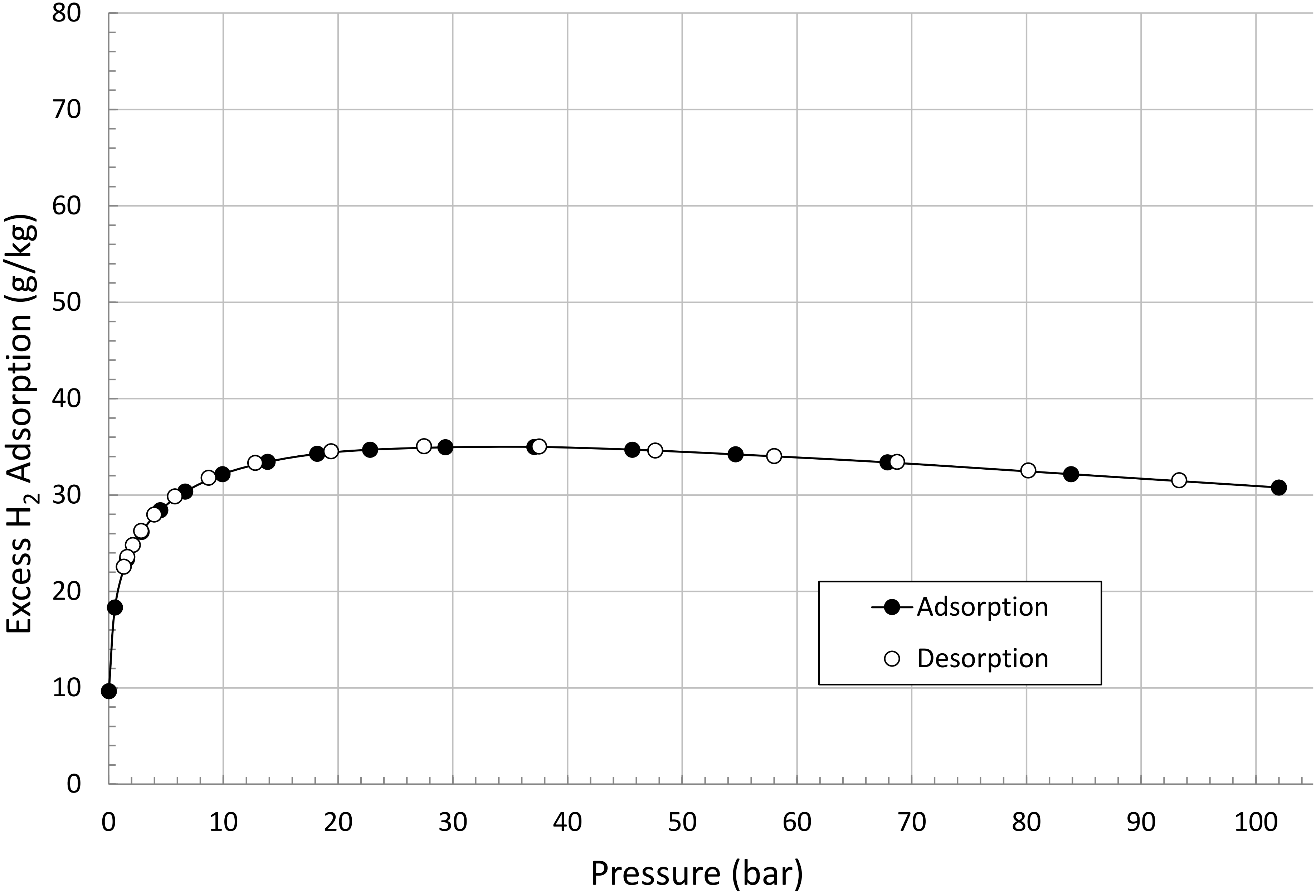
Excess H_2 Adsorption (g/kg)
0
10
20
30
40
50
60
70
80
Pressure (bar)
0
10
20
30
40
50
60
70
80
90
100
Adsorption
Desorption

MOF-177

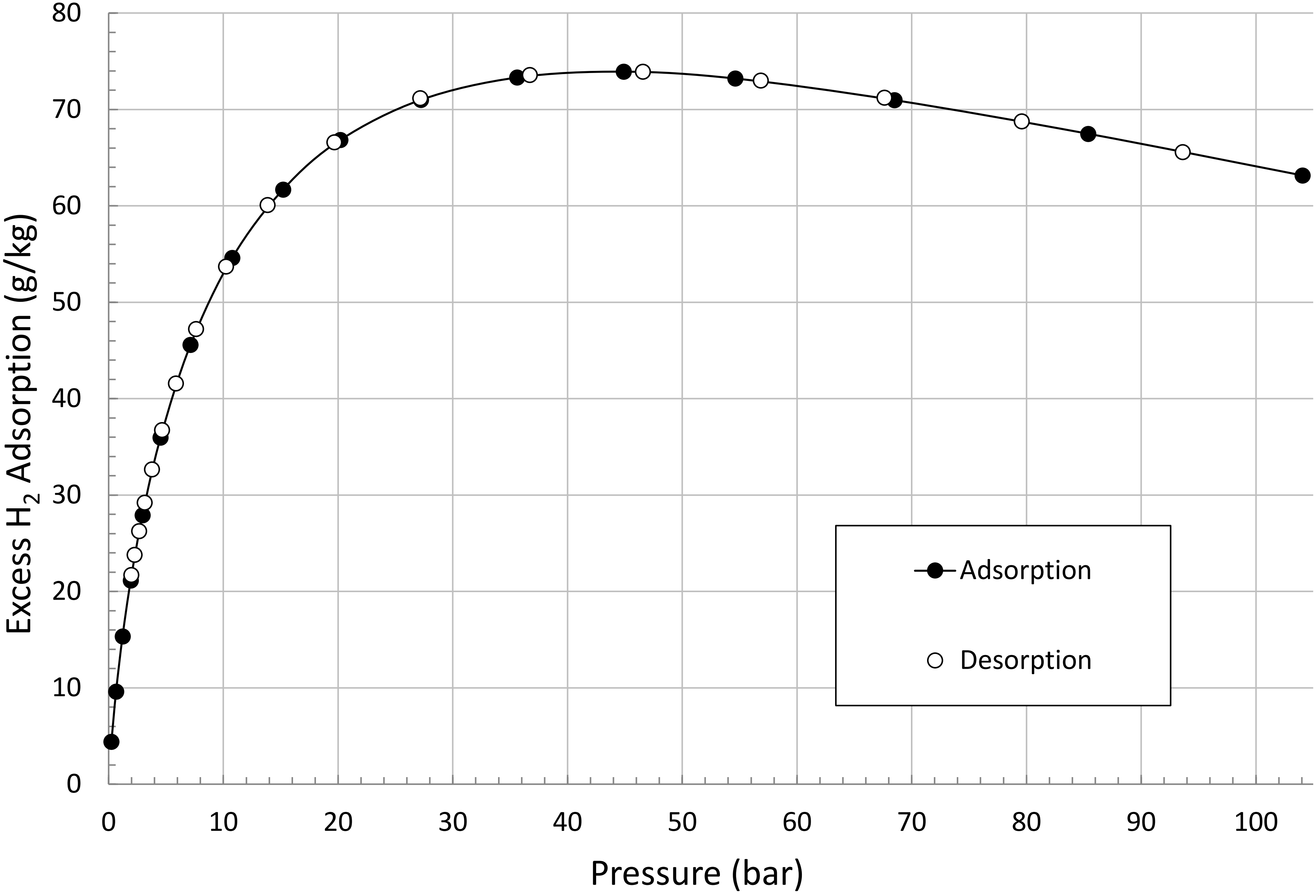
80
70
60
50
40
30
20
10
0
Excess H_2 Adsorption (g/kg)
0
10
20
30
40
50
60
70
80
90
100
Pressure (bar)
Adsorption
Desorption

NH_2-MIL-101 (Al)
(BASF A120)

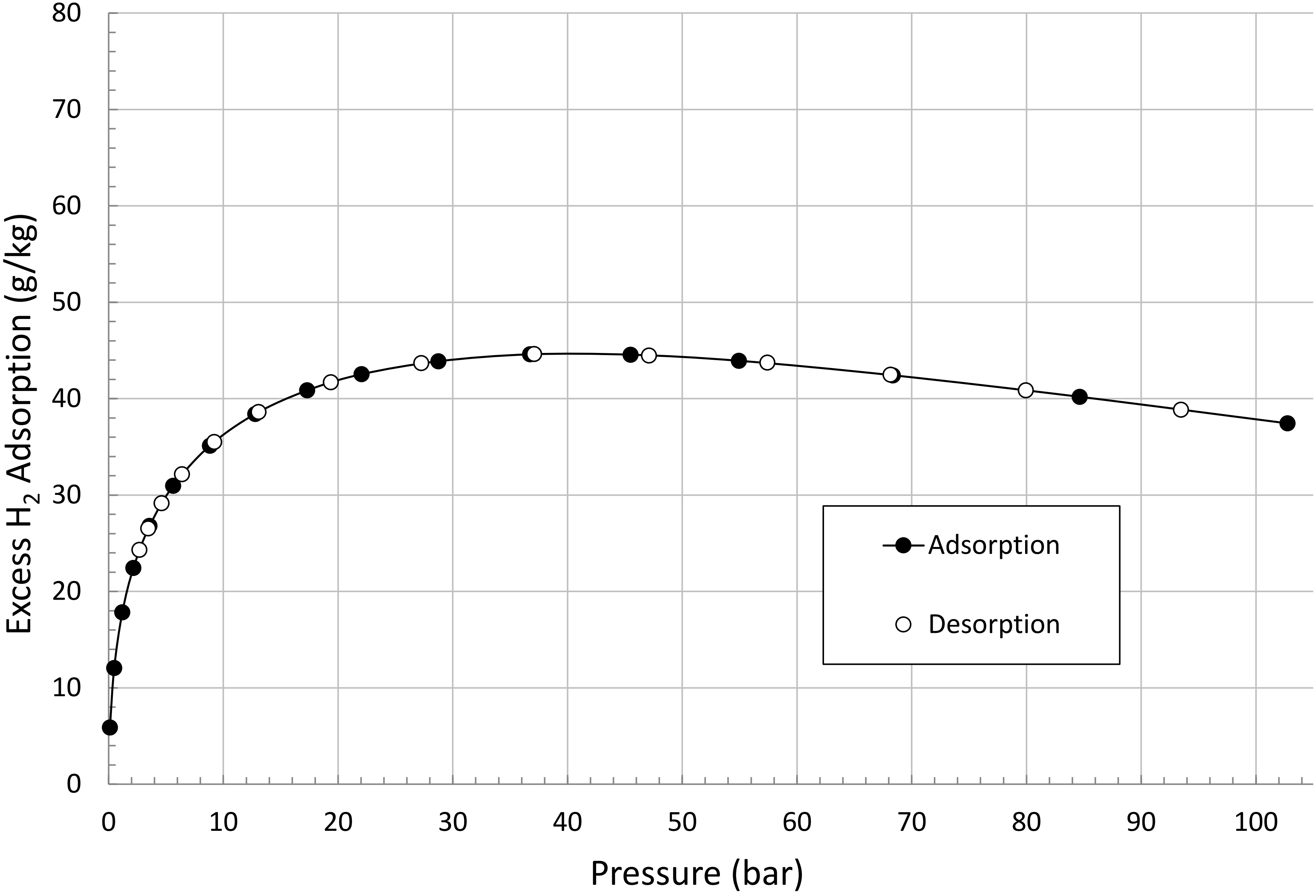

Maxsorb MSC-30

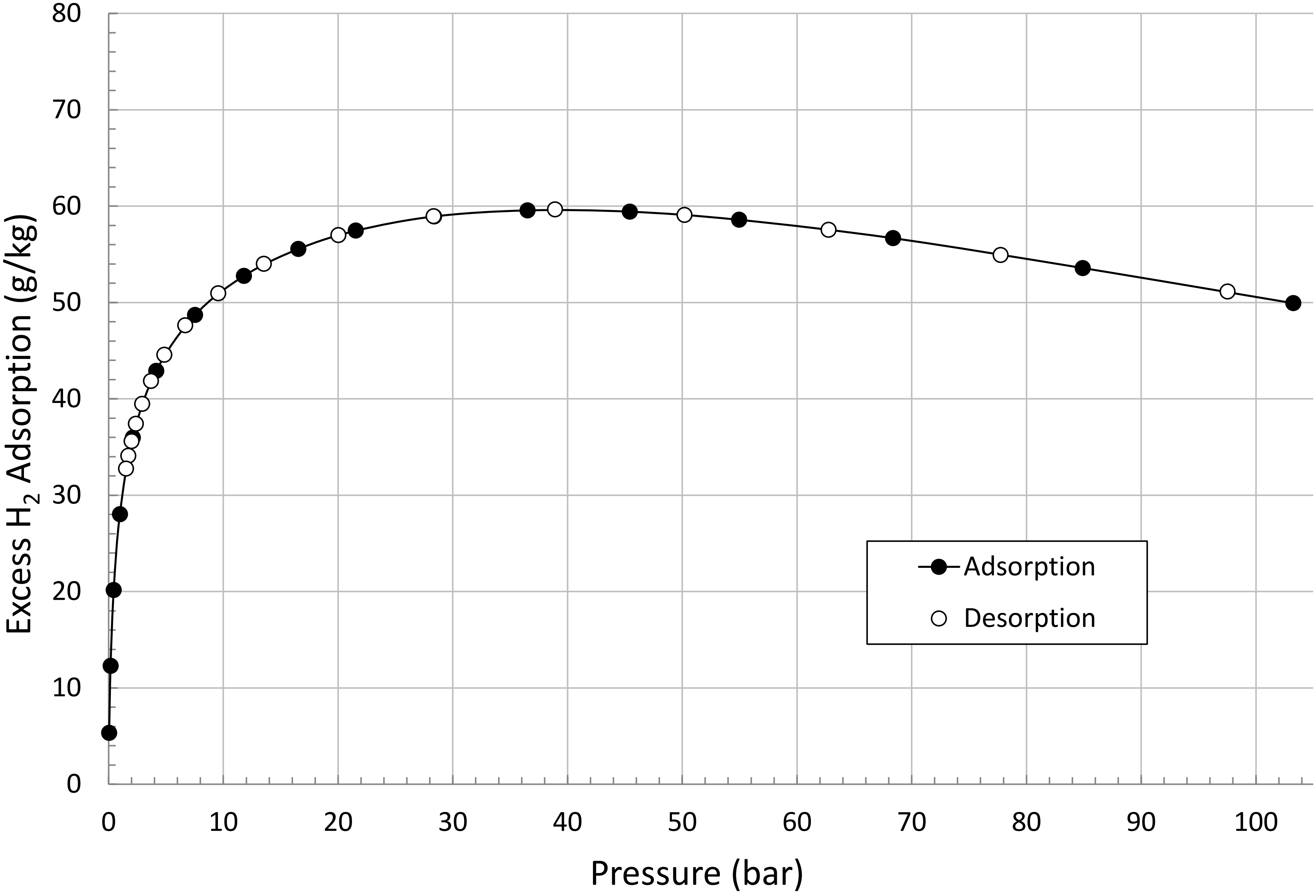

Norit Activated Carbon

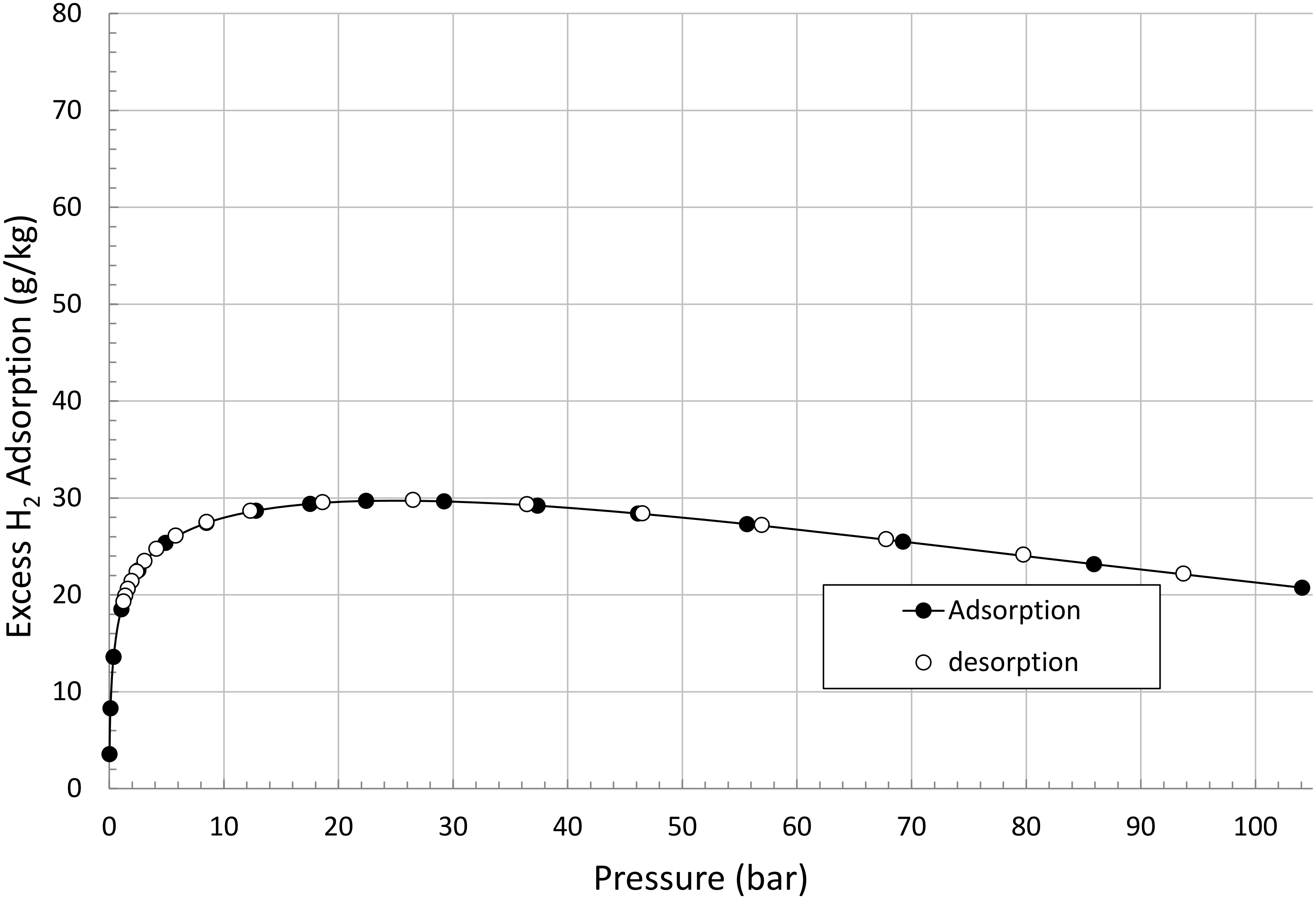

Maxsorb MSC-20

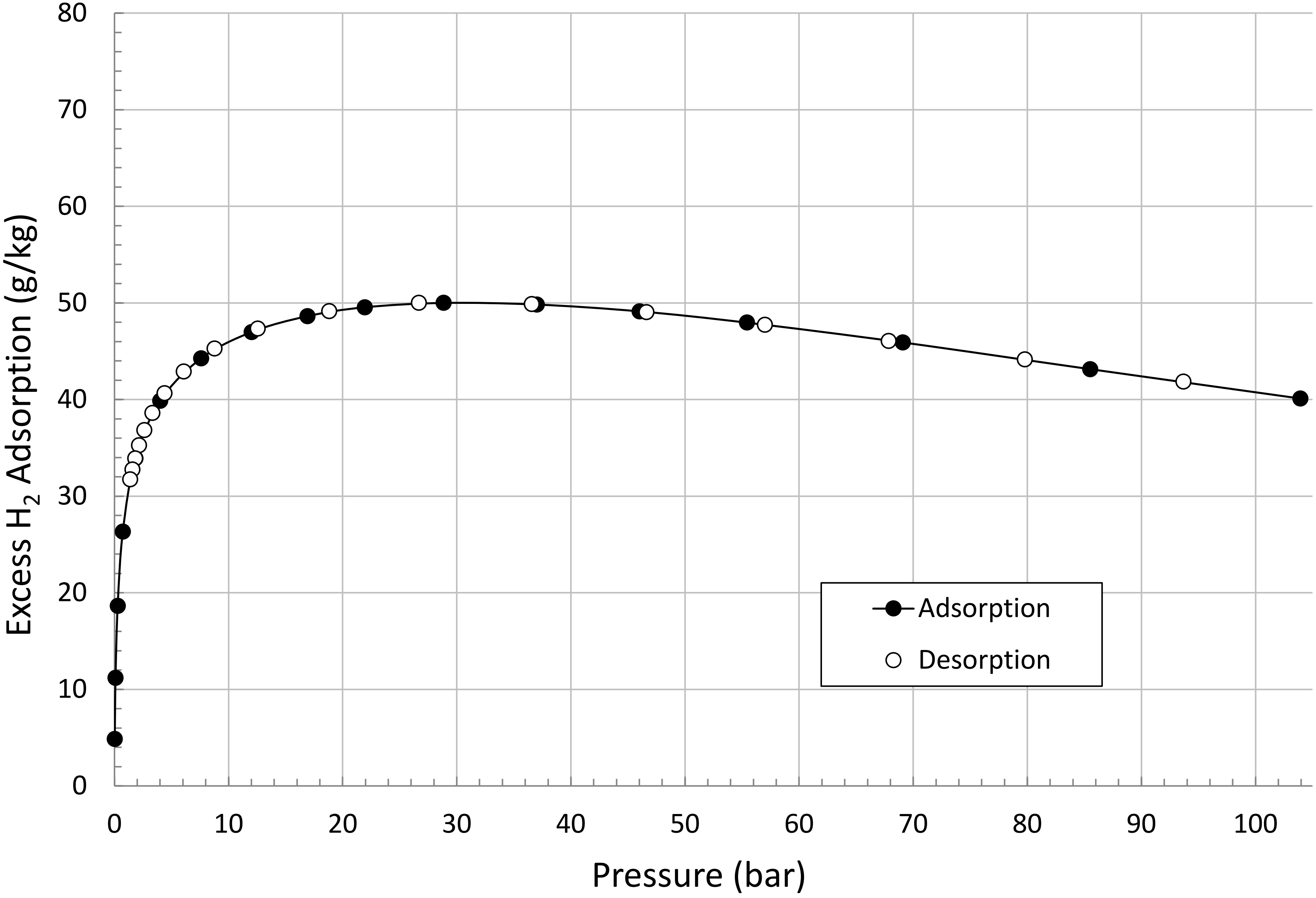

Comparison of N_2 Isotherms of Selected MOFs

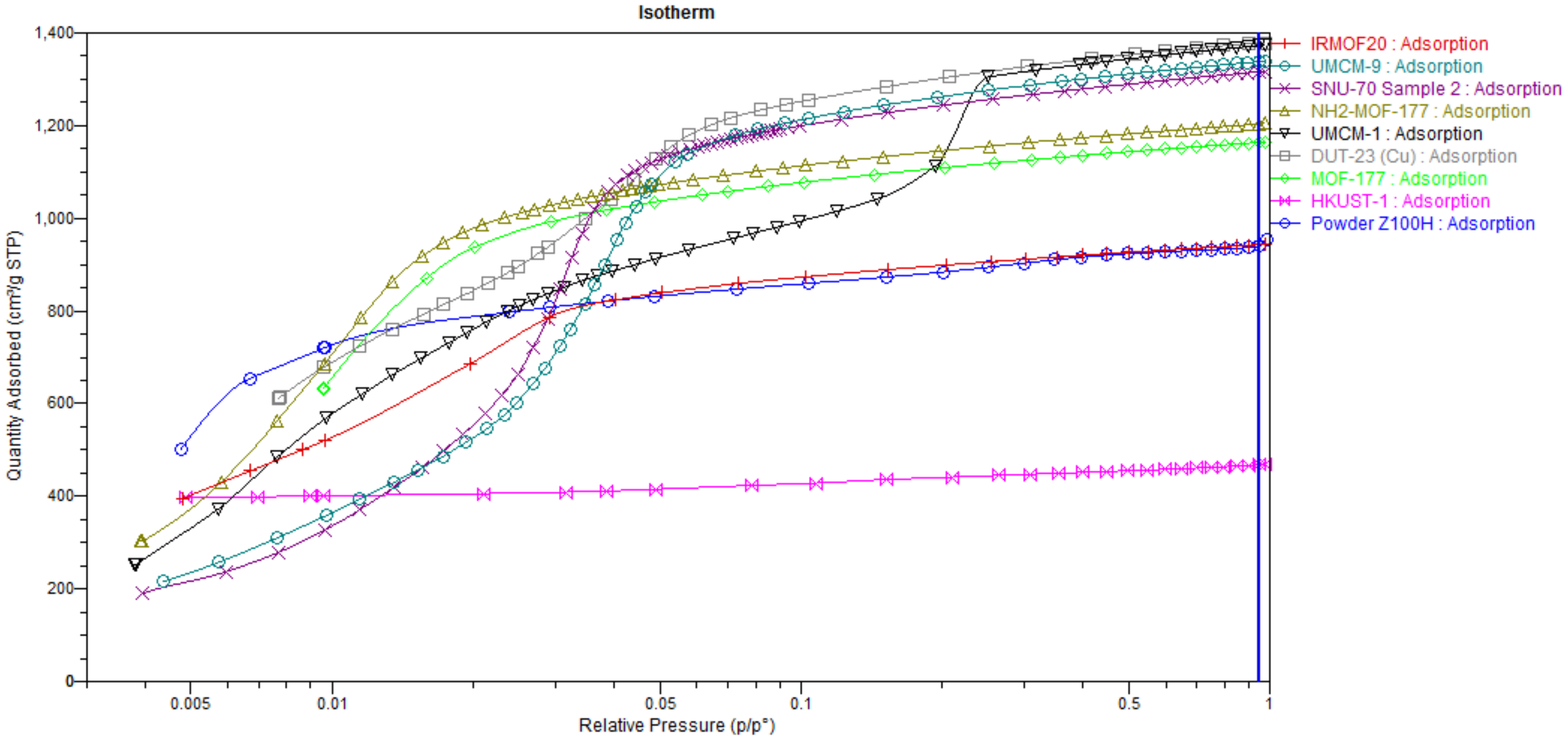

MOF-5 (BASF)

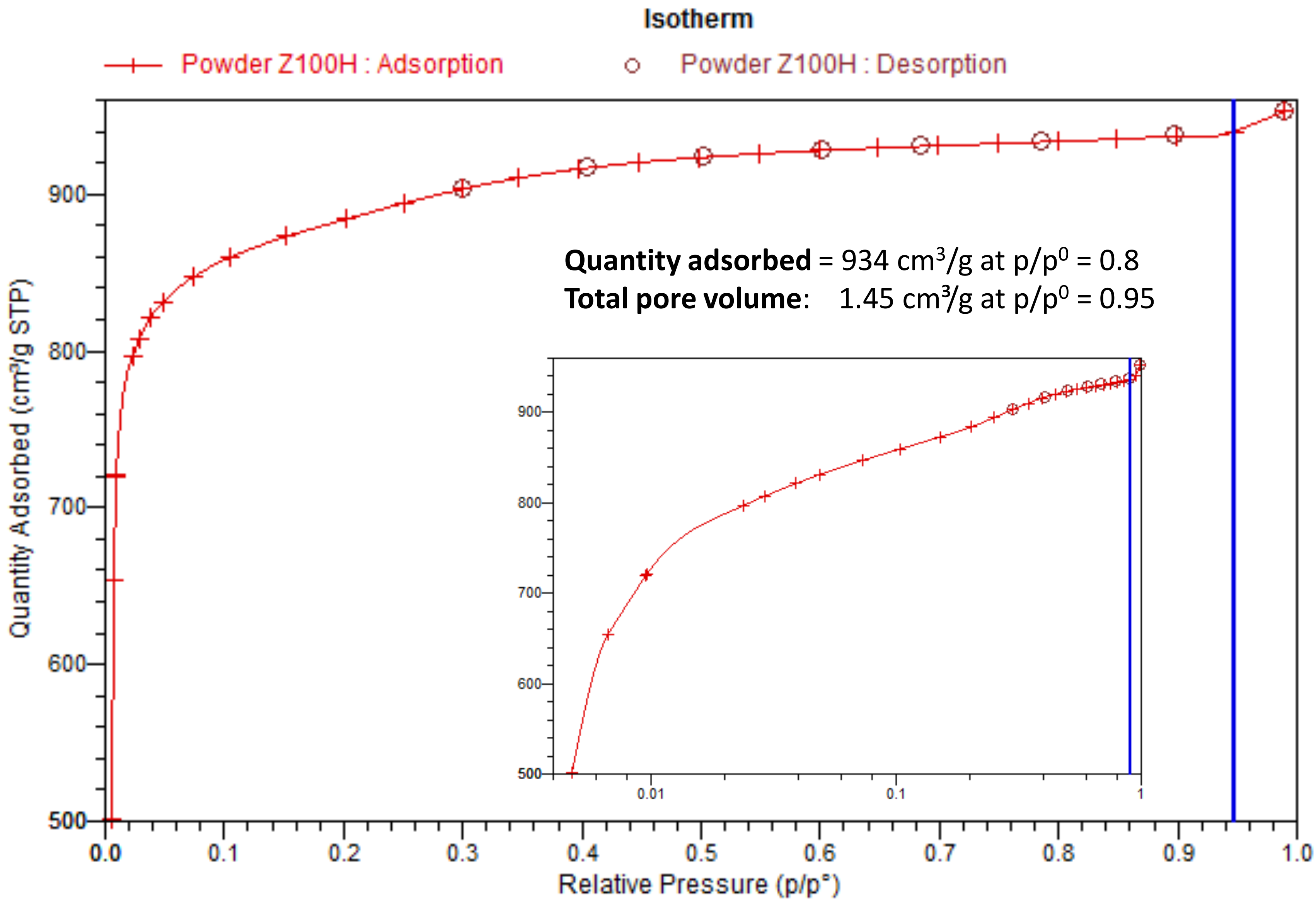

Quantity adsorbed = 934 cm^3/g at p/p^0 = 0.8
Total pore volume: 1.45 cm^3/g at p/p^0 = 0.95

Nitrogen Adsorption Isotherm

MOF-5 (BASF)

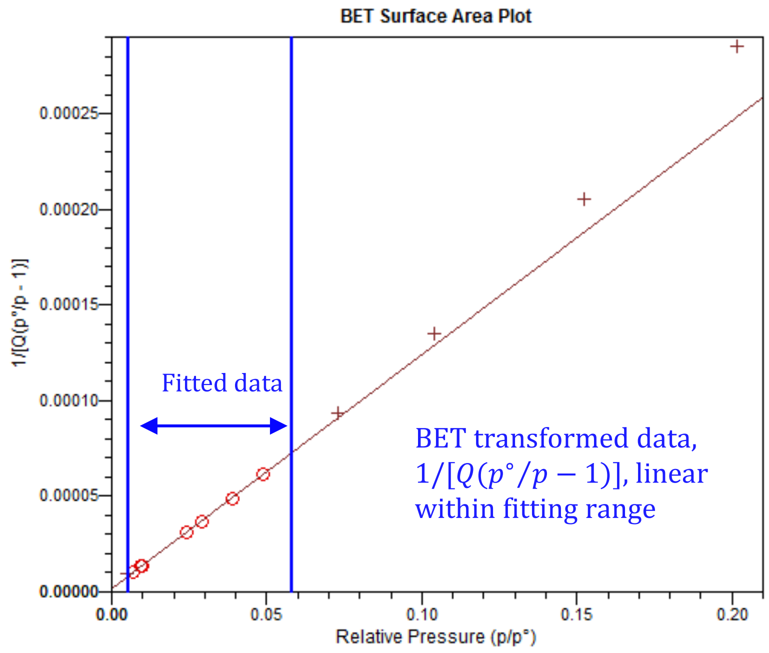

Fitted data

BET transformed data, $1/[Q(p^\circ/p-1)]$, linear within fitting range

Summary

BET surface area: 3554.9693 ± 18.5243 m²/g
Slope: 0.001223 ± 0.000006 g/cm³ STP
Y-intercept: 0.000002 ± 0.000000 g/cm³ STP
C: 695.160454
Qm: 816.7502 cm³/g STP
Correlation coefficient: 0.9999320
Molecular cross-sectional area: 0.1620 nm²

BET Fitting Range = [0.006, 0.06]

$$\left(\frac{p}{p^\circ}\right)_m = 0.035$$

$$\frac{1}{\sqrt{C}+1} = 0.0365$$

$$\text{BET Surface Area} = 3555\ \mathrm{m}^2/\mathrm{g}$$

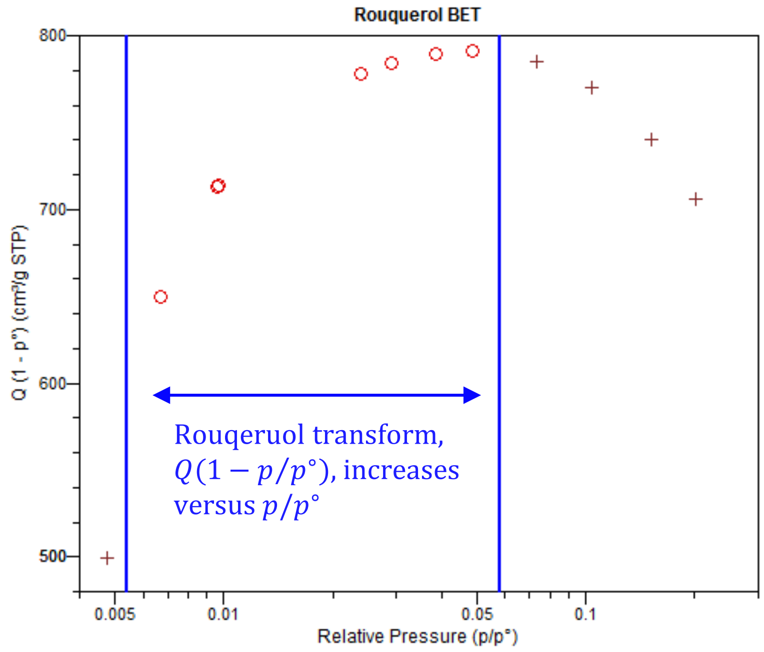

Rouqeruol transform, $Q(1-p/p^\circ)$, increases versus p/p°

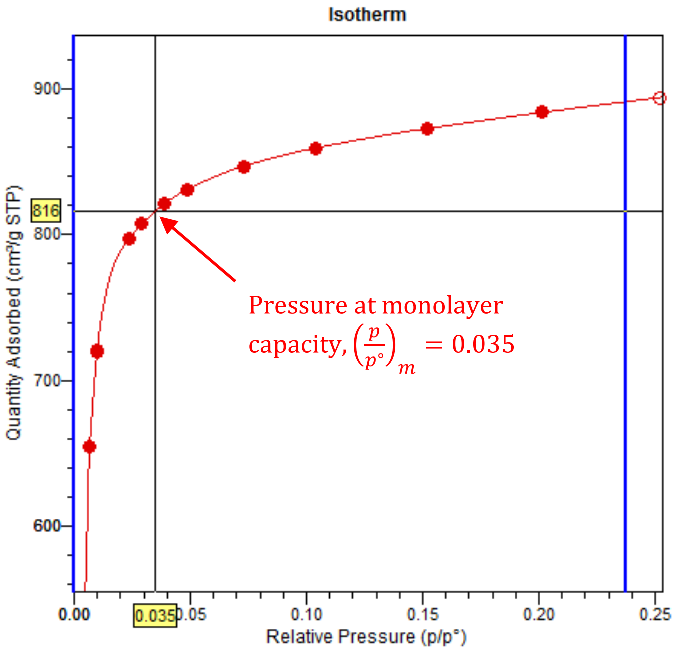

Pressure at monolayer capacity, $\left(\frac{p}{p^\circ}\right)_m = 0.035$

BET Surface Area Analysis

IRMOF-20

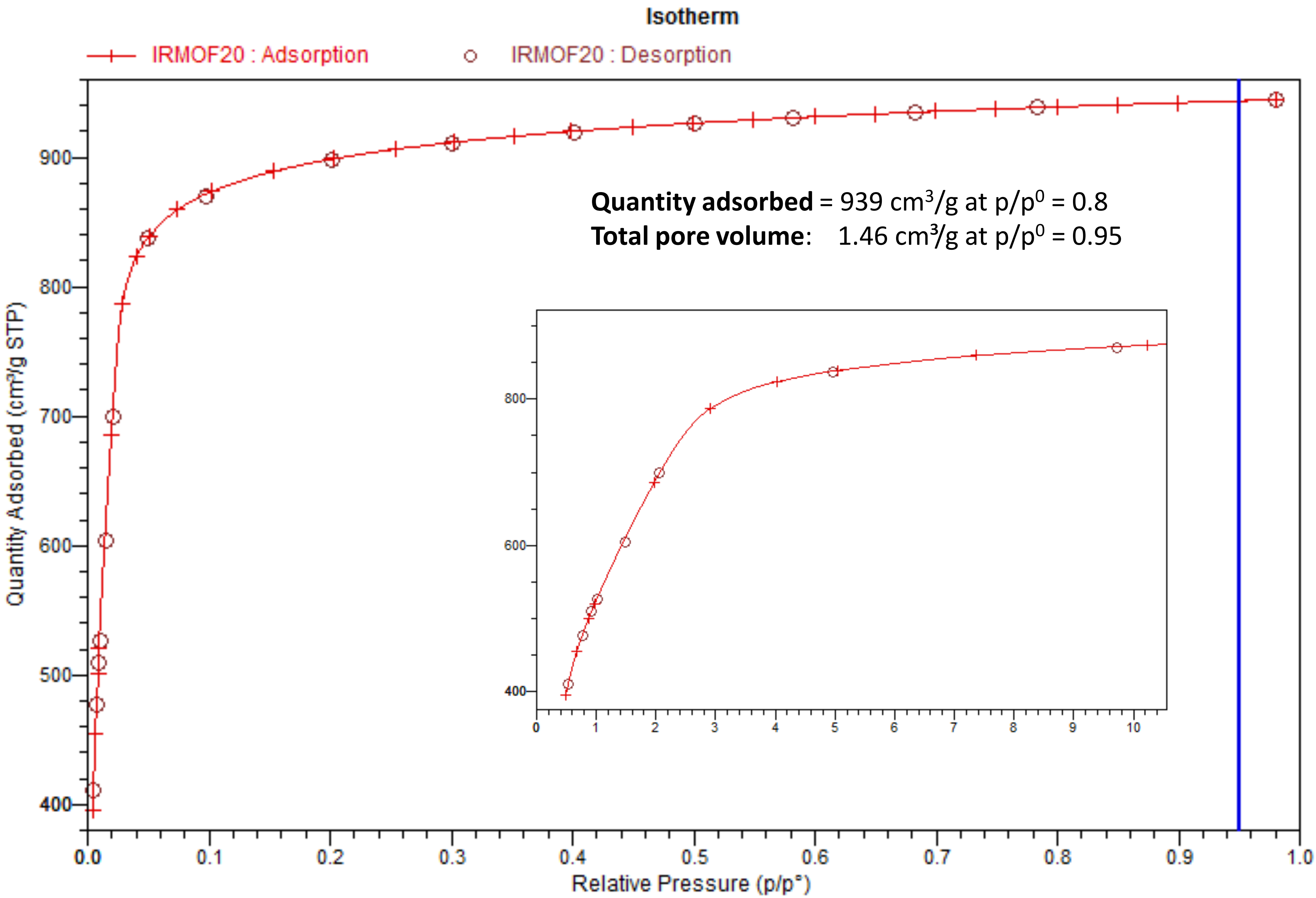

Quantity adsorbed = 939 cm^3/g at p/p^0 = 0.8
Total pore volume: 1.46 cm^3/g at p/p^0 = 0.95

Nitrogen Adsorption Isotherm

IRMOF-20

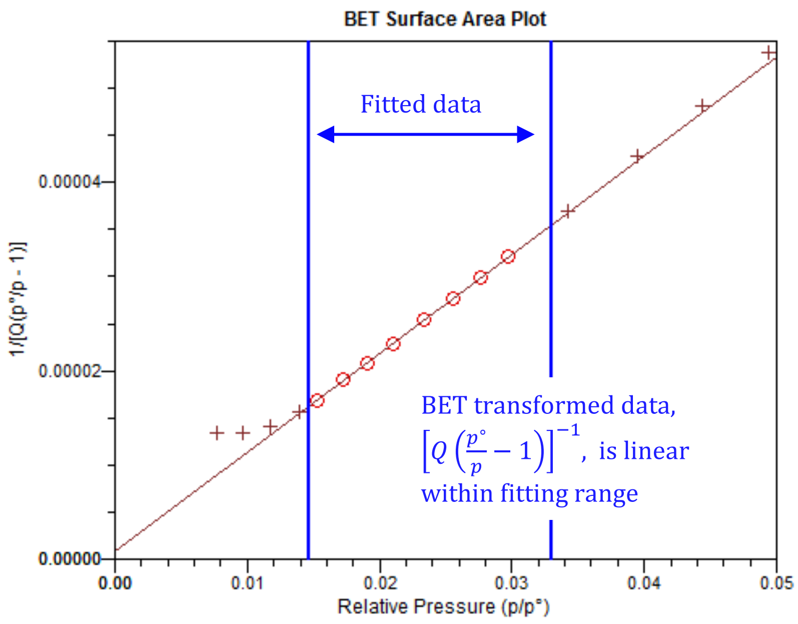

Summary

BET surface area:	4145.0814 ± 17.2898 m²/g
Slope:	0.001049 ± 0.000004 g/cm³ STP
Y-intercept:	0.000001 ± 0.000000 g/cm³ STP
C:	1221.309109
Qm:	952.3278 cm³/g STP
Correlation coefficient:	0.9999477
Molecular cross-sectional area:	0.1620 nm²

BET Fitting Range = [0.015, 0.031]

$$\left(\frac{p}{p^\circ}\right)_m = 0.0281$$

$$\frac{1}{\sqrt{C}+1} = 0.031$$

BET Surface Area = 4145 m^2/g

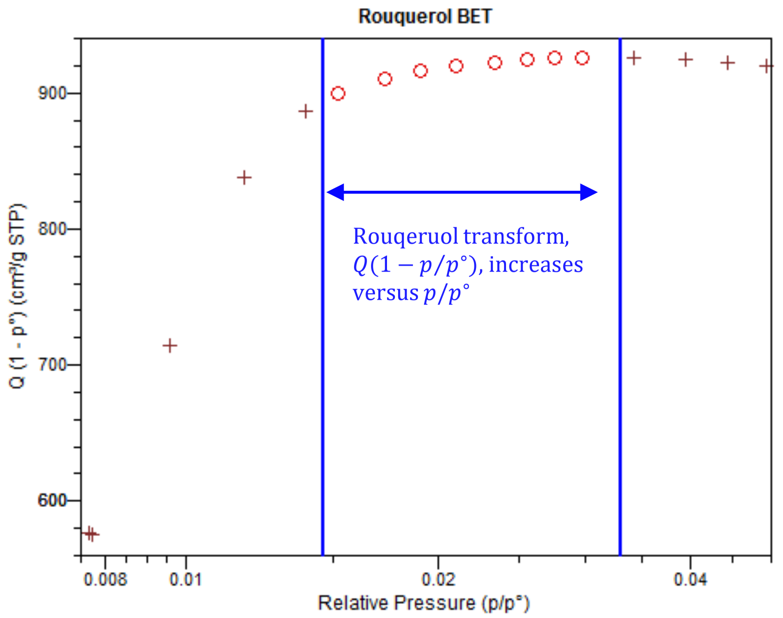

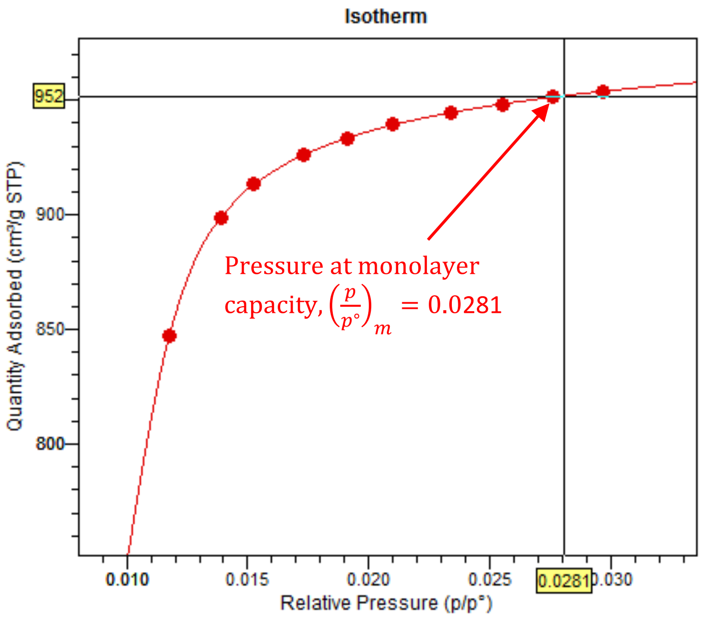

BET Surface Area Analysis

UMCM-4

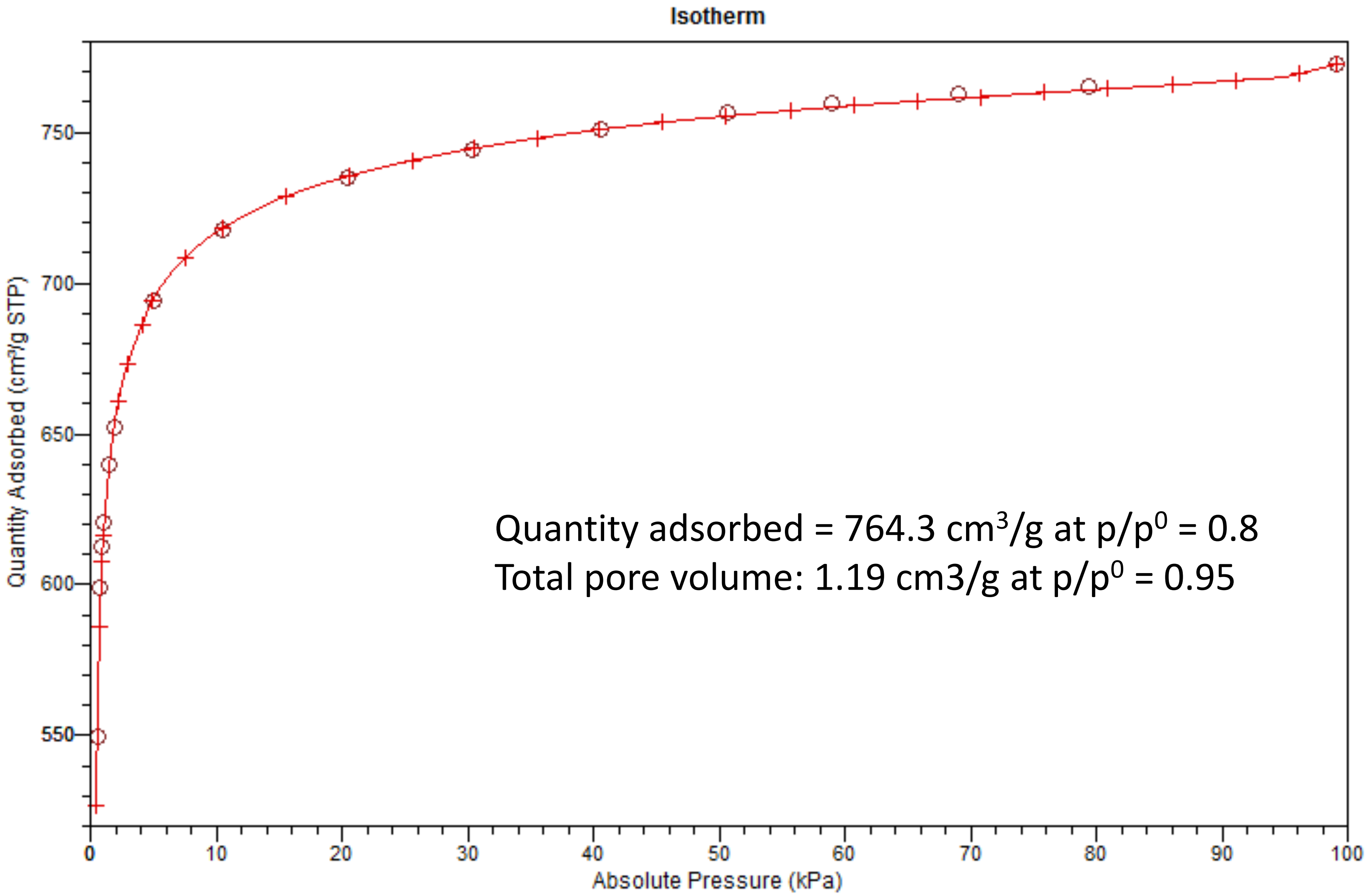

Quantity adsorbed = 764.3 cm^3/g at p/p^0 = 0.8

Total pore volume: 1.19 cm3/g at p/p^0 = 0.95

Nitrogen Adsorption Isotherm

UMCM-4

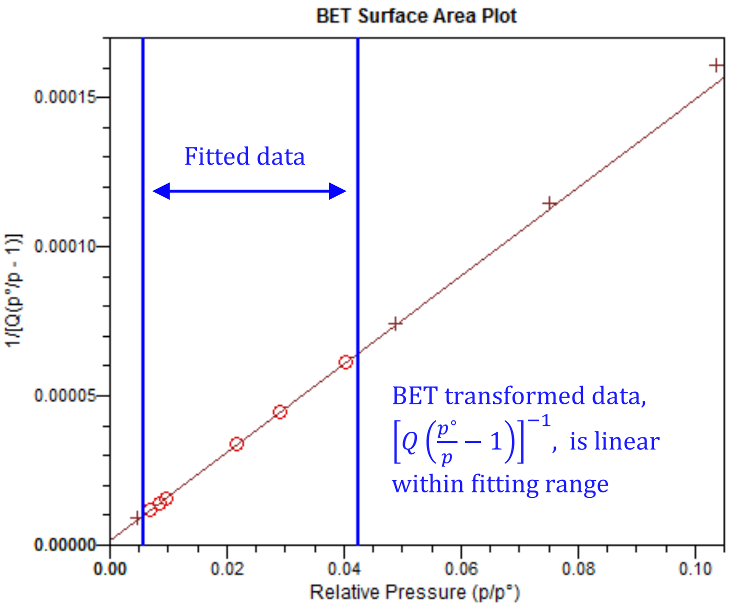

Fitted data

BET transformed data, $\left[Q\left(\frac{p^\circ}{p}-1\right)\right]^{-1}$, is linear within fitting range

Summary

BET surface area: 2942.1382 ± 3.9465 m²/g
Slope: 0.001478 ± 0.000002 g/cm³ STP
Y-intercept: 0.000002 ± 0.000000 g/cm³ STP
C: 948.129552
Qm: 675.9530 cm³/g STP
Correlation coefficient: 0.9999964
Molecular cross-sectional area: 0.1620 nm²

BET Fitting Range = [0.006, 0.04]

$$\left(\frac{p}{p^\circ}\right)_m = 0.0312$$

$$\frac{1}{\sqrt{C}+1} = 0.0314$$

BET Surface Area = 2942 m^2/g

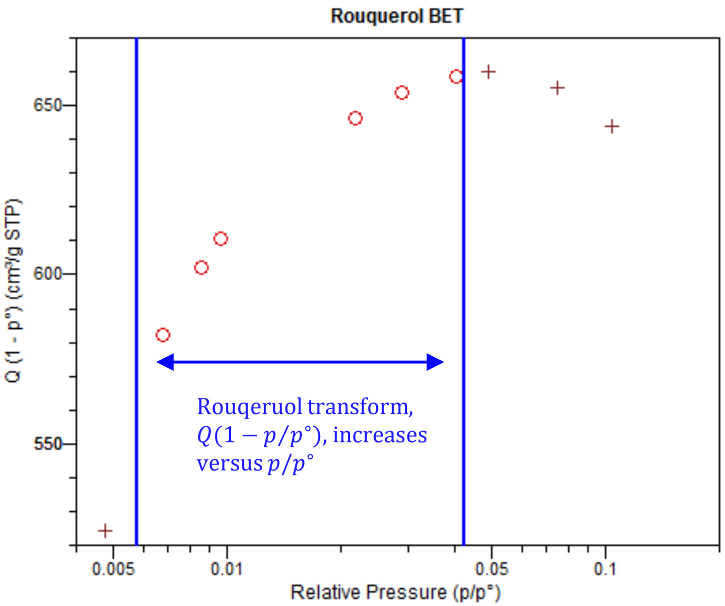

Rouqeruol transform, $Q(1-p/p^\circ)$, increases versus p/p°

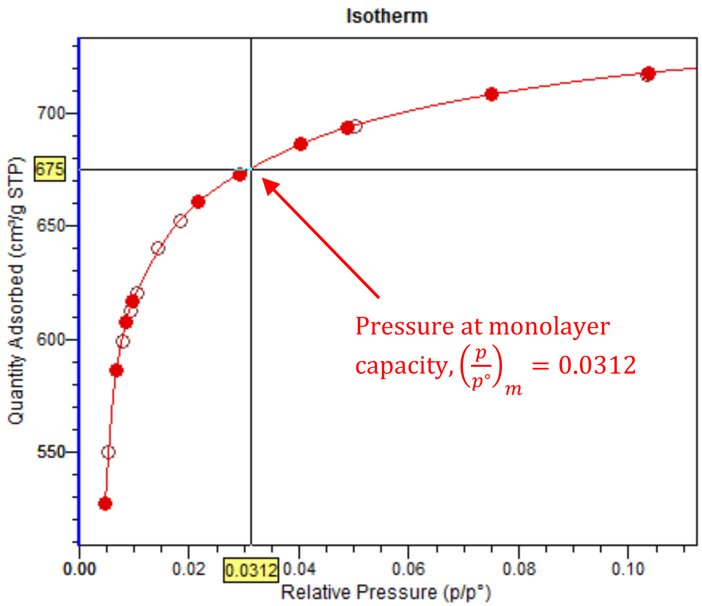

Pressure at monolayer capacity, $\left(\frac{p}{p^\circ}\right)_m = 0.0312$

BET Surface Area Analysis

Me-MOF-5 (50% Me-BDC linker)

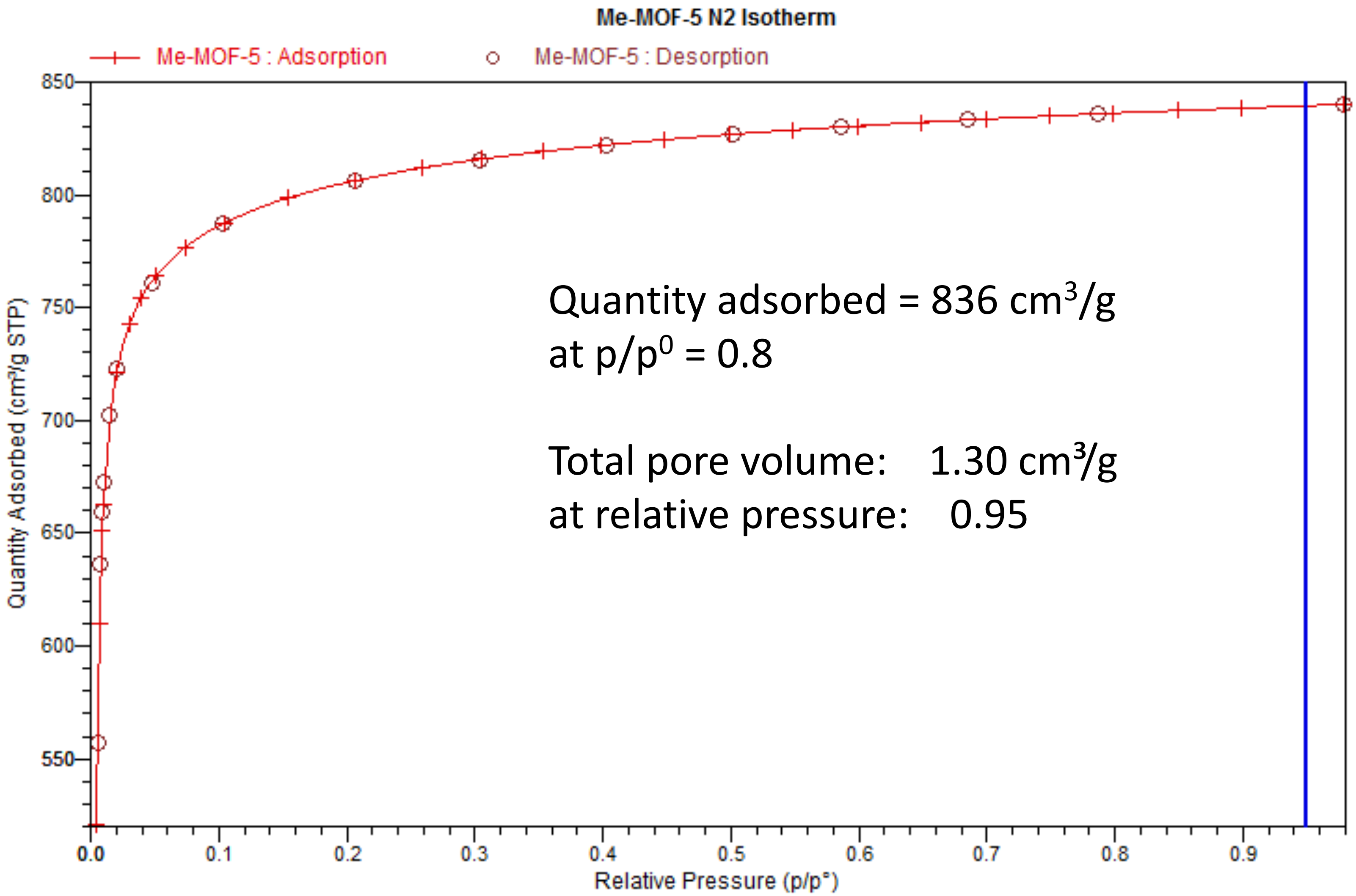

Quantity adsorbed = 836 cm^3/g
at p/p^0 = 0.8

Total pore volume: 1.30 cm^3/g
at relative pressure: 0.95

Nitrogen Adsorption Isotherm

Me-MOF-5 (50% Me-BDC linker)

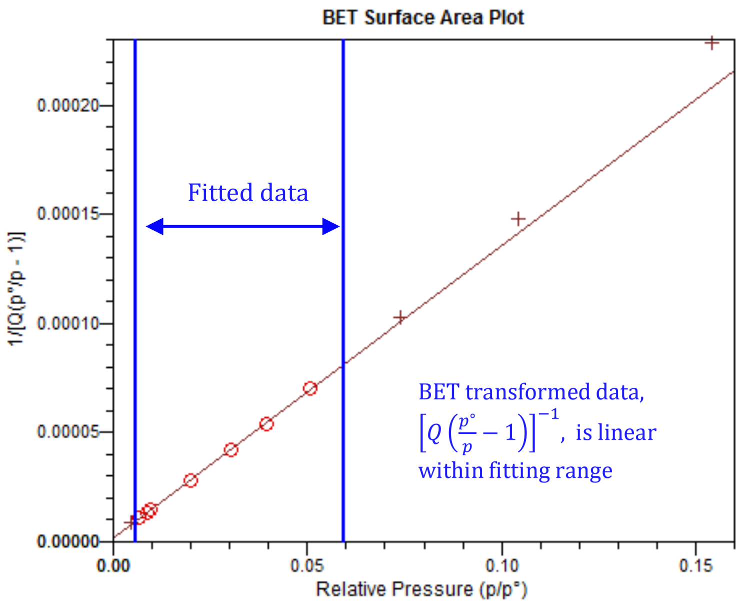

Fitted data

BET transformed data, $\left[Q\left(\frac{p^\circ}{p}-1\right)\right]^{-1}$, is linear within fitting range

Summary

BET surface area: 3247.9590 ± 15.1504 m²/g
Slope: 0.001338 ± 0.000006 g/cm³ STP
Y-intercept: 0.000002 ± 0.000000 g/cm³ STP
C: 756.049898
Qm: 746.2150 cm³/g STP
Correlation coefficient: 0.9999455
Molecular cross-sectional area: 0.1620 nm²

BET Fitting Range = [0.006, 0.055]

$$\left(\frac{p}{p^\circ}\right)_m = 0.0334$$

$$\frac{1}{\sqrt{C}+1} = 0.035$$

BET Surface Area = 3248 m^2/g

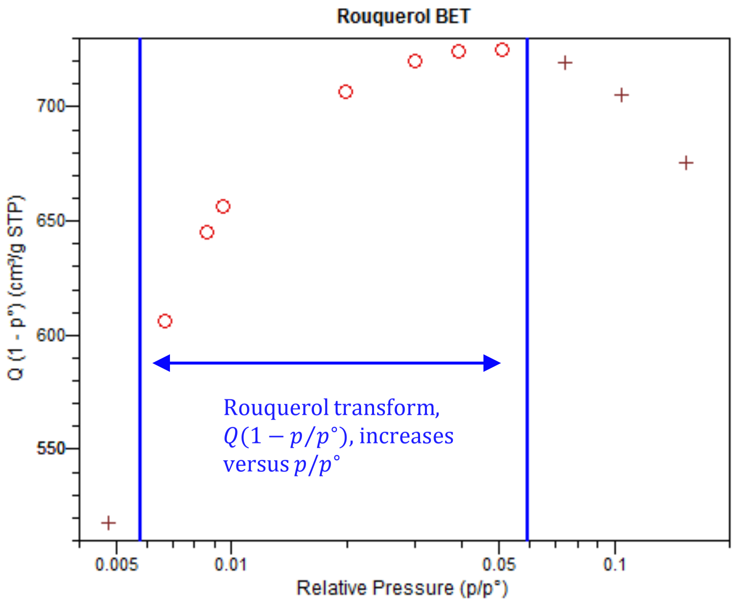

Rouquerol transform, $Q(1-p/p^\circ)$, increases versus p/p°

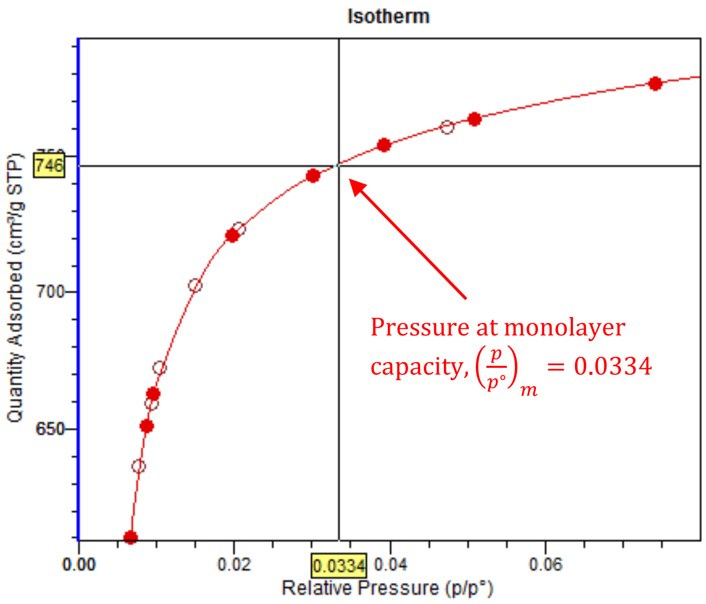

Pressure at monolayer capacity, $\left(\frac{p}{p^\circ}\right)_m = 0.0334$

BET Surface Area Analysis

UiO-66

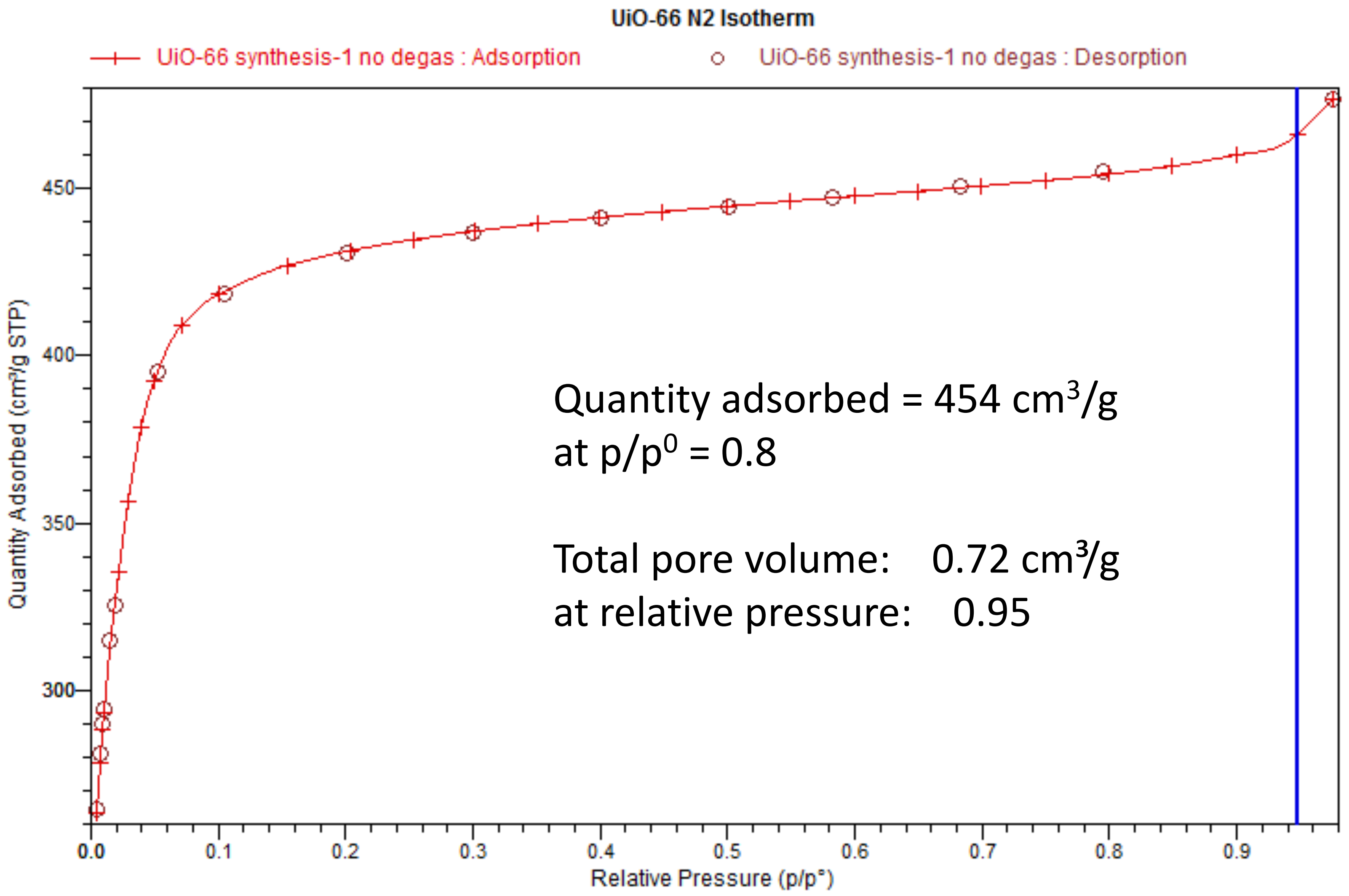

Quantity adsorbed = 454 cm^3/g
at p/p^0 = 0.8

Total pore volume: 0.72 cm^3/g
at relative pressure: 0.95

Nitrogen Adsorption Isotherm

UiO-66

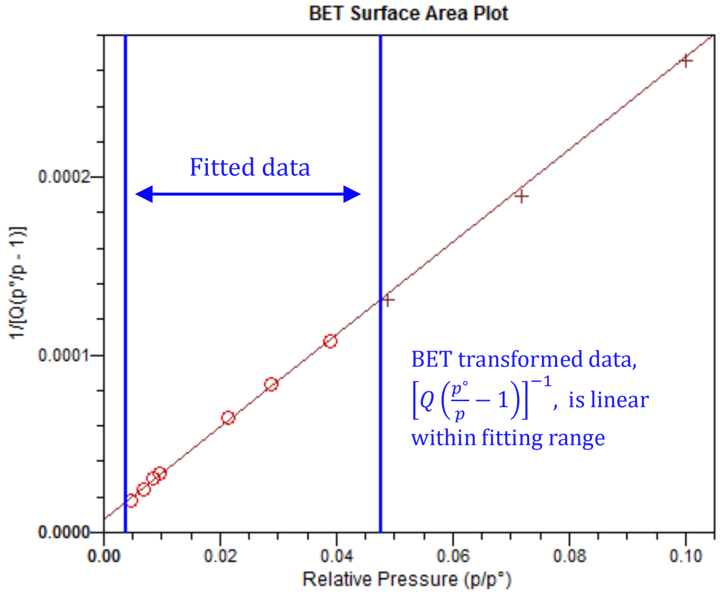

Fitted data

BET transformed data, $\left[Q\left(\frac{p^\circ}{p}-1\right)\right]^{-1}$, is linear within fitting range

Summary

BET surface area: 1667.7002 ± 29.3322 m²/g
Slope: 0.002603 ± 0.000046 g/cm³ STP
Y-intercept: 0.000007 ± 0.000001 g/cm³ STP
C: 352.104392
Qm: 383.1523 cm³/g STP
Correlation coefficient: 0.9992234
Molecular cross-sectional area: 0.1620 nm²

BET Fitting Range = [0.005, 0.045]

$$\left(\frac{p}{p^\circ}\right)_m = 0.0423$$

$$\frac{1}{\sqrt{C}+1} = 0.050$$

BET Surface Area = 1668 m^2/g

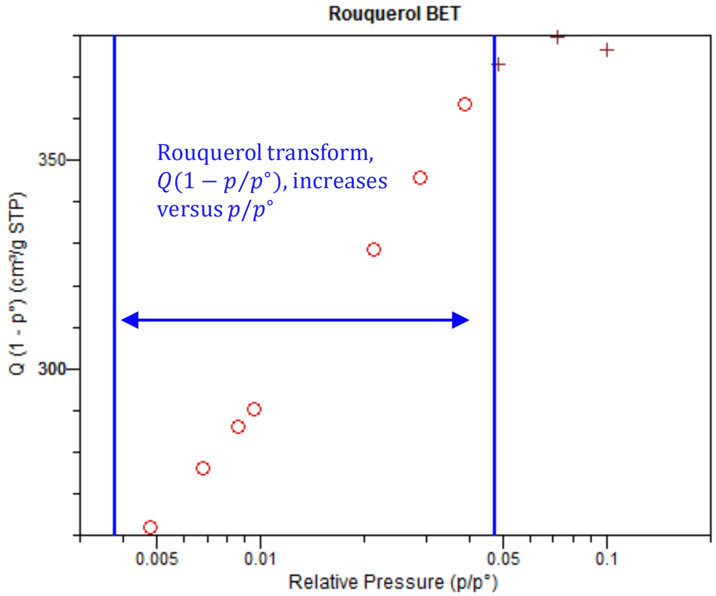

Rouquerol transform, $Q(1-p/p^\circ)$, increases versus p/p°

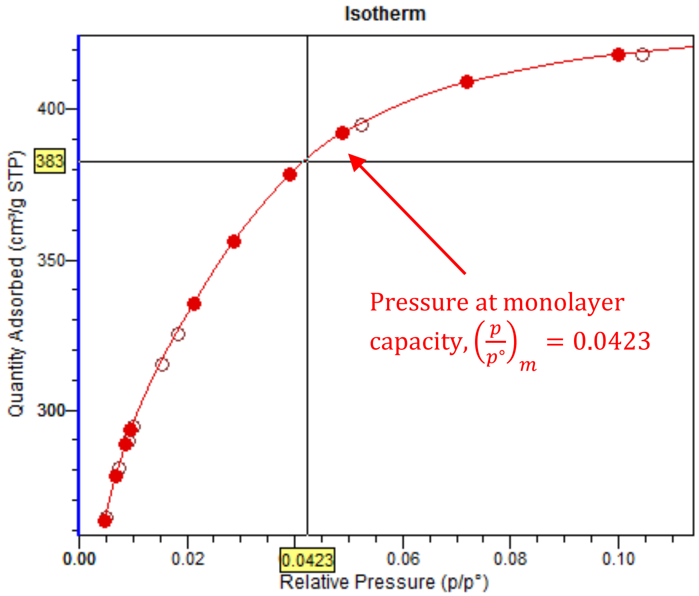

Pressure at monolayer capacity, $\left(\frac{p}{p^\circ}\right)_m = 0.0423$

BET Surface Area Analysis

UiO-67

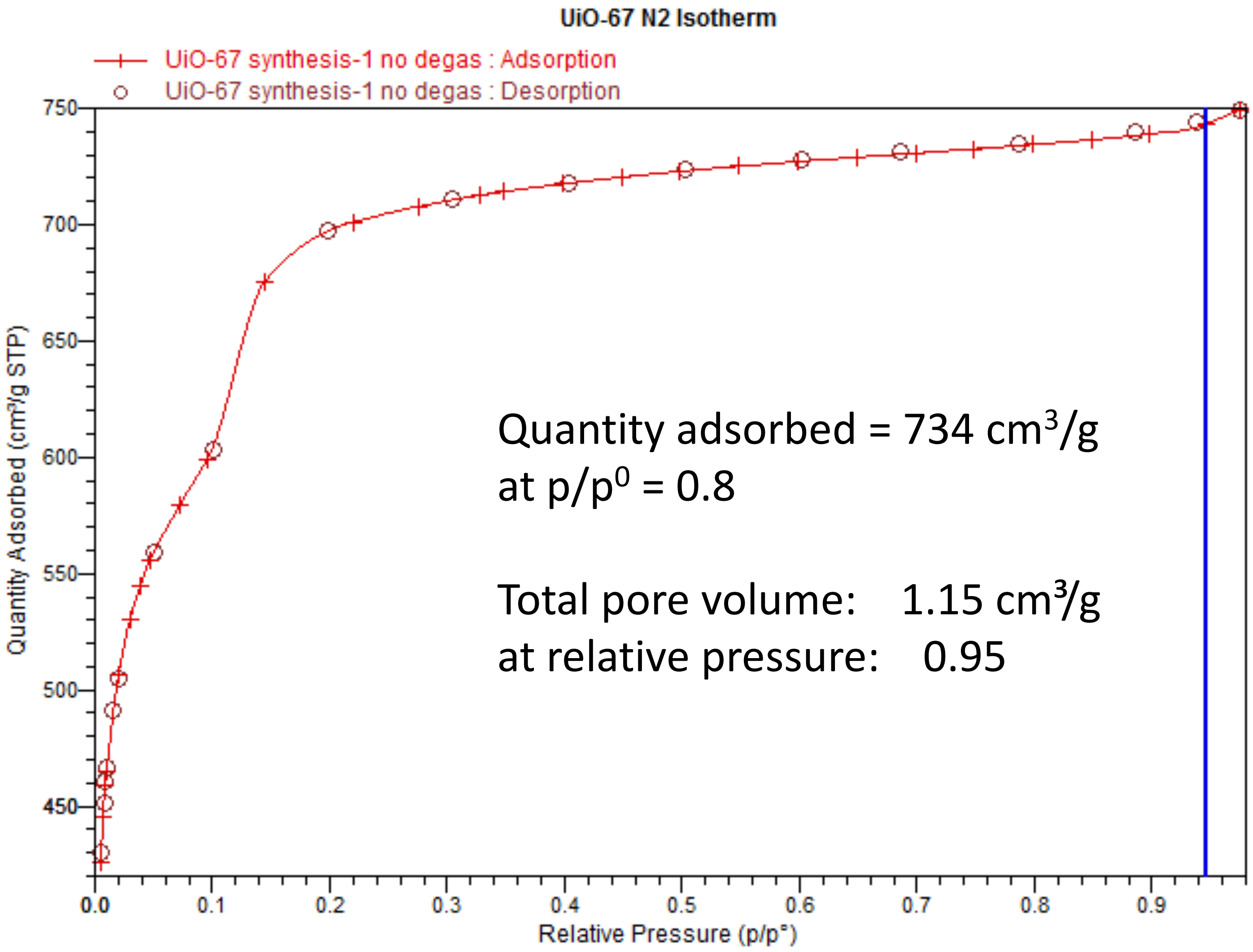

Quantity adsorbed = 734 cm^3/g
at p/p^0 = 0.8

Total pore volume: 1.15 cm^3/g
at relative pressure: 0.95

Nitrogen Adsorption Isotherm

UiO-67

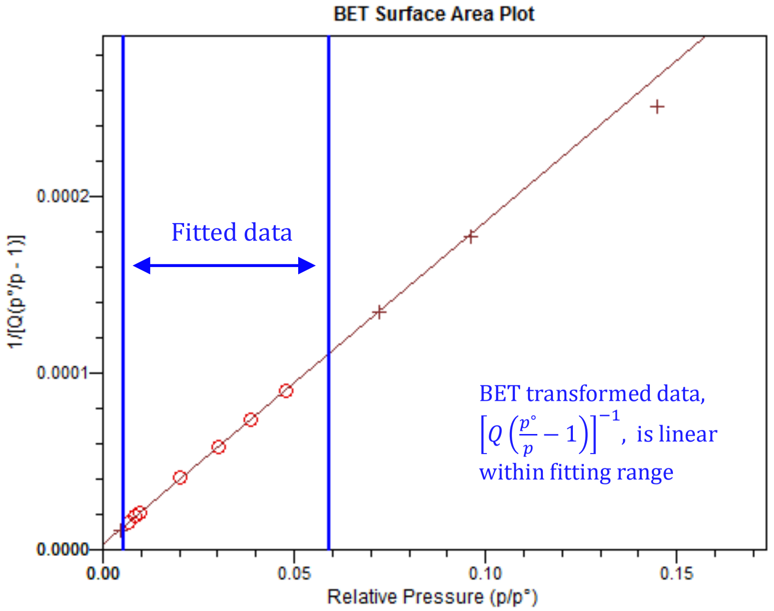

Fitted data

BET transformed data, $\left[Q\left(\frac{p^{\circ}}{p}-1\right)\right]^{-1}$, is linear within fitting range

Summary

BET surface area: 2380.8068 ± 10.9259 m²/g
Slope: 0.001825 ± 0.000008 g/cm³ STP
Y-intercept: 0.000003 ± 0.000000 g/cm³ STP
C: 551.900744
Qm: 546.9877 cm³/g STP
Correlation coefficient: 0.9999472
Molecular cross-sectional area: 0.1620 nm²

BET Fitting Range = [0.006, 0.06]

$$\left(\frac{p}{p^{\circ}}\right)_m = 0.0397$$

$$\frac{1}{\sqrt{C}+1} = 0.041$$

BET Surface Area = 2381 m^2/g

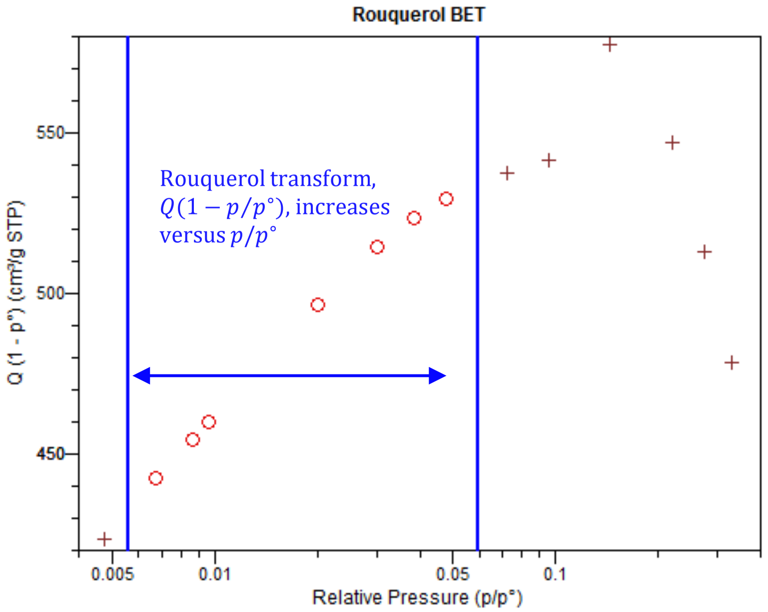

Rouquerol transform, $Q(1-p/p^{\circ})$, increases versus p/p°

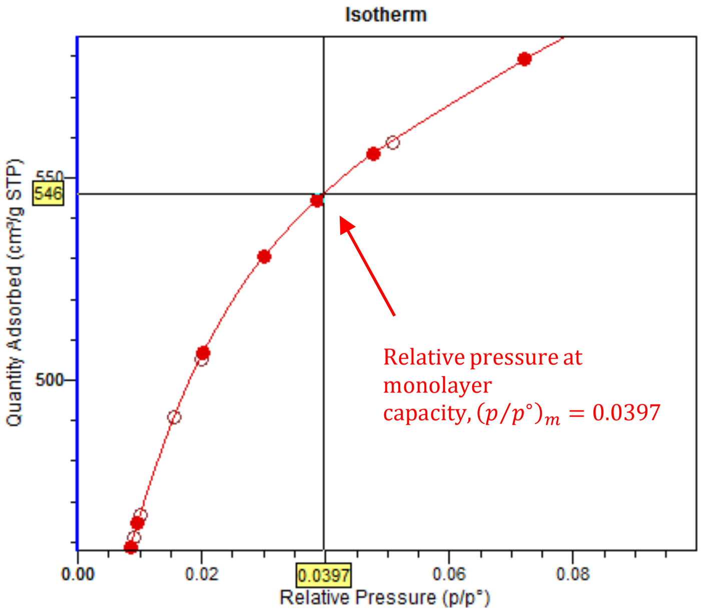

Relative pressure at monolayer capacity, $(p/p^{\circ})_m = 0.0397$

BET Surface Area Analysis

MIL-101-NH$_2$

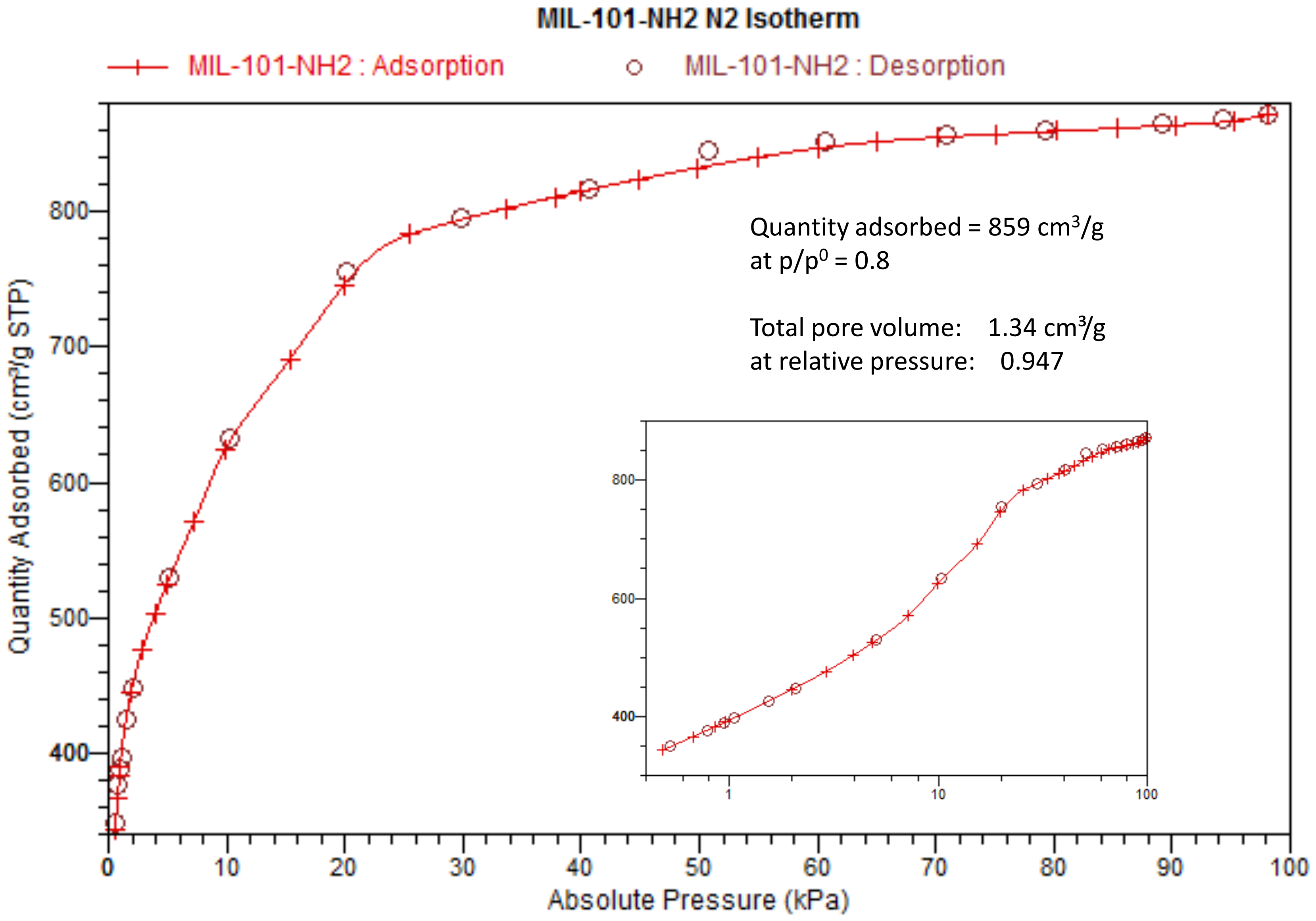

Quantity adsorbed = 859 cm^3/g
at p/p^0 = 0.8

Total pore volume: 1.34 cm^3/g
at relative pressure: 0.947

Nitrogen Adsorption Isotherm

MIL-101-NH_2

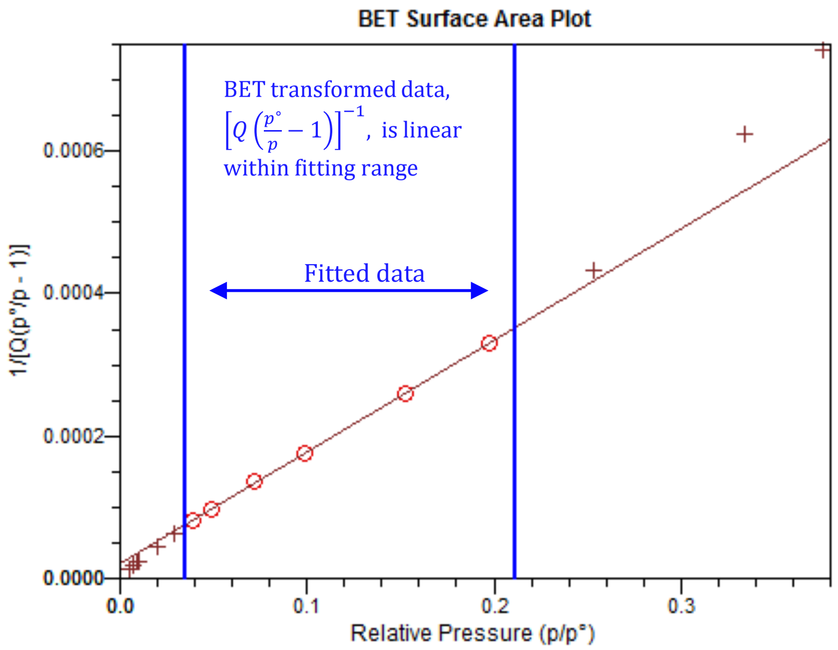

Summary

BET surface area: 2740.5234 ± 16.9253 m²/g
Slope: 0.001567 ± 0.000010 g/cm³ STP
Y-intercept: 0.000021 ± 0.000001 g/cm³ STP
C: 75.425859
Qm: 629.6322 cm³/g STP
Correlation coefficient: 0.9999227
Molecular cross-sectional area: 0.1620 nm²

BET Fitting Range = [0.035, 0.21]

$$\left(\frac{p}{p^\circ}\right)_m = 0.104$$

$$\frac{1}{\sqrt{C}+1} = 0.103$$

BET Surface Area = 2741 m^2/g

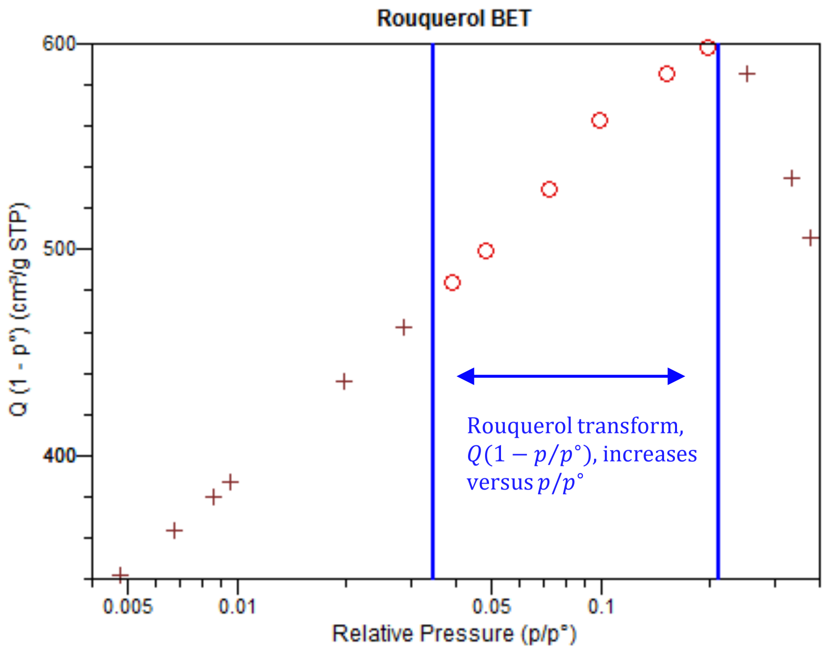

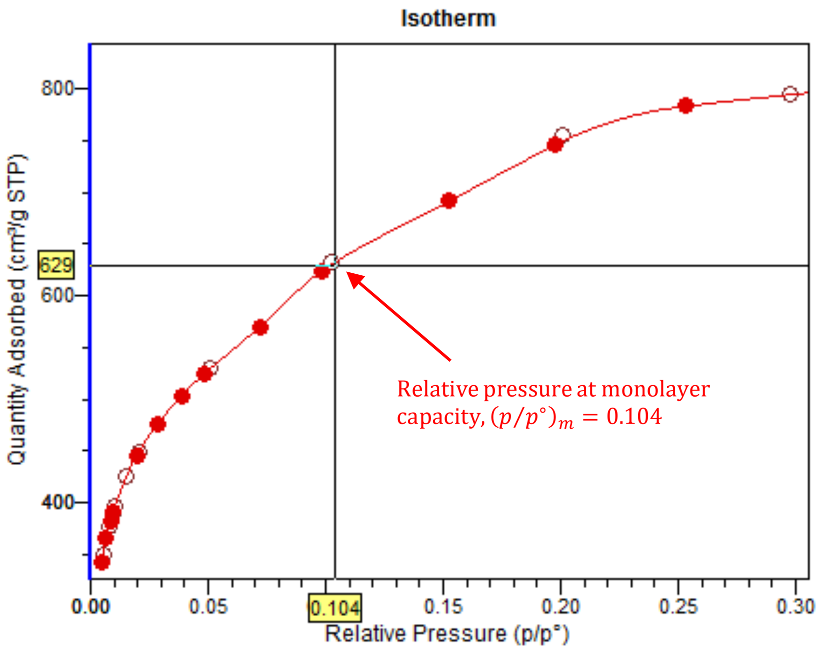

BET Surface Area Analysis

Cu-BTC (HKUST-1)

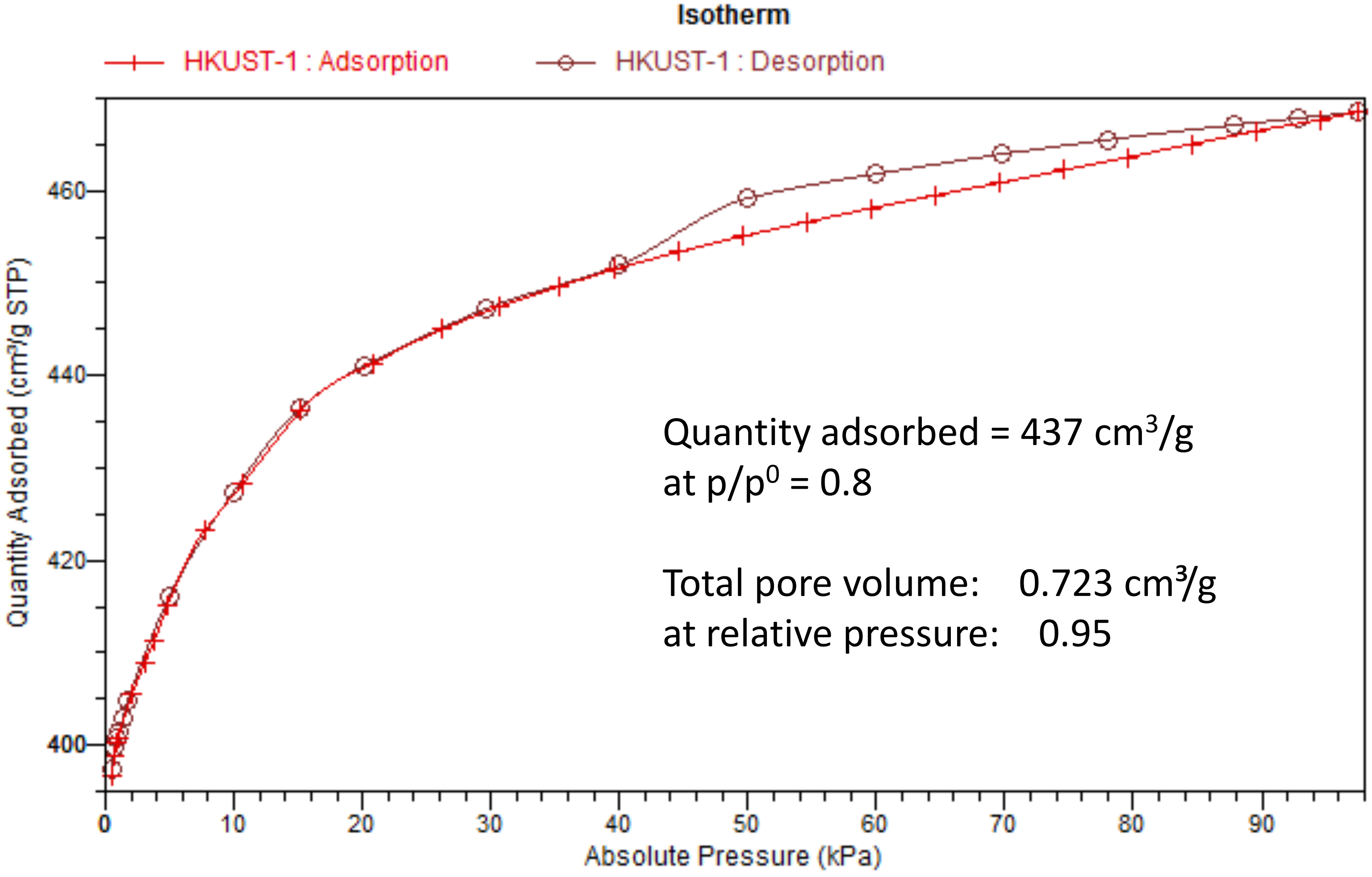

Quantity adsorbed = 437 cm^3/g
at $p/p^0 = 0.8$

Total pore volume: 0.723 cm^3/g
at relative pressure: 0.95

Nitrogen Adsorption Isotherm

Cu-BTC (HKUST-1)

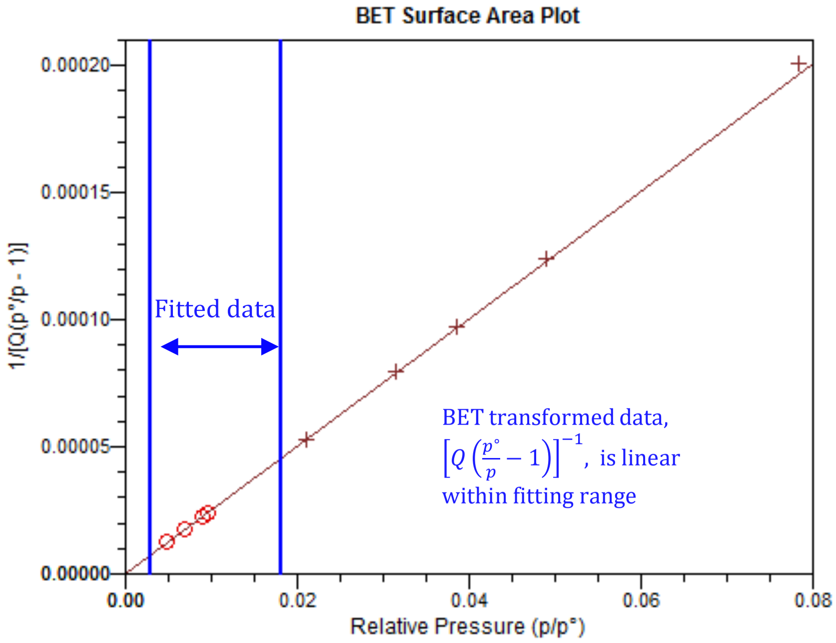

Fitted data

BET transformed data, $\left[Q\left(\frac{p^\circ}{p}-1\right)\right]^{-1}$, is linear within fitting range

Summary

BET surface area: 1736.3973 ± 0.0632 m²/g
Slope: 0.002507 ± 0.000000 g/cm³ STP
Y-intercept: 0.000000 ± 0.000000 g/cm³ STP
C: 19566.577865
Qm: 398.9353 cm³/g STP
Correlation coefficient: 1.0000000
Molecular cross-sectional area: 0.1620 nm²

BET Fitting Range = [0.003, 0.01]

$$\left(\frac{p}{p^\circ}\right)_m = 0.0074$$

$$\frac{1}{\sqrt{C}+1} = 0.0071$$

BET Surface Area = 1736 m^2/g

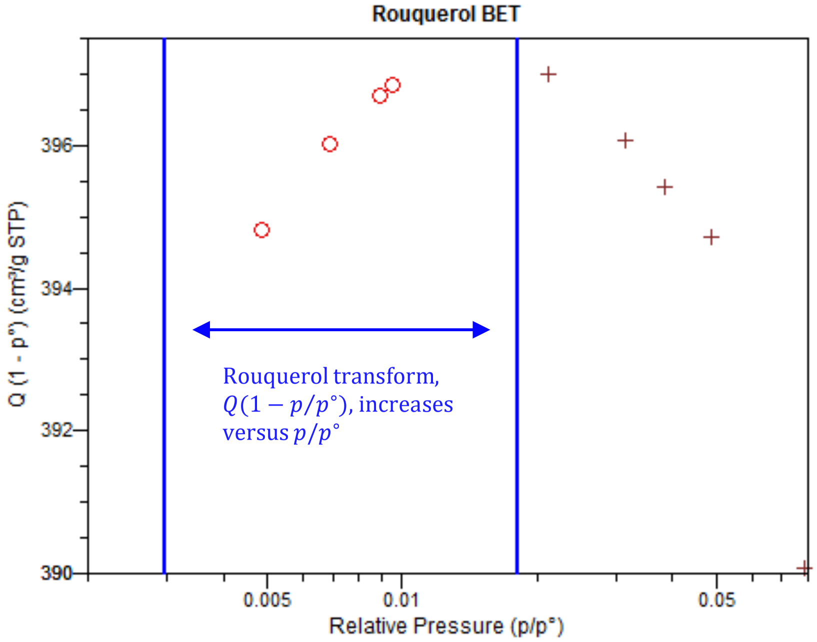

Rouquerol transform, $Q(1-p/p^\circ)$, increases versus p/p°

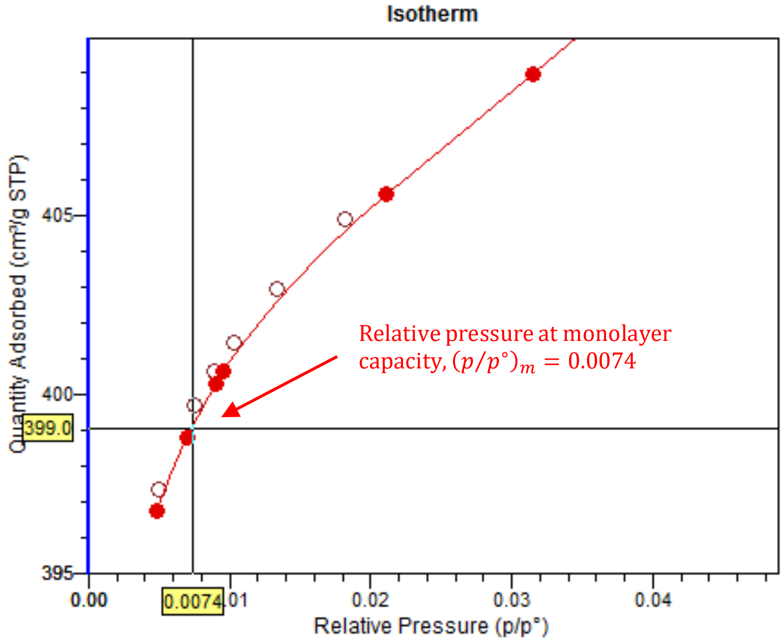

Relative pressure at monolayer capacity, $(p/p^\circ)_m = 0.0074$

BET Surface Area Analysis

MOF-177 (BASF)

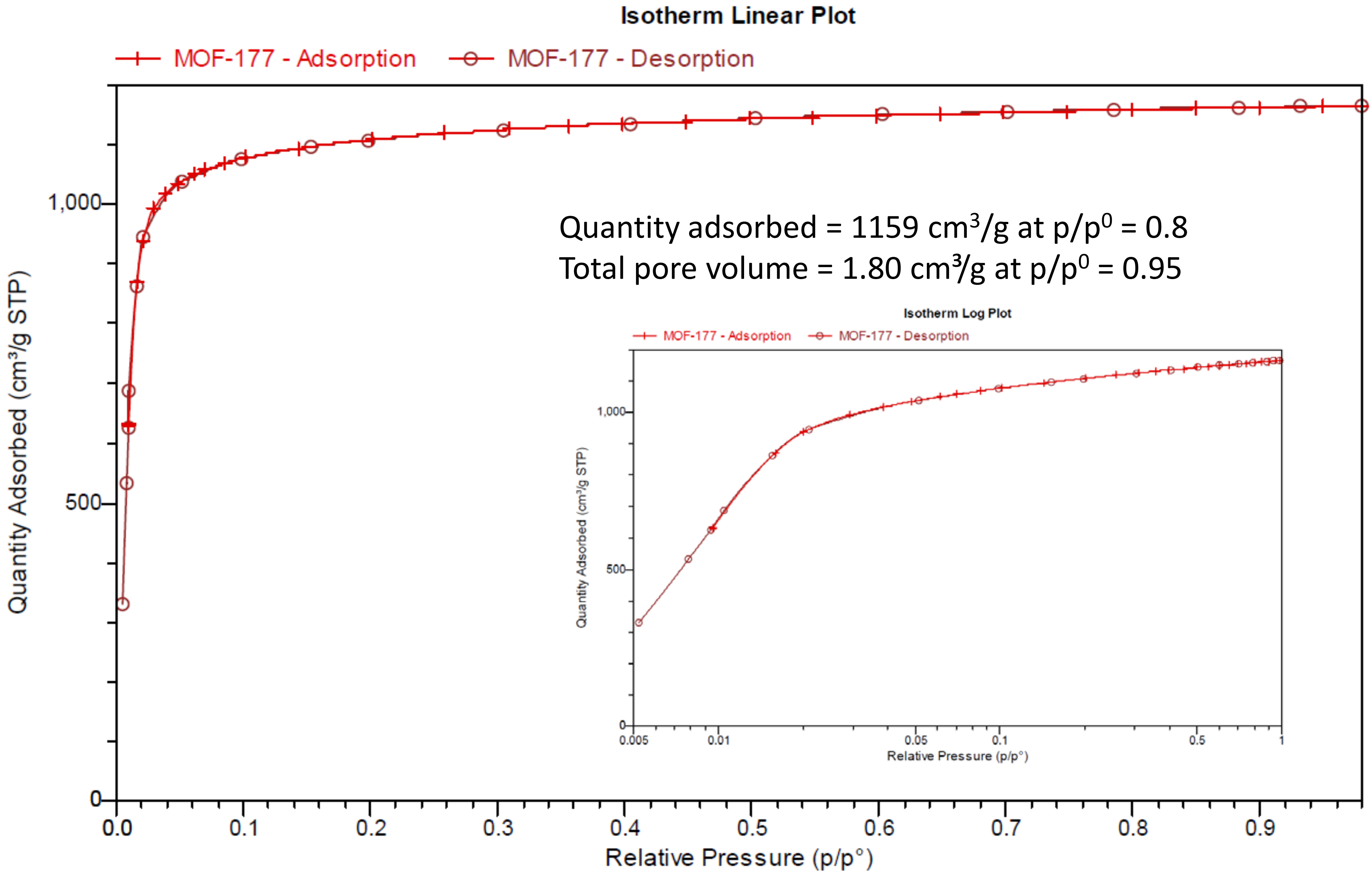

Quantity adsorbed = 1159 cm^3/g at p/p^0 = 0.8

Total pore volume = 1.80 cm^3/g at p/p^0 = 0.95

Nitrogen Adsorption Isotherm

MOF-177 (BASF)

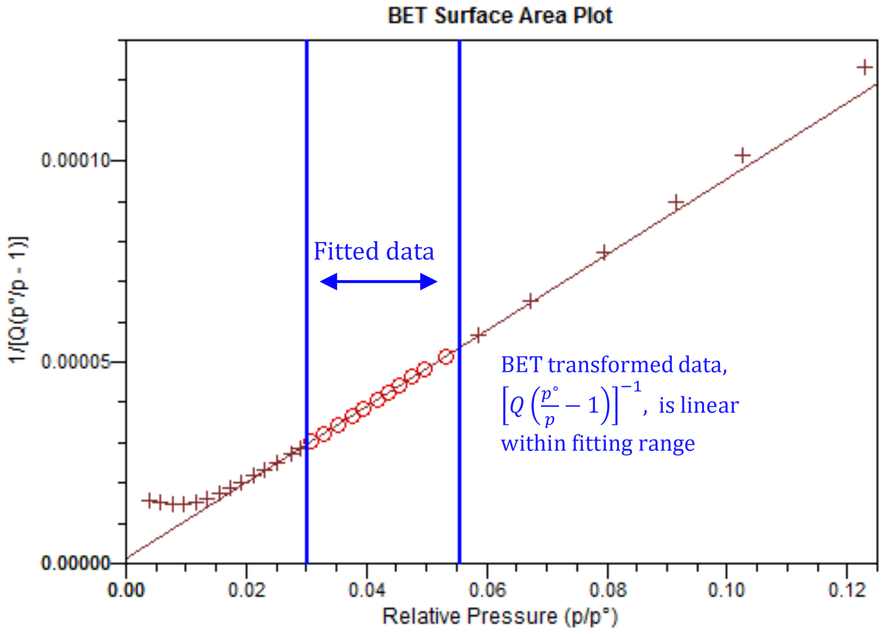

Fitted data

BET transformed data, $\left[Q\left(\frac{p^\circ}{p}-1\right)\right]^{-1}$, is linear within fitting range

Summary

BET surface area: 4608.0814 ± 9.4727 m²/g
Slope: 0.000943 ± 0.000002 g/cm³ STP
Y-intercept: 0.000001 ± 0.000000 g/cm³ STP
C: 737.995824
Qm: 1,058.7016 cm³/g STP
Correlation coefficient: 0.9999810
Molecular cross-sectional area: 0.1620 nm²

BET Fitting Range = [0.03, 0.055]

$$\left(\frac{p}{p^\circ}\right)_m = 0.0355$$

$$\frac{1}{\sqrt{C}+1} = 0.0355$$

BET Surface Area = 4608 m^2/g

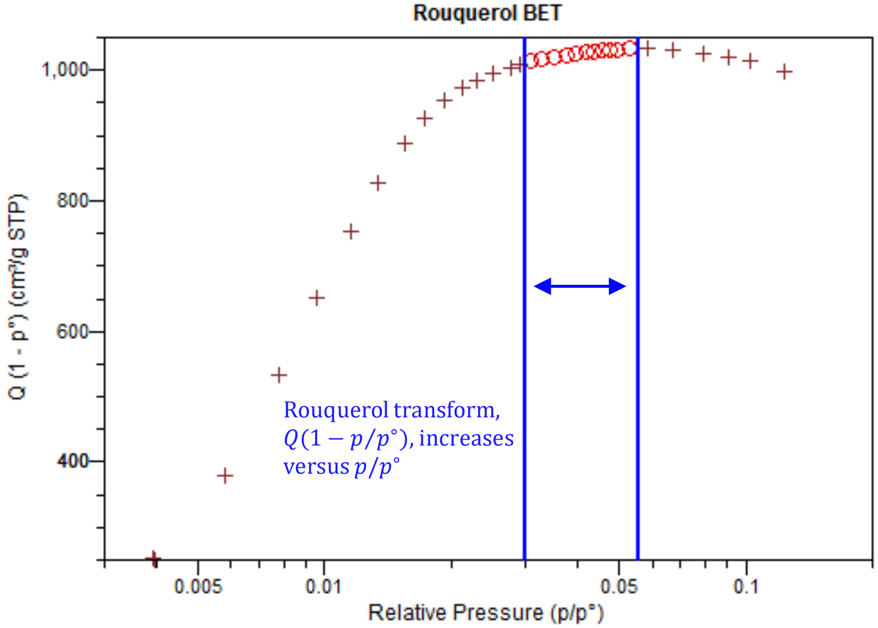

Rouquerol transform, $Q(1-p/p^\circ)$, increases versus p/p°

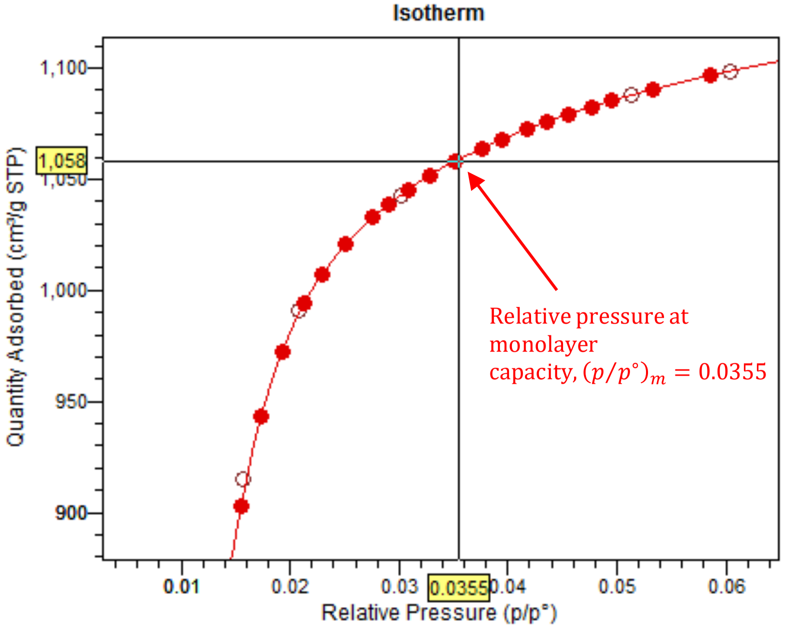

Relative pressure at monolayer capacity, $(p/p^\circ)_m = 0.0355$

BET Surface Area Analysis

DUT-23 (Co)

DUT-23 (Co) Nitrogen Isotherm at 77 K

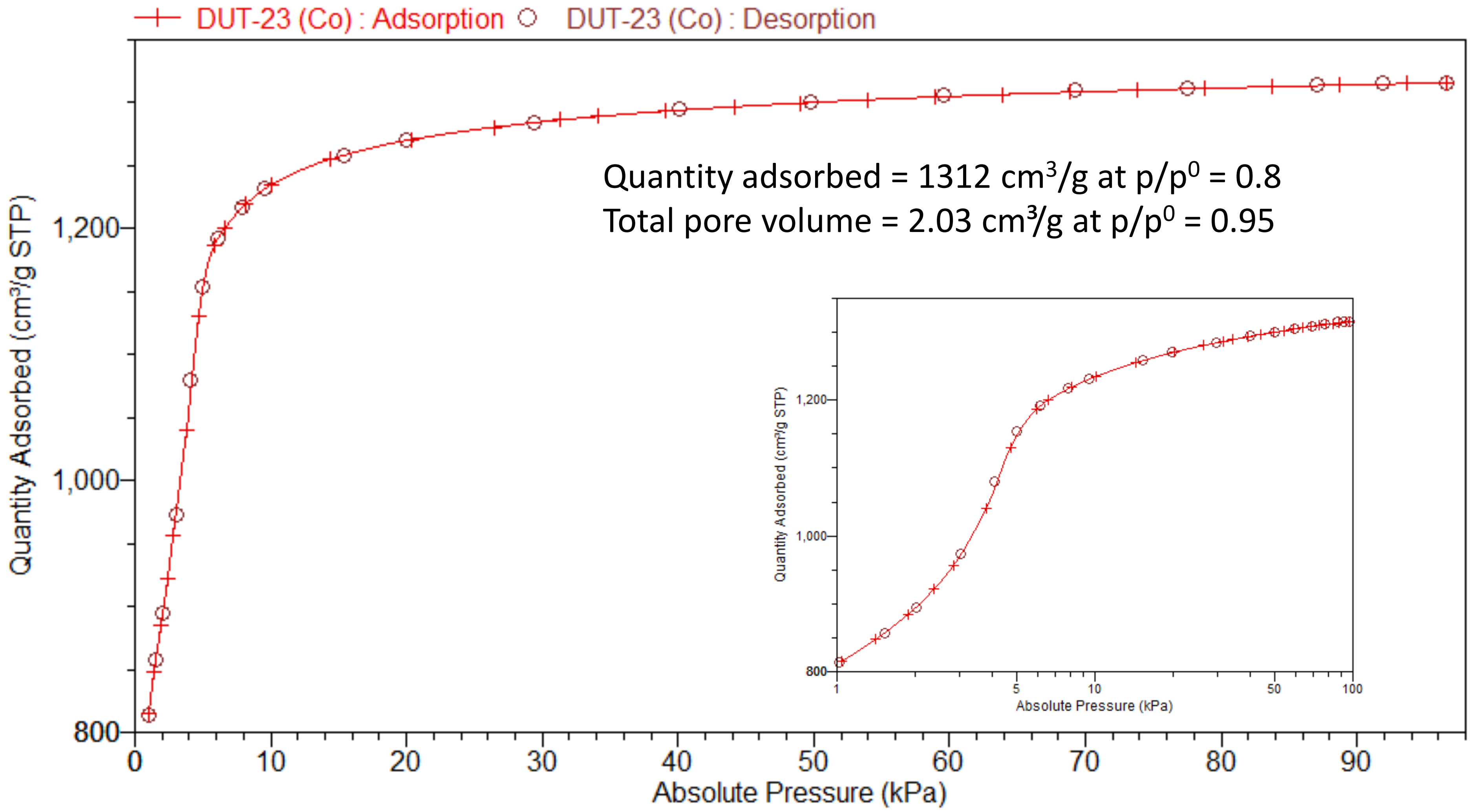

Quantity adsorbed = 1312 cm^3/g at $p/p^0 = 0.8$

Total pore volume = 2.03 cm^3/g at $p/p^0 = 0.95$

Nitrogen Adsorption Isotherm

DUT-23 (Co)

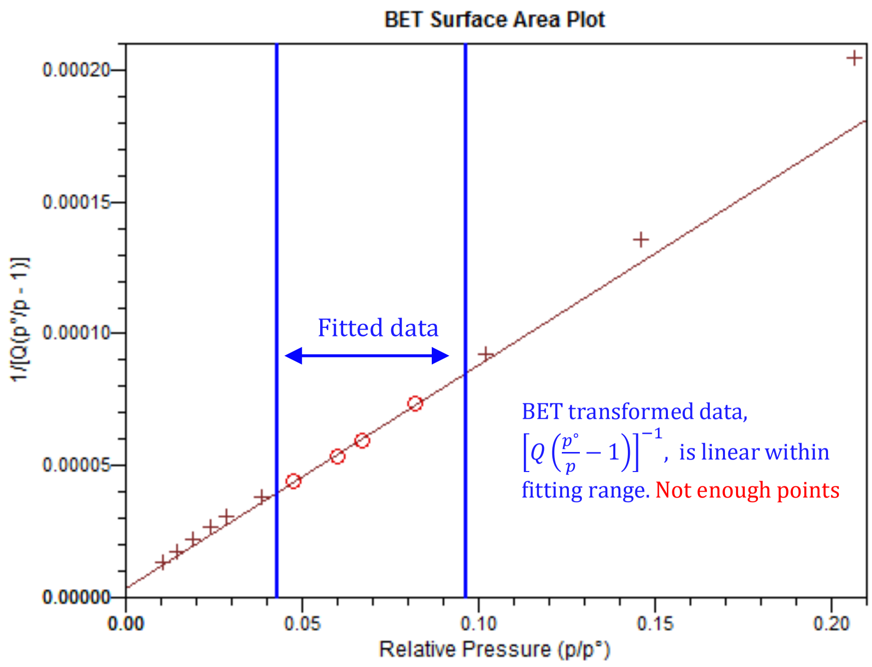

Fitted data

BET transformed data, $\left[Q\left(\frac{p^\circ}{p}-1\right)\right]^{-1}$, is linear within fitting range. Not enough points

Summary

BET surface area: 5117.1001 ± 143.6173 m²/g
Slope: 0.000847 ± 0.000024 g/cm³ STP
Y-intercept: 0.000003 ± 0.000002 g/cm³ STP
C: 248.707466
Qm: 1,175.6480 cm³/g STP
Correlation coefficient: 0.9992102
Molecular cross-sectional area: 0.1620 nm²

BET Fitting Range = [0.01, 0.1]

$$\left(\frac{p}{p^\circ}\right)_m = 0.056$$

$$\frac{1}{\sqrt{C}+1} = 0.059$$

BET Surface Area = 5117 m^2/g

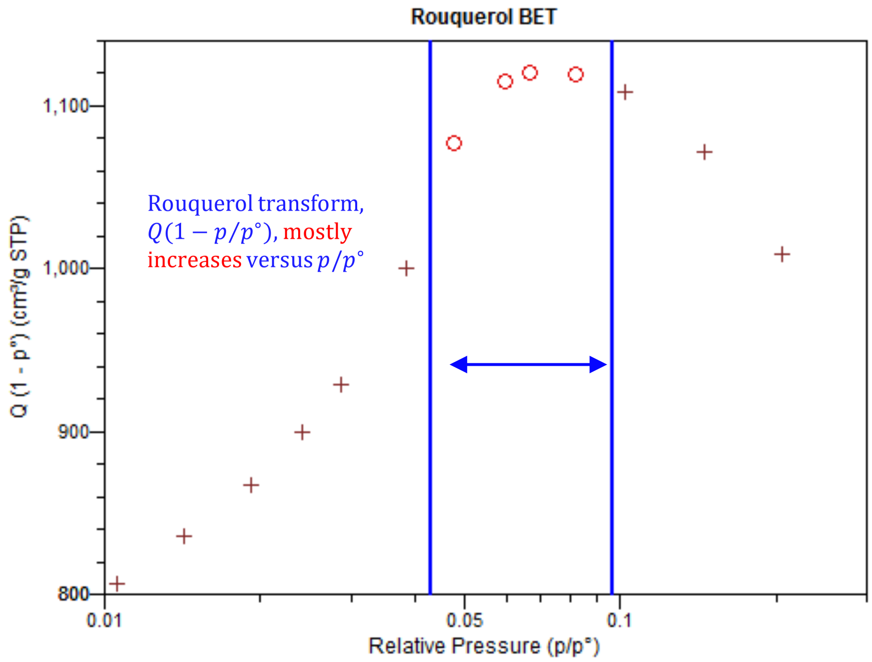

Rouquerol transform, $Q(1-p/p^\circ)$, mostly increases versus p/p°

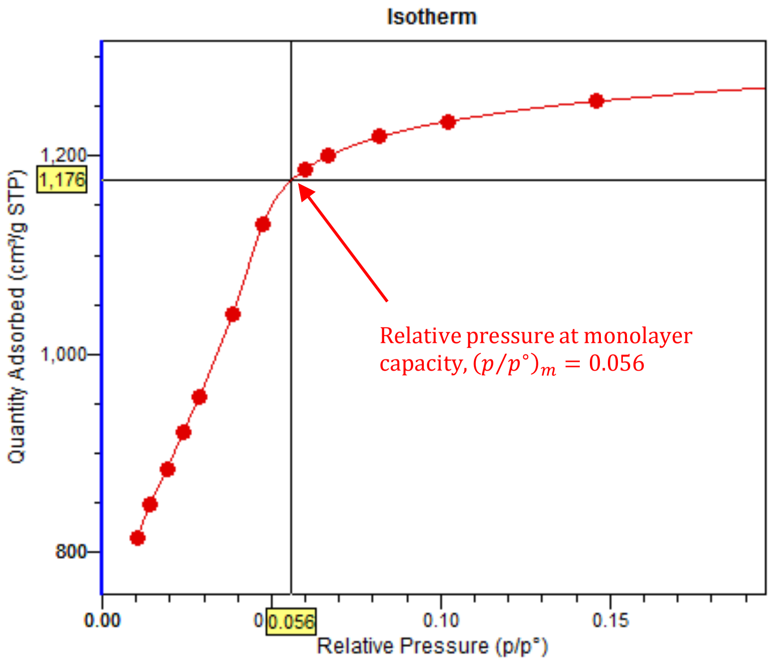

Relative pressure at monolayer capacity, $(p/p^\circ)_m = 0.056$

BET Surface Area Analysis

MSC-30 (Maxsorb)

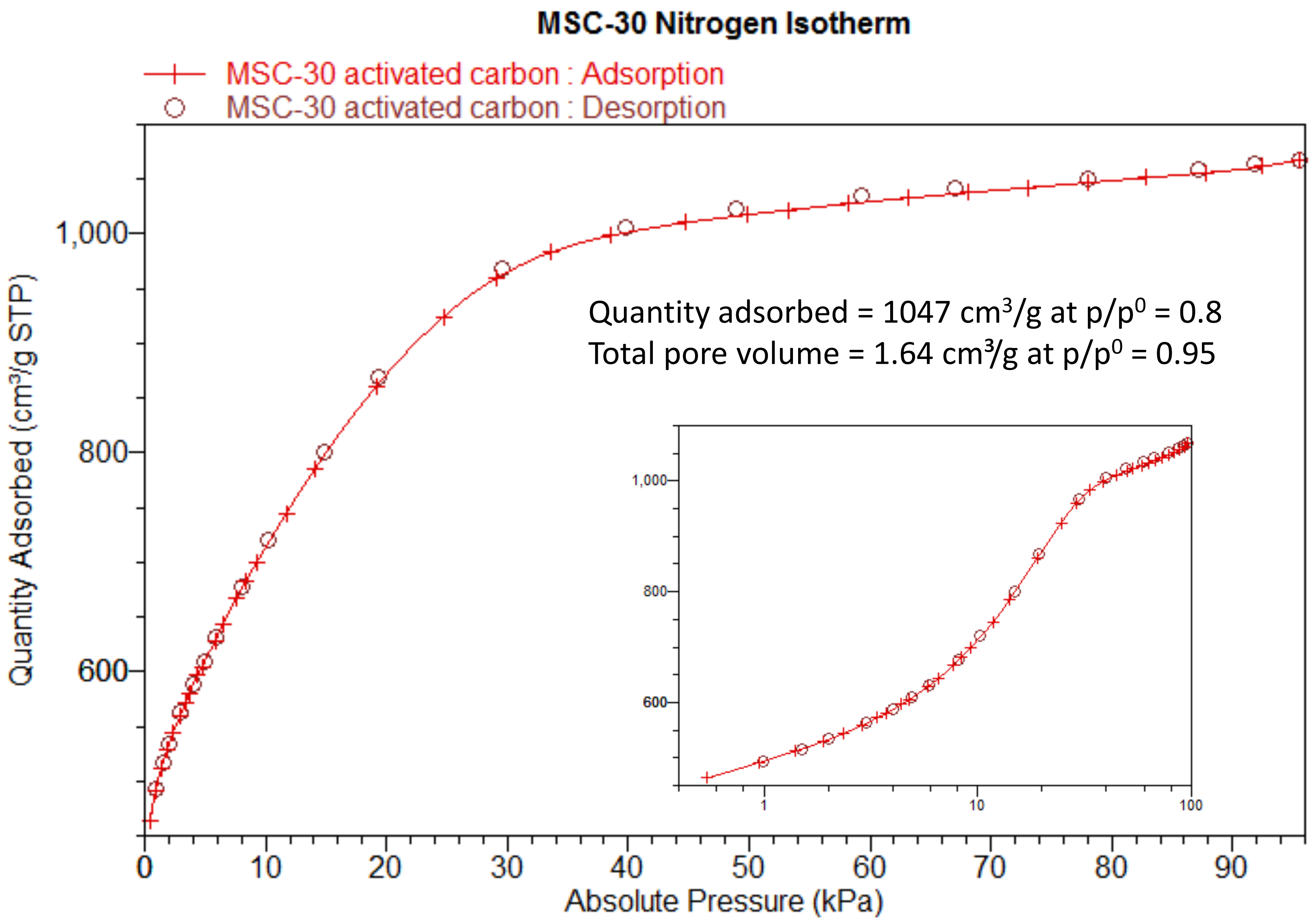

Quantity adsorbed = 1047 cm^3/g at p/p^0 = 0.8
Total pore volume = 1.64 cm^3/g at p/p^0 = 0.95

Nitrogen Adsorption Isotherm

MSC-30 (Maxsorb)

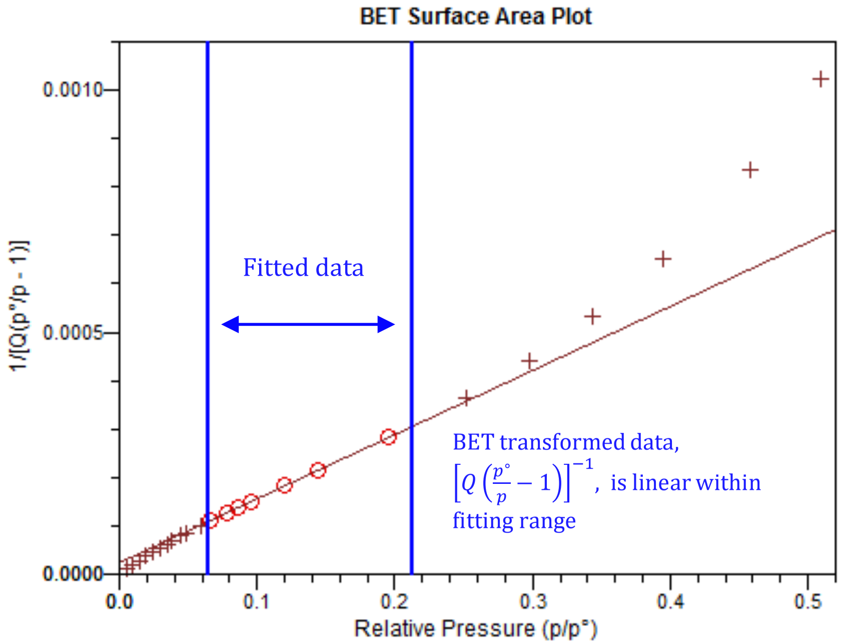

Fitted data

BET transformed data, $\left[Q\left(\frac{p^\circ}{p}-1\right)\right]^{-1}$, is linear within fitting range

Summary

BET surface area:	3228.7801 ± 13.1244 m²/g
Slope:	0.001324 ± 0.000005 g/cm³ STP
Y-intercept:	0.000024 ± 0.000001 g/cm³ STP
C:	56.925626
Qm:	741.8086 cm³/g STP
Correlation coefficient:	0.9999578
Molecular cross-sectional area:	0.1620 nm²

BET Fitting Range = [0.08, 0.2]

$$\left(\frac{p}{p^\circ}\right)_m = 0.117$$

$$\frac{1}{\sqrt{C}+1} = 0.117$$

BET Surface Area = 3229 m^2/g

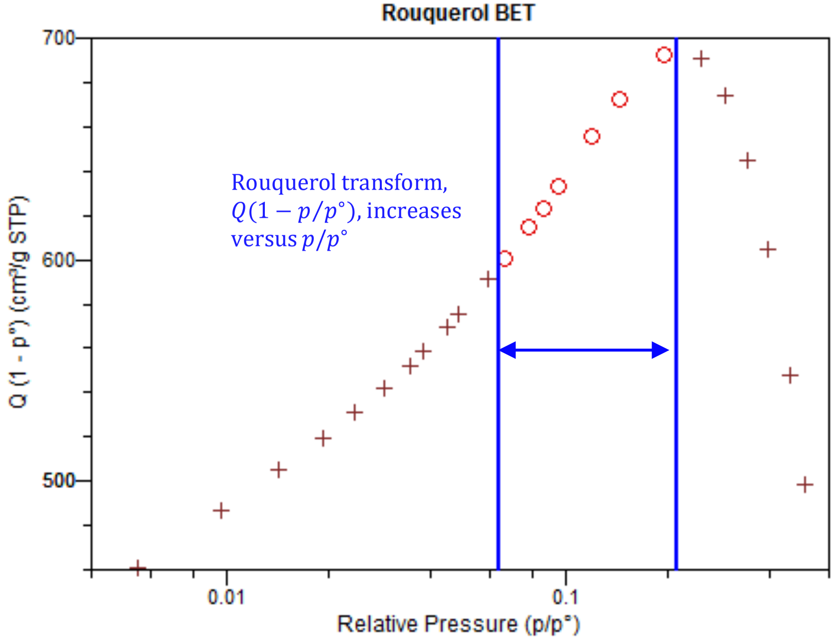

Rouquerol transform, $Q(1-p/p^\circ)$, increases versus p/p°

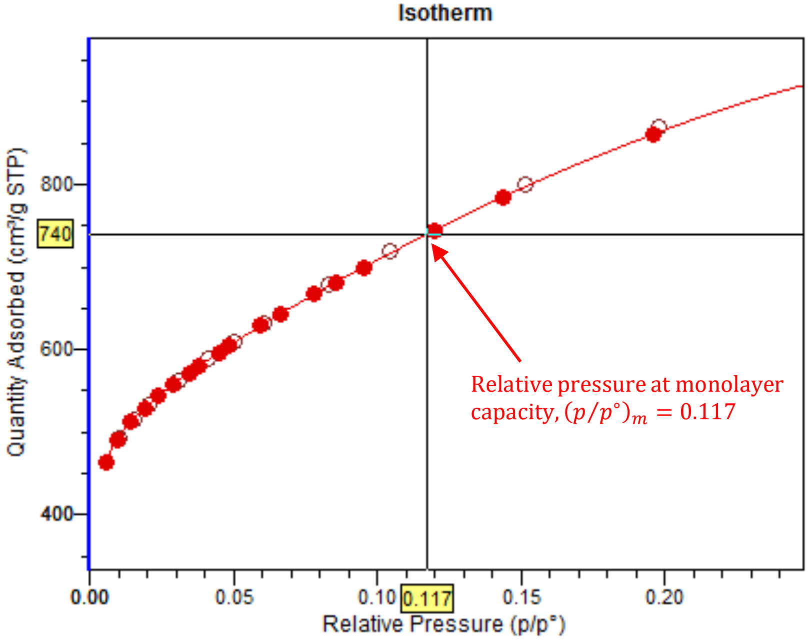

Relative pressure at monolayer capacity, $(p/p^\circ)_m = 0.117$

ZIF-8 (Basolite Z1200)

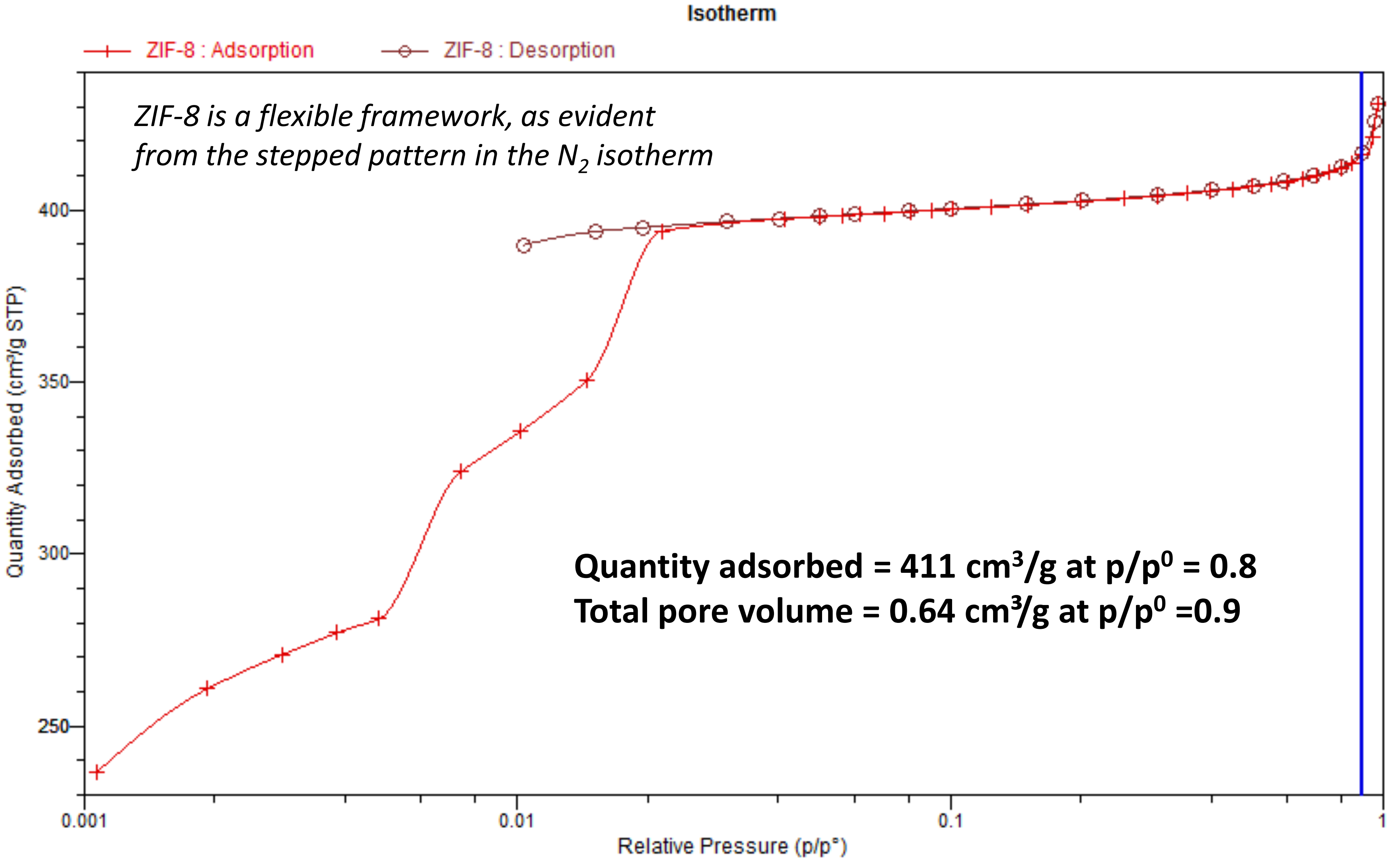

ZIF-8 is a flexible framework, as evident from the stepped pattern in the N_2 isotherm

Quantity adsorbed = 411 cm^3/g at p/p^0 = 0.8
Total pore volume = 0.64 cm^3/g at p/p^0 =0.9

Nitrogen Adsorption Isotherm

ZIF-8 (Basolite Z1200)

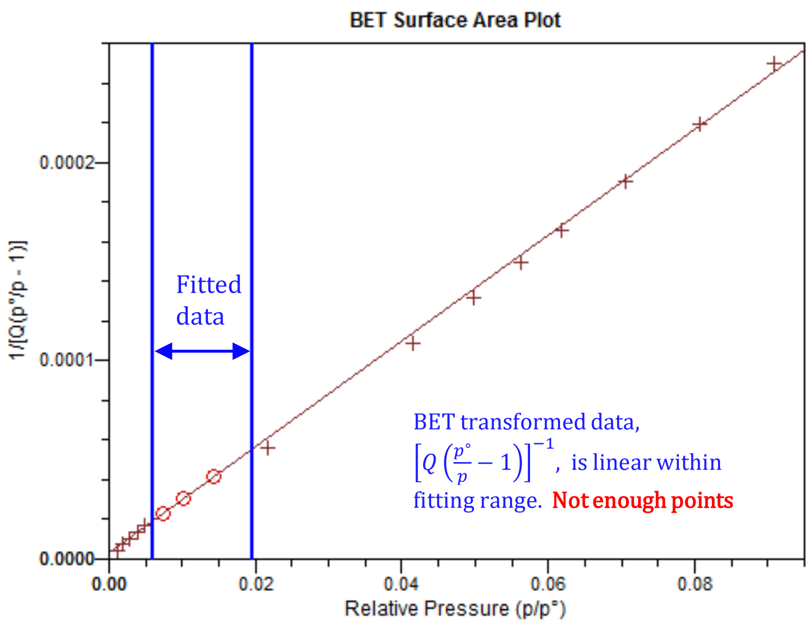

Fitted data

BET transformed data, $\left[Q\left(\frac{p^\circ}{p}-1\right)\right]^{-1}$, is linear within fitting range. Not enough points

Summary

BET surface area: 1630.8710 ± 20.3805 m²/g
Slope: 0.002665 ± 0.000033 g/cm³ STP
Y-intercept: 0.000003 ± 0.000000 g/cm³ STP
C: 790.892255
Qm: 374.6908 cm³/g STP
Correlation coefficient: 0.9999217
Molecular cross-sectional area: 0.1620 nm²

BET Fitting Range = [0.008, 0.02]

$$\left(\frac{p}{p^\circ}\right)_m = 0.0179$$

$$\frac{1}{\sqrt{C}+1} = 0.034$$

BET Surface Area = 1631 m^2/g

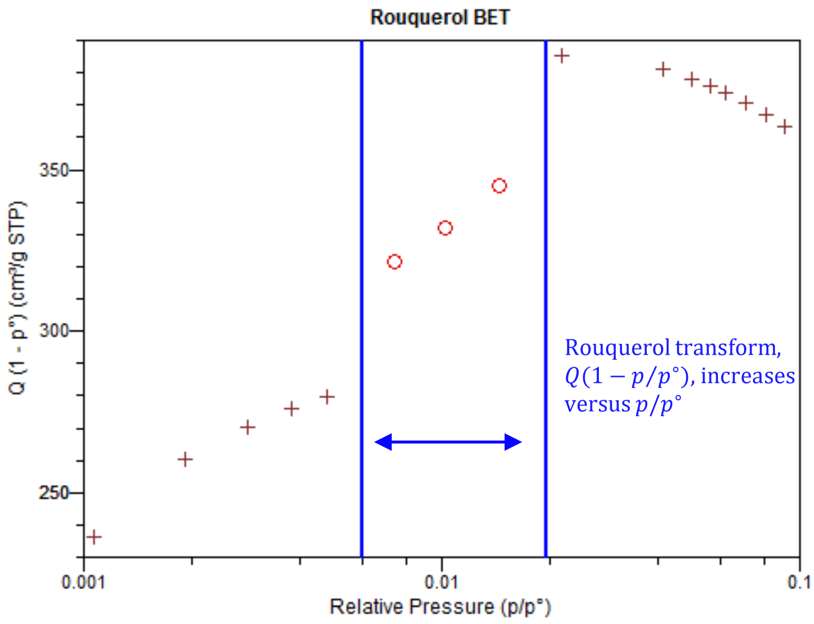

Rouquerol transform, $Q(1-p/p^\circ)$, increases versus p/p°

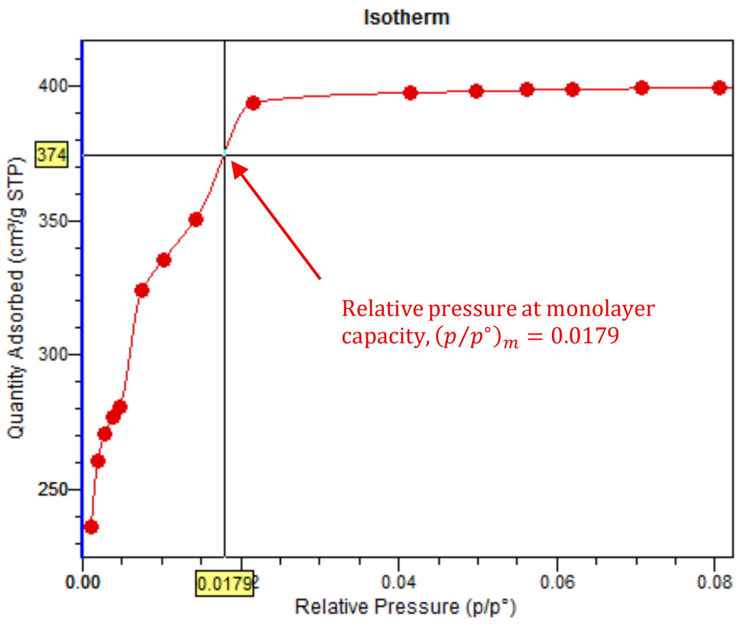

Relative pressure at monolayer capacity, $(p/p^\circ)_m = 0.0179$

BET Surface Area Analysis

Ni-MOF-74

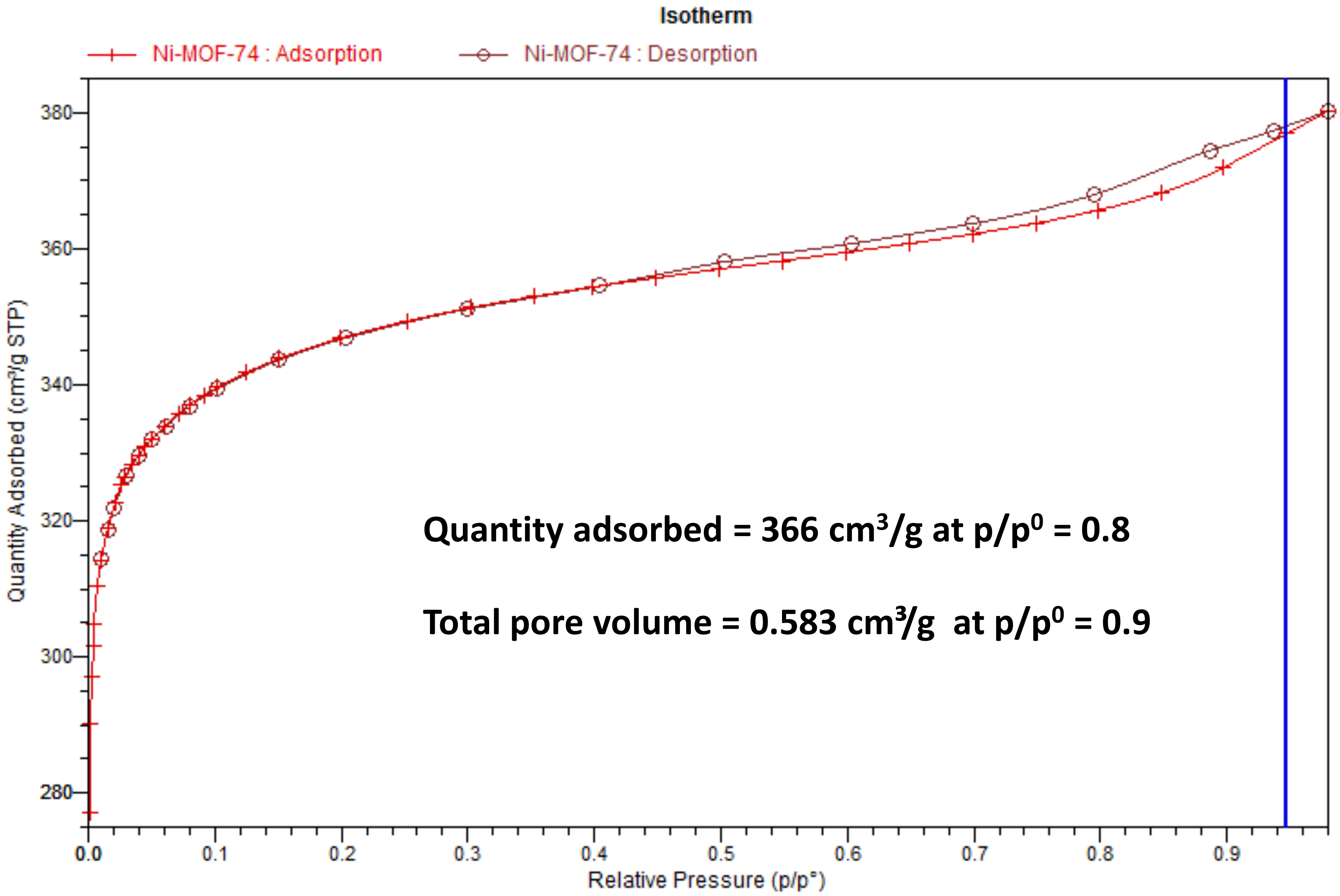

Quantity adsorbed = 366 cm^3/g at $p/p^0 = 0.8$

Total pore volume = 0.583 cm^3/g at $p/p^0 = 0.9$

Nitrogen Adsorption Isotherm

Ni-MOF-74

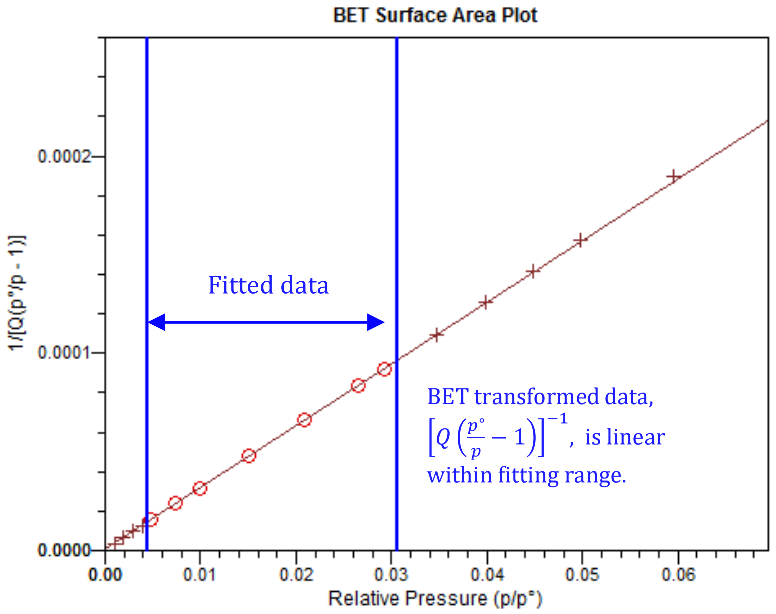

Fitted data

BET transformed data, $\left[Q\left(\frac{p^\circ}{p}-1\right)\right]^{-1}$, is linear within fitting range.

Summary
BET surface area: 1391.7811 ± 0.6455 m²/g
Slope: 0.003126 ± 0.000001 g/cm³ STP
Y-intercept: 0.000001 ± 0.000000 g/cm³ STP
C: 3691.977940
Qm: 319.7602 cm³/g STP
Correlation coefficient: 0.9999995
Molecular cross-sectional area: 0.1620 nm²

BET Fitting Range = [0.003, 0.025]

$$\left(\frac{p}{p^\circ}\right)_m = 0.015$$

$$\frac{1}{\sqrt{C}+1} = 0.016$$

BET Surface Area = 1392 m^2/g

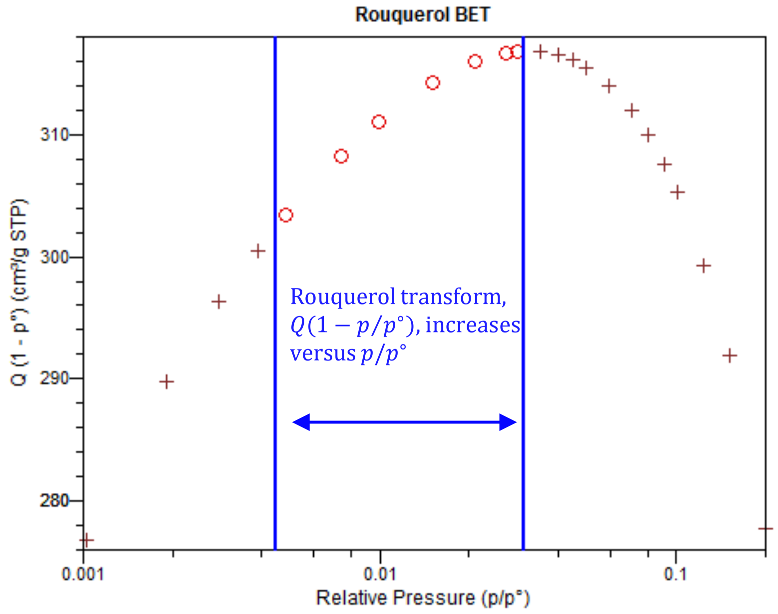

Rouquerol transform, $Q(1-p/p^\circ)$, increases versus p/p°

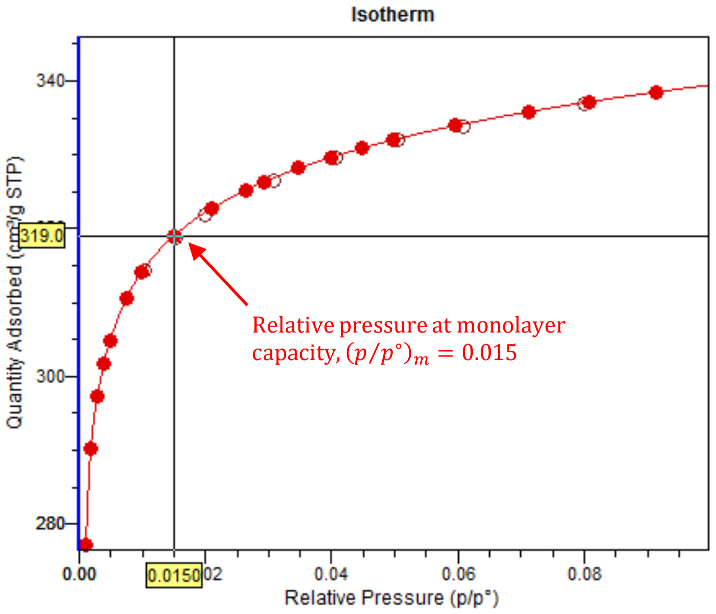

Relative pressure at monolayer capacity, $(p/p^\circ)_m = 0.015$

BET Surface Area Analysis

DUT-23 (Cu)

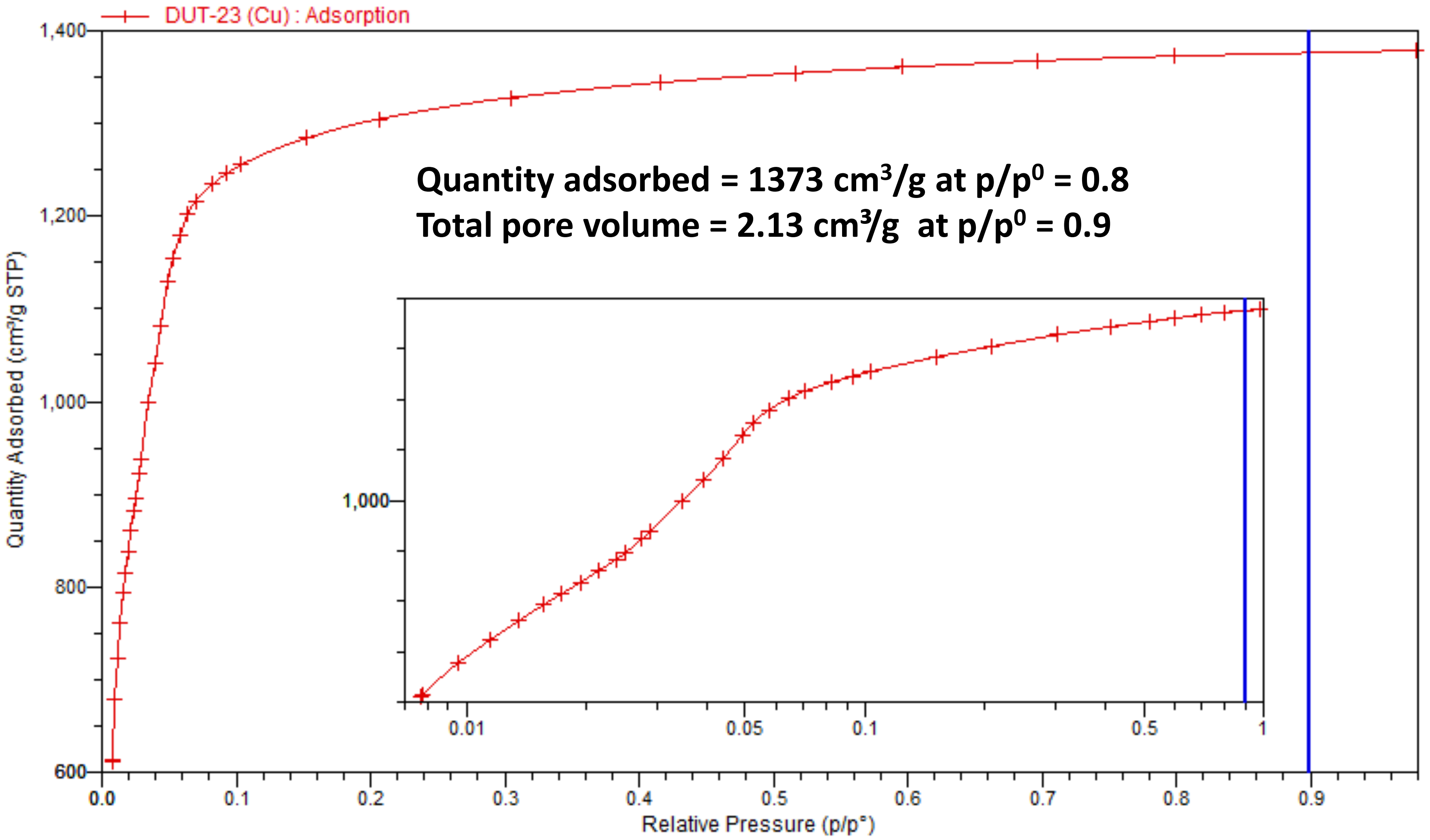

Quantity adsorbed = 1373 cm^3/g at p/p^0 = 0.8

Total pore volume = 2.13 cm^3/g at p/p^0 = 0.9

Nitrogen Adsorption Isotherm

DUT-23 (Cu)

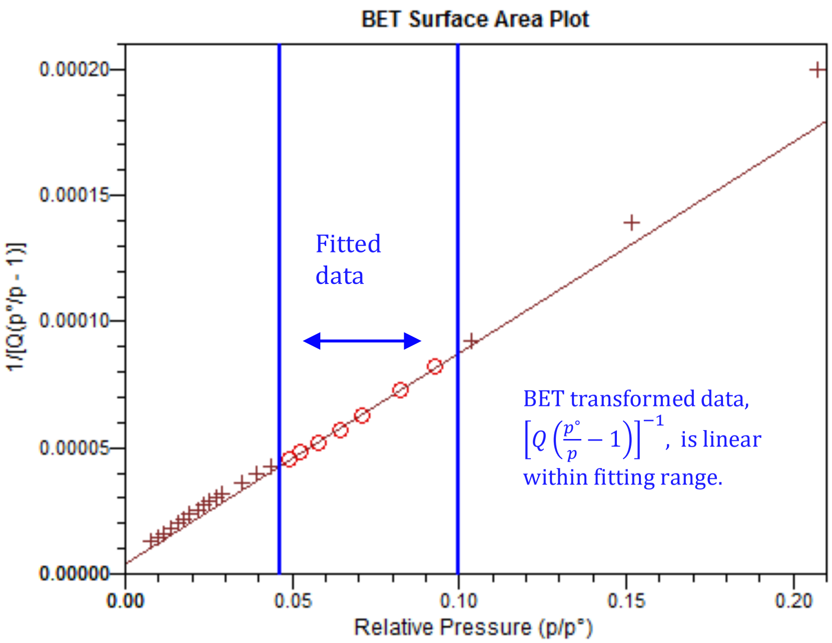

Fitted data

BET transformed data, $\left[Q\left(\frac{p^\circ}{p}-1\right)\right]^{-1}$, is linear within fitting range.

Summary

BET surface area: 5181.5452 ± 88.4866 m²/g
Slope: 0.000836 ± 0.000014 g/cm³ STP
Y-intercept: 0.000004 ± 0.000001 g/cm³ STP
C: 211.961190
Qm: 1,190.4542 cm³/g STP
Correlation coefficient: 0.9992683
Molecular cross-sectional area: 0.1620 nm²

BET Fitting Range = [0.047, 0.1]

$$\left(\frac{p}{p^\circ}\right)_m = 0.061$$

$$\frac{1}{\sqrt{C}+1} = 0.064$$

BET Surface Area = 5182 m^2/g

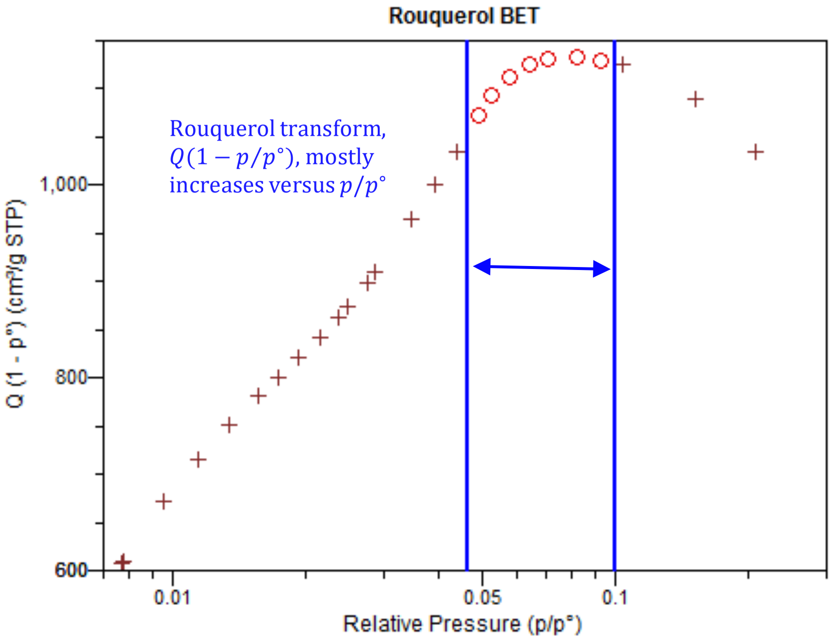

Rouquerol transform, $Q(1-p/p^\circ)$, mostly increases versus p/p°

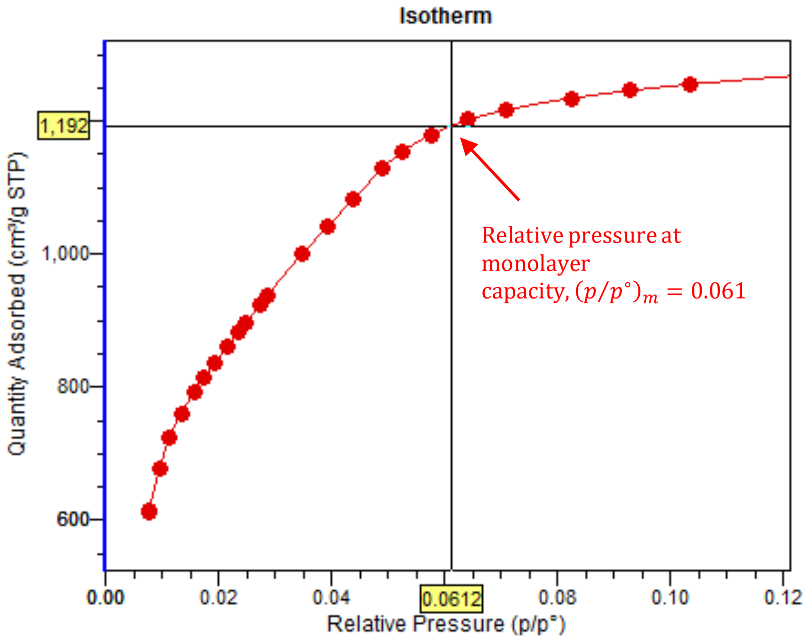

Relative pressure at monolayer capacity, $(p/p^\circ)_m = 0.061$

BET Surface Area Analysis

UMCM-1

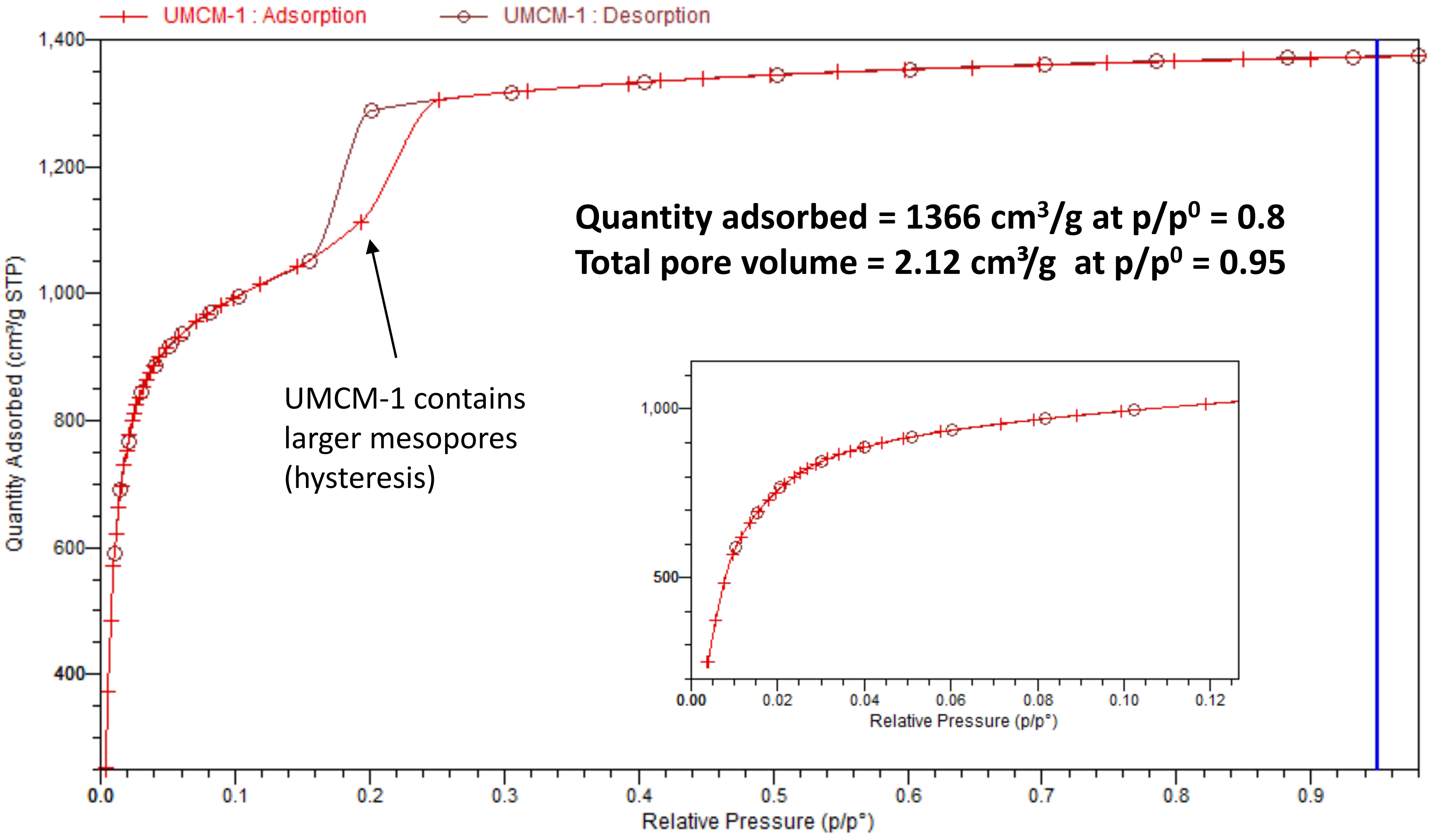

Quantity adsorbed = 1366 cm^3/g at p/p^0 = 0.8
Total pore volume = 2.12 cm^3/g at p/p^0 = 0.95

UMCM-1 contains
larger mesopores
(hysteresis)

Nitrogen Adsorption Isotherm

UMCM-1

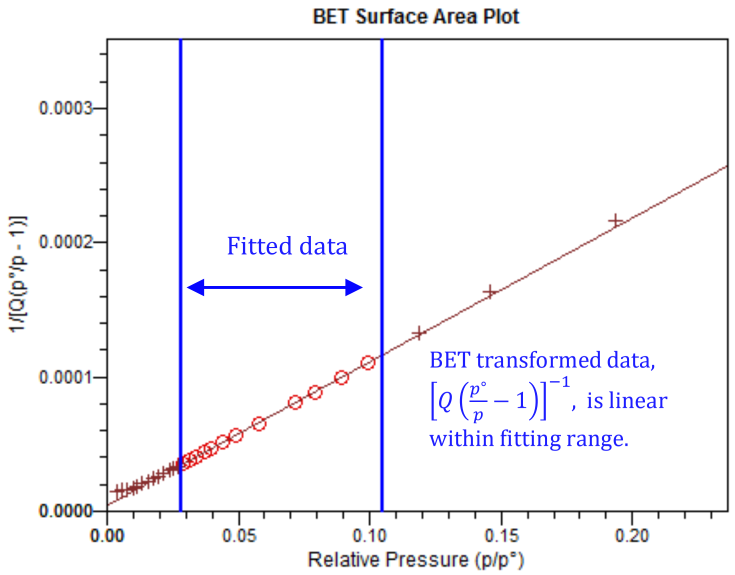

Fitted data

BET transformed data, $\left[Q\left(\frac{p^\circ}{p}-1\right)\right]^{-1}$, is linear within fitting range.

Summary
BET surface area: 4048.0325 ± 12.1646 m²/g
Slope: 0.001071 ± 0.000003 g/cm³ STP
Y-intercept: 0.000004 ± 0.000000 g/cm³ STP
C: 255.913051
Qm: 930.0310 cm³/g STP
Correlation coefficient: 0.9999547
Molecular cross-sectional area: 0.1620 nm²

BET Fitting Range = [0.025, 0.1]

$$\left(\frac{p}{p^\circ}\right)_m = 0.057$$

$$\frac{1}{\sqrt{C}+1} = 0.062$$

$$\boxed{\text{BET Surface Area} = 4048\ \mathrm{m}^2/\mathrm{g}}$$

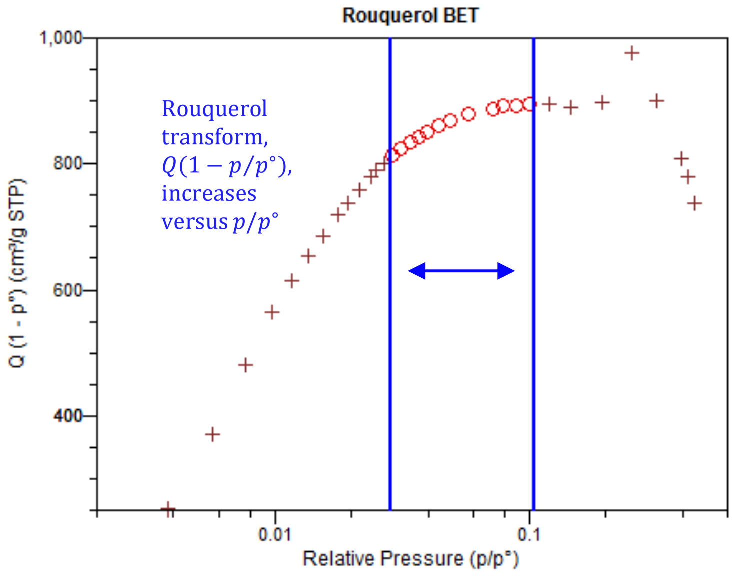

Rouquerol transform, $Q(1-p/p^\circ)$, increases versus p/p°

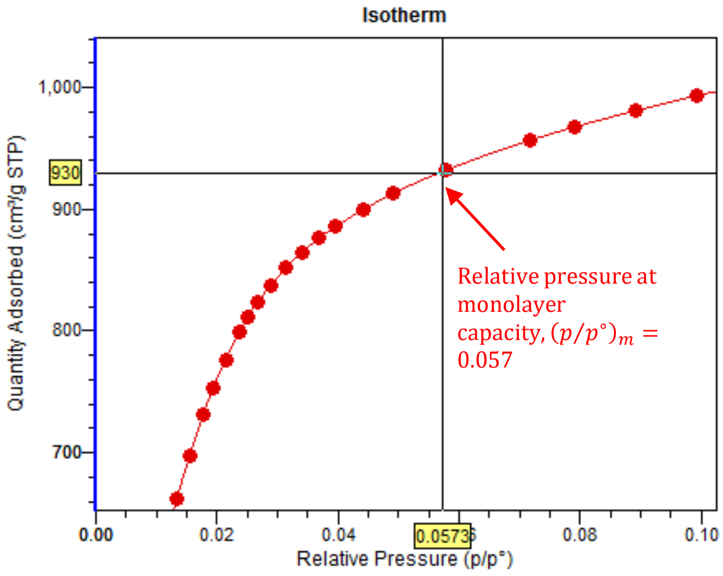

Relative pressure at monolayer capacity, $(p/p^\circ)_m$ = 0.057

NH2-MOF-177

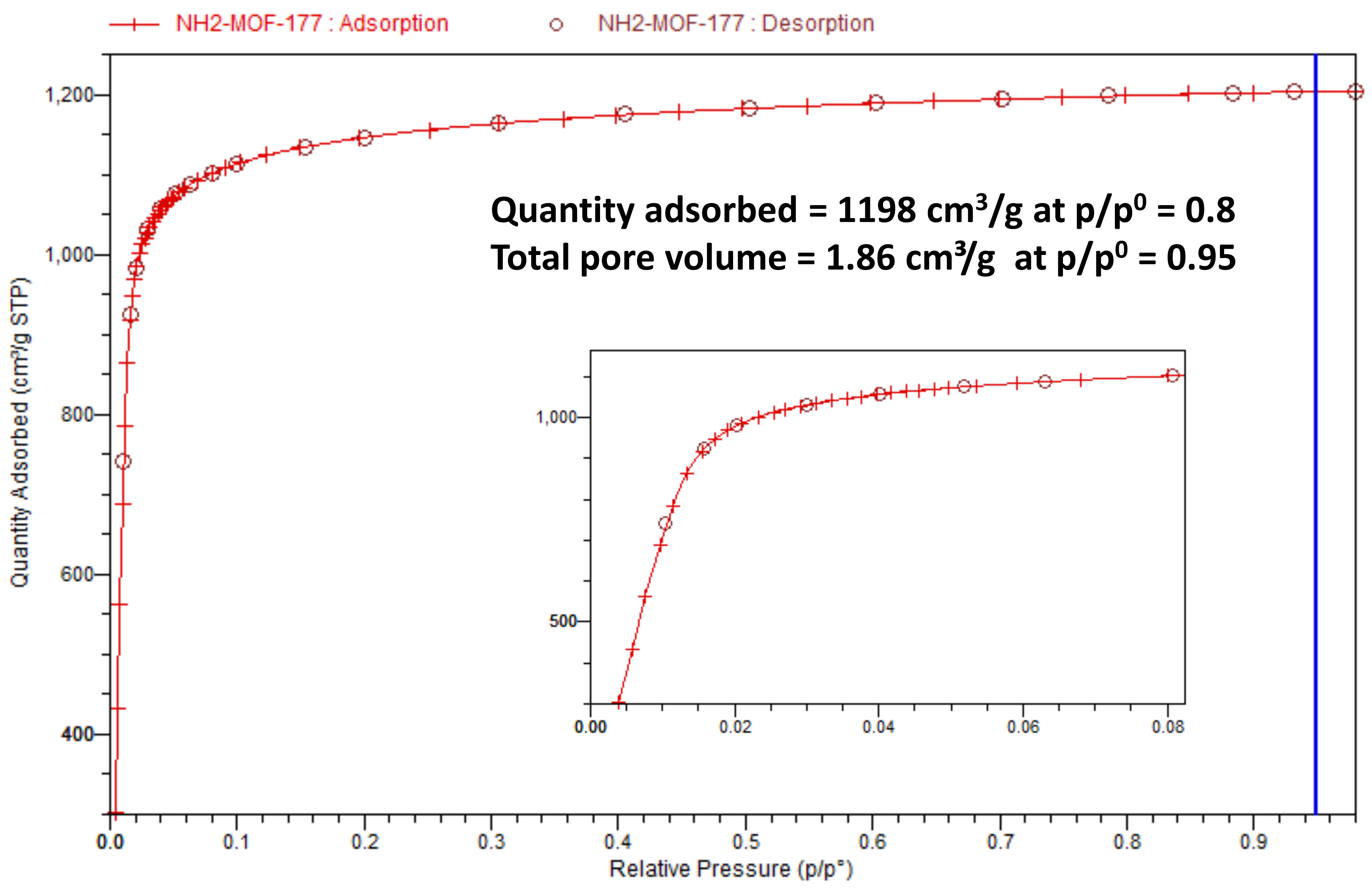

Quantity adsorbed = 1198 cm^3/g at p/p^0 = 0.8

Total pore volume = 1.86 cm^3/g at p/p^0 = 0.95

Nitrogen Adsorption Isotherm

NH2-MOF-177

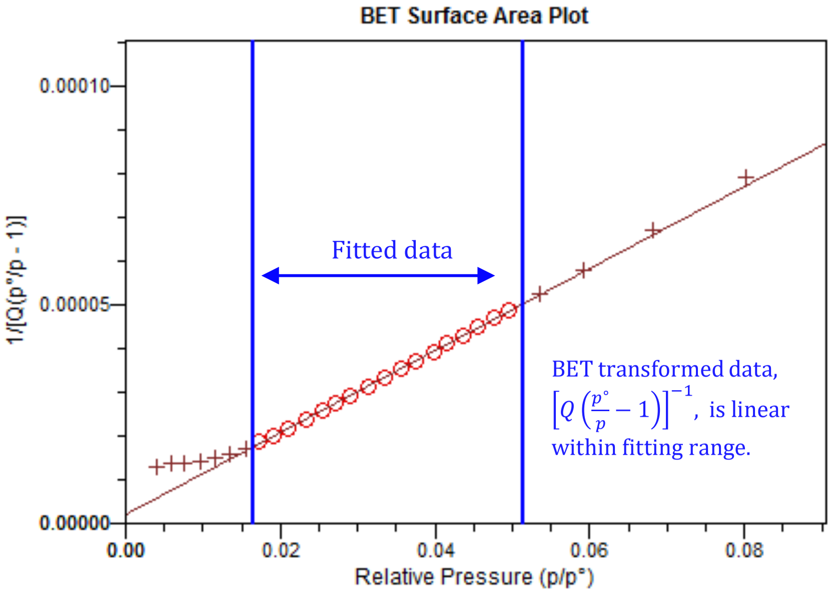

Fitted data

BET transformed data, $\left[Q\left(\frac{p^\circ}{p}-1\right)\right]^{-1}$, is linear within fitting range.

Summary

BET surface area: 4639.1474 ± 16.6317 m²/g
Slope: 0.000936 ± 0.000003 g/cm³ STP
Y-intercept: 0.000002 ± 0.000000 g/cm³ STP
C: 455.875098
Qm: 1,065.8389 cm³/g STP
Correlation coefficient: 0.9999033
Molecular cross-sectional area: 0.1620 nm²

BET Fitting Range = [0.017, 0.05]

$$\left(\frac{p}{p^\circ}\right)_m = 0.045$$

$$\frac{1}{\sqrt{C}+1} = 0.045$$

BET Surface Area = 4639 m^2/g

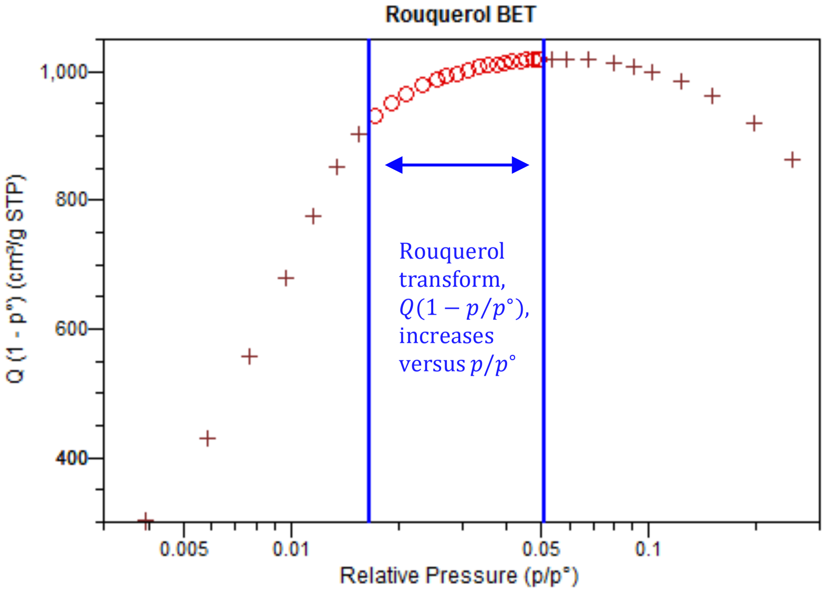

Rouquerol transform, $Q(1-p/p^\circ)$, increases versus p/p°

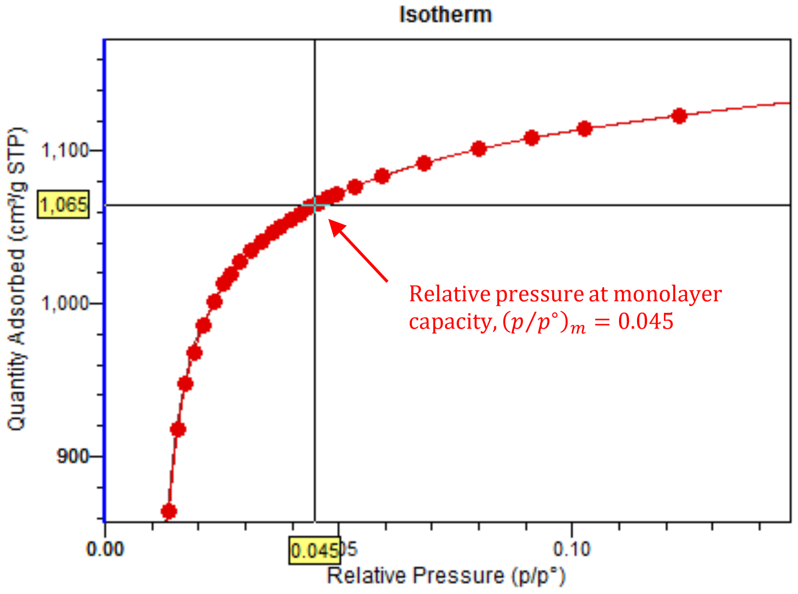

Relative pressure at monolayer capacity, $(p/p^\circ)_m = 0.045$

BET Surface Area Analysis

SNU-70

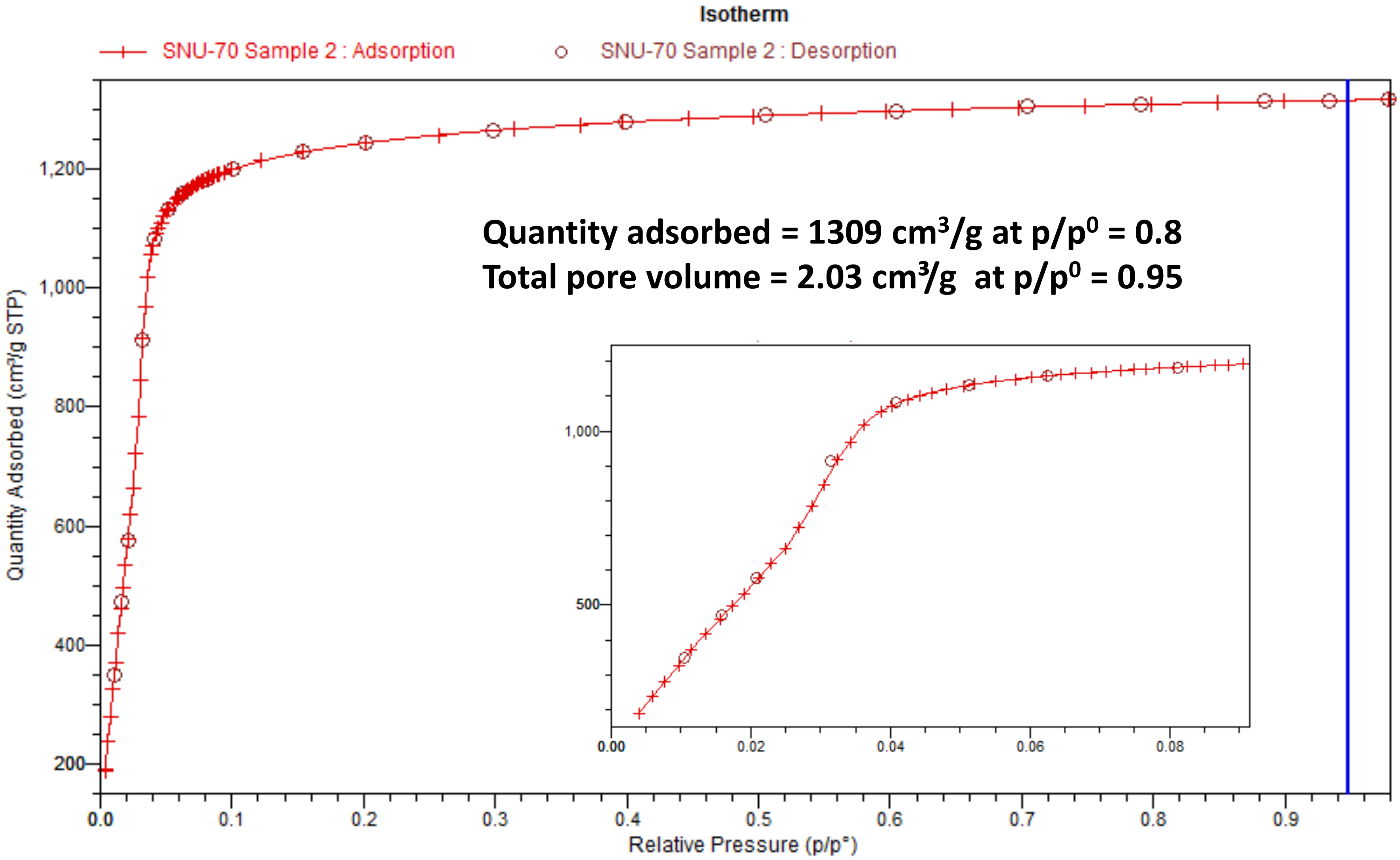

Quantity adsorbed = 1309 cm^3/g at $p/p^0 = 0.8$

Total pore volume = 2.03 cm^3/g at $p/p^0 = 0.95$

Nitrogen Adsorption Isotherm

SNU-70

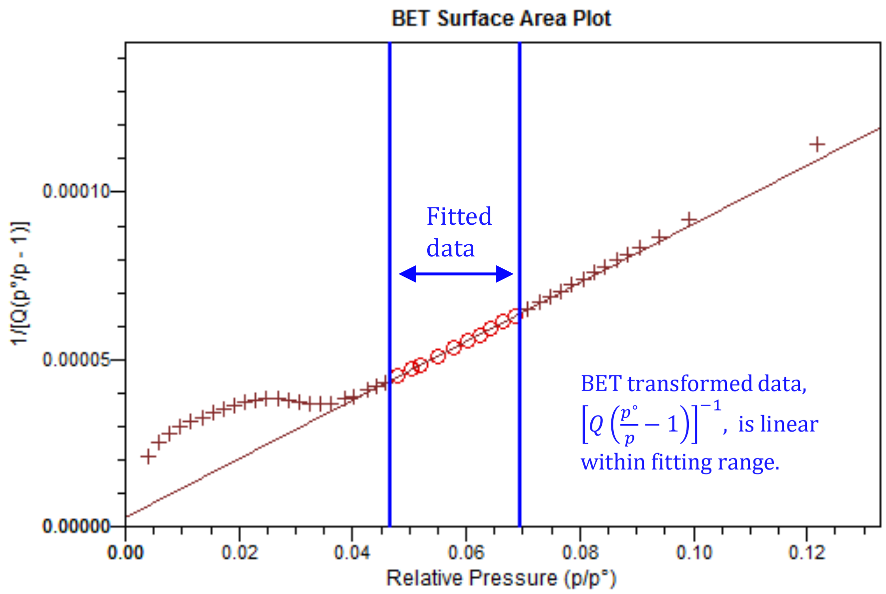

Fitted data

BET transformed data, $\left[Q\left(\frac{p^\circ}{p}-1\right)\right]^{-1}$, is linear within fitting range.

Summary

BET surface area:	4944.4237 ± 21.0064 m²/g
Slope:	0.000878 ± 0.000004 g/cm³ STP
Y-intercept:	0.000003 ± 0.000000 g/cm³ STP
C:	319.183117
Qm:	1,135.9758 cm³/g STP
Correlation coefficient:	0.9999276
Molecular cross-sectional area:	0.1620 nm²

BET Fitting Range = [0.045, 0.070]

$$\left(\frac{p}{p^\circ}\right)_m = 0.052$$

$$\frac{1}{\sqrt{C}+1} = 0.053$$

BET Surface Area = 4944 m^2/g

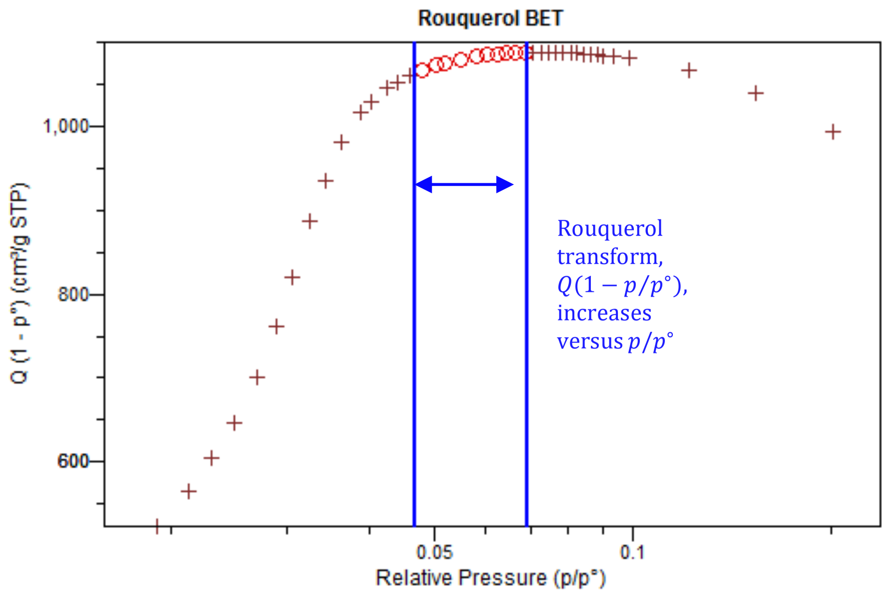

Rouquerol transform, $Q(1-p/p^\circ)$, increases versus p/p°

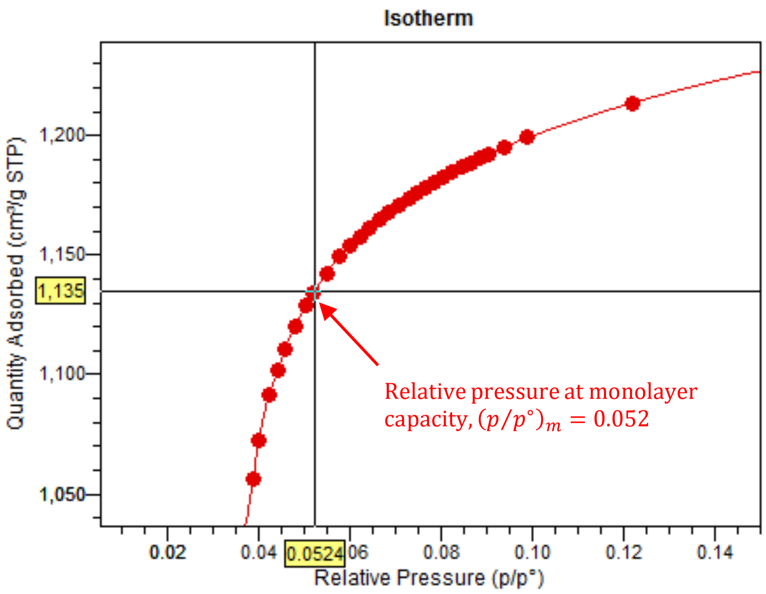

Relative pressure at monolayer capacity, $(p/p^\circ)_m = 0.052$

BET Surface Area Analysis

UMCM-9

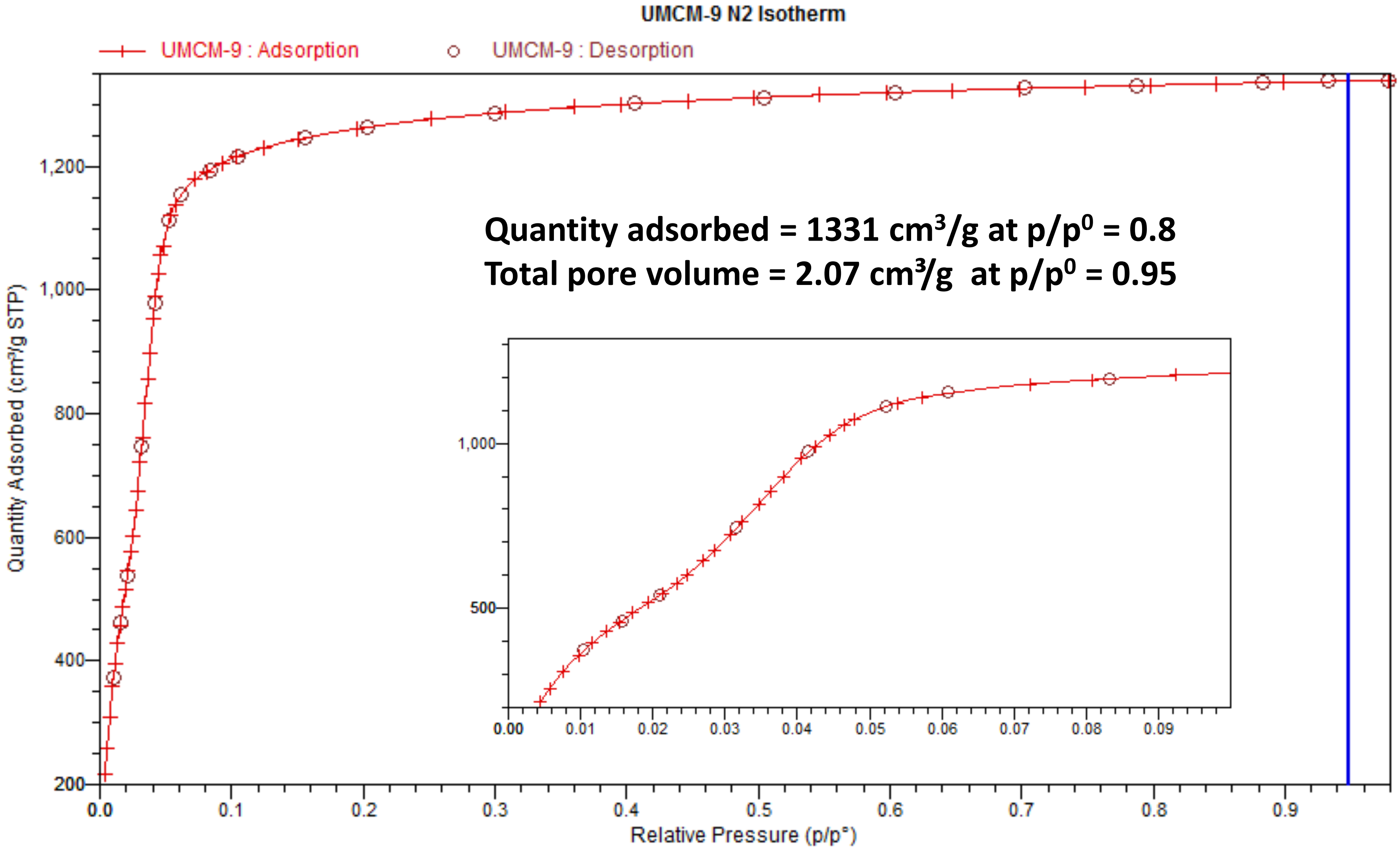

Quantity adsorbed = 1331 cm^3/g at p/p^0 = 0.8
Total pore volume = 2.07 cm^3/g at p/p^0 = 0.95

Nitrogen Adsorption Isotherm

UMCM-9

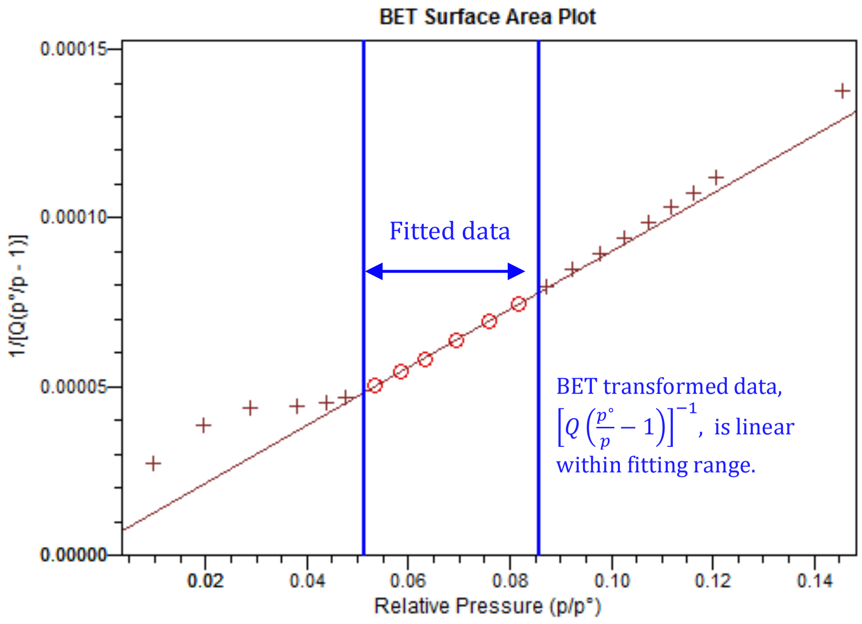

Fitted data

BET transformed data, $\left[Q\left(\frac{p^\circ}{p}-1\right)\right]^{-1}$, is linear within fitting range.

Summary

BET surface area: 5039.1737 ± 69.2001 m²/g
Slope: 0.000860 ± 0.000012 g/cm³ STP
Y-intercept: 0.000004 ± 0.000001 g/cm³ STP
C: 208.161444
Qm: 1,157.7445 cm³/g STP
Correlation coefficient: 0.9996211
Molecular cross-sectional area: 0.1620 nm²

BET Fitting Range = [0.05, 0.085]

$$\left(\frac{p}{p^\circ}\right)_m = 0.063$$

$$\frac{1}{\sqrt{C}+1} = 0.065$$

BET Surface Area = 5039 m^2/g

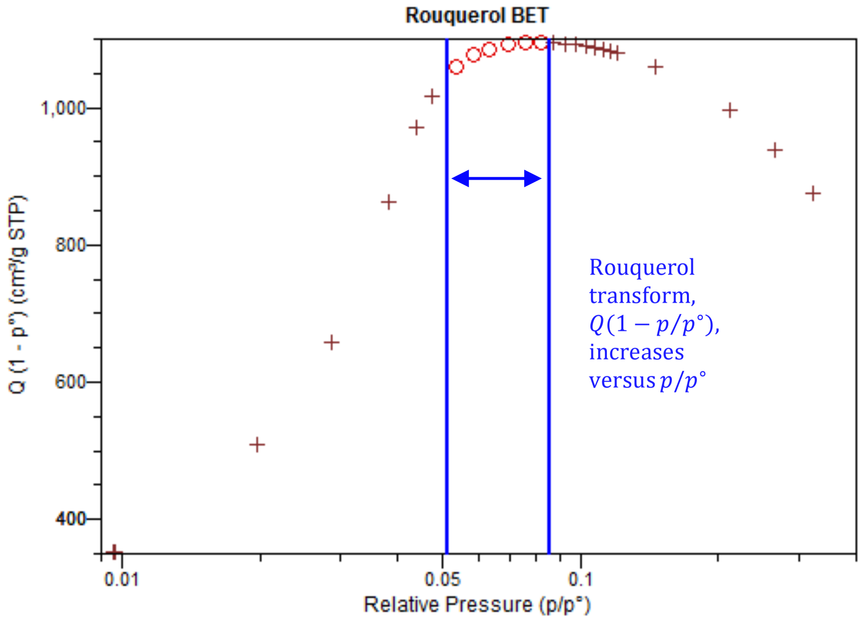

Rouquerol transform, $Q(1-p/p^\circ)$, increases versus p/p°

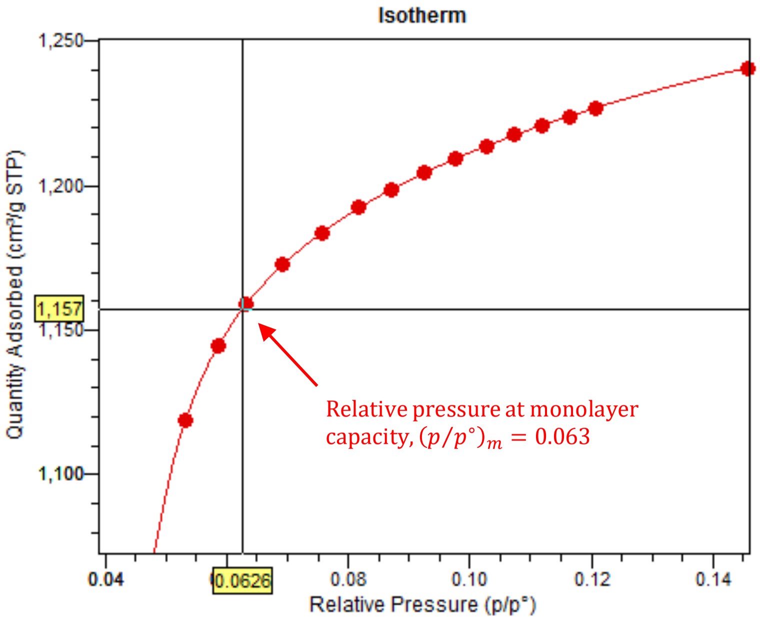

Relative pressure at monolayer capacity, $(p/p^\circ)_m = 0.063$

BET Surface Area Analysis

NU-100

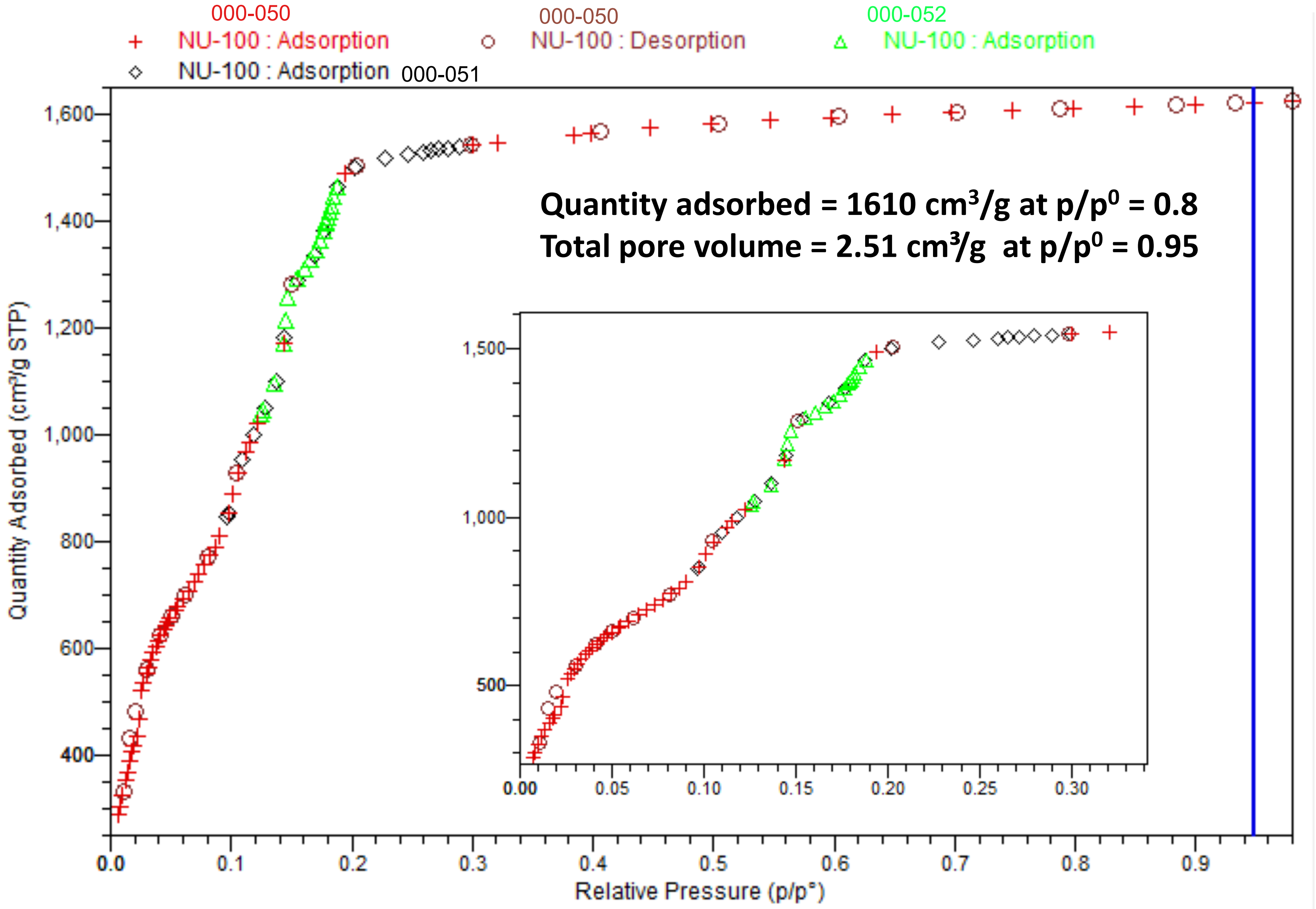

Quantity adsorbed = 1610 cm^3/g at p/p^0 = 0.8

Total pore volume = 2.51 cm^3/g at p/p^0 = 0.95

Nitrogen Adsorption Isotherm

NU-100

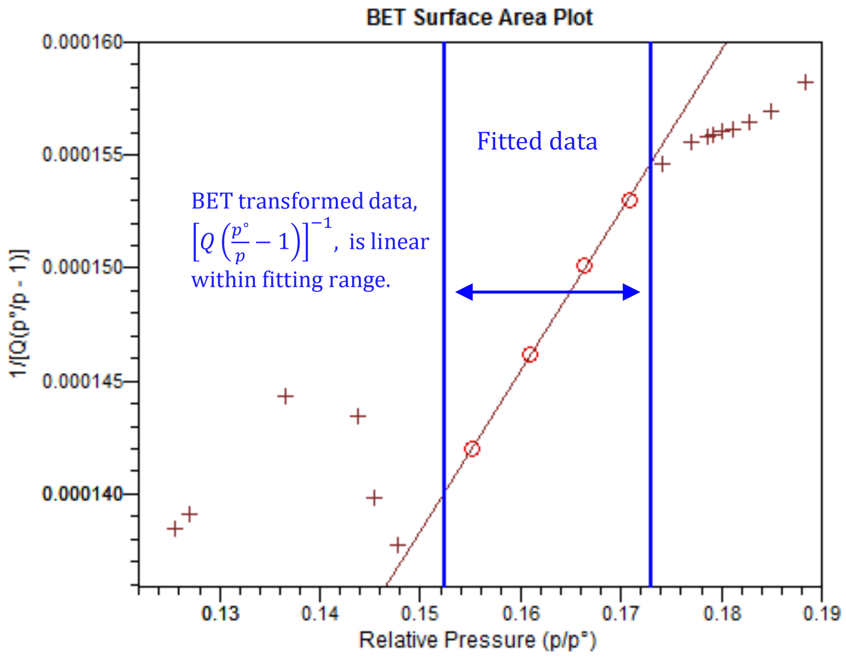

Fitted data

BET transformed data, $\left[Q\left(\frac{p^\circ}{p}-1\right)\right]^{-1}$, is linear within fitting range.

```
                                  Summary
                BET surface area: 5869.3920 ± 91.1015 m²/g
                           Slope: 0.000710 ± 0.000011 g/cm³ STP
                     Y-intercept: 0.000032 ± 0.000002 g/cm³ STP
                               C: 23.260911
                              Qm: 1,348.4863 cm³/g STP
         Correlation coefficient: 0.9997439
Molecular cross-sectional area: 0.1620 nm²
```

BET Fitting Range = [0.15, 0.173]

$$\left(\frac{p}{p^\circ}\right)_m = 0.1713$$

$$\frac{1}{\sqrt{C}+1} = 0.0.171$$

BET Surface Area = 5869 m²/g

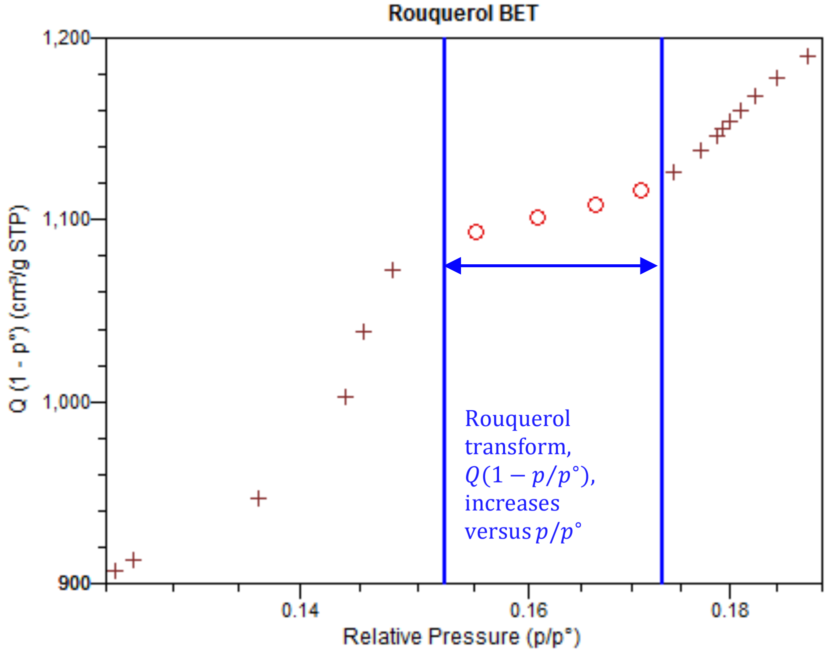

Rouquerol transform, $Q(1-p/p^\circ)$, increases versus p/p°

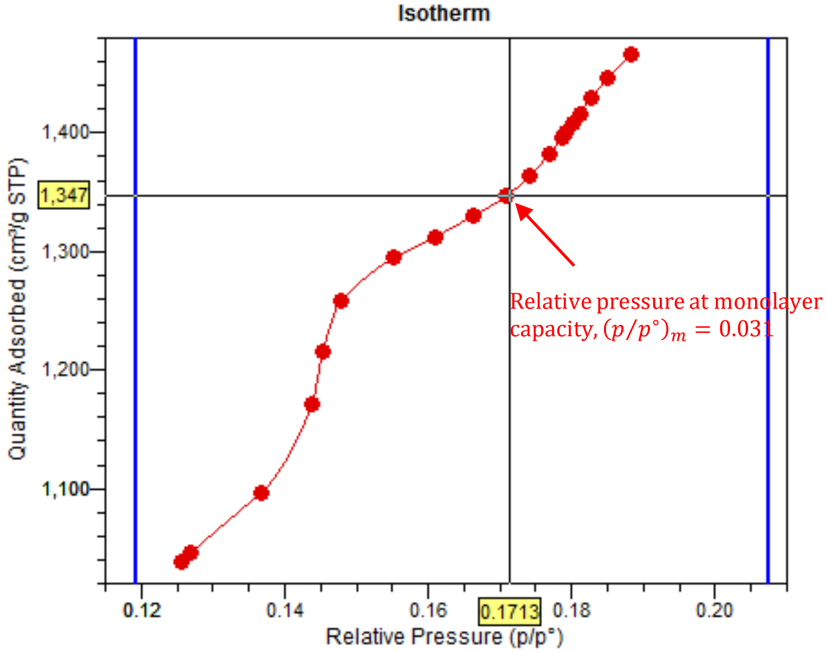

Relative pressure at monolayer capacity, $(p/p^\circ)_m = 0.031$

BET Surface Area Analysis

5. Excess Hydrogen Adsorption Isotherms of MOFs at 77 K, 87 K, 195 K, 298 K, with fits to modified D-A model

5.1 Hydrogen adsorption isotherms measured for powder MOF-5 (BASF). Data fitted to the modified D-A model. Excess adsorption (top). Total volumetric storage for packing density 0.2 g/cm^3 (bottom).

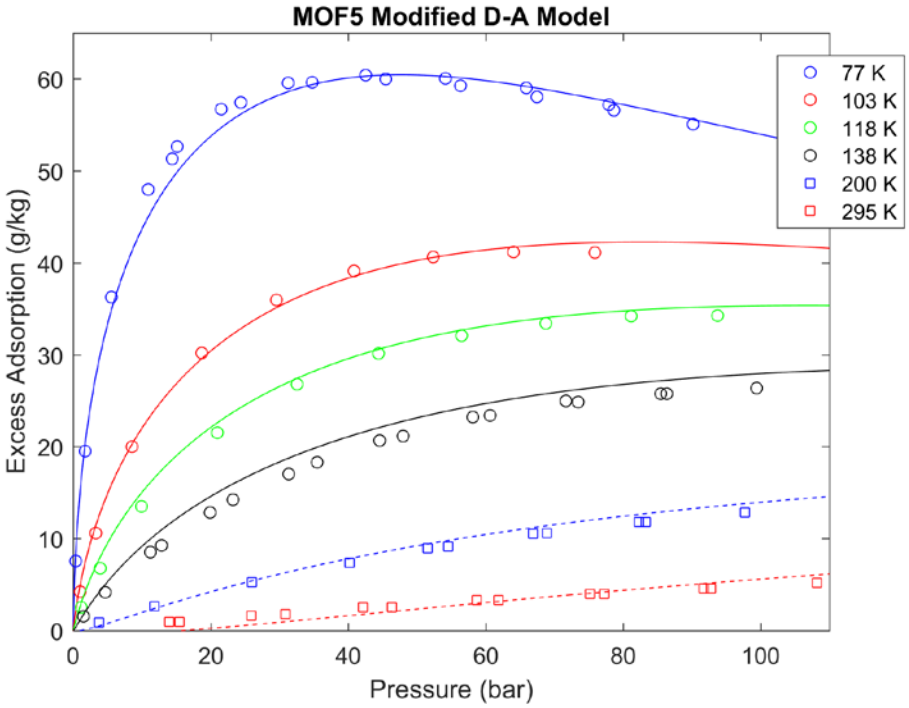

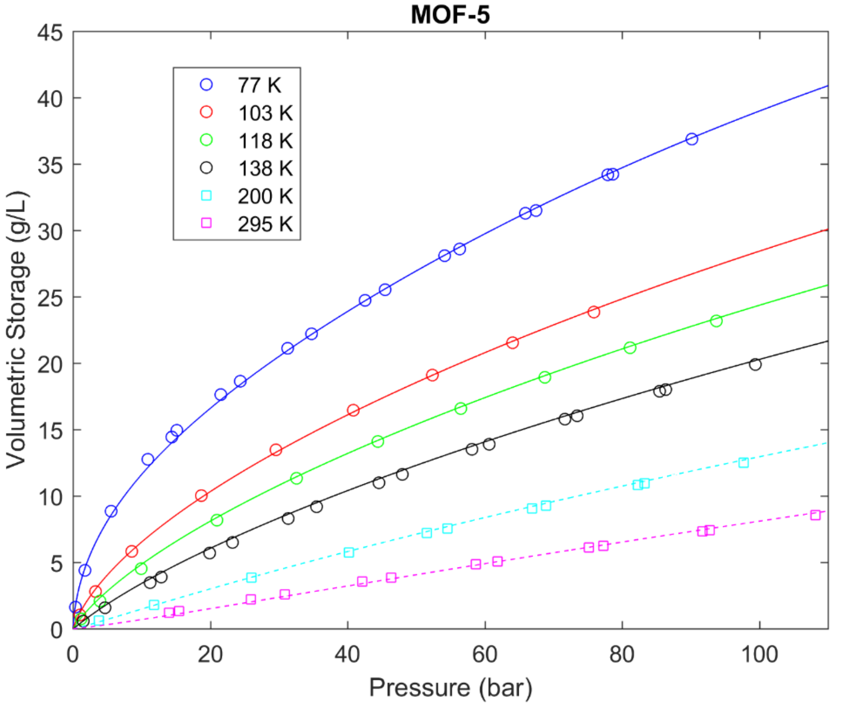

5.2 Hydrogen adsorption isotherms measured for powder IRMOF-20. Data fitted to the modified D-A model. Excess adsorption (top). Total volumetric storage for packing density 0.2 g/cm^3 (bottom).

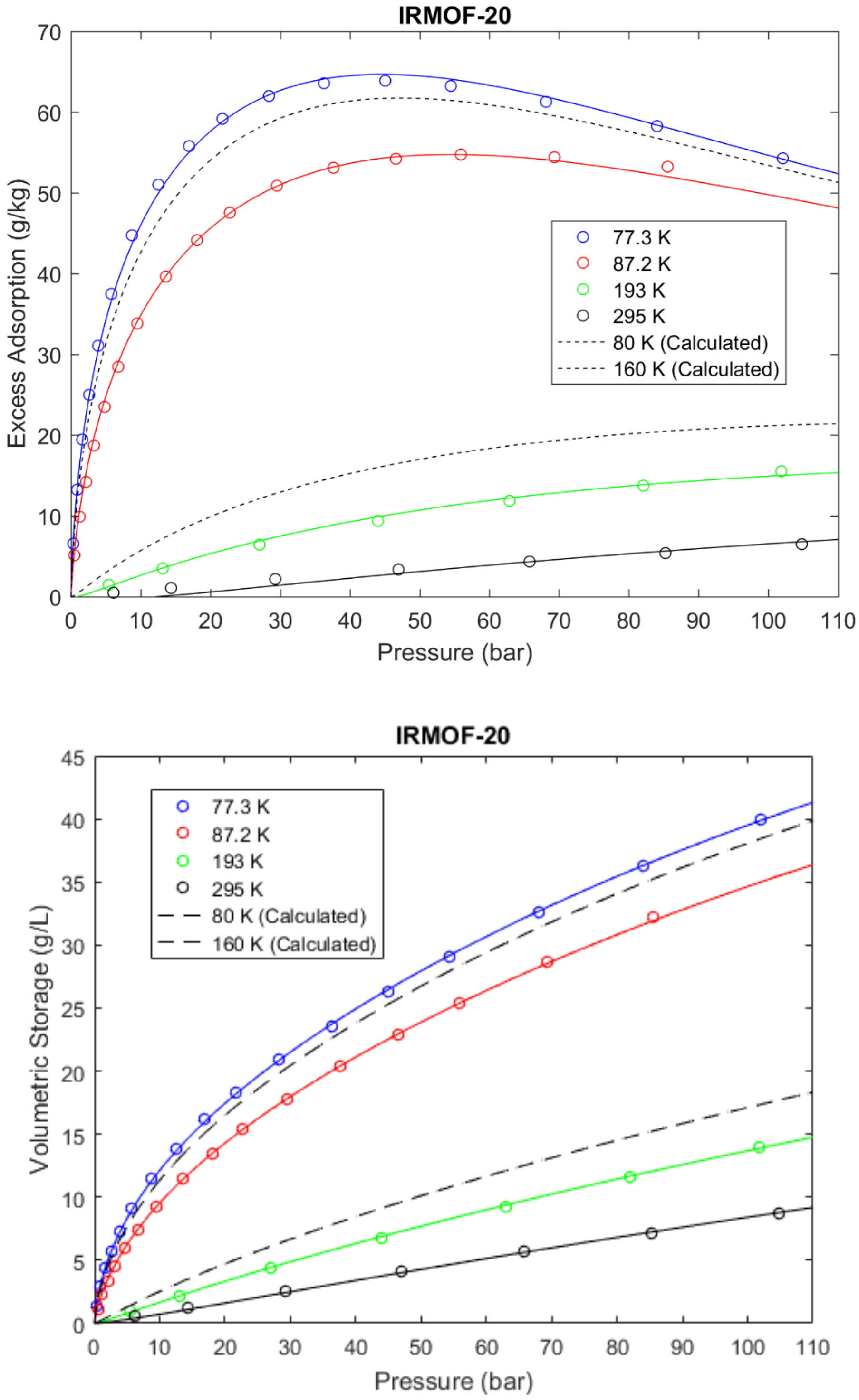

5.3 Hydrogen adsorption isotherms measured for powder DUT-23 (Co). Data fitted to the modified D-A model. Excess adsorption (top). Total volumetric storage for packing density 0.2 g/cm^3 (bottom)

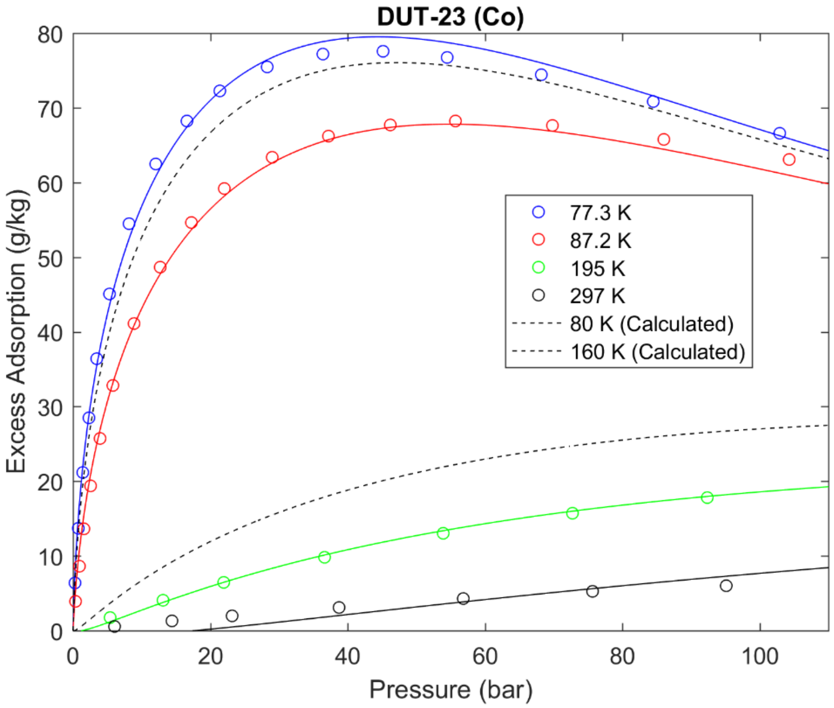

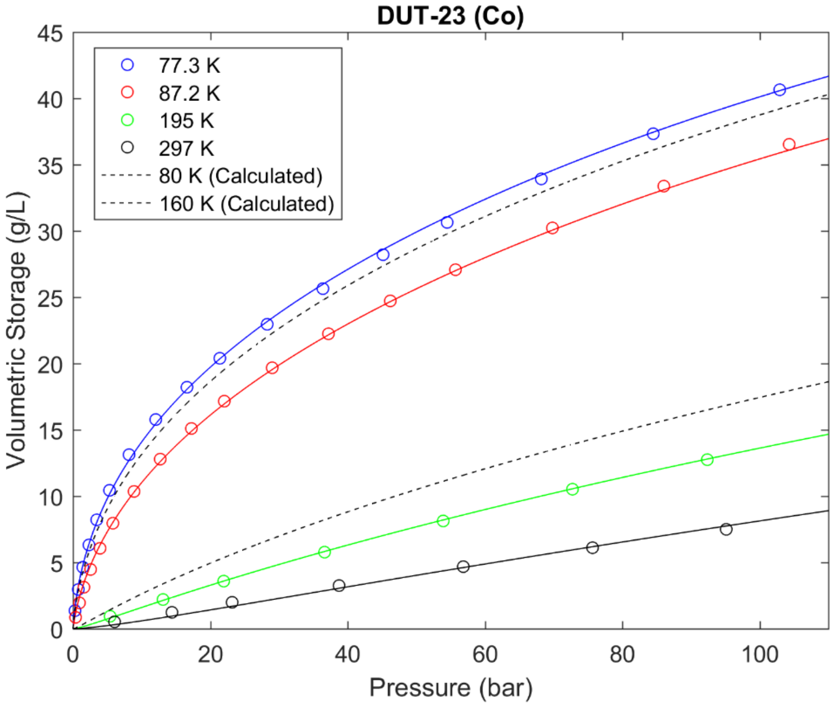

5.4 Hydrogen adsorption isotherms measured for powder MOF-177 (BASF). Data fitted to the modified D-A model. Excess adsorption (top). Total volumetric storage for packing density 0.2 g/cm^3 (bottom).

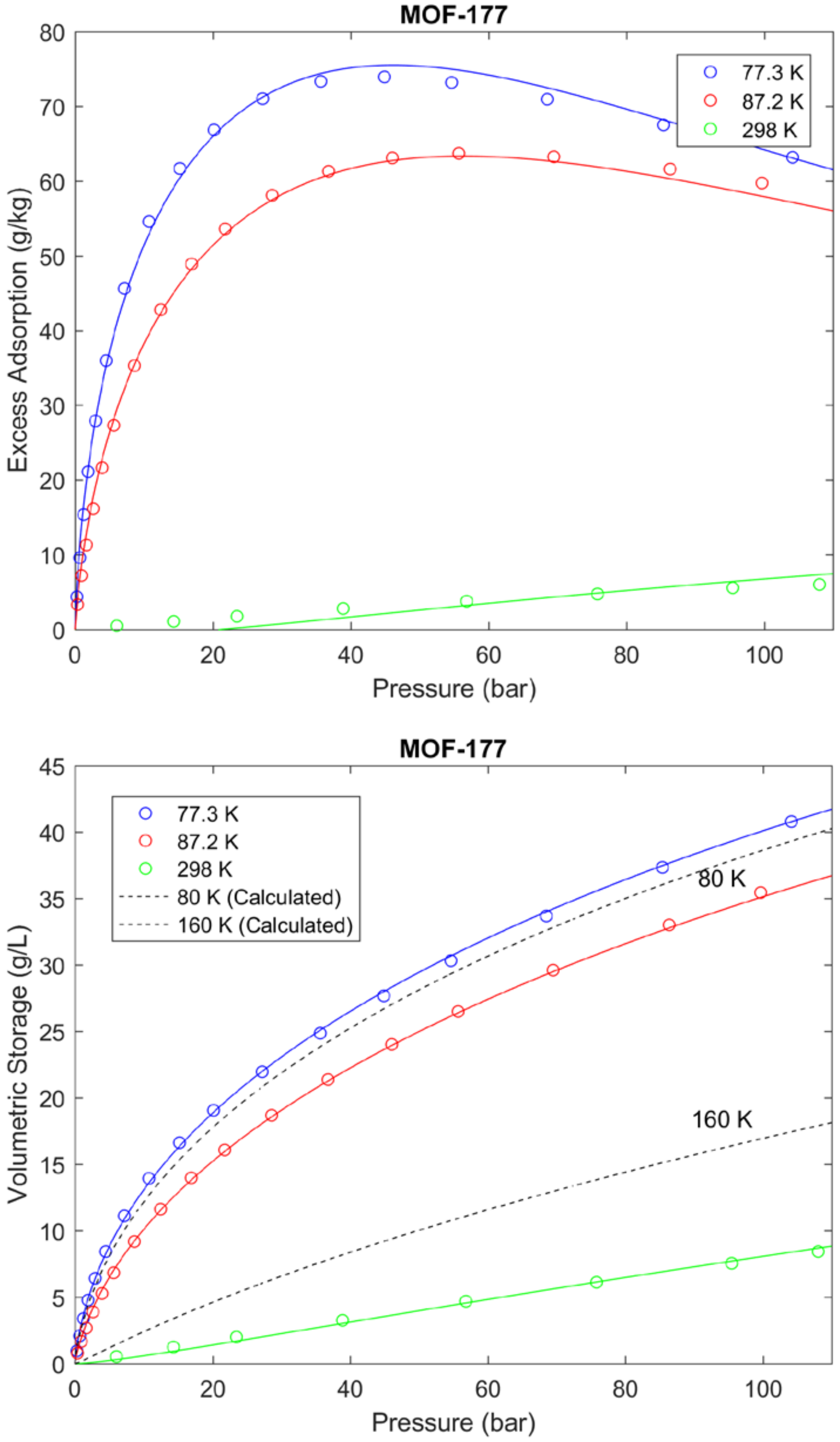

5.5 Hydrogen adsorption isotherms measured for powder SNU-70. Data fitted to the modified D-A model. Excess adsorption (top). Total volumetric storage for packing density 0.2 g/cm^3 (bottom.

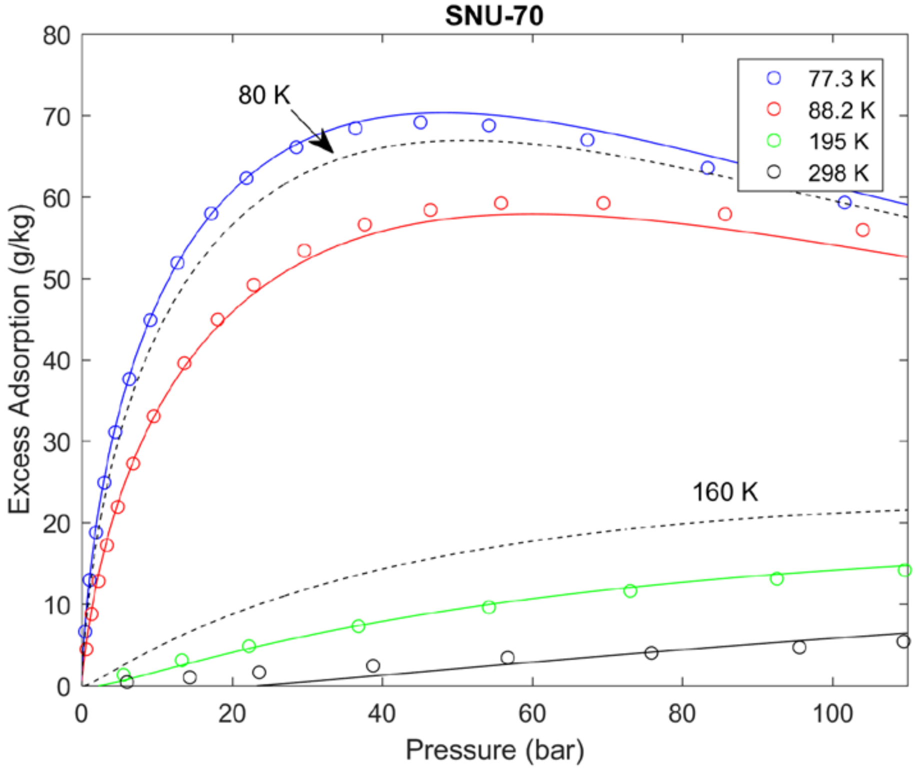

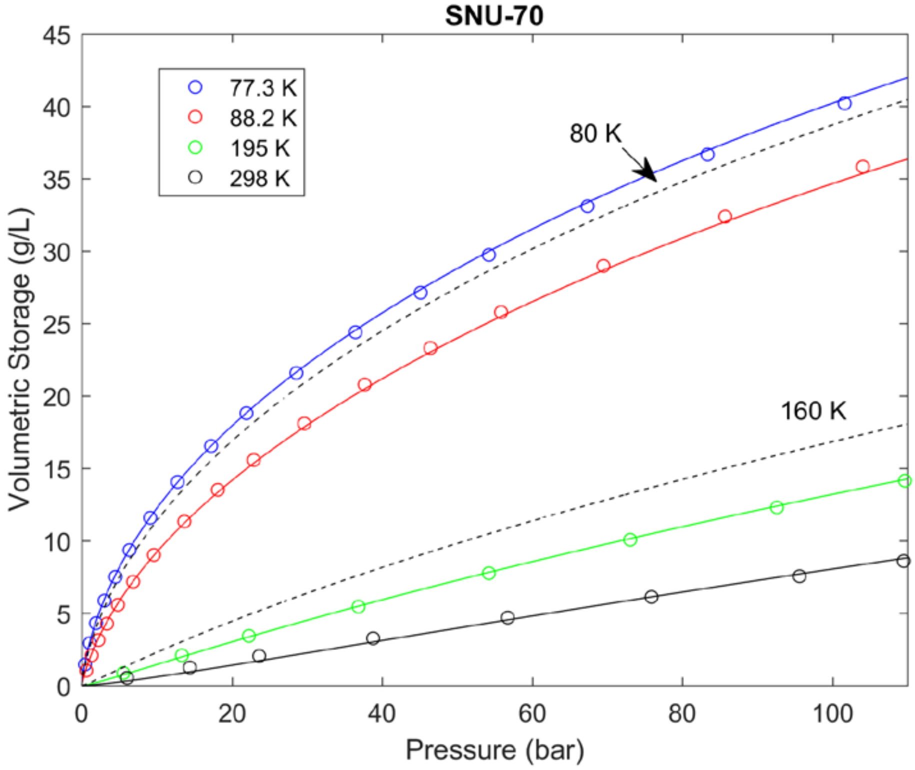

5.6. Hydrogen adsorption isotherms measured for powder UMCM-9. Data fitted to the modified D-A model. Excess adsorption (top). Total volumetric storage for packing density 0.2 g/cm^3 (bottom).

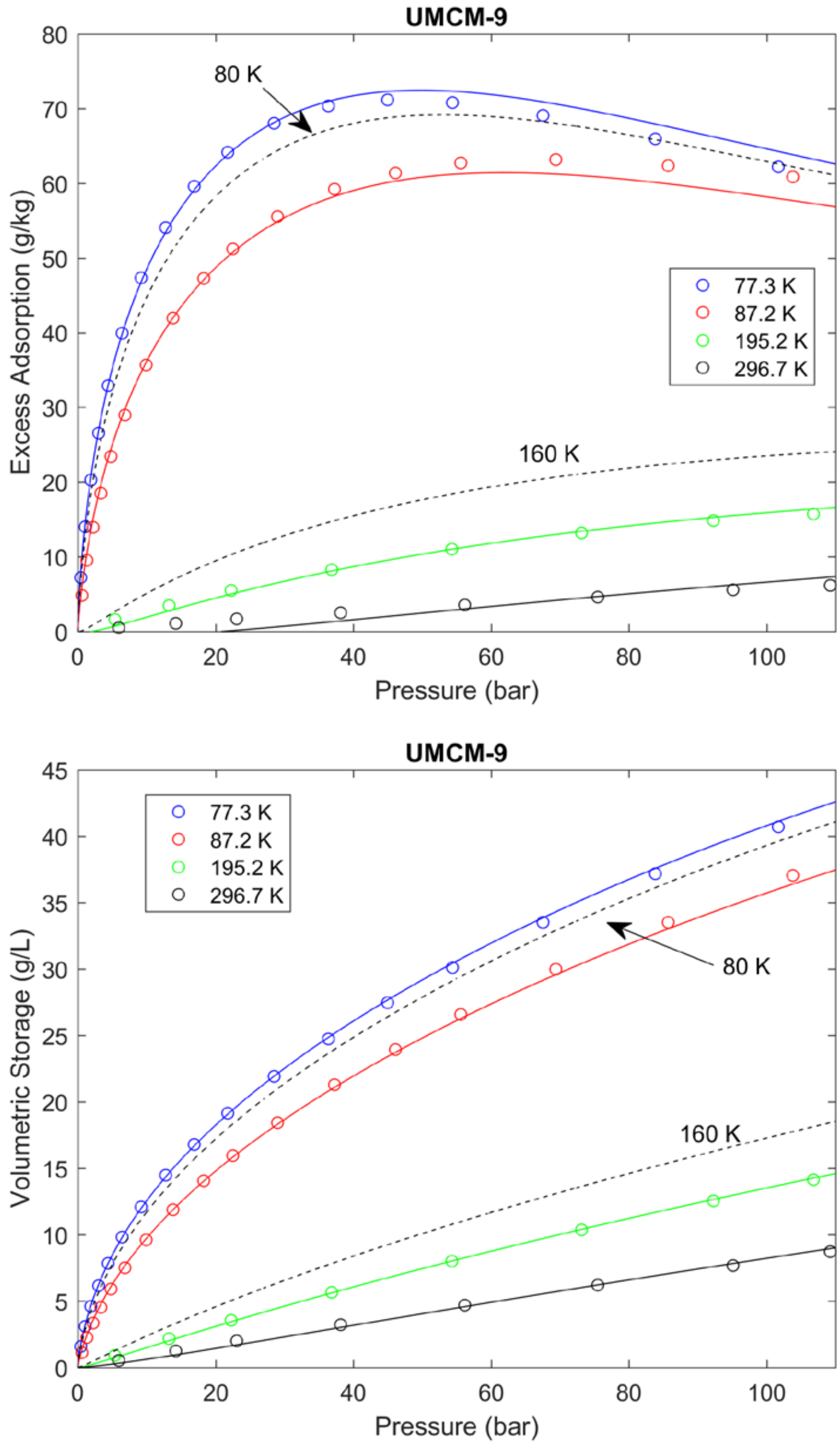

5.7 Hydrogen adsorption isotherms measured for powder NU-100. Data fitted to the modified D-A model. Excess adsorption (top). Total volumetric storage for packing density 0.2 g/cm^3 (bottom).

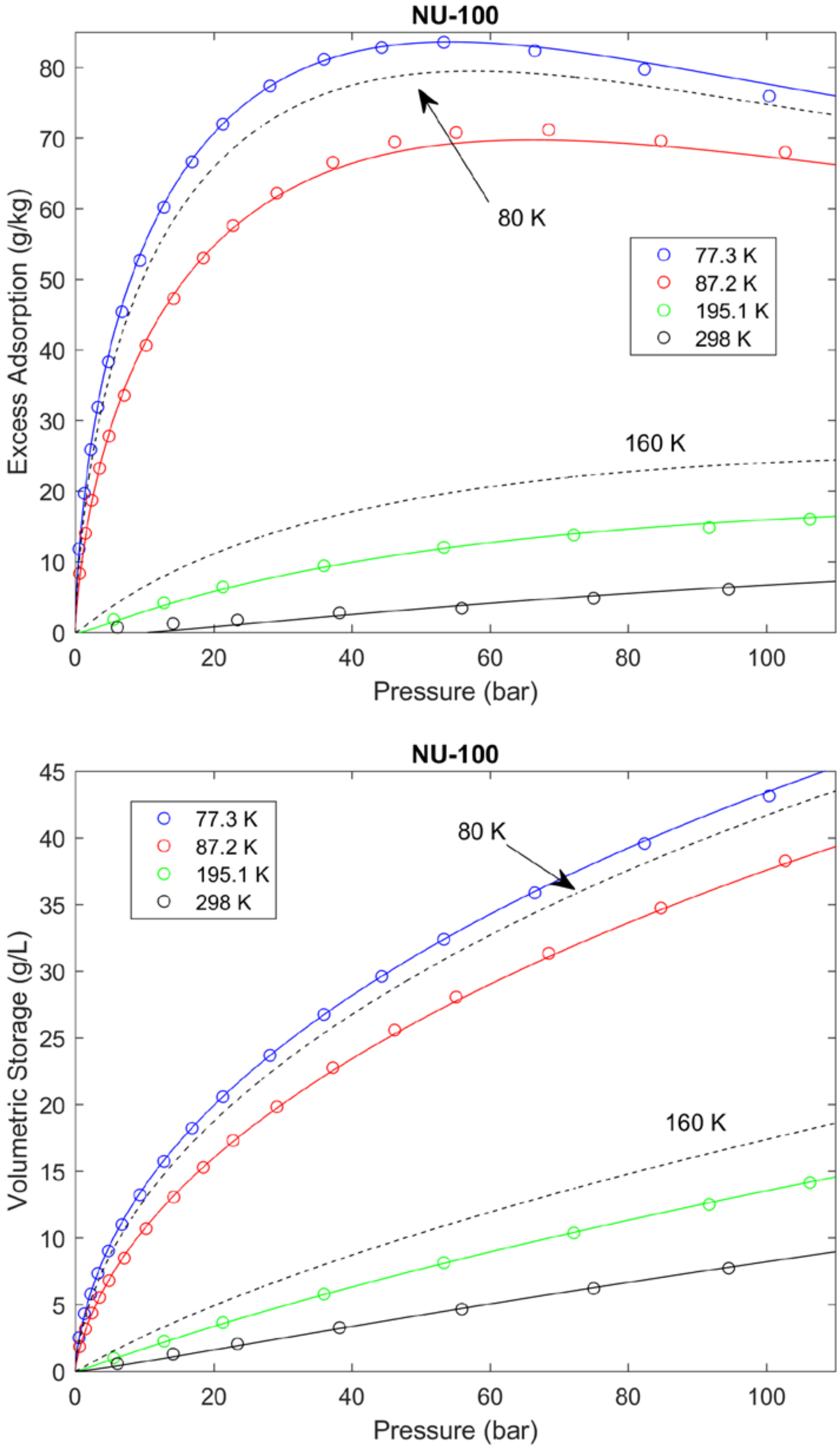

6. Differential enthalpy of hydrogen adsorption

While it is not the primary focus of this project, increasing the hydrogen adsorption enthalpy is essential for increasing storage capacity of MOFs at practical temperatures, above the cryogenic temperature investigated here. Therefore, the adsorption enthalpy was measured for many of the MOFs that were synthesized. The differential adsorption enthalpy is defined as the change in total system enthalpy based on an infinitesimal increase in the adsorption amount, such as the adsorption of a single H2 molecule. Because adsorption calorimetry is requires specialized instrument it is rarely performed. Instead the enthalpy it is calculated from adsorption isotherms utilizing the Clausius-Clapeyron equation,

$$\Delta\bar{h} = T \times \Delta v \times \left(\frac{\partial p}{\partial T}\right)_{n_a} \tag{6.1}$$

where Δv is the difference in molar volume between the gas and adsorbed phases, and the derivative describes the change in pressure versus temperature at a constant quantity of absolute adsorption (i.e., isosteric). Two approximation is typically made to this expression. First, since the molar volume of the gas phase is much larger than that of the adsorbed phase,

$$\Delta v = v_{gas} - v_{ads} \approx v_{gas} = \frac{RT}{p} \tag{6.2}$$

Second, since the enthalpy is typically calculated at low adsorption amounts where the difference between absolute and excess adsorption is very small, the absolute adsorption, n_a, can be replaced by the excess adsorption, n_{ex}. These approximations yield a simplified version of the Clausius-Clapeyron equation

$$\Delta\bar{h} = -R\left(\frac{\partial \ln p}{\partial\left(\frac{1}{T}\right)}\right)_{n_{ex}} \tag{6.3}$$

While it is preferable to measure 3 or more $\ln p$ versus $1/T$ points for each n_{ex} and determine the slope of the best-fit line, in practice it is common to measure isotherms at two temperatures, 77 K and 87 K. The adsorption enthalpy is then estimated based on the expression,

$$\Delta\bar{h} \approx -R\left(\frac{\ln p_{77} - \ln p_{87}}{\frac{1}{77.3} - \frac{1}{87.2}}\right) \tag{6.4}$$

The first step was to measure accurate hydrogen adsorption isotherms using a liquid N_2 and liquid argon bath, respectively. A high-resolution 0-1000 mbar pressure gauge was used for points below 1000 mbar. Due to the sensitivity of the calculated value to the temperatures, the daily atmospheric pressure was measured using a high accuracy barometer, and was used to determine the precise boiling point of the cryogenic bath. It is generally not necessary to measure the H_2 isotherm above 10 bar to 15 bar, because this method relies on the excess adsorption being approximately equal to the absolute adsorption (which is not valid at the higher surface coverages).

The second step is to fit the measured data to some sort of interpolating function, in order to extract the p, T pairs at fixed n_{ex} increments. A simple linear interpolation worked well (with slightly more noise in the data), but instead the data were fitted to a double Langmuir function

$$f(p) = \frac{K_1 p}{1 + b_1 \cdot p} + \frac{K_2 p}{1 + b_2 \cdot p}, \tag{6.5}$$

which provided a high fidelity fit. The third step was to use the interpolating function to resample the isotherm data over a fixed grid of excess adsorption amounts, $n_{ex,i}$, and determine the 77 K and 87 K pressures at those points. Lastly, the differential adsorption enthalpy was calculated using equation 6.4.

Differential adsorption enthalpies were measured for many of the top-performing MOFs. To facilitate meaningful comparisons, the procedure for determining $\Delta\bar{h}$ was identical for each MOF. A comparison of the experiment values are summarized in fig. 5.9 below. The main takeaway from this result is that nearly all of the MOFs have a $\Delta\bar{h}$ that falls within a similar spread, separated by less than ±0.5 kJ/mol.